eman ta zabal zazu

Universidad del País Vasco
Euskal Herriko Unibertsitatea

UNIVERSIDAD DEL PAÍS VASCO

FACULTAD DE CIENCIA Y TECNOLOGÍA

DEPARTAMENTO DE QUÍMICA INORGÁNICA

“Prussian Blue and Prussian White as electrode materials for Na-ion batteries: $A_xM[Fe(CN)_6]$ ($A = Na, K; M = Fe, Ti; 0 \leq x \leq 2$)”

By

María José Piernas Muñoz

Thesis supervisors:

Dra. Elisabet Castillo Martínez

Prof. Teófilo Rojo Aparicio

Vitoria, 19 de diciembre de 2016

RESUMEN

El presente trabajo de Tesis, titulado “Prussian Blue and Prussian White as electrode materials for Na-ion batteries: $A_xM[Fe(CN)_6]$ (A = Na, K; M = Fe, Ti; $0 \leq x \leq 2$)” se ha desarrollado bajo la supervisión y dirección del catedrático Teófilo Rojo Aparicio y la Dra. Elisabet Castillo Martínez. El trabajo de investigación se ha realizado casi en su totalidad en el centro de investigación CIC Energigune, ubicado en el parque Tecnológico de Álava, dentro de la línea de investigación de baterías de ion sodio, perteneciente al grupo de Almacenamiento de energía electroquímica liderado por el catedrático Teófilo Rojo. Y, a fin de complementar el trabajo de investigación, se realizó una estancia de 6 meses (en el periodo de Noviembre de 2015 a Mayo de 2016) en el laboratorio nacional de Argonne National Laboratory, perteneciente al Departamento de Energía de los EEUU, bajo la dirección del Dr. Christopher Johnson, líder del grupo de Materiales de la División de Ciencias e Ingeniería.

El objetivo principal de la Tesis, ha consistido en la búsqueda y caracterización de nuevos materiales para baterías de ion sodio y en concreto se han seleccionado los materiales de la familia del Azul de Prusia (*Prussian Blue* en inglés). Los motivos que nos llevaron a tal fin, así como los resultados más novedosos de este trabajo de investigación, se exponen brevemente a continuación.

El consumo energético ha experimentado un incremento exponencial durante las últimas décadas y se prevé una demanda de energía aún mayor en los años venideros. Actualmente, los combustibles fósiles son la fuente de energía dominante que sustenta la economía global. No obstante, la dependencia de estos combustibles tiene consecuencias problemáticas, entre las que destacan el suministro finito de las mismas por tratarse de fuentes agotables y las emisiones contaminantes que generan, que acidifican nuestros océanos y contribuyen al indeseado calentamiento global. Estos hechos hacen que sea necesario un cambio gradual hacia fuentes de energía renovables más sostenibles, pero tal cambio requiere del acoplamiento con sistemas de almacenamiento energético para superar la intermitencia de las fuentes renovables.

El almacenamiento de energía electroquímica y, específicamente, las baterías son una de las posibles herramientas utilizadas en aplicaciones estacionarias a gran escala, debido a su tamaño compacto, modularidad y escalabilidad. Aunque, principalmente, las baterías de ion litio se han utilizado en dispositivos para aplicaciones a pequeña y mediana escala, como en dispositivos electrónicos portátiles o en coches eléctricos, ya existen algunas plantas piloto basadas en esta tecnología para el almacenamiento estacionario de energía. Sin embargo, y a pesar de la menor densidad energética que éstas son capaces de proporcionar, las nuevas tendencias para esta aplicación a gran escala se están centrando en la sostenibilidad, disponibilidad y bajo coste de las

novedosas baterías de ion sodio, que emergen como serios competidores frente a la tecnología de litio. Además del menor coste debido a abundancia del sodio (el sexto elemento más abundante en la corteza terrestre, con aproximadamente un 2.6 %), este tipo de baterías ofrece la posibilidad de utilizar colectores de corriente de aluminio para el electrodo negativo (a diferencia de las baterías de ion litio, que necesitan cobre), lo que abarataría aún más su precio de mercado.

Si bien el sodio posee propiedades físico-químicas similares a las de litio y, en principio, el conocimiento adquirido en las baterías de ion litio (LIB) podría transferirse a las baterías de ion sodio, la realidad es totalmente distinta. Existen diferencias significativas entre ambos elementos: como el peso atómico (3 veces mayor para el sodio), el potencial electroquímico estándar (aproximadamente 0.3 V menos negativo para el sodio) y el radio iónico (1.02 Å para sodio comparado con los 0.76 Å de litio); y estas desigualdades conllevan diferencias sustanciales en la electroquímica de ambos elementos. Como ya se ha mencionado anteriormente, las baterías de ion sodio (NIB) suministran una menor densidad gravimétrica comparada con la análoga de litio, lo que se debe a la diferencia de potencial que existe entre ambos elementos. Además, el mayor radio iónico de los iones sodio en comparación con los de litio, requiere encontrar nuevos materiales para electrodos con espacios intersticiales suficientemente grandes capaces de acomodarlos a estos iones de mayor tamaño.

Uno de los materiales que fueron escasamente estudiados para baterías de ion litio, pero que durante los últimos 4 años (contemporáneo a la realización de la presente Tesis doctoral) han resurgido y se postulan como firmes candidatos en baterías de ion sodio para aplicaciones en dispositivos reales, son los *metalorganic frameworks* conocidos como *Prussian Blue* o hexacianometalatos. La fórmula general de los análogos del *Prussian Blue* se define como $AM[M'(CN)_6]\cdot xH_2O$ (A = Li, Na, K; M, M'= metal de transición; donde M = M' a veces y normalmente M'= Fe), siendo $KFe[Fe(CN)_6]\cdot xH_2O$ el compuesto conocido concretamente como *Prussian Blue*. Esta familia de compuestos se caracteriza por su facilidad de síntesis (en medio acuoso y, generalmente, a temperatura ambiente) y la abundancia de sus componentes, lo que concuerda perfectamente con la filosofía de bajo coste de la tecnología de sodio. Otra característica atractiva que presenta este tipo de compuestos es su estructura 3D metalorgánica, con canales abiertos y modulables que facilitan una rápida inserción/difusión de metales alcalinos (Li, Na, K), alcalino-térreos (Mg^{2+}, Ca^{2+}) e incluso boroideos (Al^{3+}). Los análogos del *Prussian Blue* (PBA) adoptan generalmente una estructura cúbica (grupo espacial *Fm*-3*m*) con parámetros de red de aproximadamente a = 10.18 Å, en la que el metal M'^{II} de bajo spin y el metal M^{3+} de alto spin coexisten en los vértices de un pequeño cubo conectados por aniones lineales (grupos ciano) a lo largo de las 3 direcciones del espacio, proporcionando distancias entre centros metálicos $M^{3+}\text{-N}\equiv\text{C-}M'^{II}$ de unos 5 Å. Estas cavidades tan grandes, que están semiocupadas por iones alcalinos en el caso de las especies de *Prussian Blue*, son las que permiten la inserción reversible de los mismos.

En la presente Tesis, algunos de estos compuestos *Prussian Blue* (PBA) han sido objeto de estudio. Se ha explorado su idoneidad como materiales para electrodos, principalmente en NIB, no sólo como cátodos sino también, por primera vez, como ánodos. Paralelamente, y únicamente como electrodos negativos, se han realizado estudios de la adecuación de estos materiales para baterías de ion litio (LIB). Principalmente, los *Prussian Blue* puramente de hierro, $A_xFe[Fe(CN)_6]\cdot yH_2O$ (A = Na/ K, $0 \leq x \leq 1$), y sus fases reducidas conocidas como *Prussian White* o sal de Everitt, $A_{2-x}Fe[Fe(CN)_6]$ ($x \sim 0.5$), constituyen el conjunto de compuestos en los que se ha centrado la investigación. El análogo o derivado de titanio, $A_xTi[Fe(CN)_6]\cdot zH_2O$ or $Ti[Fe(CN)_6]\cdot H_2O$, también ha sido objeto de investigación.

La síntesis del derivado de titanio del *Prussian Blue*, $Ti[Fe(CN)_6]$, se ha intentado por nuevas y diversas rutas sintéticas (síntesis en estado sólido, en medio orgánico, solvotermal, acuosa, mediante precursores y siguiendo la ruta del trifluoroacetato), con el objetivo de conseguir un material anódico potencialmente de bajo voltaje para NIB. Las diversas síntesis y la caracterización estructural de los materiales conseguidos a través de ellas, principalmente mediante difracción de rayos X (PXRD), se recoge en el capítulo 3 de este manuscrito. Únicamente los materiales obtenidos como fases puras, se destinaron al estudio electroquímico como ánodos para NIB orgánicas, cuyos resultados se presentan en el capítulo 4. De ellos se puede deducir que, a pesar de los esfuerzos invertidos para su preparación, el derivado de titanio del *Prussian Blue* es electroquímicamente inactivo a bajos potenciales para NIB.

Mediante el método de co-precipitación, se han preparado las fases sodiadas y potasiadas de *Prussian Blue* puramente de hierro (A-PB), $A_{1-x}Fe_{1+x/3}[Fe(CN)_6]\cdot yH_2O$ (A = Na, K), las más sostenibles y medioambientalmente benignas entre todos los PBA. En el capítulo 3, se presenta una amplia caracterización estructural, morfológica y fisicoquímica de las fases puras de los materiales A-PB, que incluye difracción de rayos X (PXRD), infrarrojo (IR), Raman, análisis termogravimétrico (TGA), microscopía electrónica de barrido y de transmisión (SEM, TEM), análisis elemental (H, C, N), espectroscopia de absorción/emisión atómica (AAS y/o AES), espectroscopia fotoelectrónica de rayos X (XPS) y espectroscopia ^{57}Fe-Mössbauer.

Aunque los PBA se han estudiado intensamente como cátodos, su funcionamiento en medio orgánico como ánodos ha sido escasamente analizado en LIB y permanece inexplorado en NIB. Por consiguiente, en este trabajo, se ha llevado a cabo esl estudio del comportamiento electroquímico de los A-PB (A = Na, K) en la región anódica para ambas tecnologías (véase capítulo 4). Asimismo, se ha llevado a cabo la optimización del binder (aglutinante) para la fase sodiada Na-PB en NIB. De todos los binders que se ensayaron (PVDF (polyvinylidene fluoride), CMC (sodium carboxymethyl cellulose), EPDM (ethyelene propylene diene monomer) y PTFE (teflon)), CMC proporcionó los mejores resultados. Y la combinación con styrene-butadiene rubber (SBR), contribuyó a mejorar aún más su electroquímica. Por otra parte, los resultados electroquímicos del K-PB a bajos voltajes en baterías de ion litio (LIB), proporcionaron capacidades superiores a las esperadas para un mecanismo de intercalación típico (véase capítulo 4). Para explicar la alta capacidad mostrada por K-PB, se llevaron a cabo varios experimentos *ex-situ* (XRD, IR, SEM y TEM). El análisis de los datos extraídos, nos llevó a proponer un mecanismo de conversión, por primera vez considerada para este tipo de materiales, lo cual se confirmó mediante realización de experimentos *ex-situ* de espectroscopia de absorción de rayos X (XAS) e *in-situ* Mössbauer. Cabe destacar que la celda *in-situ* Mössbauer utilizada en los experimentos ha sido desarrollado íntegramente en este trabajo de tesis como parte de la investigación (como se muestra en el capítulo 2).

También, se han realizado investigaciones con el Na-PB para NIB en el rango de alto voltaje, tal y como recoge el capítulo 5. Dada la amplia gama de combinaciones reportadas en la bibliografía, se ha llevado a cabo un estudio sistemático para determinar el electrolito y el binder óptimos para Na-PB cuando actúa como cátodo en baterías de ion sodio orgánicas. Una gran variedad de mezclas de carbonatos utilizando $NaClO_4$ y $NaPF_6$ como sales (12 electrolitos en total), se testaron realizando medidas galvanostáticas y de impedancia. El electrolito óptimo resultó ser 1M $NaPF_6$ en EC: PC: FEC (49:49:2) (EC = carbonato de etileno, PC = carbonato de propileno, FEC = carbonato de fluoroetileno). Se hicieron experimentos con los mismos 4 binders usados para Na-PB a bajos voltajes. En este caso, en el rango catódico, PVDF resultó ser el mejor binder.

Además, se ha llevado a cabo un estudio comparativo del rendimiento de Na-PB a altos voltajes en NIB acuosas. Los primeros resultados indicaron que, de los 2 procesos redox que tiene lugar cuando se cicla el material, el proceso a más alto voltaje solapaba con la oxidación del H_2O, y consecuente evolución de O_2. En ese proceso, el material además presentaba inestabilidad, posiblemente a consecuencia de la peptización del mismo. Por consiguiente, la ventaja de potencial tuvo que reducirse para estudiar únicamente el proceso que tiene lugar a bajo voltaje. En este rango, se consiguieron buenos resultados, con capacidades comparables a las reportadas en la literatura para otros análogos y excelentes eficiencias culómbicas. Además, de una polarización despreciable, en comparación a las medidas resultantes llevadas a cabo en medio orgánico.

Mediante un nuevo método de síntesis (desarrollado en esta tesis) se obtuvieron fases cúbicas de Prussian White puramente de hierro y enriquecidas en álkali (K-PW), $A_{2-x}Fe_{1+x/2}[Fe(CN)_6]\cdot yH_2O$ (A = Na, K), y se caracterizaron exhaustivamente (PXRD, IR, Raman, TGA, SEM, TEM, análisis elemental, AAS y/o AEX, XPS y espectroscopia ^{57}Fe-

Mössbauer), tal como se recoge en el capítulo 3. Estas fases, presentan mejores propiedades electroquímicas como materiales para cátodos en NIB orgánicas, como alta capacidad, mayor eficiencia coulómbica en el primer ciclo y ciclabilidad a largo plazo, en comparación con Na-PB (véase capítulo 5). Curiosamente, se observó un aumento beneficioso de 0.35 V en el plateau a alto voltaje de la fase potasiada, que resultó ser consecuencia de la inserción de K^+ en lugar de Na^+ en ese proceso. Por tanto, se descubrió que la utilización K-PW en NIB proporciona una batería de ion sodio-potasio híbrida. Es digno de mencionar que las propiedades de la fase de potasio superan a las de su análogo de sodio, probablemente debido a su naturaleza híbrida y al efecto sinergístico que tiene lugar entre el Na y el K.

Finalmente, y con el fin de evaluar la posible aplicación de algunas de estas fases en un futuro prototipo, se ensamblaron/construyeron con éxito celdas completas de ión sodio con todos los cátodos evaluados en la presente tésis, es decir, Na-PB, Na-PW y K-PW, utilizando como ánodo hard carbon comercial. Los mejores valores de energía gravimétrica se obtuvieron con las fases de Prussian White. Curiosamente, y en contra de lo esperado, los valores obtenidos para las baterías completas utilizando A-PW, fueron exactamente los mismos. Las medidas se realizaron en la etapa final del proceso de tésis y únicamente se pudo llevar a cabo una primera aproximación. En cualquier caso y, a pesar de que un mejor balance de masas podría haber proporcionado una mayor energía, las celdas completas desarrolladas en este trabajo de tesis, sirven como prueba de concepto para la utilización de materiales como el Na-PB o los Prussian White en aplicaciones reales de baterías.

Abstract

Energy consumption has suffered an exponential increase in the last decades and even a growing energy demand is forecasted for future years. Fossil fuels are currently the dominant source of energy powering the global economy. Nevertheless, the dependence in them has problematic consequences, as the contaminant emissions that are acidifying our oceans and creating global warming and the finite supply of these depletable sources. These facts make necessary a gradual shift towards more sustainable renewable energies, but such change requires coupling with energy storage systems to overcome their intermittency in output power. Electrochemical energy storage and specifically batteries are one of the possible tools deployed for large-scale stationary applications, as a result of its compact size, modularity and scalability. Indeed, pilot plants for stationary energy storage based on Li-ion battery technology are now a reality. However, new tendencies are focusing on the sustainability, availability and low price of Na-ion batteries, which emerge as a promising competitor of the lithium technology. Although sodium presents similar physico-chemical properties to lithium, the larger ionic radio of sodium makes necessary to find host electrode materials with sufficiently large interstitial space to accommodate the bigger sodium ions.

In this thesis, some Prussian Blue materials (PBA) have been the object of study. Given the open and tunable 3D channels they present, its suitability as electrode materials mainly in Na-ion batteries (NIB), both as anodes and cathodes, have been explored. Also, some studies in Li-ion batteries (LIB) have been conducted.

The synthesis of the titanium Prussian Blue derivative, $Ti[Fe(CN)_6]$, has been attempted by several new synthetic routes, with the aim of achieving a potential low-voltage anode material for NIB. Its structural and electrochemical characterization as anode material for Na-ion batteries is under study in this manuscript.

Purely iron based Prussian Blue sodiated and potassiated (A-PB), $A_{1-x}Fe_{1+x/3}[Fe(CN)_6]\cdot yH_2O$ (A = Na, K), the most sustainable and environmentally benign among all the PBA, have been prepared following the traditional co-precipitation method. A wide structural, morphological and physico-chemically characterization of the single phase A-PB materials is presented along this work. Although PBA have been intensively studied as cathodes, their operation as anode materials is scarcely exploited in LIB and unexplored for NIB. Consequently, the electrochemical performance of A-PB (A = Na, K) was investigated in the anodic region for both technologies in this work. On the one hand, a binder optimization was carried out for Na-PB in NIB. On the other hand, the reaction mechanism that K-PB undergoes in LIB at such low voltages has also been unveiled. Several *ex-situ* experiments, including PXRD, IR, SEM and TEM, led us to propose a conversion mechanism to explain the high capacity delivered by K-PB. The realization of *ex-situ* XAS and *in-situ* Mössbauer experiments allowed confirming the conversion reaction, for the first time proposed for this type of materials. Noteworthy to say that the in-situ Mössbauer cell used in the experiments has been developed as part of this thesis research work.

On the other hand, investigations in the high voltage range (cathode) have also been performed to determine the optima electrolyte and binder for Na-PB in NIB, given the wide

range of combinations of the former encountered in the literature. Besides, a comparative study of the Na-PB performance in aqueous NIB has also been performed.

Purely iron based alkali rich cubic Prussian White (K-PW), $A_{2-x}Fe_{1+x/2}[Fe(CN)_6]\cdot yH_2O$ (A = Na, K), have also been obtained through a novel synthesis (here developed) and have been thoroughly characterized. These phases presented enhanced electrochemical properties as cathode materials in NIB, such as high capacity, higher first cycle coulombic efficiencies and long-term cyclability, compared to Na-PB. Interestingly, a beneficial increase of 0.35 V in the upper voltage plateau was observed in the potassiated phase, as a result of insertion of K^+ instead of Na^+. Therefore, it was discovered that the utilization of K-PW in NIB provides a hybrid Na,K-ion battery.

Finally, sodium-ion full cells of Na-PB, Na-PW and K-PW were successfully assembled using commercial hard carbon as anode in order to evaluate the possible application of these phases for a future prototype.

Agradecimientos / Acknowledgements

Aún no me puedo creer que haya llegado este momento... Han sido cuatro años estupendos de los que no cambiaría ni el más mínimo detalle.

La tesis doctoral realizada durante estos años es la suma de muchos esfuerzos y por eso quiero agradecer el trabajo y el apoyo que he recibido de muchas personas.

En primer lugar me gustaría agradecer a mis directores de tesis, la Dra. Elisabet Castillo Martínez y el catedrático D. Teófilo Rojo Aparicio. Muchas gracias por haberme dado la oportunidad de hacer realidad uno de mis sueños. No os hacéis una idea de lo que esto significa para mí. Gracias por vuestra inestimable dedicación, implicación, esfuerzo, apoyo, ayuda y compresión pero, sobre todo, por haberme guiado tan bien a lo largo de este camino (aunque, a veces, no fuera fácil) y por todo lo que me habéis enseñado y yo he podido aprender de vosotros.

También quiero agradecer al CIC Energigune por la oportunidad de poder desarrollar este trabajo de tesis, así como al Gobierno Vasco por la beca predoctoral (PRE_2013_1_790) concedida durante los 3 años y por la beca EGONLABUR (EP_2016_1_0036) para realizar una estancia de 3 meses en Argonne National Laboratory.

I would also like to aknowledge Dr. Christopher Johnson, Group Leader of the Materials Group within the CSE Division at Argonne National Laboratory (ANL). Thank you for hosting me so nicely and sharing with me your extensive knowledge. Also, I would like to thank the experts of XAS, Dr. Timothy Fister and Dr. Soojeong Kim, for their help with the synchrotron measurements. Of course, I could not forget all the people that allow me to have a fantastic stay at ANL and that treated me so kindly: Anna, Naresh, Nicole, Ling-Hong, Javier, Ira, Andy, E. J. and Arturo. And special thanks to Fred Aguesse, my CIC Energigune coworker and friend, for taking care of me and put up with me.

I would like to give special thanks to Prof. Michel Armand for sharing with us his wisdom. It has been an honor for me to meet you and work with you.

Me vais a permitir darles las gracias a los catedráticos Mª Dolores Santana Lario y Gabriel García Sánchez, de la Universidad de Murcia, quienes me abrieron las puertas al mundo de la investigación, con el que yo tanto disfruto.

También, quiero agradecer al Dr. Garitaonaindia, a la Dra. Estíbaliz Legarra de la UPV/EHU y a la Dra. Eider Goikolea del CIC Energigune por su inestimable ayuda en la realización de los experimentos de Mössbauer. A los servicios generales de investigación de la UPV/EHU (SGIKER). Así como a mis compañeros del CIC Energigune: Egoitz Martín, María Jauregui, Jon Ajuria, Yan Zhang, Francisco Bonilla, Wei Zhang, Alex Bondarchuk, Vladimir Roddatis, Juan Luis Gómez, Antonio Fernández, Montse Casas… que han contribuido en este trabajo.

Quisiera dar las gracias a todas aquellas personas que han hecho mi día a día más fácil en el transcurso de esta tésis. A mis compañeros "de escritorio": Edurne Redondo, Egoitz Martín, Laida Otaegui, Aitor Villaverde, Marine Reynaud, Gurpreet Singh y Guillermo Liendo. Ha sido un placer compartir con vosotros estos años de mi vida. Gracias por el buen ambiente de trabajo y compañerismo del que hemos disfrutado. Daba gusto llegar los lunes por la mañana y comenzar la semana poniéndonos al día de lo que habíamos hecho a lo largo del fin de semana. Tenéis que saber que cada vez que me coma una gominola, me acordaré de vosotros… A Maider Zarrabeitia, por esos findes de ciencia al máximo que nos hemos pegado en los últimos 2 años. A Adriana Navarro, por su energía y por estar siempre dispuesta a organizar un plan (echaré de menos los pintxo-potes y que me llames "grandma"). A Naira Soguero, JuanLu Gómez y Unai Narcue por esos maravillosos y divertidos viajes en coche. A Noel Díez y Dani Carriazo por esas conversaciones tan interesantes y entretenidas durante la hora de la comida. A Begoña Acebedo y Nuria Gómez por recibirme siempre con una sonrisa, cada vez que les preguntaba por algún material de laboratorio u otras cosas.

Quiero agradecer, en especial, a varias personas que comenzaron siendo compañer@s pero que, con el transcurso del tiempo se han hecho un hueco en mi corazón. A mi madrileña Elena Gonzalo y a mi catalana Montse Galcerán. Comenzamos nuestra andadura en el CIC casi al mismo tiempo. Ya ha llovido, ¿eh? Gracias por estar siempre pendientes de mí, por ayudarme con la ciencia y con lo personal, por cuidarme y por entenderme. Habéis sido esas hermanas mayores, que todos quieren tener. Antes de que me marche, tenemos que repetir el bocata en La Riojana… I would like to thanks William Manalastas, for getting me out a smile every single time we met each other. It has been a pleasure to meet such a great scientist and nice person as you are. I will miss those days we stayed late at work side by side. Thanks also to Emilie Bekaert and Lucienne Buannic for their trust, support and the fantastic evenings/days we have spent together in the Lake, Senda-Viva or just going out. We have pending a stone massage! And talking about French friends… Thanks to my "cacahuete" Morgane Giner. Thanks for joining me when I needed to go to CIC, even if it was a weekend day. But above all, thanks for your nice conversations, joy, support, kindness and for always showing up with a smiley face. Y cómo no, gracias a mi asturiana favorita, Cris Botas. Gracias por "obligarme" a salir a dar paseos durante el transcurso de la escritura de la tésis para ayudarme a desconectar. Gracias por tu apoyo y por tu confianza, porque contigo siempre es fácil hablar de cualquier cosa. Thanks to all for the good times we have shared during the "pintxo-pote´s night", the Saturday´s nights, Halloween parties or those days in "The Lake". Simply, thank you for being there! Os echaré de menos/I will miss you!

A mis amigas de Murcia, porque aunque físicamente no nos hayamos podido ver todo lo que quisiéramos, vuestra amistad en estos años ha sido imprescindible. Gracias por esos mensajes y llamadas de ánimo y apoyo y por estar ahí siempre, tanto en los momentos buenos como en los malos. Sois increíbles. (¡Ya lo celebraremooooos!)

A esa superfamilia que tengo, que siempre se interesa por cómo estoy, cómo va la investigación y cómo va todo. Gracias. Es un orgullo formar parte de una familia como la nuestra. En especial, a mi abuela, por todo lo que la pobre ha sufrido porque estaba lejos de casa y, sobre todo, cuando estuve de estancia en USA.

Por último, quiero dar las gracias a mis padres Antonio y Jose, a mi hermano Antonio y a novio/prometido Mariano (Siii! Por fin, podremos empezar a organizar la boda ;)). Es difícil expresar con palabras lo que ahora mismo siento... sólo puedo decir que esta tésis no habría sido posible sin vosotros. A pesar de la distancia, habéis sido mi apoyo más incondicional. Gracias por haberme animado en los momentos más difíciles, por hacerme ver la vida siempre con positividad y por alentarme a alcanzar mis metas. Estoy muy agradecida de tener en mi vida a unas personas tan maravillosas como vosotras. Esta recompensa, que siempre decís que no tiene lugar sin esfuerzo, os pertenece también a vosotros. Os quiero.

Table of contents

Chapter 1. Introduction

Chapter 2. Experimental techniques

Chapter 3. Synthesis and structural, morphological and physico-chemical characterization of the materials

Chapter 4. Prussian Blue phases as anodes in Na-ion and Li-ion batteries

Chapter 5. Prussian blue phases as cathodes in Na-ion batteries

Chapter 6. Development of Na-ion full cells based on Prussian Blue and Prussian White materials

Chapter 7. Conclusions and perspectives

Appendix

Chapter 1

Introduction

1 .-) Introduction

This introduction chapter begins with a general overview of the current energy demand and production of energy, and continues enumerating the major energy storage systems available to date. In the following section, attention is focused on the electrochemical energy storage by means of battery systems. This section includes a brief classification of the most remarkable primary and secondary batteries and, then, presents a more detailed vision of the Li-ion and Na-ion battery technologies. A synopsis of the Prussian Blue materials and their performance in rechargeable batteries, especially in Na-ion batteries, is collected at the end of the chapter, which leads to stablish the targets of this thesis work.

1.1 Energy and sources of energy

Energy is defined as the capacity of a physical system to perform work. During the last few decades, energy consumption has drastically increased (as shown in Figure 1.1a) to fuel the higher levels of activity and living standards derived from the continuous economic and social development that we are experiencing. As the world population and economy keeps on expanding, the energy demand will continue growing to cover the requirements (by 34% between 2014-2035).

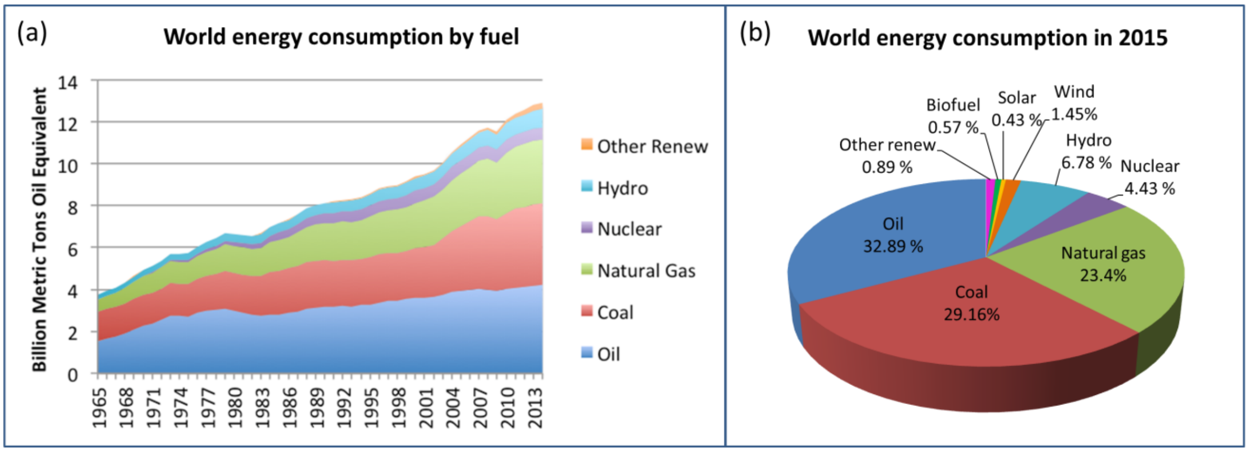

Figure 1.1. a) World energy consumption along the last decades and b) World energy consumption by fuel type in 2015, according to the BP Statistical Review of World Energy 2016.[1]

There are different energy sources used to produce the valuable energy.[2, 3] According to the energy reserves and the capacity of regeneration, energy sources can be classified into:

- **Non-renewable**: they proceed from limited resources on Earth, i.e., they are exhaustible and cannot be replenished in a short period of time. Non-renewable sources include: *fossil fuel* (petroleum, coal, natural gas) and *nuclear*.
- **Renewable**: they are coming from practically unlimited natural reserves, thus, they are inexhaustible and are freely regenerated in a short period of time. Renewable sources include: *hydropower, wind, solar, biomass, geothermal, oceanic*.

Until the date, fossil fuel continue being the dominant source of energy powering the global economy, accounting for *ca*. 85.5 % of the total energy production in 2015 (as Figure 1.1b illustrates), according to the BP Statistical Review of World Energy 2016.[1] However, the dependence on fossil fuels presents several risks and drawbacks. Aside from the hazard of monopolization and the socio-political instability derived from controlling the resources, fossil fuels are unsustainable sources that eventually will decline

---

[1] BP Statistical Review of World Energy 2016. http://www.bp.com/en/global/corporate/energy-economics/statistical-review-of-world-energy.html

[2] W. H. Wiser. Energy Resources. Springer. Occurrence, Production, Conversion, Use. Springer, 2000.

[3] E. E. S. Michaelides. Alternative Energy Sources. Green Energy and Technology, 2012.

in production due to its limited nature.[4] Besides, since fossil fuels are mainly based on organic carbon compounds, their combustions lead to the release of CO_2 and other volatile compounds into the atmosphere, contributing to pollution, the undesirable global warming and the greenhouse effect.[5]

Nuclear plants generate toxic and radioactive residues capable of emitting radiation from tens to hundreds of years. The storage and disposal of such wastes, extremely harmful to humans and the natural life, thus entails one of the major problems associated with this type of energy.[3] In 2015, the amount of energy produced from nuclear energy represented only a 4.4 %.[1]

Worldwide governments are aware of the negative effects above mentioned and have decided to invest in more sustainable energy sources,[6] resulting in a growth of the renewable energy production. In the order of 10% of the global energy produced in 2015 has been achieved by means of renewable sources[1] and a considerable boost up to 19.6 % is expected by 2030.[7] By far, the hydropower is the most popular clean source, contributing with almost 70% of the total renewable energy.[1] Despite the several advantages renewable energies possess, they also present some disadvantages, including the reliability of supply (reliability on the weather for its source of power) and the intermittency of supply (also subject to time, season and weather conditions).

One countermeasure to mitigate the fluctuations in output power derived from renewable sources and stabilizing power grids consist of integrating energy storage systems.

1.2 Energy storage

An energy storage system (or device) is an apparatus used for storing electric energy when needed (off-peak periods) and releasing it when required (peak load demand periods). Based on the form of energy stored, energy storage systems can be categorized into[8, 9]:

- **Electrical:** *capacitors.*[8, 10]
- **Magnetic:** *superconducting magnetic energy storage (SMES).*[8, 10]
- **Mechanical:** *pumped hydroelectric storage (PHS),*[9, 12] *compressed air energy storage (CAES),*[8, 12] *flywheels.*[8, 10, 12]

---

[4] Energy security: Economics, Politics, Strategies and Implications. C. Pascual, J. Elkind. Brookings Institution Press 2010. Page 210.

[5] D. J. Webbles, A. K. Jain. *Fuel Processing Technology* 2001, **71** (1-3), 99-119. "Concerns about climate change and the role of fossil fuel use".

[6] 1997 Kyoto Protocol to the United Nations Framework Convention on Climate Change (UNFCCC).

[7] International Energy Agency (IEA). World Energy Outlook 2015 - Special report on Energy and Climate Change. Page 154.

[8] X. Luo, J. Wang, M. Dooner, J. Clarke. *Appl. Energy* 2015, **137**, 511-536. "Overview of current development in electrical energy storage technologies and the application potential in power system operation".

[9] H. Ibrahim, A. Illinca, j. Perron. *Renewable and Sustainable Energy Reviews* 2008, **12**, 1221-1250. "Electrochemical storage systems - Characteristics and comparisons".

[10] H. Chen, T. N. Cong, W. Yang, C. Tan, Y. Li, Y. Ding. *Prog. Nat. Sci.* 2009, **19**, 291-312. "Progress in electrical energy storage systems: A critical review".

- **Thermal energy storage:** *sensible heat storage, latent heat storage, thermochemical storage (TCS).*[8]
- **Electrochemical:** *fuel cells,*[11] *supercapacitors*[8, 11, 12] *and rechargeable batteries.*[13,14, 8, 10]

No single electrical energy storage technology can meet the requirements for all power system applications. Several important factors, such as size (related to the power ($W \cdot l^{-1}$), energy densities ($Wh \cdot l^{-1}$)), weight (related to the specific power ($W \cdot Kg^{-1}$), specific energy ($Wh \cdot Kg^{-1}$)), cycle efficiency or round-trip efficiency (associated to the storage duration), self-discharge (indicator of the energy dissipation), lifetime and cyclability (that affect the overall cost) and time of response, determine the technology to be used for each application.[8] Figure 1.2 illustrates the current EES systems according to their discharge time and power module sizes, and also provides a guiding range for potential applications. [15]

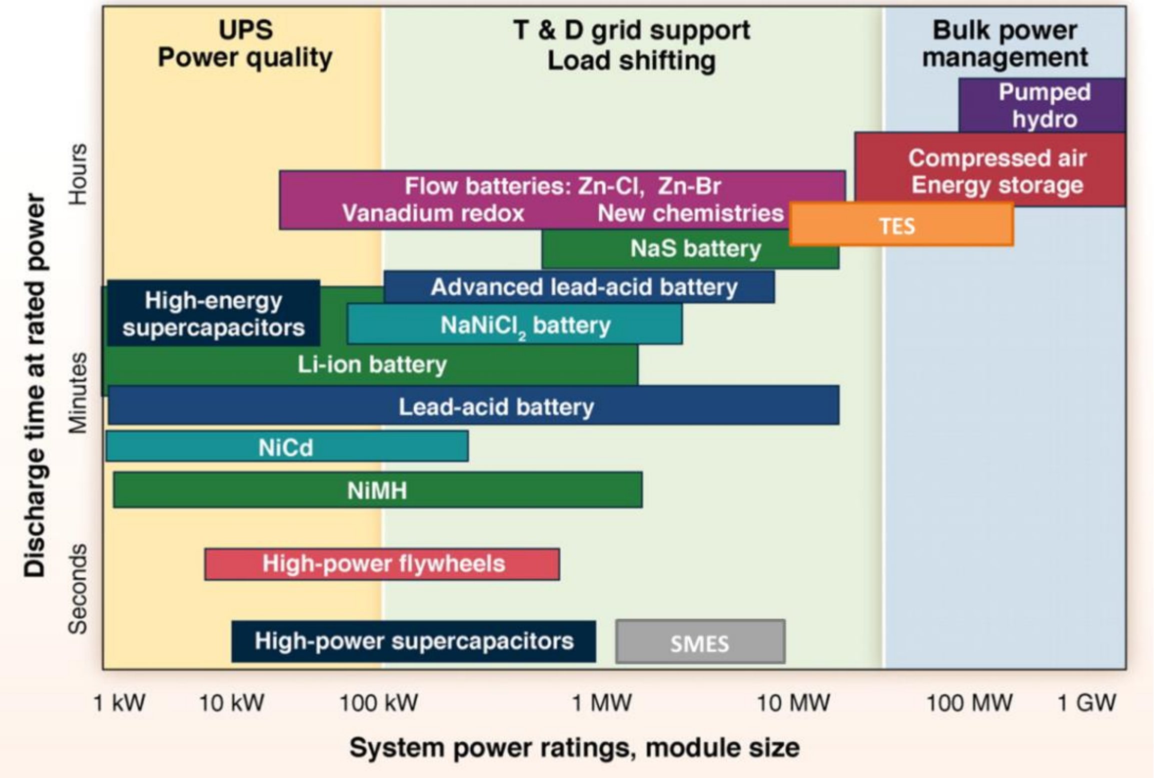

Figure 1.2. Comparison of discharge time and power rating for various EES technologies. The comparisons are of a general nature because several of the technologies have broader power ratings and longer discharge times than illustrated.[15] (UPS stands for uninterruptible power source. T & D stands for transmission and distribution).

PHS and large-scale CAES present the lower specific energy ($Wh \cdot Kg^{-1}$) and require very large emplacements, thus they are mainly used for large-scale energy storage. Although TES have high specific

---

[11] M. Winter and R. J. Brodd. *Chem. Rev*. 2004**, 104**, 4245-4269. "What are batteries, fuel cells and supercaps?"

[12] I. Hadjipaschalis, A. Poullikkas, V. Efthimiou. *Renew. Sust. Energ. Rev.* 2009, **13**, 1513-1522. "Overview of current and future energy storage technologies for electric power applications".

[13] M. Armand, J-M. Tarascon. *Nature*, 2008, **451**, 652-657. "Building better batteries".

[14] J. B. Goodenough. *Acc. Chem. Res.* 2013, **46 (5)**, 1053-1061. "Evolution strategies for Modern Rechargeable Batteries".

[15] B. Dunn, H. Kamath, J-M. Tarascon. *Science* 2011, **334**, 928. "Electrical Energy Storage for the Grid: A Battery of Choices."

energy, its specific power (W·Kg^{-1}) is low, making it also appropriate for large-scale applications. SMES, capacitors and supercapacitors have low specific energy but high specific power and fast time of response, thereby they are more suitable for power quality applications in electric power delivery. Flywheel, flow batteries and most conventional rechargeable batteries have moderate specific energy and specific power, making them suitable to small/medium-scale energy applications. Fuel cells, however, present the higher specific energy but moderate-high specific power, therefore they are destined to small/medium-scale energy applications as well.[8]

The rechargeable battery is one of the most widely used electrochemical energy storage (EES) technologies in industry and daily life. Its portability, simplified operational principle and the relatively short period of time invested in its construction, are some of the appealing features related to batteries. On the other hand, relatively low cycling times and high maintenance costs have been considered as the main barriers to implementing large-scale facilities. This thesis work is focused on the search of new materials for rechargeable batteries. In consequence, in the following section, an overview on batteries current scenario will be presented.

1.3 Batteries

1.3.1 Looking back to the origin

Electrochemistry is the science in charge of studying the chemical processes (reduction and oxidation, namely redox) caused by the pass of an electrical current and vice-versa, i.e., the generation of electrons movement due to certain chemical reactions.

Electrochemistry began with the achievements of two Italian researchers at the end of the 18th century, Luigi Galvani and Alessandro Volta. Galvani discovered electrochemistry indirectly. Volta invented the first d.c. power source, the “Voltaic Pile”, consisting of a column of alternatively packed silver and zinc plates able to split water into hydrogen and oxygen. Such landmark credits him as the founder of electrochemistry.

Many different electrochemical batteries were developed through the 19th and 20th centuries by improving Volta´s Pile, such as the electrical generators devised by Daniell, Planté or Leclanché, among others.[16] The principal milestones achieved are illustrated in Figure 1.3.

---

[16] *EPJ Web of Conferences* 2013, **54**, 01018. A. J. McEvoy. “Fundamentals and applications of electrochemistry”.

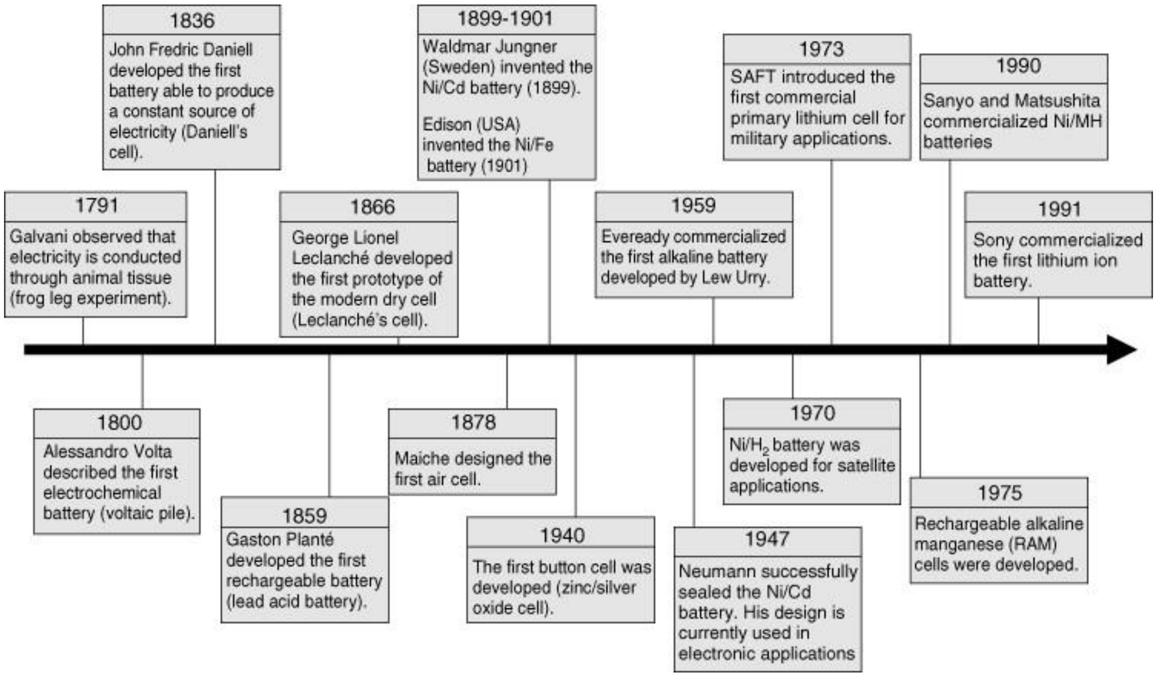

Figure 1.3. Timeline for the major events in the history of batteries.[17]

1.3.2 Battery components. How does a battery work?

A battery or electrochemical cell consists of two electrodes (an anode and a cathode), an electrolyte and some type of cell container.

Anode: is the negative electrode. Anodes are made of materials with very few electrons in their valence shell. In most of the cases, anodes are made of either metals or compounds that include them.

Cathode: Is the positive electrode. Cathodes are made of materials that have nearly full valence shells. Typically, they are made of compounds that include oxygen, chlorine, or both.

Electrolyte: is the ionic conductor. Electrolytes can be liquid (aqueous (either acids or alkaline) or an organic solvent containing salt in solution), ceramic or polymeric.

Separator: The separator provides insulation between the anode and cathode while allowing ionic transport between the electrodes and it is required if the electrolyte is liquid.

When the anode is connected to the cathode through an external circuit, the cell undergoes discharge spontaneously (see Figure 1.4). During discharge, the anode material releases electrons (is oxidized) and the cathode accepts electrons (is reduced). That is, redox reactions occur and electrons flow from the anode to the cathode through an external circuit. Simultaneously, the newly formed ions in the surface of the electrodes also travel through the electrolyte to maintain the electrical neutrality. Cell voltage depends on the potential of the electrodes and its theoretical value is given by the difference in the "standard reduction potential" between the two materials. For rechargeable batteries, applying a voltage in the reverse direction, the cell undergoes charge, instituting redox processes in the opposite

---

[17] Batteries: Basic Principles, Technologies and Modeling. Encyclopedy of Electrochemistry. G. G. Botte. Wiley, 2007.

direction.[14, 15] Conventional rechargeable batteries can bi-directionally convert energy between electrical and chemical energy.

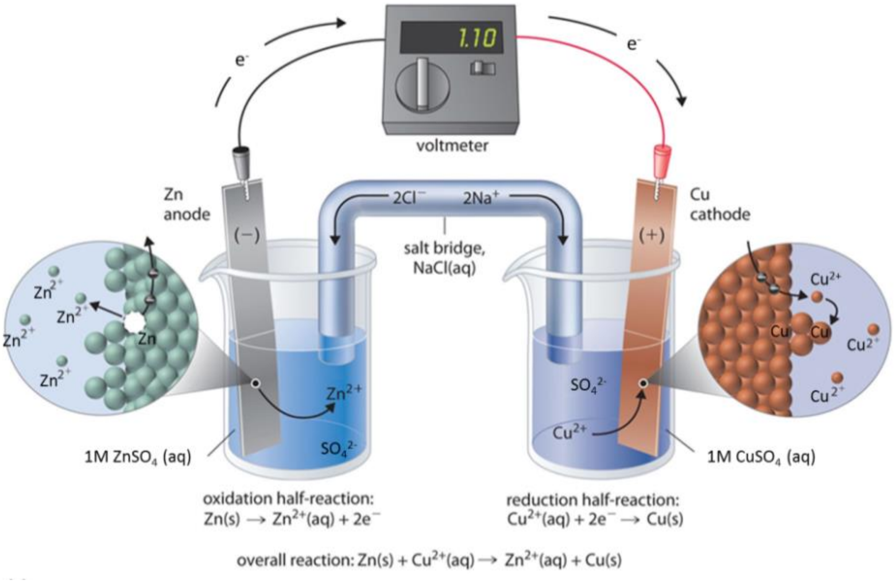

Figure 1.4. The two half-cell form of the Daniell cell.[18] In this particular case, zinc and copper electrodes are immersed in an aqueous solution of zinc (II) sulfate or copper (II) sulfate, respectively. The salt bridge is acting as electrolyte and no separator is required due to the disposition of the half-cells. The figure illustrates the reactions corresponding to the discharge process, since Daniell cell is a primary battery.

1.3.3 Battery classification

Batteries can be divided into two major categories:

- ✓ **Primary batteries**. A primary battery is a disposable battery that cannot be recharged, thus cannot be used for storing the energy generated in any power source. It is supplied fully charged, and discarded once discharged.[19] Typical primary batteries are: *zinc-carbon (Leclanché), alkaline, silver oxide, mercury, lithium and zinc-air*.

  Table 1.1 summarizes the electrochemical reactions that occur in the primary-type batteries previously enumerated. For each kind of battery, the anodic half-reaction (-) is detailed first, followed by the cathodic half-reaction (+), to finally display the overall reaction (o) occurring in the battery. The nominal voltage (abbreviated as NV) and specific energy density (abbreviated as SED)[20] provided by each primary battery are also reflected in the table. Additionally, their most remarkable characteristics and applications[19] (adapted from Table 7.1, page 7.6 of Handbook of Batteries. D. Linden, T. B. Reddy. McGraw Hill Handbooks, 3rd edition, 1995) are also collected in Table 1.1.

---

[18] http://chem2u.blogspot.com.es/2013/07/daniel-cell.html.

[19] Handbook of Batteries. D. Linden, T. B. Reddy. McGraw Hill Handbooks, 3rd edition, 1995. Chapters 7 (pages 7.6), 8 (8.1, 8.4, 8.5), 10 (10.1, 10.3, 10.4), 11 (11.1, 11.2, 11.4), 12 (12.1-12.3), 13 (13.1-13.3), 14 (14.1, 14.6), 22 (22.7), 23 (23.1, 23.6, 23.7), 26 (26.1, 26.4), 29 (29.1-29.3), 35 (35.1, 35.5, 35.6), 40 (40.1, 40.3, 40.4).

[20] Battery Reference Book, 3rd edition. T. R. Crompton. Elsevier, 2000. Chapter 2 (page 2/4).

Table 1.1. Electrochemical reactions (occurring at the anode (-), at the cathode (+) and the resulting overall reaction (o)), nominal voltages and energy densities[20] of the main primary batteries available. Major characteristics and applications of primary batteries[19] (adapted from Table 7.1, page 7.6 of Handbook of Batteries. D. Linden, T. B. Reddy. McGraw Hill Handbooks, 3rd edition, 1995) are also included.

Battery*	**Electrochemical reactions**	**NV (V) / SED ($Wh \cdot kg^{-1}$)**	**Characteristics**	**Applications**
Zinc-carbon (Leclanché)	(-): $Zn \rightarrow Zn^{2+} + 2e^-$ (+): $2\ MnO_2 + 2\ NH_4^+ + 2e^- \rightarrow Mn_2O_3 + 2\ NH_3 + H_2O$ O: $Zn + MnO_2 + 2NH_4Cl \rightarrow Mn_2O_3 + Zn(NH_3)_2Cl_2 + H_2O$	1.5 V / 55-77	Common, low-cost primary battery, available in a variety of sizes	Flashlight, portable radios, novelties, instruments
Alkaline	(-): $Zn + 2OH^- \rightarrow Zn(OH)_2 + 2e^-$ (+): $2MnO_2 + H_2O + 2e^- \rightarrow 2MnO(OH) + 2OH^-$ O: $Zn + 2MnO_2 + H_2O \rightarrow Zn(OH)_2 + 2MnO(OH)$	1.5 V / 66-99	Good low temperature, high rate performance, moderate cost	Most popular general-purpose primary battery: used in a variety of portable battery equipments
Silver oxide	(-): $Zn + 2OH^- \rightarrow ZnO + H_2O + 2e-$ (+): $Ag_2O + H_2O + 2e^- \rightarrow 2Ag + 2OH^-$ O: $Zn + Ag_2O \rightarrow ZnO + 2Ag$	1.6 V / 110-126	Highest capacity (by weight) of conventional type, flat discharge, good shelf life, costly	Hearing aids, photography electric watches, missiles, underwater and space application
Mercury (Ruben-Mallory)	(-): $Zn + 2OH^- \rightarrow ZnO + H_2O + 2e-$ (+): $HgO + H_2O + 2e^- \rightarrow Hg + 2OH^-$ O: $Zn + HgO \rightarrow ZnO + Hg$	1.35 V / 99-123	High capacity primary battery, long shelf life	Hearing aids, medical devices (pacemakers), photography, detectors, military equipment
Lithium	(-): $Li \rightarrow Li^+ + 1e-$ (+): $MnO_2 + Li + 1e- \rightarrow MnOOLi$ O: $MnO_2 + Li \rightarrow MnOOLi$	3 V / 280	High energy density, good performance, wide temperature operation, long shelf life, competitive cost	Wide range of applications
Zinc-air	(-): $Zn + 2\ OH^- \rightarrow ZnO + H_2O + 2e^-$ (+): $O_2 + H_2O + 2e- \rightarrow 2OH^-$ O: $Zn + O_2 \rightarrow ZnO + 2OH^-$	1.4 V / > 220	Highest energy density, low cost, dependent of environmental conditions	Special applications, hearing aids, pagers, medical devices, portable electronics

*The electrolyte used in most of the primary batteries is an alkali solution of KOH. Except for the Zn-carbon and the lithium battery, that consists of NH_4Cl and $LiClO_4$, respectively.

- ✓ **Secondary batteries**. Secondary batteries are rechargeable batteries that can be recharged many times for reuse, when they have been discharged. They are also known as accumulators. Rechargeable batteries can be classified in: *lead acid, nickel-cadmium, nickel-metal hydride, lithium ion and sodium-sulphur.*

The electrochemical reactions taking place in these batteries are summarized in Table 1.2. Their nominal voltage (NV), specific energy density (SED)[**21**], main characteristics and applications[19] are also collected in Table 1.2.

Other interesting secondary batteries which are currently the focus of research efforts are: *redox flow batteries*[8] and *beyond lithium-ion*. The latter include: sodium-ion (Na-ion) batteries, magnesium ion (Mg-ion) batteries, aluminum-ion (Al-ion) batteries, M-air (M = metal = Li, Na) batteries and lithium-sulfur (Li-S) batteries.[22, 23]

Figure 1.5 contrasts the volumetric and gravimetric energy density of some of the secondary batteries above mentioned.

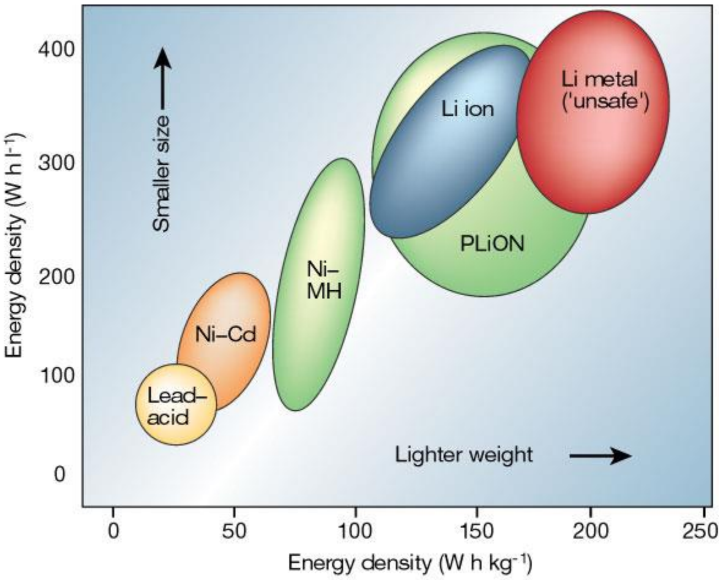

Figure 1.5. Comparison of the different rechargeable battery technologies in terms of volumetric and gravimentric energy density.

Among the rechargeable batteries, the Li-ion battery has both a high energy density and a high power density (as shows Figure 1.5). This has contributed to widespread its use in portable devices, to position them as the most promising technology in transportation to substitute lead-acid and also to postulate them for other EES applications.[22, 24] In the order of 63% of worldwide sales in portable batteries is accounted for Li-ion batteries.[24] Given its importance, a wider vision about this system is addressed in the following section.

---

[21] http://batteryuniversity.com/learn/article/secondary_batteries. (Last updated on 2016-04-11).

[22] J. W. Choi, D. Aurbach. *Nat. Rev. Mat.* 2016. DOI: 10.1038/natrevmats.2016.13. "Promise and reality of post-lithium ion batteries with high energy densities".

[23] M. Armand, J-M. Tarascon. *Nature* 2008, **451**, 652-657. "Building better batteries".

[24] J-M. Tarascon, M. Armand. *Nature* 2001, **414**, 359-367. "Issues and challenges facing rechargeable lithium batteries".

Table 1.2. Electrochemical reactions (occurring at the anode (-), at the cathode (+) and the resulting overall reaction(o)), nominal voltages and specific energy densities[21] of the main secondary batteries available for EES. Major characteristics and applications of these secondary batteries (adapted from Table 22.1, page 22.7 of Handbook of Batteries)[19] are also included.

Battery	Electrochemical reactions*	NV (V)/ SED ($Wh \cdot kg^{-1}$)	Characteristics	Applications
Lead acid	(-): $Pb + SO_4^{2-} \leftrightarrow PbSO_4 + 2e^-$ (+): $PbO_2 + 4\ H^+ + SO_4^{2-} + 2e- \leftrightarrow PbSO_4 + 2\ H_2O$ O: $Pb + PbO_2 + 2\ H_2SO_4 \leftrightarrow 2\ PbSO_4 + 2\ H_2O$	2.1 V / 30-50	Popular, low-cost secondary battery, moderate specific energy, high rate, low temperature operation, maintenance-free designs	Automotive (motor vehicle engine starting, electric and hybrid motors), back-up power supplies
Ni-Cd	(-): $Cd + 2OH^- \leftrightarrow Cd(OH)_2 + 2e^-$ (+): $2\ NiO(OH) + 2\ H_2O + 2e^- \leftrightarrow 2\ Ni(OH)_2 + 2\ OH^-$ O: $Cd + 2\ NiO(OH) + 2\ H_2O \leftrightarrow Cd(OH)_2 + 2\ Ni(OH)_2$	1.2 V / 45-80	Good high rate, low temperature capability, flat voltage, excellent cycle life, maintenance free	Aircraft batteries, industrial and emergency power applications, consumer electronics and portable tools
Ni-MH	(-): $MH + OH^- \leftrightarrow M + H_2O + e^-$ (+): $NiO(OH) + H_2O + e^- \leftrightarrow Ni(OH)_2 + OH^-$ O: $MH + NiO(OH) \leftrightarrow M + Ni(OH)_2$	1.32 V / 60-120	Sealed, maintenance free, higher capacity than Ni-Cd batteries	Consumer electronics and other portable applications, electric and hybrid electric vehicles
Li-ion	(-): $Li_xC_6 \leftrightarrow x\ Li^+ + C_6 + x\ e-$ (+): $Li_{1-x}CoO_2 + x\ Li^+ + xe^- \leftrightarrow LiCoO_2\ (0 \leq x \leq 0.45)$ O: $x\ LiC_6 + Li_{1-x}CoO_2 \leftrightarrow x\ C_6 + LiCoO_2$	3.9 V / 150-190	High specific energy and energy density, long cycle life, low maintenance	Portable electronics, electric vehicles and aerospace applications
Li-ion	(-): $Li_xC_6 \leftrightarrow x\ Li^+ + C_6 + x\ e-$ (+): $Li_xMn_2O_4 + x\ Li^+ + xe^- \leftrightarrow Li_{2x}Mn_2O_4\ (0 \leq x \leq 1)$ O: $x\ LiC_6 + Li_{1-x}Mn_2O_4 \leftrightarrow x\ C_6 + Li_{2-x}Mn_2O_4$	4.1 V / 100-135		
Li-ion	(-):$Li_xC_6 \leftrightarrow x\ Li^+ + C_6 + x\ e-$ (+): $FePO_4 + x\ Li^+ + x\ e^- \leftrightarrow LiFePO_4$ O: $x\ LiC_6 + FePO_4 \leftrightarrow x\ C_6 + LiFePO_4$	3.45 V / 90-120		
Na-S	(-): $2\ Na \leftrightarrow 2\ Na^+ + 2e-$ (+): $x\ S + 2e- \leftrightarrow S_x^{2-}$ O: $2\ Na + x\ S \leftrightarrow Na_2S_x$	2.08 V / 240	Potential low cost, high cycle life, good energy and power density, high energy efficiency, insensitive to ambient conditions	Power leveling and other stationary applications

*Reactions are written in the direction of the discharge. The processes are reversed during the charge.

1.3.4 Li-ion rechargeable batteries

Although secondary Li batteries were launched in 1990s, the safety problems associated to the utilization of metallic lithium as anode, namely the plating of Li during charge processes that can result in the growth of dendrites across the electrolyte and subsequent short-circuit of the cell with dangerous consequences, abruptly interrupted their commercialization.[25] Since then, tremendous effort has been invested in the development of secondary lithium batteries, due to its potential. The so-called Li-ion batteries (LIB) or "rocking chair" technology, first commercialized by Sony in 1991 (see Figure 1.6), owes its name to the exchange of the Li-ion between the graphite (Li_xC_6) anode and the layered oxide ($Li_{1-x}MO_2$, M= transition metal) cathode.[26] That is to say, Li-ion batteries mainly deploy lithium intercalation compounds as the positive and negative materials, where the lithium ions "rock" back and forth between them as the cell is charged and discharged, as already mentioned.

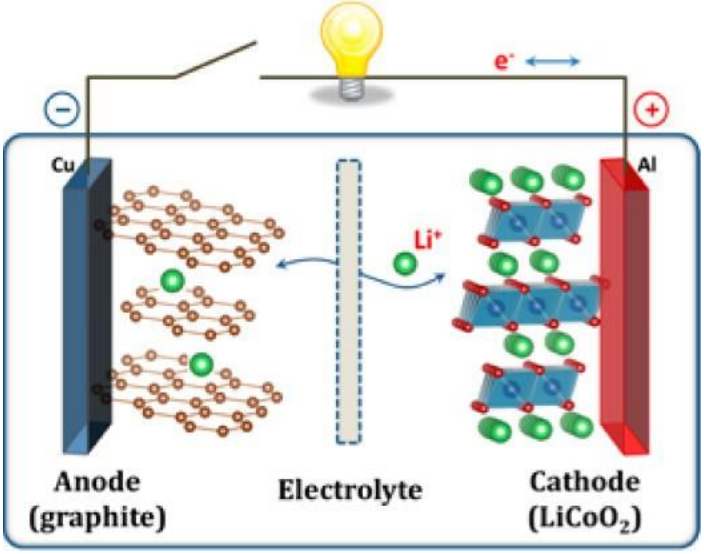

Figure 1.6. Schematic illustration of the first Li-ion battery (graphite/Li^+ electrolyte/$LiCoO_2$).[27]

During the last 3 decades, an intensive search of new materials for LIB and improvements in those already existent has been carried out, constituting the revolution of Li-ion batteries. In the following paragraphs, an overview of the most representative and remarkable materials available and currently used in this technology for room temperature (RT) will be discussed.

1.3.4.1 *Cathodes for LIB*

The most studied intercalation cathode materials for RT LIB can be classified in three types: *layered oxides, spinel-type oxide and polyanionic compounds*.

---

[25] J. B. Goodenough, Y. Kim. *Chem. Matter.* 2010, **22** (3), 587-603.. "Challenges for Rechargeable Li Batteries".
[26] T. Nagura, K. Tozawa. *Prog. Batteries Solar Cells* 1990, **9**, 209. "Lithium ion rechargeable battery".
[27] J. B. Goodenough, K-S. Park. *J. Am. Chem. Soc.* 2013, **135** (4), pp 1167–1176. "The Li-ion Rechargeable Battery: A perspective."

Layered oxides. Layered oxide refers to those materials whose general formula is $LiMO_2$, where M = transition metal. $LiCoO_2$ (see Figure 1.7a) constitutes the most commercially successful form of layered oxide cathode. Its appealing resides in the relatively high theoretical specific capacity (274 $mAh \cdot g^{-1}$). However, its major limitations are high cost, low thermal stability and fast capacity fade at high current rates due to severe structure stability degradation. $LiNiO_2$ has similar theoretical capacity (C_{th} = 275 $mAh \cdot g^{-1}$) and lower cost than $LiCoO_2$, but it presents even lower thermal stability and the inconvenient that Ni^{2+} tends to substitute Li^+ sites during delithiation, blocking the diffusion pathways and resulting in capacity fading. A cheaper and less toxic alternative to $LiCoO_2$ or $LiNiO_2$ is $LiMnO_2$ (C_{th} = 285 $mAh \cdot g^{-1}$), although it tends to change into spinel structure during Li extraction and suffers from Mn dissolution, leading to poor cycle stability.[28]

Improvements in the layered transition metal oxides include the development of binary $LiNi_xM_{1-x}O_2$,[29, 30] ternary $LiNi_xCo_yMn_{1-x-y}O_2$,[31, 32] and the so-called Li-rich integrated layered-layered cathode $[LiNi_xCo_yMn_{1-x-y}O_2]_{(1-a)} \cdot [Li_2MnO_3]_a$[33, 34].

Spinel-type oxide. Spinel $LiMn_2O_4$ benefits from the abundance, low cost and environmentally friendliness of manganese. Its 3D structure allows a fast and multidirectional diffusion of Li ions (see Figure 1.7b). However, $LiMn_2O_4$ presents a relatively low theoretical capacity (148 $mAh \cdot g^{-1}$) and a moderate electrode potential of 4.0 V *vs*. Li^+/Li.[35] In addition, it exhibits a serious problem of capacity fading, as consequence of the irreversible structural transition from spinel to tetragonal structure caused by the Jahn-Teller distortion of Mn^{3+} and the dissolution of Mn ions in the electrolyte.[34, 36]

The main strategy addressed to mitigate the above-mentioned drawbacks of $LiMn_2O_4$ consists of doping the material with other metals, with the aim of suppressing the Jahn-Teller distortion and stabilizing the structure. Being the most promising doped spinel structure, the derivative $LiNi_{0.5}Mn_{1.5}O_4$, whose redox activity gets over 140 $mAh \cdot g^{-1}$ and approach the 4.8 V due to the $Ni^{2+} \rightarrow Ni^{3+} \rightarrow Ni^{4+}$ transition it experiments.[37]

Polyanionic compounds. Polyanions stands for $Li_xM_y(XO_4)_z$ (M = metal, X = S, P, Si, As, Mo, W). The most representative polyanionic material, the $LiFePO_4$ olivine-structure, was introduced as new cathode at the end of the 1990s.[19] $LiFePO_4$ is naturally abundant, inexpensive, environmentally benign and has a relatively high theoretical capacity (170 $mAh \cdot g^{-1}$) but a considerable low potential of 3.45 V vs. Li^+/Li compared to layered oxides and spinel-type materials. Despite its favorable reversibility, resultant from

---

[28] N. Nitta, F. Wu, J. T. Lee, G. Yushin. *Materials Today* 2015, **18** (5), 252-264. "Li-ion battery materials: present and future."

[29] Y. Makimura, T. Ohzuku. *J. Power Sources* 2003, **117**, 156-160. "Lithium insertion of $LiNi_{1/2}Mn_{1/2}O_2$ for Advanced Lithium-Ion Batteries".

[30] K. Kang, Y-S. Meng, J. Bréger, C. P. Grey, G. Ceder. *Science* 2006, **311**, 977. "Electrodes with high power and high capacity for rechargeable lithium batteries".

[31] K. M. Shaju, P. G. Bruce. *Adv. Mater.* 2006, **18** (17), 2330-2334. "Macroporous $Li(Ni_{1/3}Co_{1/3}Mn_{1/3})O_2$: A High-Power and High-Energy Cathode for Rechargeable Lithium Batteries".

[32] Manthiram, A., Knight, J. C., Myung, S.-T., Oh, S.-M. & Sun, Y.-K. *Adv. Energy Mater.* 2015, **6**, 1501010. "Nickel-rich and lithium-rich layered oxide cathodes: progress and perspectives."

[33] C. S. Johnson, J-S. Kim, C. Lefief, N. Li, J. T Vaughey, M. M. Thackeray. *Electrochem. Comm*. 2004, **6**, 1085. "The significance of the Li_2MnO_3 component in "composite" $xLi_2MnO_3 \cdot (1-x)LiMn_{0.5}Ni_{0.5}O_2$ electrodes".

[34] M. Hu, X. Pang, Z. Zhou. *J. Power Sources* 2013, **237**, 229-242. "Recent progress in high-voltage lithium ion batteries"

[35] M. M. Thackeray, P. J. Jahnson, L. A. De Piccioto, P. G. Bruce, J. B. Goodenough. *J. Mater. Res. Bull.* 1984, **19** (2), 179-187. "Electrochemical extraction of lithium from $LiMn_2O4$".

[36] V. Etacheri, R. Marom, R. Elazari, G. Salitra, D. Aurbach. *Energy Evironm. Sci.* 2011, **4**, 3243-3262. "Challenges in the development of advanced Li-ion batteries: a review".

[37] Y. Talyosef, B. Markovsky, G. Salitra, D. Aurbach. *J. Power Sources* 2005, **146**, 664-669. "The study of $LiNi_{0.5}Mn_{1.5}O_4$ 5-V cathodes for Li-ion batteries".

its robust 3D structure (as shown in Figure 1.7c), the performance of $LiFePO_4$ was compromised by its very low electronic and ionic conductivity.[38] Along the years, the poor transport properties of $LiFePO_4$ have been drastically improved by the preparation of carbon-coated nanoparticles, allowing its commercialization with a practical capacity very close to the theoretical (165 $mAh \cdot g^{-1}$).[39]

Besides, other olivine phases such as $LiCoPO_4$, $LiMnPO_4$ and $LiNiPO_4$have been investigated, considering the similar theoretical capacities but higher redox potential they exhibit compared to $LiFePO_4$ (4.1 V, 4.8 and 5.1 V *vs*. Li^+/Li, respectively).[40] Unfortunately, common organic electrolytes are not yet stable at such high potentials. Other noteworthy cathodes are the NASICON $Li_3V_2(PO_4)_3$, that exhibits good capacity (197 $mAh \cdot g^{-1}$) and a cell voltage of 4.0 V [41], and the tavorite-type fluorinated phase $LiFeSO_4F$, that offers a 3.6 V cell voltage and reasonable specific capacity (151 $mAh \cdot g^{-1}$),[42] competitive with $LiFePO_4$.

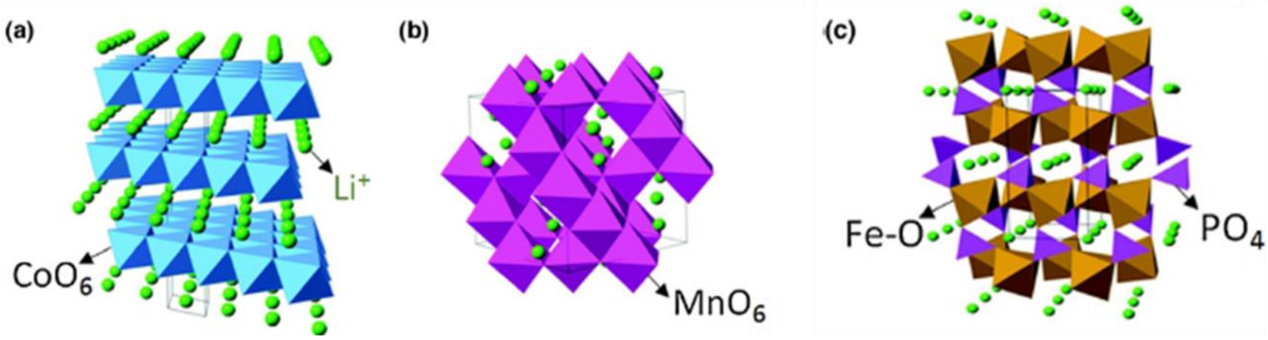

Figure 1.7. Crystal structures of representative intercalation cathodes: a) layered oxides ($LiCoO_2$), spinel ($LiMn_2O_4$) and c) olivine ($LiFePO_4$).

1.3.4.2 *Anodes for LIB*

The anodic material par excellence in LIB is graphite. It is cheap, abundant, benign and presents high electrical conductivity, high Li^+ diffusivity and relatively low volume change during the lithiation/delithiation process. The intercalation/deintercalation (see Figure 1.8) of Li into graphene planes occurs with a low delithiation potential vs. Li^+/Li (0.1 V). Besides, graphite can store up to 1 Li atom per 6C, offering a reversible capacity as high as 350 $mAh \cdot g^{-1}$ of the theoretical 372 $mAh \cdot g^{-1}$.[43] Other alternatives to graphite under R&D are:

***Intercalation anodes* - Titanates.** Titanium oxides constitute another type of intercalation anode materials. In particular, $Li_4Ti_5O_{12}$ has attracted attention as promising candidate to meet the requirements for electric vehicles (EVs). $Li_4Ti_5O_{12}$ undergoes a highly reversible insertion of Li^+ with zero-strain,

---

[38] A. K. Padhi, K. S. Nanjundaswamy, J. B. Goodenough. *J. Electrochem. Soc.* 1997, **144**, 1188. “Phospo-olivines as Positive-Electrode Materials for Rechargeable Lithium Batteries”.

[39] F. Cheng, J. Liang, Z. Tao, J. Chen. *Adv. Mater.* 2011, **23**, 1695-1715. “Functional Materials for Rechargeable Batteries”.

[40] G. Jeong, Y-U. Kim, H. Kim, Y-J. Kim, H-J. Sohn. *Energy Environm. Sci.* 2011, **4**, 1986-2002. “Prospective materials and applications for Li secondary batteries”.

[41] H. Huang, S-C. Yin, T. Kerr, N. Taylor, L. F. Nazar. *Adv. Mater.* 2002, **21** (14), 1525. “Nanostructured Composites: A high capacity, fast rate $Li_3V_2(PO_4)_3$/Carbon cathode for rechargeable lithium batteries”.

[42] N. Recham, J-N. Chotard, L. Dupont, C. Delacourt, W. Walker, M. Armand, J-M. Tarascon. *Nat. Mater.* 2010, **9** (1), 68. “A 3.6 V lithium-based fluorosulphate insertion positive electrode for lithium-ion batteries”.

[43] T. Ohzuku, Y. Owakoshi, K. Sawai. *J. Electrochem. Soc.* 1993, **140** (9), 2490-2498. “Formation of Lithium-Graphite Intercalation Compounds in Nonaqueous Electrolytes and Their Applications as Negative Electrode for a Lithium Ion (Shuttlecok) Cell”.

delivering 150-160 mAh·g^{-1} at 1.5 V *vs*. Li$^+$/Li. Despite the low specific capacity and the relatively high voltage for an anode system, the material exhibits long-cycle life and an enhanced safety, respectively, as a result of the structure stability (zero strain) and the suppression of both SEI formation and Li plating at such operating voltage.[44] As an alternative to $Li_4Ti_5O_{12}$, TiO_2 emerged with larger theoretical capacity value (335 mAh·g^{-1}), being anatase-TiO_2 and bronzetype TiO_2 the TiO_2 polymorphs providing the best electrochemical performance.[40]

***Conversion anodes* – Transition metal oxides and binary compounds.** There are other transition metal oxides that can be reversibly reduced in presence of lithium M_xO_y (M = Fe, Co, Ni, Mn, Cu, etc.). These materials are capable of incorporating more than 1 Li$^+$, giving significantly higher electrochemical capacities than those of graphite, because they get reduced from M^{y+} to metal nanoparticles M^0 through a conversion reaction (as shown (Eq. 1.1).

$$M_xO_y + 2yLi^+ + 2e^- \leftrightarrow yLi_2O + xM \qquad \textbf{(Eq. 1.1)}$$

These reactions involve a complete change in the structure of the materials (see Figure 1.8), but with impressive reversibility.

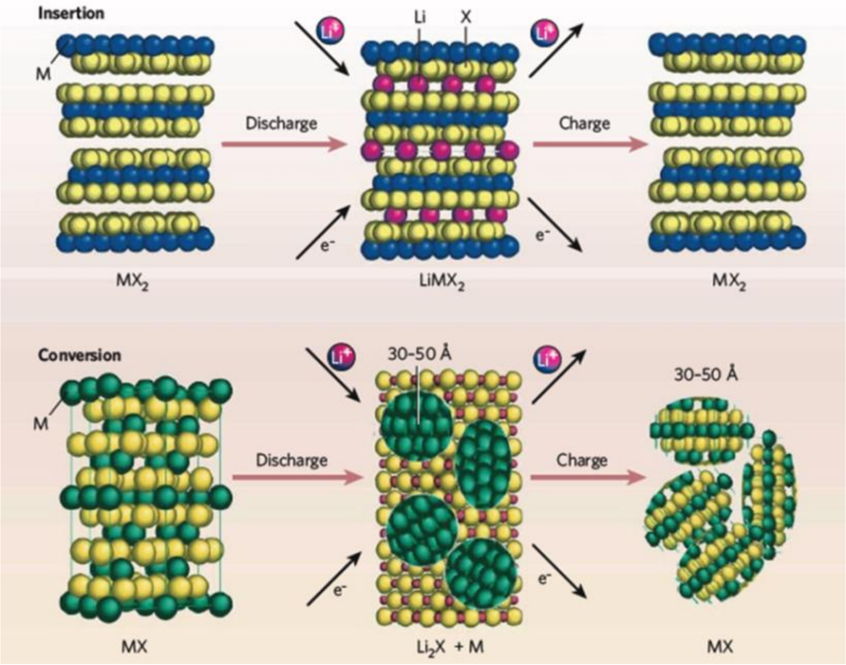

Figure 1.8. Schematic representation showing the contrasting reaction mechanisms occuring during discharge for insertion (top) and conversion reactions (bottom).[23]

The range of capacities oscillates between 600 - 1000 mAh·g^{-1} depending on the transition metal oxide. On the other hand, poor energy efficiency is achieved with conversion materials, because of the high average operating voltages (from 1.8 – 2.0 V *vs*. Li$^+$/Li), low initial coulombic efficiency and inherent large voltage separation (hysteresis) between the charge and discharge profiles.[39]

---

[44] Y. Tang, L. Yang, Z. Qiu, K. Huang. *J. Mater. Chem*. 2009, **19**, 5980. "Template-free synthesis of mesoporous spinel lithium titanate microspheres and their application in high-rate lithium ion batteries".

Other binary compounds M_xZ_y (Z = N, F, S, P and even H), besides transition metal oxides, have also demonstrated to function following a conversion or displacement reaction mechanism.[40]

Alloying anodes – Si, Sn. Lithium metal alloys are the most promising candidates to replace graphite in LIB. The most representative elements that undergo reversible alloying with lithium, are Si and Sn. The more relevant feature of alloys is the high specific capacities they could deliver (993 mAh·g^{-1} for $Li_{4.4}Sn$ and 3590 mAh·g^{-1} for $Li_{4.4}Si$), but they also present moderate operating potentials (below 1V). Nevertheless, a common phenomenon for these alloying processes is a volume expansion of about 300% upon lithiation. The volume change also involves a mechanical stress that finally destroys the integrity of the material as well as loss of electronic conducting paths, leading to capacity fading. [36, 39, 40] Between the proposed solutions to overcome the volume variation problem, it should be noted the strategies of nanostructuration (nanowires, nanotubes) and preparation of nanocomposites.[22]

To sum up and conclude this section dedicated to Li-ion batteries, an illustrative comparison of the different type of materials above exposed, as a function of the voltage and specific capacities, is presented in Figure 1.9.

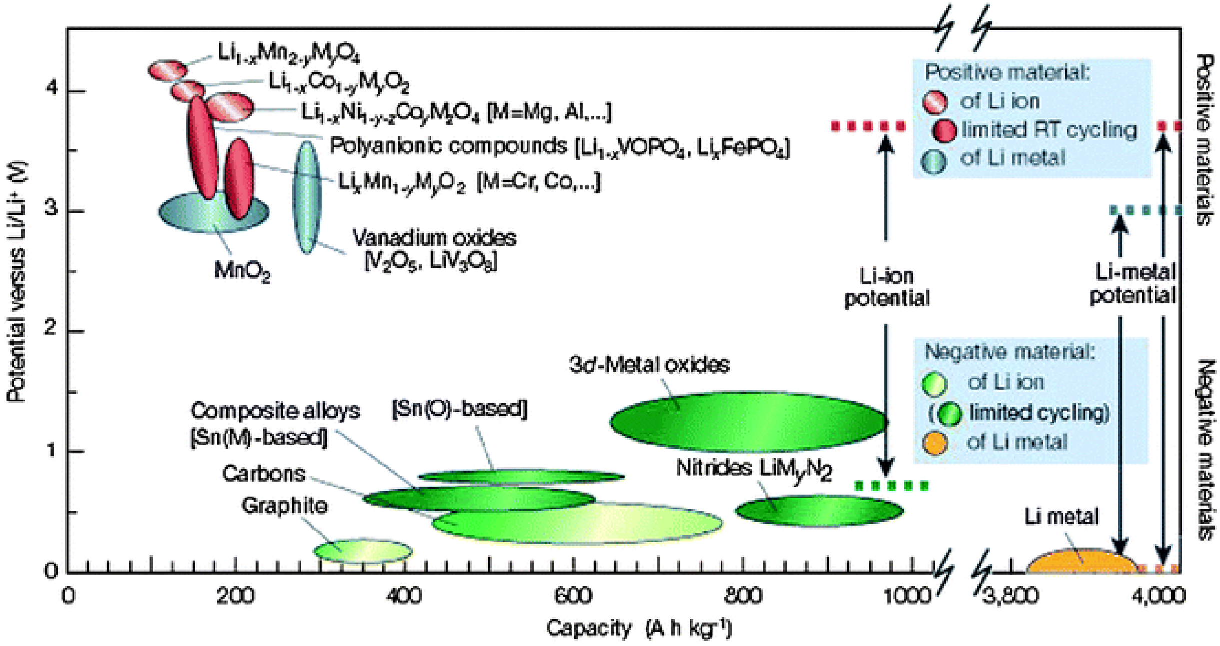

Figure 1.9. Voltage *vs*. capacity for positive and negative electrode materials presently used and under serious consideration for the next generation of rechargeable Li-based cells[45].

---

[45] D. Liu, G. Cao. *Energy Environ. Sci*. 2010, **3**, 1218–1237. "Engineering nanostructured electrodes and fabrication of film electrodes for efficient lithium ion intercalation".

1.3.5 Na-ion batteries

An emerging alternative to LIB that have recently gained increased recognition are Na-ion batteries (NIB).[46] Although sodium presents similar physico-chemical properties to lithium and, in principle, the knowledge acquired for LIB could be transferred to NIB, the reality is other.[47] There are significant differences between the two elements, such as the atomic weight (Na is 3 times heavier than Li), the ionic radio (larger for sodium (1.02 Å *vs*. the 0.76 Å of lithium)) and the standard electrochemical potential (0.34 V higher for Na^+/Na). These differences translates into lower gravimetric and volumetric energy density for NIB, when contrasted to LIB, and in the necessity of finding host electrode materials with sufficiently large interstitial space to accommodate the bigger sodium ions.[48] Nevertheless, NIB are potential candidates for next-generation large-scale energy storage systems, owing to significant cost advantages stemming from the high natural abundance and broad distribution of sodium resources. Sodium is the sixth most abundant element in the Earth´s crust (*ca*. 2.6 %). Additionally, NIB offers the the possibility of using Al as current collector in the anode electrode (instead of copper, necessary in LIB), lowering its cost.

Following the same scheme than for LIB, a resume of the main materials under research for room temperature NIB will be covered in the subsequent sections.

1.3.5.1 *Cathodes for NIB*

The most studied intercalation cathode materials for room temperature NIB can be sorted out in: *layered oxides, polyanionic compounds, organic materials and Prussian Blue analogues*.

$NaMO_2$ oxides.

Layered structure oxides. Adapted from LIB, layered $NaMO_2$ are highly active as sodium insertion host (M = Ti, V, Cr, Mn, Fe, Co, Ni, etc.) and benefits from high capacity. However, layered $NaMO_2$ compounds are very sensitive to water and CO_2, resulting in phase changes and decreased reversibility.[49, 50] According to the notation proposed by Delmas *et al.*, layered $NaMO_2$ oxides can be classified as O2-, O3-, P2- and P3-type depending on the stacking sequence of oxygen layers (O2: AB AC, O3: AB CA BC, P2: AB BA, P3: AB BC CA) and whether sodium is located in octahedral (O) or prismatic (P) sites. [51] See Figure 1.10 for further details.

---

[46] V. Palomares, P. Serras, I. Villaluenga, K. B. Hueso, J. Carretero-González, T. Rojo. *Energy Environm. Sci.* 2012, **5**, 5884-5901. "Na-ion batteries, recent advances and present challenges to become low cost energy storage systems".

[47] S-W. Kim, D-H. Seo, X. Ma, G. Ceder, K. Kang. *Adv. Energy Mater.* 2012, **2**, 710-721. "Electrode Materials for Rechargeable Sodium-Ion Batteries: Potential Alternatives to Current Lithium-Ion Batteries".

[48] N. Yabuuchi, K. Kubota, M. Dahbi, S. Komaba. *Chem. Rev.* 2014, **114**, 11636-11682. "Research Development on Sodium-Ion Batteries".

[49] V. Palomares, M. Casas-Cabanas, E. Castillo Martínez, M. H. Han, T. Rojo. *Energy Environm Sci.* 2013, **6**, 2312-2337. "Update on Na-based battery materials. A growing research path".

[50] H. Kim, H. Kim, Z. Ding, M. H. Lee, K. Lim, G. Yoon, K. Kang. *Adv. Energy Mater.* 2016, **6** (19). DOI: 10.1002/aenm.201600943. "Recent progress in Electrode Materials for Sodium-Ion Batteries".

[51] C. Delmas, C. Fouasssier, P. Hagenmuller. *Physica B+C* 1980, **99** (1-4), 81-85. "Structural classification and properties of the layered oxides".

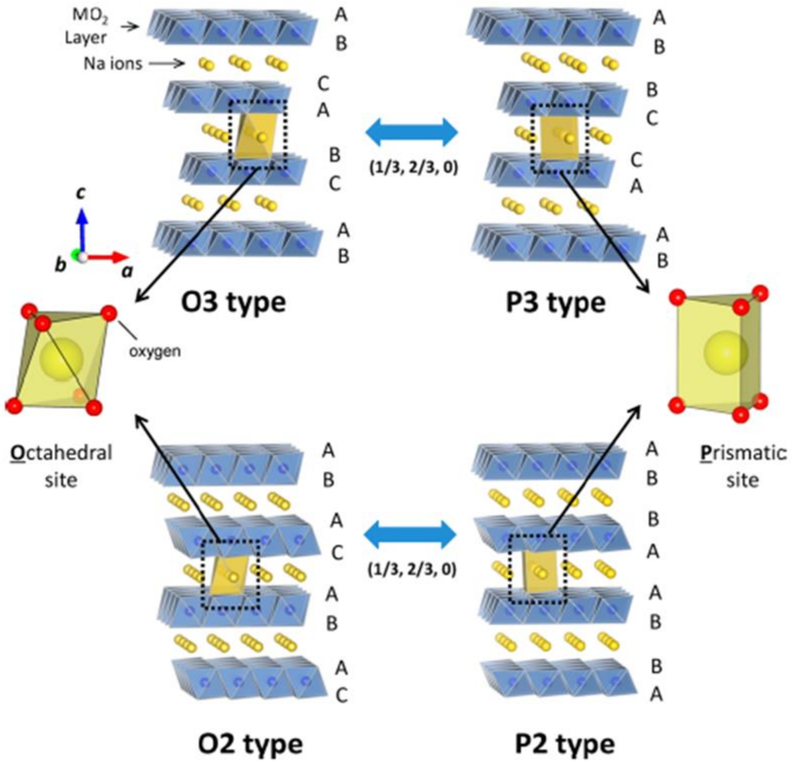

Figure 1.10. Classification of $NaMO_2$ layered oxides structures.[48]

Na_xCoO_2 comprises O3, P3 and P2 phases in the $0.46 < x < 1$ range, which can deliver, respectively, 140, 130 and 120 $mAh·g^{-1}$, showing several phase transitions on the sodiation/ desodiation process.[48] Among the three polymorphs, O3 presents a wider reversible range while P2 exhibits higher Na diffusion rates. Of Na_xMnO_2, both phases P2 and O3 are known. Despite Na_xMnO_2 can provide reversible capacities as high as 180 $mAh·g^{-1}$, these compounds exhibit poor structural reversibility as a consequence of the strong Jahn-Teller effect of Mn^{3+}, and result in capacity fading and poor cyclability.[50] P2- and O3- α-Na_xFeO_2 offers the advantage of lower price and non-toxicity but delivers low reversible capacities (below 100 $mAh·g^{-1}$), due to instability of Fe^{4+} at high voltage.[52] Only O3-phases of Na_xMO_2 (M = Ni, Cr) are known. Na_xNiO_2 provides up to 147 $mAh·g^{-1}$ along the first discharge that rapidly decay down to 120 $mAh·g^{-1}$ in the second cycle, due to an irreversible phase change and the Jahn-Teller distortion of Ni^{3+}, whereas Na_xCrO_2 delivers reversible capacities of 120 $mAh·g^{-1}$ with good reversibility for a considerable number of cycles.[48, 50]

To enhance the electrochemical performance of layered oxide materials, binary $Na_xM_yM'_{1-y}O_2$ and ternary $Na_xM_yM'_zM''_{1-y-z}O_2$ combinations ($M \neq M' \neq M''$; M, M´, M´´ = Cr, Mn, Fe, Co, Ni, etc.) are also being extensively investigated, but will not be here detailed.[53] Additionally, cationic substitution with inactive metals (Mg^{2+}, Ti^{4+} and Ca^{2+}) is another effective strategy to improve the cycling performance of transition metal oxides due to an enhancement of the structural stability.[54]

---

[52] M. D. Slater, D. Kim, E. Lee, C. Johnson. *Adv. Funct. Mater*. 2013, **23**, 947–958. "Sodium-ion Batteries".

[53] M. H. Han, E. Gonzalo, G. Singh, T. Rojo. *Energy Environm. Sci*. 2015, **8**, 81-102. "A comprehensive review of sodium layered oxides: powerful cathodes for Na-ion batteries".

[54] X. Xiang, K. Zhang, J. Chen. *Adv. Mater.* 2015, **27**, 5343-5364. "Recent advances and Prospects of Cathode Materials for Sodium-Ion Batteries".

Other transition metal oxides. The tunneled-structure $Na_{0.44}MnO_2$ has been widely investigated. The initial reversible capacity, 80 $mAh \cdot g^{-1}$ at 0.1 C and poor cyclability,[54] delivered by $Na_{0.44}MnO_2$ were promptly overcome by modifying the synthesis method and optimizing its morphology. For instance, $Na_{0.44}MnO_2$ nanowires provided 128 $mAh \cdot g^{-1}$ and 77% of the initial capacity after 1000 cycles.[52] Other attractive cathode materials for NIB are vanadium oxides, VO_x, considering their open framework structure and their multivalent character.[50] Nanostructured electrodeposited V_2O_5 is a 3 V cathode able to exhibit more than 200 $mAh \cdot g^{-1}$ after 300 cycles.[49] It is also worthy to mention the α-MoO_3, capable to reversibly insert/de-insert $1Na^+$, and the Na_2RuO_3 compound, that delivers 150 $mAh \cdot g^{-1}$ at an average voltage of 3 V *vs*. Na^+/Na.[48]

Polyanionic compouds.

Polyanionic compounds, $Na_xM_yX_z$ (M = transition metal, X = $(PO_4)^{3-}$, $(SO_4)^{2-}$, $(SiO_4)^{4-}$, $(P_2O_7)^{4-}$), benefits from structural robustness owing to the strong covalent "non-metal-O" (non-metal = P, S, Si, B) and the inductive effect of the polyanionic group that ensures high operating voltage.[50]

Phosphates. $NaFePO_4$ has the highest theoretical specific capacity among the phosphates. Two phases are known for $NaFePO_4$, olivine and maricite. The olivine phase, obtained by delithiation of $LiFePO_4$ and subsequent sodiation, has been predominantly studied. Although its electrochemical properties are not as impressive as those observed in LIB, roughly 80% of the theoretical capacity (154 $mAh \cdot g^{-1}$) can be achieved. Maricite is thermodynamically more stable and, despite it was initially considered electrochemically inactive, recent works have proved that nano-sized maricite $NaFePO_4$ can reach capacities of 142 $mAh \cdot g^{-1}$ stable along 200 cycles.[54, 50]

NASICON, Na super-ionic conductor $Na_xMM'(XO_4)_3$ (M and M´= transition metal; X = Si, P, S, Mo), features a 3D structure with large Na diffusion channels. An interesting NASICON compound is $Na_3V_2(PO_4)_3$, that displays two plateaus at 3.4 (V^{3+}/V^{4+}) and 1.6 V (V^{2+}/V^{3+}) vs. Na^+/Na delivering, respectively, 120 and 59 $mAh \cdot g^{-1}$, and enabling it working both as cathode and anode. [47, 55]

Fluorophosphates. The introduction of electronegative F^- in the structure, allows reaching high-voltage electrodes. Na_2FePO_4F has been widely examined, showing a fair electrochemical activity for NIB (ca. 100 $mAh \cdot g^{-1}$ at ca. 3 V operation). Conversely, Na_2MnPO_4F is almost inactive, unless it is treated with C-coating.[47, 49] One of the main candidates for NIB is $Na_3V_2(PO_4)_2F_3$, because of its high operating voltage and good specific capacity. $Na_3V_2(PO_4)_2F_3$ is able to provide 95 $mAh \cdot g^{-1}$ at 5C, showing a couple of plateaus at 3.65 and 4.1 V similarly to the other $Na_3(VO_x)_2(PO_4)_2F_{3-2x}$ main candidate.[49]

Apart from the above-mentioned phases, several other polyanionic compounds, such as sulphates, fluorosulphates and pyrosphosphates are under study. [50, 54]

Organic cathodes.

Organic compounds are being developed to fabricate green rechargeable batteries on the basis of their abundance, low cost, designability, recyclability and high theoretical capacity.

---

[55] L. P. Wang, L. Yu, X. Wang, M. Srinivasan, Z. J. Xu. *J. Mater. Chem. A* 2015, **3**, 9353–9378. "Recent developments in electrode materials for sodium-ion batteries".

Disodium rhodizonite ($Na_2C_6O_6$) exhibits a reversible capacity of 170 mAh·g^{-1} with an average working voltage of 2.8 *vs*. Na^+/Na. However, the capacity is dramatically decreased after 40 cycles as a result of the dissolution of $Na_xC_6O_6$ into the organic electrolyte. Another example of organic material is the aniline/o-nitroaniline copolymer (PAN-NA), able to deliver 180 mAh·g^{-1} at an average voltage of 3.2 V and retain 173 mAh·g^{-1} after 50 cycles. A more stable material in terms of cyclability is given by the 3, 4, 9, 10 – perylene-tetracarboxylic acid-dianhydride (PTCDA), that displays 140 mAh·g^{-1} at 10 mA·g^{-1} and retains 77% of the initial capacity after 195 cycles.[50, 54] However, organic cathode materials must overcome problems such as low redox potential and unfavorable dissolution, with which they are commonly associated.

Prussian Blue compounds.

Prussian Blue analogues (PBA) have been proposed as alternative to the conventional layered oxides and polyanionic compounds.[50, 54, 55] Since the aim of this PhD dissertation is the development and utilization of these materials as electrode for NIB, they will be further described in detail in a posterior section (1.4).

A comparative among the different cathodic materials revisited above is shown in Figure 1.11.

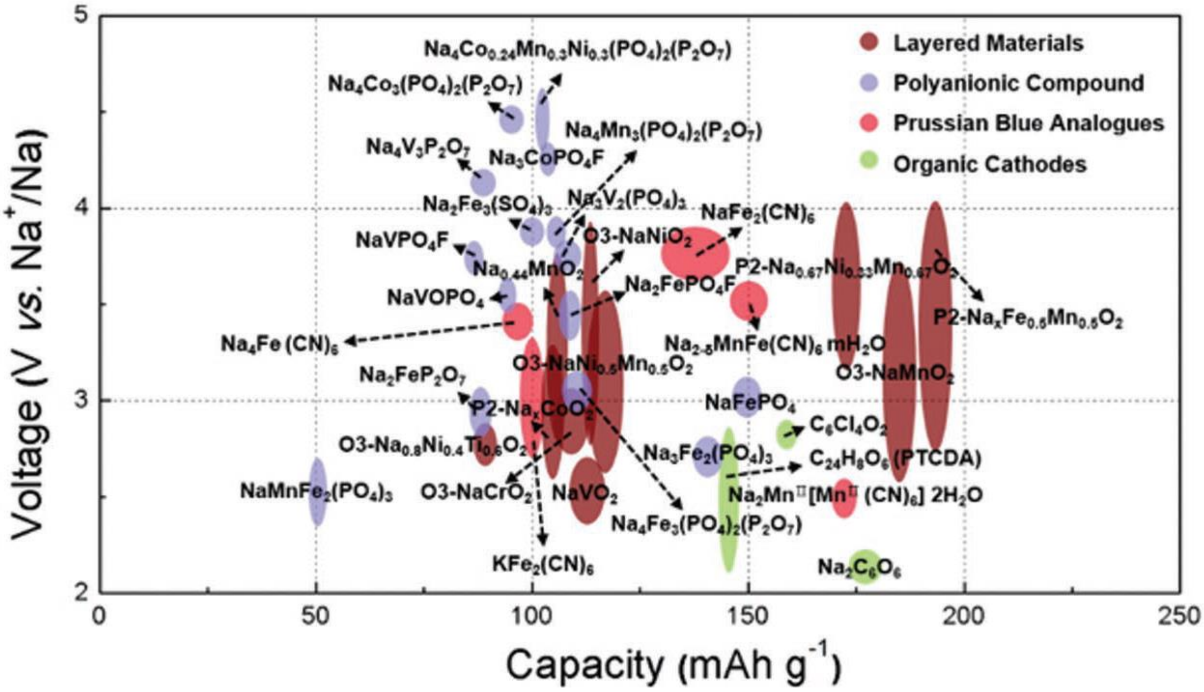

Figure 1.11. Voltage vs. capacity of representative positive electrode materials for NIB.[50]

1.3.5.2 *Anodes for NIB*

The possible anode materials for room temperature NIB, can be classified as: *carbonaceous materials, metal oxides, alloys and organic materials.*

Carbonaceous materials

Carbon materials have been widely studied as potential anode for NIB because of their low cost, environmentally friendliness and excellent electrochemical stability. An important difference with regard to LIB, is the fact that Na^+ is unable to reversible intercalate into graphite or form graphitic intercalation compounds as NaC_6 or NaC_8, since they are thermodynamically unfavorable. Therefore, graphite cannot be used as anode for NIB. Some rational solutions have been proposed to overcome it, such as preparing "expanded graphite" by partial reduction of graphite oxide (approach 1) or using "solvent co-intercalation", but they are still far from the optimum performance of graphite in LIB.[56]

Soft carbons are disordered carbons that undergo graphitization at temperatures over 2800 ˚C. Some of the soft carbons studied are petroleum coke,[57] pitch derived carbon fibers[58] and carbon black.[59] Although soft carbons have demonstrated to intercalate Na, an important irreversible capacity is still observed in the initial cycle.

Hard Carbons are non-graphitizable disordered carbons. Its structure depends on the synthesis conditions, but the general model postulates that hard carbons are composed of carbon layers (graphene-like) and nanosized pores. Hard carbon (pyrolized glucose) can deliver a high reversible specific capacity of ca. 300 $mAh \cdot g^{-1}$, close to that of Li intercalation in graphite, making them the most promising anode material for NIB. Indeed, they are currently being used in the first NIB prototypes. The sodium storage mechanism of hard carbons, still under debate, is described as a first Na^+ intercalation between graphene sheets (slopping-voltage region from 1.2 V to 0.1 V) followed by the filling of nanopores with Na^+ or Na^+ adsorption (plateau region at and below 0.1 V).[60] On the other hand, given the low operating voltage, hard carbon presents the risk of electroplating, since the electrochemical potential of Na insertion into hard carbon is close to that of the metal itself.[61]

Additionally, few recent works have reported really good performance of graphene-based (400 $mAh \cdot g^{-1}$ at 50 $mA \cdot g^{-1}$) and reduced graphene oxide (rGO, 174 $mAh \cdot g^{-1}$) as anode materials for NIB.

Metal oxides

Intercalation compounds. The most common intercalation metal oxides for anodic purposes contain titanium. Even though TiO_2 has no d-electrons and therefore is an electronic insulator, the polymorphs of TiO_2, such as nano-sized anatase, rutile, and amorphous TiO_2, have shown electrochemical activity for Na^+ insertion. The Na storage mechanism is believed to involve the reduction of Ti^{4+} to Ti^{3+} and partially generation of Ti^0 and NaO_2. The oxide $Li_4Ti_5O_{12}$, used in LIB, can also accommodate Na ion de/intercalation

---

[56] C. Bommier, X. Ji. *Isr. J. Chem.* 2015, **55** (5), 486-507. "Recent Development on Anodes for Na-ion Batteries".

[57] M. M. Doeff, Y. P. ma, S. J. Visco, L. C. Dejonghe. *J. Electrochem. Soc.* 1993, **140**, L169-L170. "Electrochemical Insertion of Sodium into Carbon"

[58] P. Thomas, D. Billaud. *Electrochim. Acta* 2000, **46**, 39-47. "Effect of mechanical grindin of pitch-based carbon fibers and graphite on their electrochemical sodium insertion".

[59] R. Alcántara, J. M. Jimenez-Mateos, P. Lavela, J. L. Tirado. *Electrochem. Commun.* 2001, **3**, 639-642. "Carbon black: a promising electrode material for sodium-ion batteries".

[60] D. A. Stevens, J. R. Dahn. *J. Electrochem. Soc.* 2000, **147**, 1271-1273. "High Capacity Anode Materials for Rechargeable Sodium-Ion Batteries".

[61] D. Kundu, E. Talaie, V. Duffort, L. F. Nazar. *Angew. Chem. Int. Ed.* 2015, **54**, 2-20. "The emerging Chemistry of Sodium Ion Batteries for Electrochemical Energy Storage".

reversibly, delivering reversible capacities of 150 mAh·g^{-1} with a redox potential of 0.9 V *vs*. Na^{+}/Na.[62] Nevertheless, the most promising anodic oxide is $Na_2Ti_3O_7$. $Na_2Ti_3O_7$ is capable of exhibiting 200 mAh·g^{-1} at an average voltage of 0.3 V *vs*. Na^{+}/Na, which is the lowest voltage ever reported for an oxide in NIB and much lower than its Li analogue ($Li_2Ti_3O_7$), *ca*. 1.7 V *vs*. Li^{+}/Li.[63] However, the sodiated phase presents structural instability, that results in poor cyclability, as a consequence of the instability of the SEI formed.[64]

Conversion compounds. Similarly to conversion compounds for LIB, these materials undergo multiple electron reaction per transition metal (through the same mechanism than that described in (Eq. 1.1, but replacing Li by Na), present high hysteresis and high average operating voltages. However, unlike for LiB, the practical specific capacities obtained for NIB are far lower from the theoretical value, suggesting sluggish kinetics of Na ion transfer because of the larger ion size and different nature of the SEI layer formed.[50] Some of the conversion materials examined as anode materials for NIB, include Fe_2O_3, Co_3O_4, CuO[50], the spinel $NiCo_2O_4$,[65] and the sulfides FeS_2, Ni_3S_2, SnS_2, Sb_2S_3, MoS_2.[47, 56]

Alloys

Na-based alloys typically exhibit large theoretical capacities, since a single atom may combine with multiple Na ions, but significantly lower volumetric energy density compared to Li-based alloys. Similarly to Li-based alloys, their main problem lies in the volume expansion, that penalize the cycle life and the speed of charge-discharge of the batteries.[62] The strategies to improve the electrochemical performance are coincident to those reported for LIB (nanostructuration, morphology modification and composite preparation).

No electrochemical activity has been found for Na-Si alloys. Conversely, tin, antimony and phosphorus form binary alloys with sodium. Na-Sn system delivers up to 760 mAh·g^{-1} (3.75 Na atoms) at a low average operating voltage (*ca*. 0.2 V) if Sn nanoparticles are coated onto carbon. However, it shows insufficient capacity retention (less than 20 cycles). Sb micrometric and Sb–C composites offers a high capacity of 610 mAh·g^{-1} (3 Na ions), for more than 100 cycles when the additive FEC (fluoroethylene carbonate) is added, although the average voltage is higher than those based on tin. Meanwhile, phosphorus can provide higher specific capacity compared to Sn and Sb, because of its lower atomic weight. Phosphorus has three main allotropes: white, red and black phosphorus. Amorphous red phosphorus-C composite is reported to undergo 3-electron reversible redox process (to store 3 Na atoms), forming Na_3P and delivering 1890 mAh·g^{-1} at 0.4 V vs. Na^{+}/Na, when FEC is added. Other Na-metal alloys involve Ge and some other binary combinations.[66]

---

[62] M. Dahbi, N. Yabuuchi, K. Kubota, K. Tokiwa, S. Komaba. *Phys. Chem. Chem. Phys.* 2014, **16**, 15007-15027. "Negative electrodes for Na-ion batteries".

[63] P. Senguttuvan, G. Rousse, V. Seznce, J-M. Tarascon, M. R. Palacín. *Chem. Mater.* 2011, **23**, 4109. "$Na_2Ti_3O_7$: Lowest Voltage Ever Reported Oxide Insertion Electrode for Sodiumm Ion Batteries".

[64] M. A. Muñoz-Márquez, M. Zarrabeitia, E. Castillo-Martínez, A. Eguía-Barrio, T. Rojo, M. Casas-Cabanas. *ACS Appl. Mater. Interfaces* 2016, **7** (14), 7801-7808. "Composition and Evolution of the Solid-Electrolyte Interphase in Na2Ti3O7 Electrodes for Na-ion Batteries: XPS and Auger Parameter Analysis".

[65] R. Alcántara, M. Jaraba, P. Lavela, J. L. Tirado. *Chem. Mater.* 2002, **14**, 2847-2848."$NiCo_2O_4$ Spinel: First Report on a Transition Metal Oxide for the Negative Electrode of Sodium-Ion Batteries".

[66] Y. Kim, K-H. Ha, S. M. Oh, K. T. Lee. *Chem. Eur. J.* 2014, **20**, 11980-11992. "High-Capacity Anode Materials for Sodium-Ion Batteries".

Organic anodes

Sodium organic anodes have received considerable attention because of their potentially high capacity, low cost and sustainability. Among the organic anodes, the conjugated carboxylates ($Na_2C_8H_4O_4$) exhibited a reversible capacity of 250 mAh·g^{-1} at 0.29 V *vs*. Na$^+$/Na, but suffer from poor rate and cyclability. Juglone-rGO composites and Na_2DBQ (Di-sodiated 2,5-dihydroxy-1,4-benzoquinone) also exhibited respectable capacities of 350 and 265 mAh·g^{-1}, respectively.[50] Schiff-based electrodes provided 350 mAh·g^{-1} below 1 V *vs*. Na$^+$/Na.[67] Nonetheless, it should be noted that the organic materials present an instinct drawback of low volumetric energy density, because of its low weight density, highly branched structure and large porosity.

A comparative illustration of the different anodic materials addressed above is presented in Figure 1.12.

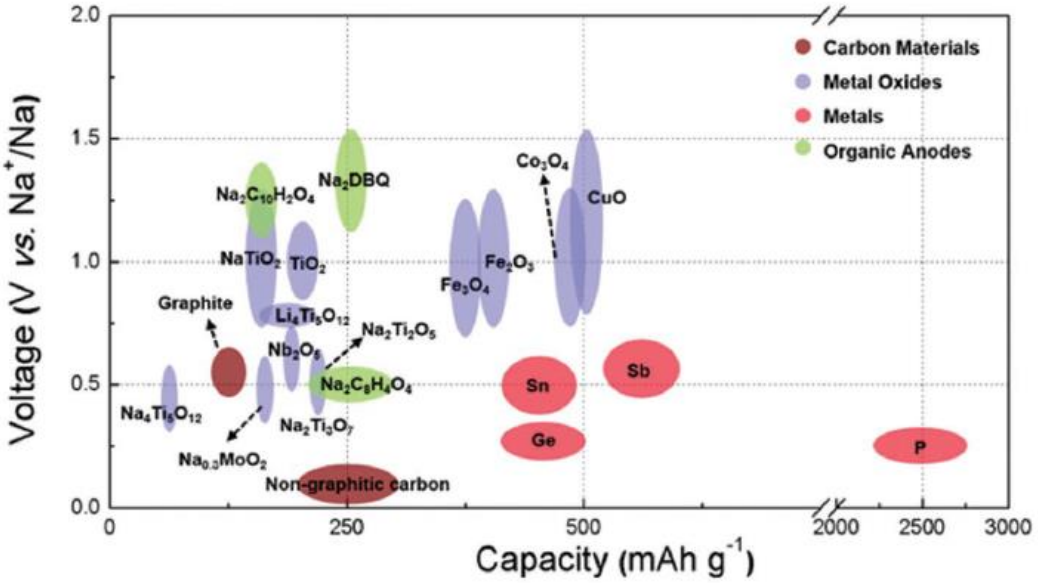

Figure 1.12. Voltage vs. capacity of representative negative electrode materials for NIB.[50]

1.3.5.3 *Electrolytes for NIB*

Only few studies have been performed in aqueous media, provided the limited voltage window stability of water-based electrolytes (*ca*. 1.23 V). Notwithstanding, aqueous Na-based systems offer much higher ionic mobility, low cost and are simpler to manufacture.[49]

Most of the studies developed in NIB have been conducted in non-aqueous solvents. In contrast to the standard $LiPF_6$ in EC: DMC (sometimes containing VC (vinylene carbonate) additive) established for LIB, several different electrolytes were initially deployed for NIB, such as $NaPF_6$ in EC: DMC or $NaClO_4$ in PC.

---

[67] E. Castillo-Martínez, J. Carretero-González, M. Armand. Angew. Chem. 2014, **126** (21), 5445-5449. "Polymeric Schiff bases as Low-Voltage Redox Centers for Sodium-Ion Batteries".

Indeed, the discovery of the different nature (thickness and composition) of the solid electrolyte interphase (SEI) formed in NIB systems compared to LIB, even when using the same solvent, required the search for the appropiate electrolyte for the new NIB technology. [62, 68] To this end, several systematic studies have been reported, defining $NaPF_6$ in EC: PC, as the most attractive combination to be adopted as a standard electrolyte for the in NIB,[68] and even better if it additionally contains a 10% of DMC.[69]

As in LIB, other possibilities to replace organic solvents are based on the use of ionic liquids or solid polymer electrolytes. Ionic liquids provide excellent thermal and electrochemical stabilities, non-flammability but, conversely, they are costly, present high viscosity (low ionic conductivity) and cannot be obtained without impurities, what hinders its practical utilization so far. Polymers are also thermally and chemically stable, low cost, non-toxic, have dual functionality (separator and electrolyte) and prevent dendrite formation, although they suffer from poor interfacial contact with the electrodes and low ionic conductivity at room temperature.[70] Consequently, hegemony of the organic electrolytes is indisputable till the date.

1.4 Prussian Blue

As discussed above, Prussian Blue materials have emerged as viable electrode material in rechargeable NIB, although as it will be in the following section, it has been explored for many other chemistries.

Prussian Blue (PB) and its analogues, also called hexacyanometallates, have become serious candidate cathode materials for NIB along the last 4 years. The general formula of PBA can be ideally described as $AM[M'(CN)_6]\cdot xH_2O$ (A = Li, Na, K; M, M'= transition metal; sometimes M = M'; typically M'= Fe), being $KFe[Fe(CN)_6]\cdot xH_2O$ the so-called Prussian Blue. Interstitial Fe^{3+} and $[Fe(CN)_6]^{4-}$ vacancies (the latter represented as ☐) are the usual defects.[71] This family of compounds is characterized by their easiness of synthesis (in aqueous media and usually at room or close to room temperature) and abundance of the component elements, what aligns with the low-cost philosophy of NIB technology.[50] Another appealing feature ascribed to Prussian Blue Analogues (PBA) relies on their 3D metalorganic host structure with tunable and open channels that allow rapid insertion/diffusion of "A" species.[72] PBA generally adopt a cubic structure (space group *Fm*-3*m*) with lattice parameter a = *ca*. 10.178 Å, where LS M'^{II} and HS M^{3+} coexist on alternate corners of a small cube connected by linear cyanide anions along the three directions of space, giving a $M^{3+}\text{-N}\equiv\text{C-}M'^{II}$ bond length of about 5 Å. Such a large empty cavities are half-ocuppied by alkali ions and favor the reversible insertion of A^+.[73]

---

[68] A. Ponrouch, E. Marchante, M. Courty, J-M. Tarascon, M. R. Palacín. *Energy Environm. Sci.* 2012, **5**, 8572-8583. "In search of an optimized electrolyte for Na-ion batteries".

[69] A. Ponrouch, R. Dedryvère, D. Monti, A. E. Demet, J. M. A. Mba, L. C. Croguennec, C. Masquelier, P. Johansson, M. R. Palacín. *Energy Environ. Sci.* 2013, **6**, 2361-2369. "Towards high energy density sodium ion batteries through electrolyte optimization".

[70] A. Ponrouch, D. Monti, A. Boschin, B. Steen, P. Johansson, M. R. Palacín. *J. Mater. Chem.* 2015, **3**, 22-42. "Non-aqueous electrolytes for sodium-ion batteries".

[71] H. J. Buser, D. Schwarzenbach, W. Petter, A. Ludi. *Inorg. Chem.* 1977, **16** (11), 2704- 2710. "The crystal structure of Prussian Blue: $Fe_4[Fe(CN)_6]_3\cdot xH_2O$ "

[72] Colin D. Wessels et al. *Nature Comm.* 2011, **2**, 550. "Copper hexacyanoferrate battery electrodes with long cycle life and high power".

[73] J. F. Keggins, F. D. Miles. *Nature* 1936, **137**, 577-578. "Structure and formulae of the Prussian Blues and Related Compounds".

Prussian Blue can evolve electrochemically into two different forms: the totally oxidized specie called Berlin Green, $M[M'(CN)_6]\cdot xH_2O$, where the transition metals are in oxidation state 3^+ and contains no alkali atoms on the structure; or its reduced form known as Prussian White or Everytt salt, $A_2M[M'(CN)_6]$, in which all the iron atoms are in oxidation state 2^+ and the vacancies are fully occupied by alkali atoms (as shown in Figure 1.13).[73]

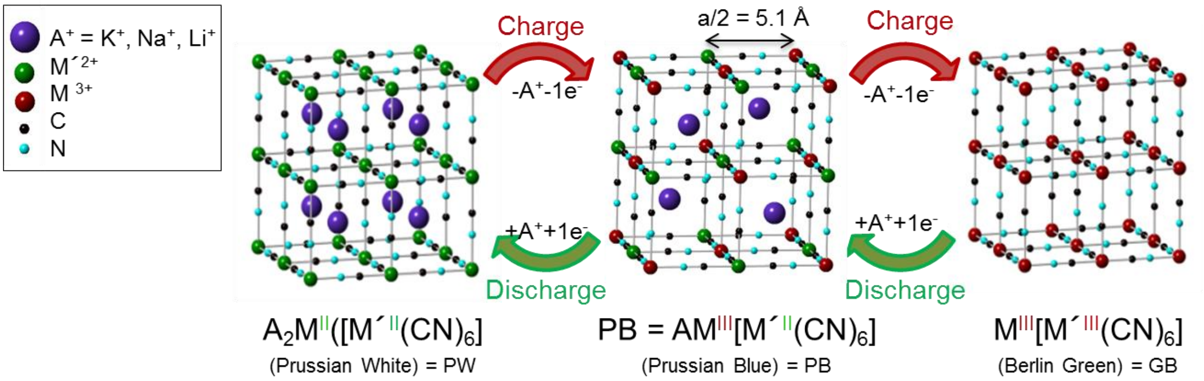

Figure 1.13. Prussian blue structure and its corresponding oxidized (Berlin Green) and reduced (Prussian White) species.

While the totally oxidized phase, BG, mantains the cubic symmetry (either if electrochemically oxidized or directly produced in that state), the totally reduced phases tend to have lower symmetry, either monoclinic or rhombohedral depending on the specific chemical formula and thus the material undergo a phase transition during electrochemical cycling.

The electrochemical behavior of Prussian Blue was first reported more than 30 years ago, in aqueous electrolyte.[74, 75,] More recently, PBAs have been revisited as cathode materials for organic rechargeable alkali-ion batteries (LIBs,[76] K-ion batteries (KIBs)[77] and, in the last four years, NIBs[78]) with encouraging results.

1.4.1 Prussian Blue phases in aqueous batteries

As already mentioned electrochemical behavior of Prussian Blue in aqueous electrolyte was first explored by Neff more than 30 years ago, with possible applications in electrochromic devices and batteries.[79, 80]

---

[74] V. D. Neff. *J. Electrochem. Soc.* 1978, **125**, 886-887. "Electrochemical oxidation and reduction of thin films of Prussian Blue".

[75] D. Ellis, M. Eckhoff, V. D. Neff. *J. Phys. Chem.* 1981, **85**, 1225-1231. "Electrochromism in the mixed-valence hexacyanides. 1. Voltammetric and spectral studies of the oxidation and reduction of thin films of prussian blue".

[76] N. Imanishi , T. Morikawa, J. Kondo, Y. Takeda, O. Yamamoto, N. Kinugasa, T. Yamagishi. *J. Power Sources* 1999, **79**, 215–219. "Lithium intercalation behavior into iron cyanide complex as positive electrode of lithium secondary battery".

[77] A. Eftekhari. *J. Power Sources* 2004, **126**, 221-228. "Potassium secondary cell based on Prussian blue cathode".

[78] Y. Lu, L. Wang, J. Cheng, and J. B. Goodenough. *Chem. Commun.* 2012, **48**, 6544-6546. "Prussian blue: a new framework of electrode materials for sodium batteries".

[79] V. D. Neff. *J. Electrochem. Soc.* 1985, **132**, 1382-1384. "Some performance characteristics of a Prussian Blue battery".

[80] K. Itaya, H. Akahoshi, S. Toshima. *J. Electrochem. Soc.* 1982, **129**, 1498-1500. "Electrochemistry of Prussian Blue modified electrodes: an electrochemical preparation method".

Recently, several works have also exploited the potential of the PBA systems in aqueous rechargeable batteries. Led by the group of Prof. Cui at Standford University, a spin off company (Alveo Energy) was founded and is developing commercial batteries. Aqueous batteries systems offer higher ionic mobility and even lower cost compared to organic batteries, which is a driving force in their commercialization. On the other hand, they present limited voltage window stability, what translates into lower energy density.

The electrochemical performance of nanostructured nickel hexacyanoferrate (NiHCF) in 1 M $NaNO_3$ and 1 M KNO_3 solutions acidified to pH = 2 was reported in 2011 by Wessells *et al.* to deliver 52 mAh g^{-1} of reversible capacity at 3.3 V *vs.* Na^+/Na and almost no capacity fading was detected after 5,000 cycles at 8.3C (498 mA g^{-1}).[81] The same group soon reported the effect of the insertion of different monovalent cations (K^+, Na^+, Li^+ and NH_4^+) into nanostructured copper hexacyanoferrate (CuHCF) and NiHCF.[82] Rapid kinetics and long cycle life were observed for K^+ insertion into CuHCF, and for both Na^+ and K^+ insertion into NiHCF. Divalent cations, such as Mg^{2+}, Ca^{2+}, Sr^{2+} and Ba^{2+}, have also been inserted into the Ni based PBA.[83] Wu *et al*. later developed a full cell based on the redox couple NiHCF-$NaTi_2(PO_4)_3$. This full cell presented an average output voltage of 1.27 V, a specific energy of 42.5 Wh kg^{-1} and a capacity retention of 88% after 250 cycles at 5C rate (325 mA g^{-1}).[84] A full cell based only in PBA was reported by Pasta *et al*. with CuHCF as positive electrode and manganese hexacyanoferrate (MnHCF) as negative electrode and delivered a maximum specific energy of 27 Wh kg^{-1}at 1C rate with an average voltage of 0.95 V.[85] Regarding the cheaper and less polluting Fe-based compounds, Wu *et al.*[86] have recently shown the electrochemical performance of BG and sodium PB as cathodes for aqueous Na-ion batteries with capacities over 100 mAh g^{-1}, although the very poor coulombic efficiency still remains to be improved (around 80% at 1C).

1.4.2 Prussian Blue phases in organic rechargeable batteries

One of the first works regarding the use of PB as cathode material in **LIBs** was reported by Imanishi et al. Li^+ intercalation occurs at 3 V *vs*. Li^+/Li and specific capacities up to 120 mAh·g^{-1} can be obtained.[76] Recent studies using PBAs such as $K_2Mn[Mn(CN)_6]$[87], $LiMn[Fe(CN)_6]$ [88] and $Fe[Fe(CN)_6]$ (Berlin Green, BG)[89] demonstrated enhanced Li-ion storage properties with capacities as high as 200 mAh·g^{-1}, 145 mAh·g^{-1}

---

[81] C. D. Wessells, S. V. Peddada, R. A. Huggins, Y. Cui. *Nano Lett.* 2011, **11**, 5421-5425. “Nickel hexacyanoferrate nanoparticle electrodes for aqueous sodium and potassium ion batteries”.

[82] C.D. Wessells, S. V. Peddada, M. T. McDowell, R. A. Huggins, Y. Cui. *J. Electrochem. Soc.* 2012, **159**, A98-A103. “The effect of insertion species on nanostructured open framework hexacyanoferrate battery electrodes”.

[83] R. Y. Wang, C. D. Wessells, R. A. Huggins, Y. Cui. Nano Lett. 2013, **13**, 5748-5752. “Highly Reversible Open Framework Nanoscale Electrods for Divalent Ion Batteries”.

[84] X. Wu, Y. Cao, X. Ai, J. Quian and H. Yang. *Electrochem. Commun.* 2013, **31**, 145-148. “A low cost and environmentally benign aqueous rechargeable sodium-ion battery based on $NaTi_2(PO_4)_3$-$Na_2NiFe(CN)_6$”.

[85] M. Pasta, C. D.Wessells, N. Liu, J. Nelson, M. T. McDowell, R. A. Huggins, M. F. Toney, Y. Cui. *Nat. Commun.* 2014, **5**, 3007. “Full open-framework batteries for stationary energy storage”.

[86] X. Wu, Y. Luo, M. Sun, J. Quian, Y Cao, X Ai, H. Yang. *Nano Energy* 2015, **13**, 117-123. “Low-defect Prussian blue nanocubes as high capacity and long life cathodes for aqueous Na-ion batteries”.

[87] D. Asakura, M. Okubo, Y. Mizuno, T. Kudo, H. Zhou, K. Ikedo, T. Mizokawa, A. Okazawa, N. Kojima. *J. Phys. Chem. C* 2012, **116**, 8364-8369. “Fabrication of a cyanide-bridged coordination polymer electrode for enhanced electrochemical ion storage ability”.

[88] Y. Kurihara, T. Matsuda, Y. Moritomo, *Jpn. J. Appl. Phys.* 2013, **52**, 017301 1-6. “Structural properties of Manganese hexacyanoferrates against Li concentration”.

[89] L. Shen, Z. Wang, L. Chen. *Chem. Eur. J.* 2014, **20**, 1-5. “Prussian Blue as a cathode material for lithium ion batteries”.

and 140 mAh·g^{-1}, respectively. However, poor cyclability was found in the cases of $K_2Mn[Mn(CN)_6]$ and $LiMn[Fe(CN)_6]$ which was accordingly attributed to the lattice expansion by 17 % leading to a high mechanical strain and to the phase separation into cubic and tetragonal phases when the Li content decreases. Interestingly, Sung and coworkers, as well as Zhang *et al*. reported the electrochemical properties of PBA based on Co and Mn for the first time as negative electrode for LIB, in 2013 and 2014, respectively, coincident with the first and second year of this thesis work (and our own research work on Fe-based PB as anode in LIB (see chapter 4, section 4.3)). Their experiments with Co-based PBA showed that this material can deliver reversible capacities of 400 mAh·g^{-1} in the 0.01-3.0 V range.[90, 91]

Given the higher abundance of potassium in contrast to lithium, Eftekhari tested PB in **KIBs** with an experimental capacity of 87 mAh·g^{-1} and similar redox potential to that obtained vs. Li^+/Li.[77] Recently, another work reported the enhanced capacity of Prussian Green as compared to PB, reaching even 121.4 mAh·g^{-1}.[92]

Even more abundant and sustainable are **NIB**. Na^+ reversible intercalation was first explored in 2012 for PBA with M = Mn, Fe, Co, Ni by Goodenough *et al.*[78] and the non-PBA-structured M = Zn by Lee and co-workers.[93] The largest capacity, around 100 mAh·g^{-1}, was achieved with M = Fe, which reacts at 2.9 and 3.6 V *vs*. Na^+/Na. Since then, many investigations have been conducted. One year later, in 2013, single-crystal nanoparticles of cubic Berlin Green $Fe[Fe(CN)_6]\cdot H_2O$ displayed 120 mAh·g^{-1} (1.52 Na^+ insertion) and a maintained coulombic efficiency of *ca*. 100% for more than 600 cycles.[94] In the last 2 years, several implementations have been achieved. By preparing graphene-oxide Prussian Blue composites, the capacity was boosted up to 150-160 mAh·g^{-1}.[95, 96, 97] Another highlight has starred in the high-quality purely iron based sodium PB (Na-PB) nanocubes, $Na_{0.61}Fe[Fe(CN)_6]_{0.94}\square_{0.06}$, reported by You et al. in 2014, which exhibited up to 170 mAh·g^{-1} at 25 mA·g^{-1} with no apparent capacity loss after 150 cycles as a consequence of the low H_2O and $[Fe(CN)_6]^{4-}$ vacancies content.[98]

Prussian White has also been investigated as superior low cost cathode material for sodium ion batteries. The beneficial enriching in alkali content would prevent the first cycle inefficiency, in contrast to PB phases. Moritomo et al. explored $Na_{2-\delta}M_xFe_y(CN)_6$ (M= Co/ Mn, $\delta \geq 0.4$), which showed capacities up to

---

[90] M. Shokouhimehr, S-H. Yu, D-C. Lee, D. Ling, T. Hyeon and Y-E. Sung. *Nanosci. Nanotechnol. Lett.* 2013, **5** (7), 770-774. "Metal Hexacyanoferrate Nanoparticles as Electrode Materials for Lithium Ion Batteries".

[91] P. Nie, L. Shen, H. Luo, B. Ding, G. Xu, J. Wang, X. Zhang. *J. Mater. Chem A* 2014, **2**, 5852-5857. "Prussian blue analogues: a new class of anode materials for lithium ion batteries".

[92] P. Padigi, J. Thiebes, M. Swan, G. Groncher, D. Evans. R. Solanki. *Electrochimica Acta* 2015, **166**, 32-39. "Prussian Green: A high Rate Capacity Cathode for Potassium Ion Batteries".

[93] H. Lee, Y-L. Kim, J-K. Park, J. W. Choi. *Chem. Commun.* 2012, **48**, 8416-8418. "Sodium zinc hexacyanoferrate with a well-defined open framework as positive electrode for sodium ion batteries".

[94] X. Wu, W. Deng, J. Qian, Y. Cao, X. Ai, H. J. Yang. *J. Mat. Chem. A* 2013, **1**, 10130-10134. "Single-crystal $FeFe(CN)_6$ nanoparticles: a high capacity and high rate cathode for Na-ion batteries".

[95] D. Yang, J. Xu, X-Z. Liao, H. Wang, Y-S. He, Z-F. Ma. *Chem Comm* 2015, **51**, 8181-8184. "Prussian blue without coordinated water as a superior cathode for sodium-ion battereis".

[96] Y. Jiang, S. Yu, B. Wang, Y. Li, W. Sun, Y. Lu, M. Yan, B. Song and S. Dou. *Adv. Func. Mat.* 2016. DOI: 10.1002/adfm.201600747. "Prussian Blue@C Composite as an Ultrahigh-Rate and Long-Life Sodium-Ion Battery Cathode".

[97] S. J. R. Prabakar, J. Jeong, M. Pyo. *RSC Adv.* 2015, **5**, 37545-37552. "Highly crystalline Prussian blue/graphene composites for high-rate performance cathodes in Na-ion batteries".

[98] You Y., Wu X-L., Yin Y-X., Guo Y-G. *Energy Environm. Sci.* 2014, **7**, 1643-1647. "High-quality Prussian blue crystals as superior cathode materials for room-temperature sodium-ion batteries".

135 mAh·g^{-1} and fast Na$^+$ intercalation/de-intercalation with no structural phase transition.[99, 100, 101] Nonetheless, when M = Mn and $\delta \leq 0.3$, a structural transformation from cubic to rhombohedral occurs, maintaining similar capacities to those previously reported are obtained.[102] On the other hand, a purely Mn-based sodium-rich monoclininc PW, $Na_{1.96}Mn[Mn(CN)_6]_{0.99}\cdot\square_{0.01}\cdot 2H_2O$, studied by Cui *et al.*, exhibited up to 209 mAh·g^{-1} at 40 mA·g^{-1} due to the possible insertion of 3 Na$^+$ in the structure and the reduction from Mn^{3+}-N-C-Mn^{III} to Mn^{2+}-N-C-Mn^{I}. A structural phase transition from the as-synthesized monoclinic PW to an orthorhombic phase along the de-insertion process has also been observed, to finally reach a cubic structure at the end of charge.[103] Besides, in an attempt to combine the good specific capacity observed in $Na_{1.8}Mn[Fe(CN)_6]_{0.99}\cdot\square_{0.01}$ and the coulombic efficiency of $Na_{1.86}Ni[Fe(CN)_6]_{0.96}\cdot\square_{0.04}$, Ma and coworkers prepared and tested the ternary Prussian blue analogue (PBA), $Na_{1.76}Ni_{0.12}Mn_{0.88}[Fe(CN)_6]_{0.98}\cdot\square_{0.02}$. It displayed a specific capacity of 123.3 mAh·g^{-1}, coulombic efficiency of 92.71% in the first cycle (and above 98% after 5 cycles) and 83.3% of capacity retention after 800 cycles when cycled at 100 mA·g^{-1}.[104] Interestingly, a couple of purely iron based PW cathode material, $Na_{2-x}Fe_2(CN)_6$, were reported in 2015 only by Guo *et al.* [105] and Goodenough *et al.* [106] This compound presents a rhombohedral structure and delivers capacities of 150 mAh·g^{-1} at 10-25 mA·g^{-1} and fairly good cycling performance. About 90% of the initial capacity is retained after 200 cycles at 25 mA·g^{-1} in Guo´s report and 80% is observed after 750 cycles in Goodenough´s study, when it is charged at 75 mA·g^{-1} and discharged at 300 mA·g^{-1}. One of the most recent work concerning the utilization of Prussian White in SIB has been reported by Wu et al. [107] The study presents a rhombohedral Co-Fe based Prussian White, $Na_{1.85}Co[Fe(CN)_6]_{0.99}\cdot\square_{0.01}\cdot 1.9\ H_2O$, with high capacity, 150 mAh·g^{-1}, and cyclability of 90% over 200 cycles at 100 mA g^{-1}.

It is evident the intense research activity that Prussian Blue have awakened as cathode materials, especially along the 4 last years in the NIB technology, since this thesis work started. Thus, PBA seems to postulate as firm candidates for real applications in NIB. Firm proofs of it are the projects under developing of companies as Alveo Energy (for aqueous) and SHARP (for organics), in which these materials are involved.

---

[99] M. Takachi, T. Matsuda, Y. Moritomo. *Jpn J. Appl. Phys.* 2013, **52**, 090202. “Redox reactions in Prussian Blue Analogue Films with Fast Na$^+$ Intercalation”.

[100] M. Takachi, T. Matsuda, Y. Moritomo. *Appl. Phys. Express* 2013, **6**, 025802. “Cobalt hexacyanoferrate as cathode material for Na$^+$ secondary battery”.

[101] T. Matsuda, M. Takachi, Y. Moritomo. *Chem. Commun.* 2013, **49**, 2750-2752. “A sodium manganese ferrocyanide thin film for Na-ion batteries.”

[102] L. Wang, Y. Lu, J. Liu, M. Xu, J. Cheng, D. Zhang, J. B. Goodenough. Angew. *Chem. Int. Ed.* 2013, **52**, 1-5. “A Superior Low-Cost Cathode for a Na-Ion Battery”.

[103] H.-W. Lee, R. Y. Wang, M. Pasta, S. W. Lee, N. Liu, Y. Cui. *Nat. Commun*. 2014, **5**, 5280. “Manganese hexacyanomanganate open framework as a high-capacity positive electrode material for sodium-ion batteries”.

[104] D. Yang, J. Xu, X-Z. Liao, Y-S. He, H. Li, Z-F. Ma. *Chem. Commun.* 2014, **50**, 13377-13380. “Structure optimization of Prussian blue analogue cathode materials for advanced sodium ino batteries”.

[105] Y. You, X-Q. Yu, Y-X. Yin, K.W. Nam, Y-G. Guo. *Nano Res.* 2015, **8**, 117-128. “Sodium iron hexacyanoferrate with high Na content as a Na-rich cathode material for Na-ion batteries”.

[106] L. Wang, J. Song, R. Qiao, L. A. Wray, M. A. Hossain, Y-D. Chuang, W. Yang, Y. Lu, D. Evans, J-J. Lee, S. Vail, X. Zhao, M. Nishijima, S. Kakimoto, J. B. Goodenough. *J. Am. Chem. Soc.* 2015, **137**, 2548-2554. “Rhombohedral Prussian White as Cathode for Rechargeable Sodium-Ion Batteries”.

[107] X. Wu, C. Wu, C. Wei, L. Hu, J. Qian, Y. Cao, X. Ai, J. Wang, H. Yang. *ACS Appl. Mat. Interfaces* (2016). DOI: 10.1021/acsami.5b12620. “Highly crystallized $Na_2CoFe(CN)_6$ with Suppressed Lattice Deffects as Superior Cathode Material for Sodium-Ion Batteries”.

1.5 Scope of this thesis

Given the rapid development of PB materials for NIB and LIB along the years of development of this thesis work, this project has focused on extending the use of PB materials for anodes in rechargeable Na- and Li-ion batteries, as well as improving the performance of cathode materials for NIB.

Considering the scenario described in the previous section (1.4), the main targets of this thesis work include:

- Synthesis and structural, morphological and physico-chemical characterization of the titanium Prussian Blue analogue, low-cost purely iron-based Prussian Blue (from now on Prussian Blue) and alkali rich Prussian White (hereinafter Prussian White) containing either Na or K as alkali metals in the structure.
- Study of the electrochemical properties of titanium Prussian Blue derivative and Prussian Blue (both sodiated and potassiated) as novel anode materials for NIB.
- Study of the electrochemical performance of Prussian Blue (both sodiated and potassiated) as negative electrode for LIB.
- Systematic study to optimize the electrolyte and binder of Prussian Blue at high voltage range in NIB.
- Aqueous study of the sodium Prussian Blue as cathode material for NIB.
- Study of the electrochemical properties of sodiated and potassiated Prussian White as cathode materials for NIB.
- Full cell development based on Prussian Blue and Prussian White as cathode materials.

The introduction and reasons behind this thesis work have been presented in the present chapter (chapter 1). A summary of the experimental techniques deployed for determining the structural, morphological and physicochemical characteristics of the materials, as well as for their electrochemical investigations, is described in chapter 2. The synthetic routes and the structural, morphological and physicochemical characterization of the materials is covered in chapter 3. Then, the following chapters assess the electrochemical study of the previously defined materials. Respectively, chapter 4 comprises the investigate of the titanium derivate and Prussian Blue as anode materials, chapter 5 is dedicated to explore Prussian Blue and Prussian White as cathodes and chapter 6 briefly introduces the results of a NIB full cell based in Prussian Blue materials.

Chapter 2

Experimental techniques

2.-) Experimental techniques

This chapter is devoted to the description of the equipment and the experimental conditions at which the different techniques were utilized for characterizing the materials. Firstly, a summary of all the structural, morphological and physico-chemical techniques required for analyzing and determining the structure and nature of the materials is presented. Then, the techniques deployed for testing and evaluating the electrochemical properties of the materials are detailed. Special emphasis is given to the description of a new electrochemical cell to perform *in-situ* Mössbauer measurements during electrochemical cycling of the materials, that was developed in collaboration with the UPV/EHU as a part of this PhD thesis.

2.1. Structural, morphological and physico-chemical techniques

2.1.1. X-ray powder diffraction (PXRD)

X-ray powder diffraction (PXRD) is a rapid and non-destructive analytical technique primarily used for phase identification of a crystalline material that can provide information on the atomic arrangement and unit cell dimensions. The interaction of the incident X-ray waves with electrons in the sample generates scattered X-rays which are dispersed in particular directions. Despite most of the X-rays are cancelled by destructive interference, those which satisfy Bragg´s law ((Eq. 2.1) produce a constructive interference (Figure 2.1.a) and reach the detector generating a maximum of intensity, also called reflection. Bragg´s law is expressed as:

$$n\,\lambda = 2d_{hkl}\sin\Theta \qquad (\textbf{Eq. 2.1})$$

and relates the wavelength (λ) of the X-rays to the diffraction angle (Θ, known as Bragg angle) and the spacing between the lattice planes (d_{hkl}) in a crystalline sample. The value of n is the diffraction order and can always be taken as unity, since any multiple of λ can be accounted for the diffraction or Miller indices h, k, l of any particular reflection.[1, 2, 3]

The intensity of the diffracted X-rays is continuously recorded as the source or the spinner and the detector rotate through their respective angles. When the crystal contains lattice planes with d_{hkl}-spacings appropriate to diffract X-rays at that value of θ, a peak in intensity or maxima occurs. Results are commonly presented as peak positions at 2θ along x axis and X-ray counts (intensity) along y axis in the form of an x-y plot called diffractogram.

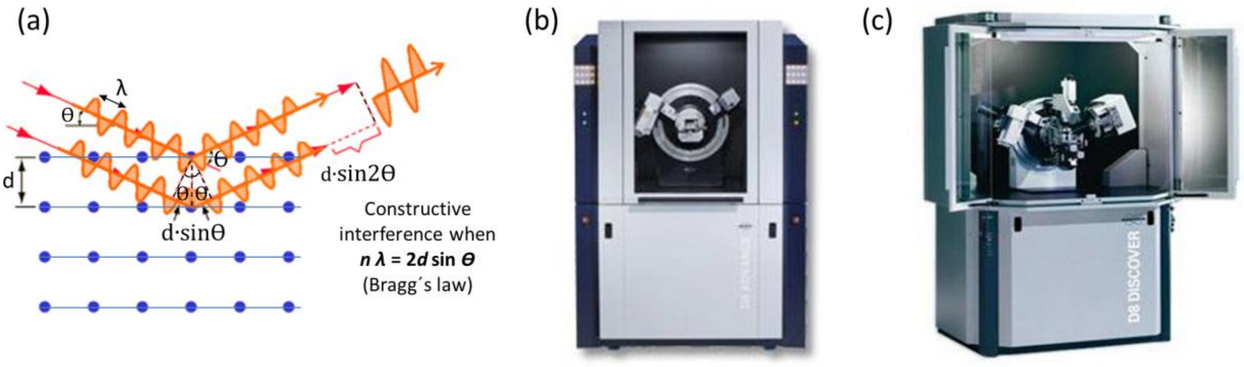

Figure 2.1. a) Schematic description of the diffraction of lattice planes, following Bragg´s law, b) Bruker D8 Advance diffractometer and c) Bruker D8 Discover diffractometer deployed in this work.

---

[1] Crystal Structure and Analysis (Principles and Practices), 2nd edition. A.J. Blake, W. Clegg, J. M. Cole, J. S. O. Evans, P. Main, S. Parson, D. J Watkin. International Union of Crystallography – Oxford Science Publications, 2009.

[2] The Basics of Crystallography and Diffraction, 2nd edition. C. Hammond. International Union of Crystallography – Oxford Science Publications, 2011.

[3] Fundaments of crystallography, 3rd edition. C. Giacovazzo. International Union of Crystallography – Oxford Science Publications, 2011.

The instrumentation utilized for acquiring the X-ray diffractograms of the materials were a Bruker D8 Advance ($\lambda_{CuK\alpha1}$ = 1.54056 Å, $\lambda_{CuK\alpha2}$ = 1.5443 Å) and D8 Discover ($\lambda_{Cu,K\alpha}$ = 1.54056 Å) diffractometers (Figure 2.1.b and c). PXRD data were collected in the range from 2ϴ = 5˚ to 80˚, with a step width of 0.0194˚. For air-sensitive materials, kapton® film was used to cover the sample thereby protecting them from contact with the atmosphere while collecting the data.

PXRD patterns of pure samples were refined by Lebail fitting to obtain cell parameters or Rietveld fitting to additionally obtain atomic position and occupancy, using the FullProf software[4]. In some cases, crystal size was calculated according to the Scherrer equation (Eq. 2.2).

$$\tau = \frac{K\lambda}{\beta cos2\Theta} \qquad (\textbf{Eq. 2.2})$$

where τ is the mean size of the ordered crystalline domains, K is the shape factor (whose value is typically 0.9), λ is the X-ray wavelength, β is the line broadening at half of the maximum intensity (FWMH) expressed in radians (rad) and ϴ is the Bragg angle (also in rad).

2.1.2. Infrared (IR)

Infrared (IR) spectroscopy is one of the most common and widely used techniques in determining structures of chemical compounds by identifying the presence of different functional groups. As its name indicates, this technique deploys IR radiation (generally from 4000-400 cm^{-1}) to irradiate a sample. The sample absorbs the radiation when the frequency of the IR is the same as the vibrational frequency of a bond or collection of bonds, what originates transitions between two vibrational levels of the molecule in the ground state (see Figure 2.2.a).

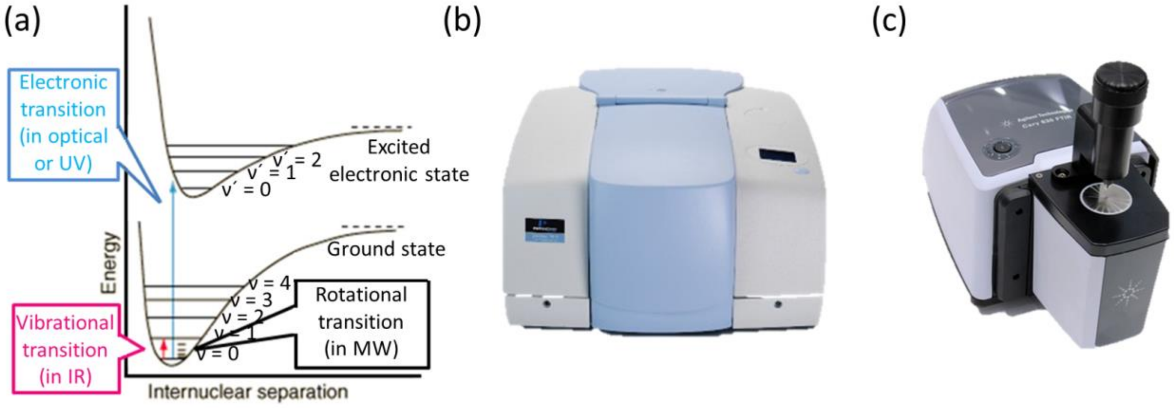

Figure 2.2. a) Energy levels of a molecule. The curves represent the electronic energy levels, the lines marked with *v* are the vibrational quantum numbers. An example for the rotational energy levels is shown as lines above the *v*=0 vibrational level. The IR absorption is drawn as a pink line. b) Perkin Elmer FTIR Spectrum 400 DTGS spectrophotometer and c) Agilent Cary 630 FTIR spectrometer.

---

[4] J. Rodríguez-Carvajal. *Physica B: Condensed Matter* 1999, **192**, 55-69. "Recent advances in magnetic structure determination by neutron powder diffraction."

Examination of the transmitted light reveals the amount of light absorbed at each frequency (or wavenumber). A typical IR spectrum is essentially a graph of infrared light transmittance (or absorbance) in the vertical axis *vs*. wavenumber on the horizontal axis. The transmittance (*T*) and the absorbance (*A*) can be calculated using equations Eq. (Eq. 2.3 and (Eq. 2.4, respectively. The latter fulfills the Beer-Lambert law.

$$T = \frac{I}{I_0} \qquad \textbf{(Eq. 2.3)}$$

$$A = \log\frac{I_0}{I} = \varepsilon bc \qquad \textbf{(Eq. 2.4)}$$

where I_0 = intensity of the incident radiation (before sample absorption), I = the intensity of the transmitted light (after sample absorption), ε = absorption coefficient, b = thickness and c = concentration of the sample. [5, 6]

IR transmission spectra were recorded in the range of wavenumber = 4000-450 cm^{-1} in a Perkin Elmer FTIR Spectrum 400 DTGS spectrophotometer (Figure 2.2.b) by preparing KBr pellets, if the material was solid, or using NaCl pellets and nujol, for liquids.

IR absorption spectra were collected in the range of wavenumber = 4000-650 cm^{-1} in an Agilent Cary 630 FTIR spectrometer (Figure 2.2.c) placed inside an Ar-filled glove box. Powdered materials or electrodes were analyzed by directly placing them in the 5 bounce ZnSe sampling window of the device.

2.1.3. Raman spectroscopy

Raman spectroscopy is another vibrational spectroscopic technique commonly used in chemistry to collect a unique fingerprint of molecules. Each molecule has a different set of vibrational energy levels, and the photons emitted have unique wavelength shifts, what allows identifying what is in a sample. It provides complementary information to IR.

The Raman effect has its origin in the electronic polarization caused by ultraviolet, visible and near-IR light. When a photon (electromagnetic radiation of specific frequency ν) reaches a molecule, it interacts with the polarizable electron density and the bonds of the molecule, exciting the molecule to a so-called virtual energy state for a short period of time. Then, the photon of frequency ν (Rayleigh scattering or elastic scattering) as well as that of frequency $\nu \pm \nu_i$ ("Raman scattering" or inelastic scattering), where ν_i represents a vibrational frequency of the molecule, are scattered (see Figure 2.3a). Raman scattering is much weaker than Rayleigh scattering, thus only a very small fraction of molecules undergoes inelastic scattering. The resulting inelastically scattered photon can be of either lower or higher energy than the incoming photon. In case the scattered photon exhibited higher frequency than the incident radiation, a blue shift is observed, generating what is called anti-Stokes lines. On the contrary, if a red shift occurs, these bands are referred as Stokes lines.[5, 6]

---

[5] The Handbook of Infrared and Raman Characteristic Frequencies of Organic Molecules. D. Lin-Vien, N. B. Colthup, W. G. Fateley and J. G. Graselli. Academic Press INC, 1991.

[6] Infrared and Raman Spectra of Inorganic and Coordination Compounds (Part A), 6th edition. K. Nakamoto. Wiley, 2009.

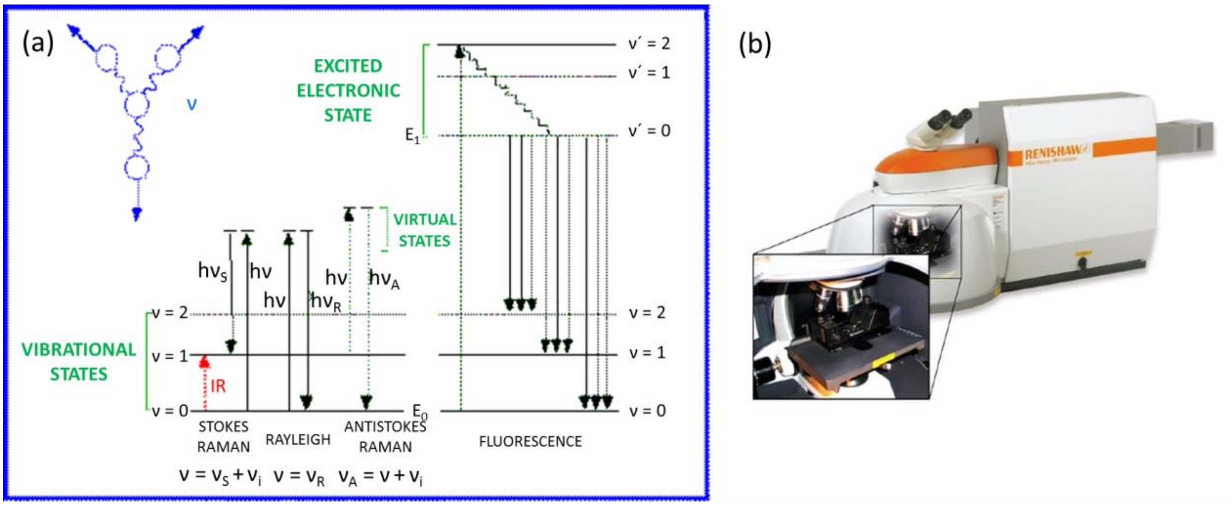

Figure 2.3. a) Energy level transitions of the Raman effect: Stokes Raman and Anti-Stokes Raman. Besides, Rayleigh scattering, IR absorption and fluorescence are visually explained. b) Ranishaw Invia spectrometer.

Different peaks in the spectrum correspond to different Raman excitations.

Raman analyses were conducted in the range 100-4000 cm^{-1} with resolution 4 cm^{-1} using a Ranishaw InVia spectrometer (as shown Figure 2.3b) equipped with a 532 nm green laser operated at a power of 0.5 mW. The laser spot size was approximately 1 mm in diameter.

2.1.4. Thermogravimetric analysis (TGA)

Thermogravimetric analysis is a simple technique in which the mass of a sample specimen is monitored as a function of temperature and/or time under controlled temperature program in a controlled atmosphere. Indeed, in a basic TGA thermal curve, the abscissa (X-axis) can be displayed as time or temperature and the ordinate (Y-axis) can be displayed as weight (mg) or weight percent (%). The changes observed in the mass are used to detect and measure the chemical or physical processes that occur upon heating the sample. Measurements are primarily exploited to determine the composition of materials and to predict their thermal stability. [7, 8]

In our case, this technique was used to determine the water content present in pure-phase materials. For this purpose, TGA NETZSCH STA 449 F3 Jupiter (as shown Figure 2.4) was used to collect the thermogravimetric curves. Experiments were performed in the temperature range from 30 to 325 ˚C , at

---

[7] Principles and applications of Thermal Analysis. Paul Gabbott. John Wiley & Sons, 2008. Chapter 3.

[8] Vyazovkin, S. 2012. Thermogravimetric Analysis. “Characterization of Materials”. 1–12. DOI: 10.1002/0471266965.com029.pub2.

a speed rate of 10 °C min^{-1} (for Prussian Blue and microcrystalline Prussian White) and 2°C min^{-1} (for nanocrystalline Prussian White), using N_2 atmosphere.

Figure 2.4. Thermogravimetric analyzer TGA NETZSCH STA 449 F3 Jupiter.

2.1.5. Electron Microscopy

An electron microscope uses a beam of accelerated electrons as a source of illumination. The high energy electrons are produced in an electron gun typically equipped with a cathodic filament. Under vacuum, the electron beam is then accelerated by an anode at a large voltage with respect to the cathode, and finally it is focused on the sample by the use of electrostatic and electromagnetic lenses. These fast-moving electron beams are adsorbed (transmission electron microscopy) or scattered (scanning electron microscopy) by the sample so as to form an image on an electron-sensitive photographic plate that can be displayed on a computer (see Figure 2.5a). The signals that derive from electron-sample interactions reveal information about the sample including external morphology (texture), chemical composition, crystalline structure and orientation of materials making up the sample.[9, 10]

As the wavelength of an electron can be much shorter than that of visible light photons, the interaction with matter is stronger and has higher resolution, what enables determining even the structure of smaller objects.

Along this thesis, both scanning electron microscopy (SEM) and transmission electron microscopy (TEM) have been used to morphologically and structurally characterize the pure Prussian Blue and analogues materials synthesized in this work, and thus are briefly described below.

---

[9] Physical Principles of Electron Microscopy. R. F. Egerton. Springer, 2005. Chapter 1 (pages 1-25).

[10] Microscopy techniques for Material Science. A. Clarke and C. Eberhardt. Woodhead Publishing, 2002. Chapter 6 (pages 361-408).

2.1.5.1. Scanning Electron Microscopy (SEM)

The SEM produces images by scanning across a rectangular area of the sample with a fine focal electron beam, whose resolution is determined by the spot size produced by the lenses. When the electron beam interacts with the specimen, its energy is dissipated as a variety of signals produced by electron-sample interactions. These signals include secondary electrons (that produce SEM images), backscattered electrons (BSE), diffracted backscattered electrons (EBSD, that are used to determine crystal structures and orientations of the samples), photons (characteristics X-rays, which are used for elemental analysis and continuum X-rays), visible light and heat. The most common signal is that provided by the secondary electrons, which are emitted from the surface due to excitation by the interaction of the primary electron beam with the sample.

Generally, the image resolution of a SEM is at least an order of magnitude poorer than that of a TEM. It can provide magnifications between 20 and 200000 and the accelerating voltage usually varies between 1-30 kV.[11]

Materials here studied were conductive enough and their SEM images were collected in a Quanta 200 FEG (FEI) scanning electron microscope (SEM) (see Figure 2.5.b). In some cases, Energy-dispersive X-ray spectroscopy (EDX) was used to determine their chemical composition. Samples for SEM were prepared by depositing some powder over a carbon tape substrate glued onto an aluminum pin-holder so that electrons can be conducted and thus dissipated.

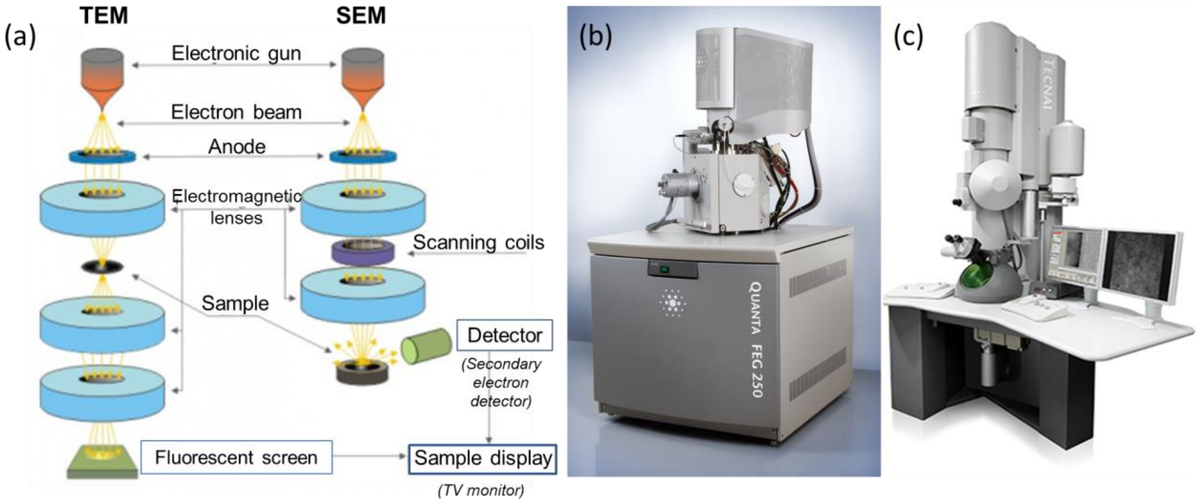

Figure 2.5. a) Illustrative diagram of the TEM and SEM operating principle, b) Quanta 200 FEG (FEI) scanning electron microscope and c) FEI Tecnai G2 transmission electron microscope.

---

[11] Scanning Electron Microscopy and Microanalysis. J. I. Goldstein, D. E. Newbury, P. Echlin, D. C. Joy, C. E. Lyman, E. Lifshin, L. Sawyer, J. R. Michael. Springer, 3rd edition, 2003. Chapter 2 (pages 21-60).

2.1.5.2. Transmission Electron Microscopy (TEM)

Unlike SEM, a transmission electron microscopy (TEM) uses a high voltage electron beam (typically of 200-300 kV) which is transmitted through the sample. Consequently, a low thickness of the specimen is recommended.

By TEM, not only images, but also diffraction information can be achieved. The spatial variation in the "image" may be viewed by projecting the magnified electron image onto a fluorescent screen (see Figure 2.5a). One advantage of electron diffraction over X-ray crystallography is that the specimen need not be a single crystal or even a polycrystalline powder.[12]

Although resolution of the TEM is limited primarily by spherical aberration, high-resolution transmission electron microscopy (HRTEM)[13] allows the production of images with resolution below 0.5 Å and magnifications above 500000 times.

A competitive technique to HRTEM, is the the scanning transmission electron microscopy (STEM), which is also capable of sub-Amstrong resolution. Bright field and dark field STEM are the two main modes of operation in STEM. Often TEM can be equipped with the scanning option and then it can function both as TEM and STEM.

At CIC EnergiGUNE, a FEI Tecnai G2 equipped with a 200kV field emission gun (FEG) high resolution TEM/STEM (see Figure 2.5c) was the instrument deployed for collecting TEM images and electron diffractions of the materials under study. At SGIKER services (Álava unit), a PHILIPS EM208S was the instrument utilized. The equipments were, respectively, operated by Dr. Vladimir Roddatis and Dr. Ana Martínez Amesti. Samples preparation consisted of depositing a drop of a suspension of the material in a holey carbon-copper grid, after dispersing it by sonication in the corresponding solvent (commonly alcohol).

Electron diffraction patterns were measured and compared to those obtained with the gold nanoparticles used for calibrating the equipment. By calculation of the camera constant obtained from the ring-type electron diffraction pattern of gold nanoparticles, the interplanar distances corresponding to the diffraction rings of the Prussian Blue materials could be deduced.

2.1.6. Atomic Absorption/Emission Spectroscopy (AAS and AES)

Atomic absorption spectroscopy (AAS) and atomic emission spectroscopy (AES) are two spectroanalytical procedures for the quantitative determination of a particular chemical element (analyte).

---

[12] Transmission Electron Microscopy: A textbook for Materials Science. David B. Williams. Springer 2009. Chapters 1 and 2 (pages 1-20 and pages 21-38).

[13] High Resolution Electron Microscopy (Monographics on the Physics and Chemistry of Materials). John C. H. Spence. Oxford Science Publications 2003.

In AAS, the analyte concentration is established based on the quantity of optical radiation absorbed by the free gas-phase atoms induced in the sample to be analyzed. Although the technique relies in the Beer-Lambert law, a working curve after calibrating the instrument with standards of known concentration is required to stablish the relation between the measured absorbance and the analyte concentration.[14]

Similarly, AES employs the intensity of light emitted for excited electrons at a definite wavelength to calculate the quantitative presence of an element in a particular sample. A characteristic set of wavelengths is emitted by each element or substance which depends on its electronic structure.[14]

To determine the Na/ Fe and the K/Fe ratio in the materials under study, AAS and AES were respectively conducted in a Perkin Elmer Analyst 200: Flame Atomic Absorption/Emission Spectrometer (Figure 2.6a), at the Central Analysis Service of SGIKer (Álava unit, UPV/EHU).

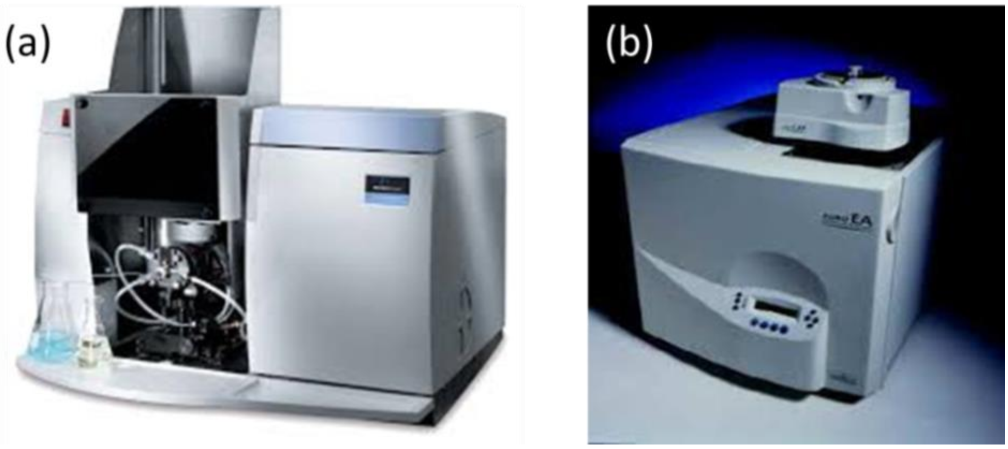

Figure 2.6. a) Perkin Elmer Analyst 200 Spectrometer and b) Euro Elemental Analyzer (CHNS).

2.1.7. Elemental Analysis (C, H, N)

Elemental analysis is an important technique to characterize and/or prove the elemental composition (C, H, N) of a sample. The major elements carbon, hydrogen, and nitrogen, are commonly determined using commercially available CHN and CHNS analyzers, in which the substance undergoes oxidative decomposition and a subsequent reduction to form the final products: carbon dioxide (CO_2), water (H_2O), elemental nitrogen (N_2), and sulfur dioxide (SO_2), which are quantitatively measured.[15]

Elemental analyses have been performed in a Euro Elemental Analyzer (CHNS) as that shown in Figure 2.6b, to check the H, C and N percentage present in the Prussian Blue materials. Analyses were conducted at the SGIKer Central Analysis Service (Bizkaia unit, UPV/EHU).

---

[14] Principles of Instrumental Analysis. Douglas A. Skoog. Cengage Learning, 6th edition, 2007. Chapters 9 (AES) and 10 (EES).

[15] V. P. Fadeeva, V. D. Tikhova, O. N. Nikulicheva. *Journal of Analytical Chemistry*, 2008, **63** (11), 1094–1106. “Elemental Analysis of Organic Compounds with the Use of Automated CHNS Analyzer”.

2.1.8. X-ray photoelectron spectroscopy (XPS)

X-ray photoelectron spectroscopy (XPS) is a standard tool for analyzing the surface chemistry of a material, based on the photoelectric effect. In XPS, a soft X-ray photon is absorbed by an atom in a molecule, leading to ionization of the molecule and the ejection of a core (inner shell) electron, from the top 1-10 nm of the material being analyzed (see Figure 2.7a). It requires high vacuum ($P \sim 10^{-8}$ mbar) or ultra-high vacuum (UHV, $P < 10^{-9}$ mbar) conditions.

Measurement of the number of electrons ejected (*y* axis) and their corresponding kinetic energy distribution (*x* axis) generates a photoelectron spectrum, that enables determining the elemental composition (called *survey spectrum*), the electronic state of such elements and the binding energy of the electrons of the surface region of the sample.[16]

For every specific element, there will be a characteristic binding energy (the energy required to remove the electron from the surface) associated with a core atomic orbital. Each element will give rise to a characteristic set of peaks in the photoelectron spectrum at kinetic energies ($E_{kinetic}$) determined by the X-ray photon energy ($E_{photon} = h\nu$), the respective binding energies ($E_{binding}$) of the electron and the work function (ϕ, which is an instrumental correction factor dependent on both the spectrometer and the material):

$$E_{kinetic} = E_{photon} - (E_{binding} + \phi) \tag{Eq. 2.5}$$

Since E_{photon} is always known, $E_{kinetic}$ can be easily transformed into $E_{binding}$. XPS spectra are usually plotted against $E_{binding}$ (*x* axis). These characteristic spectral peaks correspond to the electron configuration of the electrons within the atoms. Furthermore, the intensity is related to the concentration of the element within the sampled region, allowing quantification.[17]

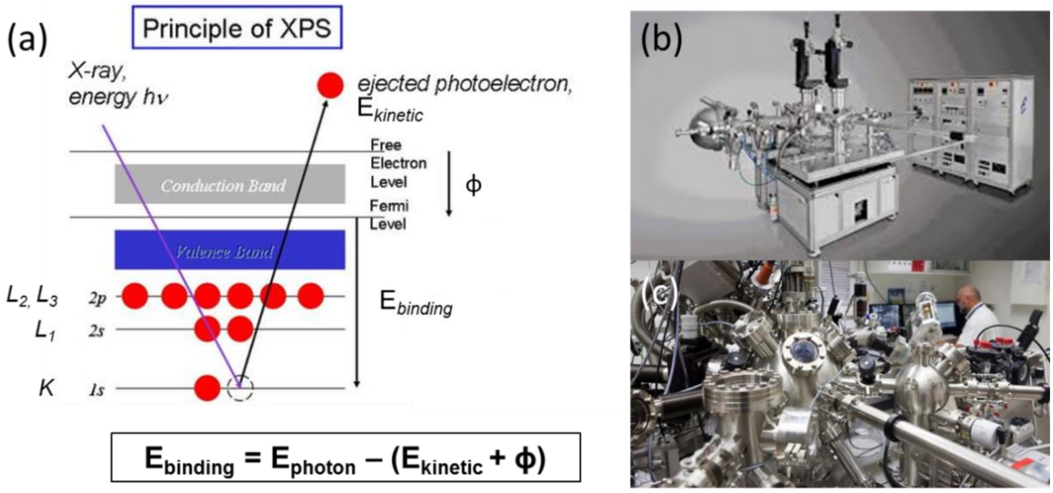

Figure 2.7. a) Illustrative diagram of the basic operation of XPS, b) electron energy analyzer PHOIBOS 150 (SPECS) and c) zoom image of the PHOIBOS 150 (SPECS).

---

[16] J. F. Watts, J. Wolstenholme. An Introduction to Surface Analysis by XPS and AES. Wiley & Sons, 2003. Chapter 1 and 3 (pages 1-17, 64-67, 75).

[17] X-ray Photoelectron Spectroscopy: An Introduction to Principles and Practices. P. van der Heide. Wiley, 2011. Chapter 1 (pages 1-12).

XPS measurements were performed at CIC EnergiGUNE by the platform manager Dr. Oleksander Bondarchuk. XPS spectra were acquired in transmission mode with pass energy of 20 eV in an UHV system equipped with a hemispherical electron energy analyzer PHOIBOS 150 (SPECS) and a twin Al/Mg anode - X-ray source XR50 (SPECS) operated at 12 keV and power 100 W (see Figure 2.7b and c). The size of the acceptance area of the analyzer was ca. 2 mm in diameter and its energy scale was calibrated against Cu $2p_{3/2}$, Ag $3d_{5/2}$ and Au$4f_{7/2}$ lines of standard Au-Ag-Cu sample. The powder samples were fixed onto the Mo sample plate using double-sided carbon tape. For air-sensitive samples, to avoid contact with ambient, the samples were transferred from the glove box where they were stored to the XPS chamber in an Ar filled air-tight container.

2.1.9. Mössbauer spectroscopy

Mössbauer spectroscopy is a spectroscopic technique based on the Mössbauer effect, which consists of the recoil-free, resonant absorption and emission of gamma rays in solids. The Mössbauer effect is only detected in a limited number of isotopes, being the most commonly studied the ^{57}Fe.

In ^{57}Fe Mössbauer spectroscopy, a ^{57}Co/Rh-source is used. The ^{57}Co source decays to an excited state of ^{57}Fe by electron capture and, then, it subsequently decays to a ground state emitting the desired gamma-ray (of 14.4 keV) (as shown in Figure 2.8), that can be absorbed by a ^{57}Fe nucleus in the sample. During Mössbauer absorption spectroscopy, the source is accelerated through a range of velocities using a linear motor to produce a Doppler effect and a detector scan the gamma ray energy transmitted through the sample within a given range. In the resulting spectra, gamma ray intensity is plotted as a function of the source velocity. At velocities corresponding to the resonant energy levels of the sample, a fraction of the gamma rays are absorbed, resulting in a drop in the measured intensity and a corresponding dip in the spectrum. The number, positions and intensities of the dips (also called peaks) provide information about the chemical environment of the absorbing nuclei and can be used to characterize the sample.

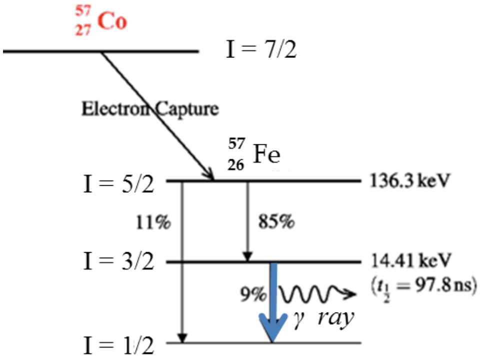

Figure 2.8. Scheme of the nuclear decay of ^{57}Co into Mössbauer active element ^{57}Fe.

If the emitting and absorbing nuclei were in identical chemical environments, the nuclear transition energies would be exactly equal and a resonant absorption would be observed. The difference in chemical environments, however, causes the nuclear energy levels to shift in different ways. The energy levels in the absorbing nuclei can be modified in three main ways, associated to what is known as Mössbauer parameters (see Figure 2.9):

Isomer shift or chemical shift (δ) is a relative measure describing a shift in the resonance energy of a nucleus due to the transition of electrons within its *s* orbital, that is, it arises from the difference in the *s* electron density between the source and the absorber. Therefore, it is affected by the oxidation state and the chemical environment of the atom. The isomer shift cannot be directly measured, so it is quoted relative to a known absorber. In the case of ^{57}Fe Mössbauer spectra, it is often quoted relative to alpha-iron at room temperature, as will be referenced in this work.

Quadrupole splitting (ΔQ) reflects the interaction between the nuclear energy levels and surrounding electric field gradient caused by nearby electrons. Nuclei in states with non-spherical charge distributions, i.e. all those with angular quantum number (I>1/2) greater than 1/2, produce an asymmetrical electric field which splits the nuclear energy levels. This produces a nuclear quadrupole moment.

Magnetic splitting (hyperfine or Zeeman effect) is a result of the interaction between the nucleus and any surrounding magnetic field. A nucleus with spin I splits into 2I + 1 sub-energy levels in the presence of magnetic field. The restriction rule of magnetic dipoles means that transitions between the excited state and ground state can only occur where m_I changes by 0 or 1.

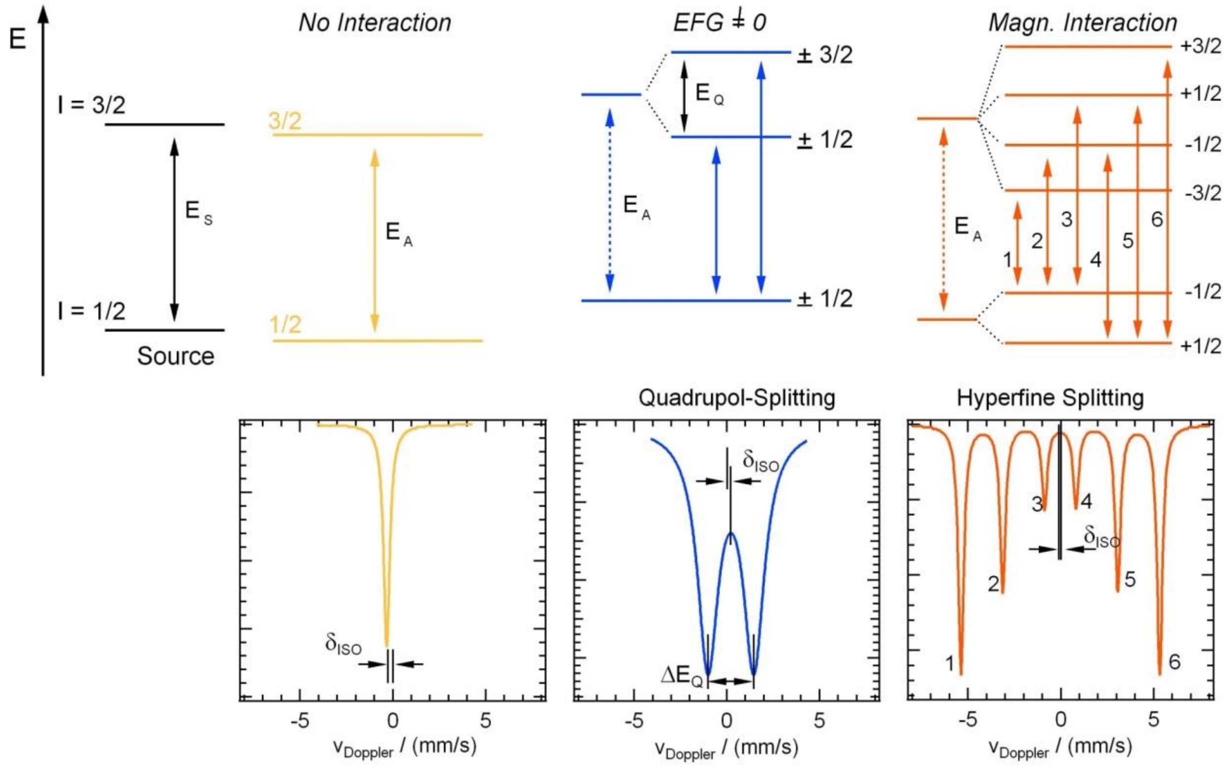

Figure 2.9. Scheme of the possible Mössbauer spectra as a result of (i) no interaction, (ii) electric interaction (EFG ≠ 0) and (iii) magnetic interaction.

The combination of isomer shift and quadrupole splitting parameters (along with the hyperfine field, in the case of magnetically ordered phases) is usually sufficient to identify the valence state and site occupancy of Fe in a given site. Graphically, quadrupole splitting is the separation between the two component peaks of a doublet, and isomer shift is the difference between the midpoint of the doublet and zero on the velocity scale. [18, 19]

Measurements of pristine materials were collected in a home-made Mössbauer spectrometer at Bizkaia Campus (UPV/EHU) by Dr. Estíbaliz Legarra and Dr. Garitaonandia, filling a 1 cm diameter plastic sample holder with powder of the materials to be studied.

The development of an electrochemical cell for collecting *in-situ* Mössbauer measurements will be addressed in a posterior section (see 2.2.4.1.1), after detailing the electrochemical measurements and setups.

2.1.10. X-ray absorption spectroscopy (XAS)

X-ray absorption spectroscopy (XAS) requires an intense and tunable X-ray source, i.e. a broad band of X-ray energies, which is achieved only by “synchrotron radiation”.

If the X-ray photon energy equals the binding energy of a core electron, a drastic increase in the absorption occurs (and in the absorption coefficient, μ(E)), producing an “absorption edge” at specific X-ray photon energies, which is characteristic of the absorbing element. This process is accompanied by the excitation of such core electron to the excited electronic states (LUMO) or to the continuum, what creates a photoelectron and a core-hole (as shown in Figure 2.10a). When the photoelectron originates, for example, from a 1s core level, the *absorption edge* is designated as K-edge. Above the absorption edge, μ(E) continues decreasing with increasing photon energy. After a short time, the core-hole is filled by an electron from a higher energy state and the corresponding energy difference is released mainly via fluorescence X-ray or Auger electron emission. In addition, when the photoelectron leaves the absorbing atom, its wave is backscattered by the neighbouring atoms. The maxima and minima after the edge correspond to the constructive and destructive interference between the outgoing photoelectron wave and backscattered wave.

XAS measures the energy-dependent fine structure of μ(E) near the absorption edge of a particular element. The absorption coefficient can be detected either directly by measuring the intensities of incoming and transmitted beam (transmission mode) or indirectly by measuring the intensity of the incoming beam and of the decay products such as fluorescent X-rays or Auger electrons (fluorescence or electron yield mode).

---

[18] Mössbauer spectroscopy. D. P. E. Dickson, F. J. Berry. Cambridge University Press, 1986. Chapter 1 (pages 1-14).

[19] Mössbauer Spectroscopy. N. N. Greenwood. Springer, 1971. Chapter 1 and 3 (pages 1-16, 46-79).

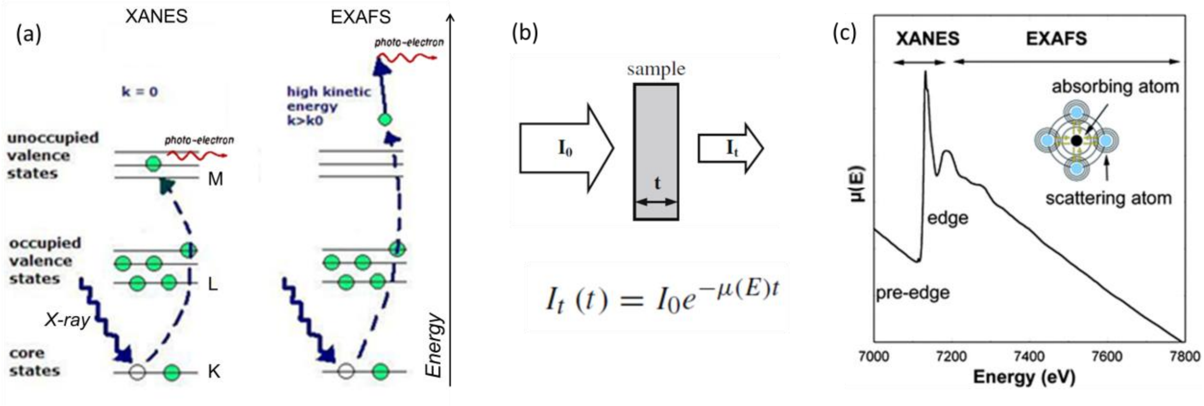

Figure 2.10. a) Visual description of XAS (k = kinetic energy), b) schematic of incident and transmitted X-ray beam and Beer-Lambert equation for transmission mode XAS, c) X-ray absorption spectrum (absorption coefficient vs. photon energy) around an absorption edge, differentiating the different regions (XANES and EXAFS).

In transmission mode, the energy-dependent X-ray absorption coefficient ($\mu(E)$) can be obtained according to Beer´s Law (see (Eq. 2.6):

$$I_t\,(t) = I_0 \cdot e^{-\mu(E)\cdot t} \qquad \textbf{(Eq. 2.6)}$$

where, I_0 and I_t are respectively the incoming and the transmitted beam measured by ion chambers and t is the thickness of the sample (see Figure 2.10b).

A XAS spectrum can be divided in two main regions (as illustrated in Figure 2.10c): X-ray absorption near-edge structure (XANES), found in the vicinity of the *edge*, and the extended X-ray absorption fine structure (EXAFS), associated to the oscillations above the edge which can extend up to 1000 eV. XANES region is especially sensitive to the formal oxidation state and geometry while EXAFS regions can reveal the radial distribution of electron density around the absorbing atom, thereby it is used for quantitative determination of bond length, type of ligands and coordination number. [20, 21]

Ex-situ Fe K-edge XAS synchrotron data were collected in the beamline 10-BM, in transmission mode, at the Advanced Photon Source (APS) belonging to Argonne National Laboratory by Dr. Timothy Fister and Dr. Soojeong Kim. As measurements were conducted in transmission mode, it was necessary to ensure the preparation and usage of homogeneous electrodes with less than 1 mg difference in their active material mass loading.

Measurements were carried out in electrodes previously cycled and stopped at different stages of the electrochemical curve. The electrochemical cells were disassembled inside a glove box, with less than 0.5 ppm of O_2 and H_2O, and their electrodes were thoroughly rinsed several times with DMC to remove any residual electrolyte. Then, they were dried at 80 ˚C overnight.Afterwards, the electrodes were covered with Mylar® to create an air and water-protective barrier and were fixed to it with Kapton® tape. Finally, each electrode was placed inside a coffee bag that was sealed with the aim of impeding the reaction with O_2 (see Figure 2.11). Electrodes were kept for ca. 24 h inside the glove box, before collecting the XAS

---

[20] X-ray Absorption Spectroscopy of Semiconductors. C. S. Schnohr, M. C. Ridgway. Springer, 2015. Chapter 1 (pages 1-27).

[21] X-ray Absorption Spectroscopy. J. E. Penner-Hahn. John Wiley & Sons, 2005.

spectra. Each scan took about 25 minutes and the energy range measured was from -300 eV below the edge to 900 eV above the edge (~ 6800 - 8000 eV).

Figure 2.11. Detailed scheme for electrode (13 mm of diameter) preparation for the *ex-situ* XAS measurements.

2.2. Electrochemical techniques

2.2.1. Galvanostatic cyclic charge-discharge measurements

There are two types of cyclic charge-discharges: potentiostatic and galvanostatic. Along this thesis, only the galvanostatic method was employed to quantitatively asses the electrochemical performance of the materials. This technique involves controlling the current (i = constant) that flows through the working electrode and recording its voltage evolution within a certain potential window. As the current applied can be the flow of either positive or negative charges, the electrode is charged and discharged in a cyclic manner.

In galvanostatic cyclic charge-discharge measurements, voltage is plotted against time (as shown Figure 2.12a). However, in the field of batteries, the usual presentation of the results implies the conversion of time in specific capacity (or in gravimetric specific capacity, $mAh{\cdot}g^{-1}$, as in this particular case), as Figure 2.12b illustrates. Being the gravimetric charge/discharge specific capacity the amount of electricity (mA·h) that 1g of material can deliver in a single charge/discharge, at a given C-rate. C-rate or current density (in $A{\cdot}g^{-1}$ or $mA{\cdot}g^{-1}$) is a measure of the rate at which a battery is charged/ discharged relative to its maximum capacity. For instance, a 1C rate means that the discharge current will discharge the entire battery in 1 hour. Other type of displaying data is by plotting the specific capacity along the cycles performed (see Figure 2.12c).

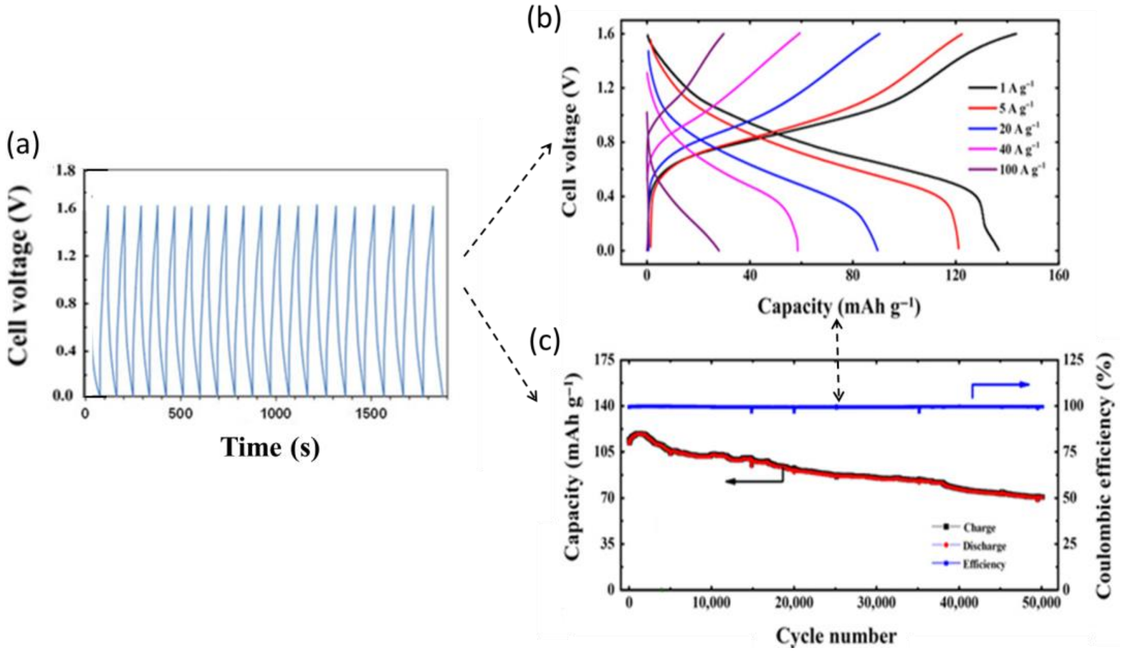

Figure 2.12. a) Voltage versus time for the first 19 galvanostatic cycles of an anode, b) Voltage *vs*. specific capacity at different C-rates and c) cycleability at a certain C-rate (specific capacity against cycle number).

Galvanostatic cyclic charge-discharge experiments at a single C-rate (abbreviated as galvanostatic measurements hereinafter) and C-rate capability tests have been carried out and are discussed in this manuscript, in chapters 4 and 5.

For all the tests conducted, the current applied was calculated as a function of the theoretical capacity (C_{th}) of the active material for the insertion of 1 electron per formula unit (as (Eq. 2.7 shows). The latter, C_{th}, is obtained as follows:

$$C_{th} = F = 96485\ \mathrm{C \cdot mol^{-1}} = 96485\ \mathrm{A \cdot s \cdot mol^{-1}} = \frac{96485}{3.6 \cdot \frac{M}{n}}\ \mathrm{mAh \cdot g^{-1}} \qquad \textbf{(Eq. 2.7)}$$

where F = Faraday constant (96485 $\mathrm{C \cdot mol^{-1}}$ of electrons), M = molecular weight and n = number of electrons involved in the reaction.

2.2.2. Cyclic voltammetry

Cyclic voltammetry (CV) is a type of potentiondyanamic electrochemical measurement. CV has become an important and widely used technique, because it offers insights in both the kinetic and thermodynamic details of many chemical systems. It is often used to study a variety of redox processes, to determine the reversibility of a reaction, the stability of reaction products, the presence of intermediates in redox reactions, the electron transfer kinetics and even the diffusion coefficient of an analyte.

In a CV experiment, the working electrode potential is ramped linearly at a fixed scan rate (mV·s-1) between two values (V_1 - V_2) in function of time, as illustrates Figure 2.13a. Once the voltage reaches V_2, the scan is reversed and the voltage is swept back to V_1. These cycles of ramps in potential may be repeated as many times as needed, leading to cyclical phases.

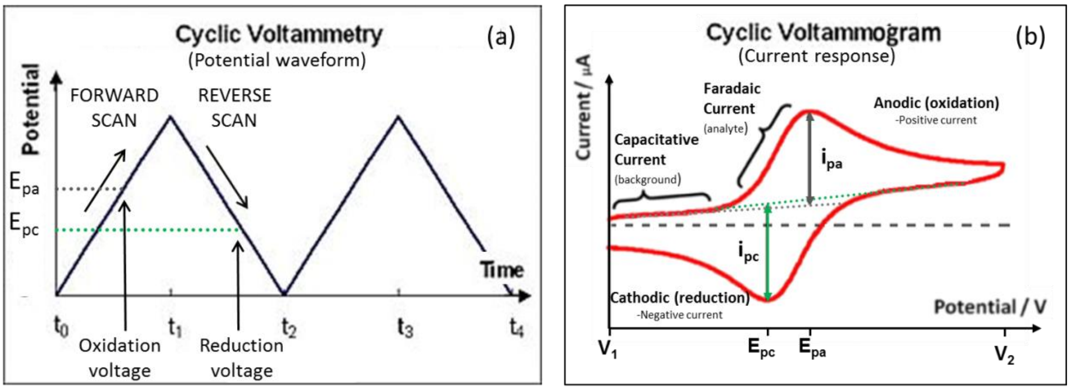

Figure 2.13. a) Cyclic voltammetry waveform and b) cyclic voltamogramm trace, where i_{pc}, i_{pa}, Epc and Epa represent, respectively, the cathodic and anodic current (i) and potential (E) values for a reversible reaction.

Typically, the potential is applied between the working electrode and the reference electrode, while the current is measured between the working electrode and the counter electrode. Therefore, the current at the working electrode (i) is plotted versus the applied potential (E) to give the cyclic voltammogram (see

Figure **2.13**b). The obtained maxima offer a rapid location of the potentials at which the different reactions occur. [22, 23]

The more reversible the redox couple is, the more similar the oxidation peak will be in shape to the reduction peak. However, the waveform of even reversible couples is complex owing to the combined effects of polarization and electron transfer.

2.2.3. Electrochemical impedance spectroscopy

Electrochemical Impedance Spectroscopy (EIS) is a non-destructive electrochemical technique based on the perturbation of an equilibrium state. EIS studies the frequency response (ω = radial frequency) of the system (an electrochemical cell) to the application of a periodic small AC amplitude signal to the DC signal. The measurements are conducted over a wide range of AC frequencies.

Like resistance, impedance ($Z(\omega)$) is a measure of the ability of a circuit to resist the flow of electrical current. The expression for Z is composed of a real and an imaginary part, as shown (Eq. 2.8:

$$Z = \frac{E}{I} = Z_0 \exp(i\phi) = Z_0(\cos\phi + i\sin\phi) \qquad \textbf{(Eq. 2.8)}$$

where E = potential, I = current, $Z_0 = E_0 / I_0$, i = complex number and ϕ = phase shift. EIS data for electrochemical cells such as fuel cells are most often represented in Nyquist and Bode plots, as Figure 2.14 shows.

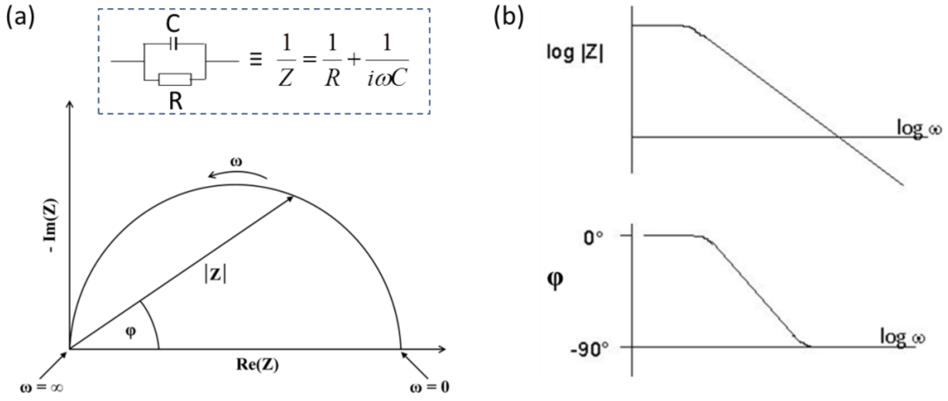

Figure 2.14. a) Nyquist plot with impedance vector |Z| and b) Bode plot. Both the Nyquist plot and the Bode plot results from the electrical circuit presented inset in Figure 2.14a, where R = resistor and C = capacitor.

---

[22] Encyclopedia of Electrochemistry, volume 3, Instrumentation and Electroanalytical Chemistry. P. Unwin. Wiley-VCH, 2003. Chapter 2 (pages 81-104).

[23] G. A. Mabbott. *J. Chem. Educ.* 1983, **60** (9), 697. “An introduction to Cyclic Voltammetry”.

A Nyquist plot depicts the imaginary impedance on the Y-axis versus the real impedance of the cell on the X-axis (see Figure 2.14a). The impedance can be represented as a vector (arrow) of length |Z|. The angle between this vector and the X-axis, commonly called the “phase angle”, is ϕ. Nyquist plots have the advantage that activation-controlled processes with distinct time-constants show up as unique impedance arcs and the shape of the curve provides insight into possible mechanism or governing phenomena. The semicircle is characteristic of a single "time constant". However, this format of representing impedance data has the shortcoming that the frequency-dependence (arrow above semicircle) is implicit and typically not detailed.

Bode plots refer to representation of both the absolute impedance ($|Z|=Z_0$) and phase angle as a function of frequency (Figure 2.14b). Because impedance and frequency often span orders of magnitude, they are frequently plotted on a logarithmic scale. Bode plots explicitly show the frequency-dependence of the impedance of the device under test.

Because both data formats have their advantages, it is usually best to present both Bode and Nyquist plots together.

Analysis of the system response contains information about the physicochemical processes taking place within the cell. The contribution of these processes can be distinguished. Each process has different characteristic time-constants and therefore it is exhibited at different AC frequencies, what can be used to identify and quantify the impedance associated with each of them. Total electrode impedance consists of the contributions of the electrolyte, the electrode-solution interface and electrochemical reactions taking place on the electrode. EIS data are commonly analyzed by fitting to an equivalent electrical circuit model (as shown in Figure 2.14a inset). Most of the circuit elements in the model are common electrical elements such as resistors, capacitors, and inductors. The type of electrical components in the model and their interconnections control the shape of the model's impedance spectrum, while the parameters of the model control the size of each feature in the spectrum. Each component of the model is postulated to come from a physical process in the electrochemical cell, therefore, the model should match with the impedance measured data.[24, 25, 26]

2.2.4. Electrochemical measurements

2.2.4.1. Instrumentation and cell assembly

The electrochemical characterization of the materials was performed using two different devices (see Figure 2.15):

- ✓ A Maccor Battery tester Series 4000®
- ✓ A Biologic VMP3 Multi-Channel Potentiostat/Galvanostat®

---

[24] Encyclopedia of Electrochemistry, volume 3, Instrumentation and Electroanalytical Chemistry. P. Unwin. Wiley-VCH, 2003. Chapter 2 (pages 196-223).

[25] Electrochemical methods. Fundamental and applications. A. J. Bard, L. R. Faulkner. John Wiley & Sons, 2nd edition, 2001. Chapter 10 (368-416).

[26] Electroanalytical Methods. F. Scholz. Wiley, 2nd edition, 2010. Chapter 2 (pages 159-177).

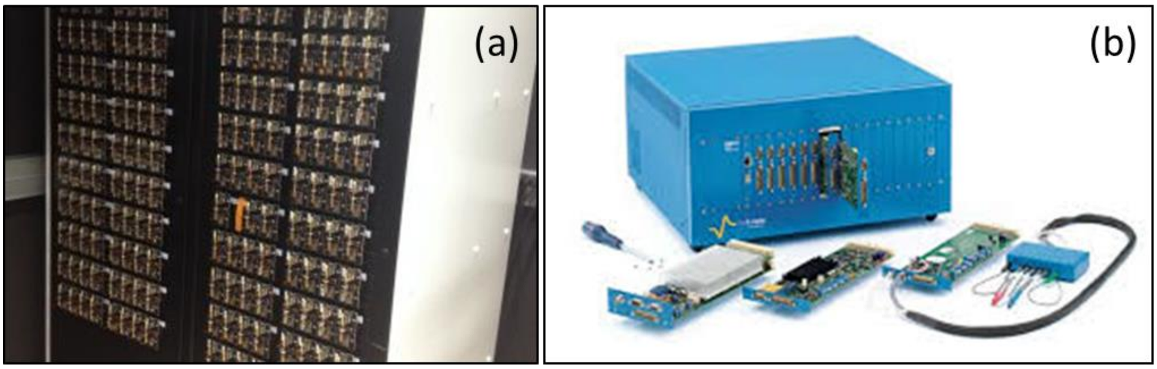

Figure 2.15. a) Maccor Battery Tester Series 4000. It is fully equipped with 192 channels; 166 for coin cell and 26 cables. b) Biologic VMP3 Multichannel Potentiostat. It contatins normal channels and some channels for performing EIS.

The Maccor Battery tester was typically used for recording galvanostatic data, using coin cells CR2032 (for further information regarding the coin cell assembly, see Figure 2.16).

The VMP3 potentiostat/galvanostat was dedicated to collect cyclic voltammograms and galvanostatic data using two-electrode and three-electrode Swagelok configuration cells (as Figure 2.17 and Figure 2.18a illustrate). EIS measurements were also conducted in the VMP3 potentionstat, using three-electrode Swagelok configuration cells (see Figure 2.18b).

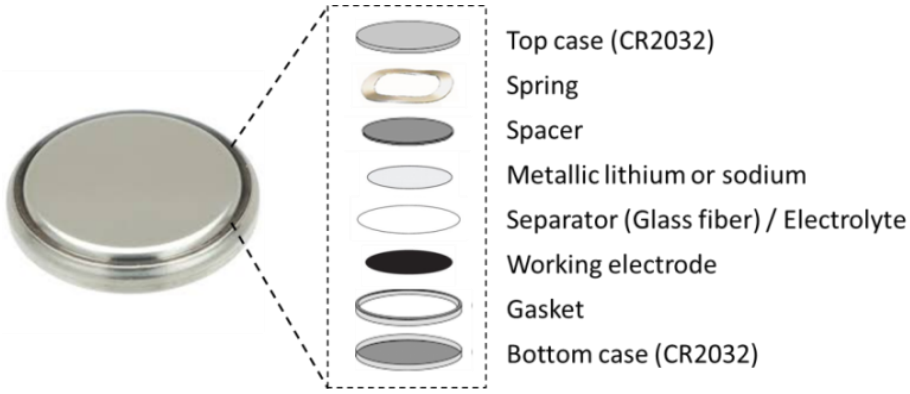

Figure 2.16. Coin cell components and order of montage (from the bottom to the top). Once assembled, the coin cell is crimped in a crimper machine. (Note that the working electrode is usually casted over a current collector).

Always and regardless the type (coin cell, Swagelok), the cell assembly process is carried out inside an Argon-filled dry glove box.

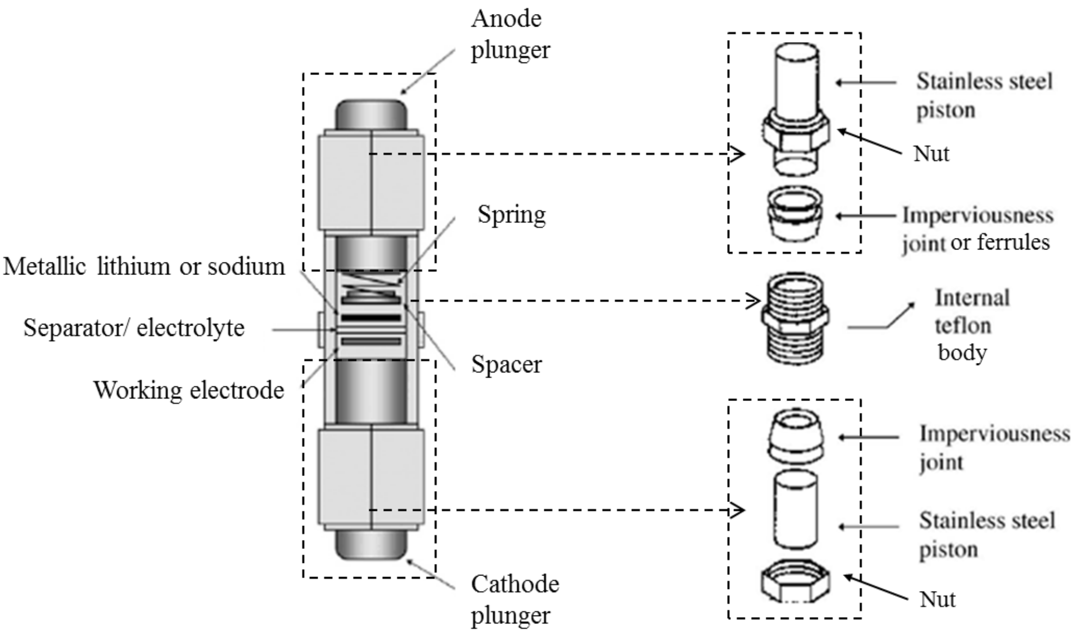

Figure 2.17. Two-electrode configuration Swagelok cell components and order of assemble.

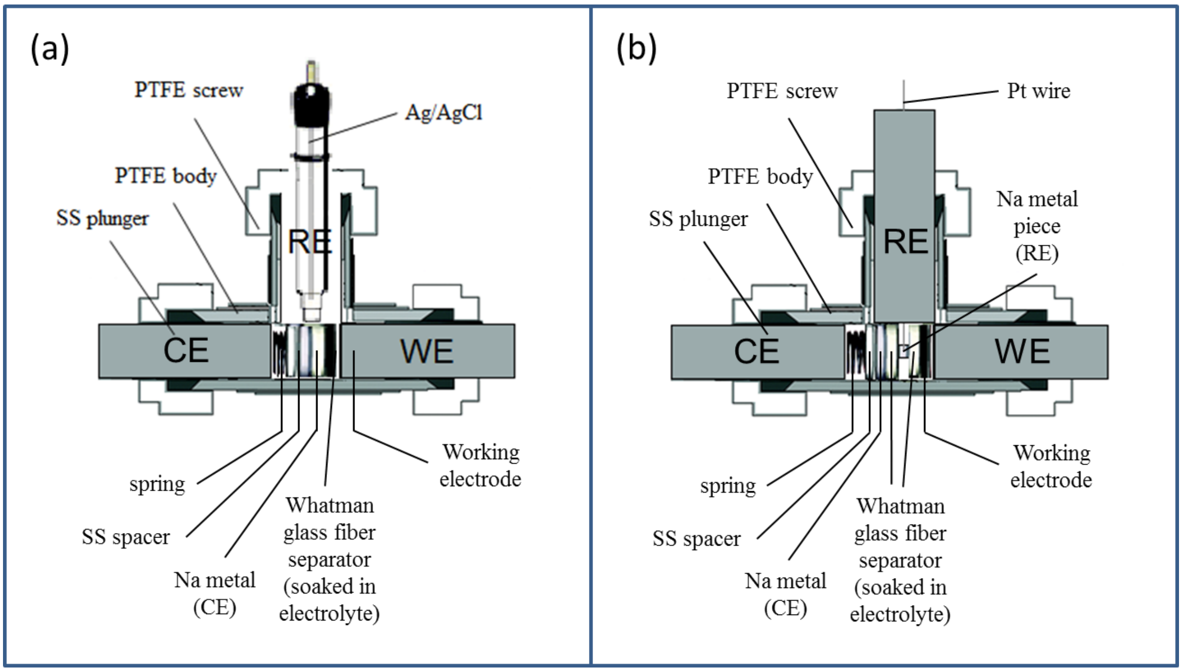

Figure 2.18. Three-electrode configuration Swagelok cell components and order of assemble: a) for aqueous measurements (CV, galvanostatic tests) and b) for EIS measurements.

As previously mentioned, the development of a novel *in-situ* Mössbauer electrochemical cell was carried out and is detailed in the following section.

2.2.4.2. Measurements in organic electrolyte

Galvanostatic measurements, using coin cells CR2032, were recorded in a Maccor Battey tester.

In measurements conducted in SIB (*vs*. Na^+/Na), metallic sodium was used as counter and reference electrode. For electrochemical characterization in LIB (*vs*. Li^+/Li), metallic lithium was used as counter and reference electrode.

A glass fiber Whatmann® GF-D was the separator of choice in all the cases. The corresponding electrolyte deployed in each case was added to the glass fiber until its whole surface was fully impregnated.

2.2.4.2.1. Preparation of working electrodes

Powdered electrodes

In measurements conducted in powder form, electrodes were easily prepared by mixing 80 wt (%) of the corresponding active material with 20 wt (%) of conductive carbon through grinding. The conductive carbon used in all the cases was Super C-65®, except for measurements with Prussian White at high voltages, in which ketjen black was used. The powder mixture was vacuum dried overnight at 80-120˚C (depending on the sample) for, later on, directly deposit it in the bottom casing of the coin cell. Powder electrodes are binder-free and current collector free and no calendering or extra processing were implemented.

Laminated electrodes

Typically, laminated electrodes consist of mixing the active material with amorphous carbon and the binder dissolved in their corresponding solvent in an 80:10:10 ratio. The binder commonly deployed is PVDF (polyvinylidene fluoride) solubilized in NMP (*N*-methyl pyrrolidone). The conductive carbon utilized was Super C-65®, except for measurements with Prussian White at high voltages, where ketjen black was used.*

The slurry obtained was stirred for 1 h and then homogeneously coated on the appropriate current collector, aluminum or copper, depending on whether it would be used for SIB or LIB. At low potential, aluminum is alloyed with lithium.[27] Consequently, to avoid this reaction, copper is the current collector used when cycling *vs.* Li^+/Li. Conversely, this alloy problem does not exist *vs.* Na^+/Na and Al is the metal of choice on which to coat. Finally, the coating was dried in vacuum overnight at 80-120 °C. Disc electrodes of 13 mm diameter were punched, pressed at 5 tons for few seconds and dried under vacuum again at 80-120°C overnight, before assembly the electrochemical cells.

**In those cases where the formulation of the laminated electrodes was not coincident with the previous proportion of mixture or any of material varies, such as to study the effect of the type or % wt. of binder, the composition will be clearly*

---

[27] Exxon Research´ & Engineering Co., Linden, NJ, USA. *Rechargeable Lithium-Aluminum anode*. BHASKARA M. L. Rao. United States Patent 4.002.492, January 11 1977.

specified. Otherwise, when referring to laminated electrodes, the formulation of the electrode will be assumed as 80 % active material: 10% C-65: 10% PVDF.

At the beginning of chapters 3 and 4, a table summarizing the composition of the electrodes prepared for the electrochemical studies, will be presented.

Self-standing electrodes for in-situ Mössbauer measurements

Self-standing electrodes for Mössbauer measurements were prepared dispersing 70% of the active material with 20% of conductive carbon (Super C-65®) and 10% of teflon (PTFE, from a 60 % wt. aqueous solution, Sigma-Aldrich) in ethanol. The preparation of self-standing electrodes has the purpose of avoiding the current collector that would decrease the intensity of the γ-rays transmitted by the sample. Additionally, electrodes with a mass loading far superior to those used in routine measurements were deployed to get a better Mössbauer signal. Mass loadings on the order of 40 mg of active material per electrode were prepared.

Cell assembly with these electrodes was already referred in section 522.2.4.1.1 (see prototype III, Figure 2.21).

2.2.4.3. Measurements in aqueous electrolyte

Cyclic voltammograms and galvanostatic measurements were recorded in a Bio-Logic VMP3 Multi-Channel Potential/Galvanostat.

Measurements were done in three-electrode Swagelok cells (see Figure 2.18a). For galvanostatic tests up to 4.1 V *vs*. Na^+/Na, titanium plungers and current collectors were used to avoid the corrosion of stainless steel (ss) that the O_2 evolution produces from such potential value onwards. Ag/AgCl (in 3 M NaCl) was deployed as reference electrode, although the potential values were recalculated to express them *vs*. Na^+/Na. Activated carbon, hereinafter AC, was used as counter electrode and was previously tested as symmetric capacitor also using 3-electrodes Swagelok-type cells (Figure 2.23a). To ensure that the working electrode is the limiting electrode and that the voltage variation owe to the supercapacitative mechanism of AC remains within the voltage window of the aqueous electrolyte (Figure 2.23b), a mass balance anode (AC): cathode (PB) ≥ 12: 1 was utilized. Deoxygenated 1 M Na_2SO_4, with pH = 6, was chosen as aqueous electrolyte. The deoxygenation was made under N_2 flow overnight. With the purpose of preventing the O_2 diffusion into the cell and thus the oxidation of the electrode material during the discharge process,[28] all aqueous cells were assembled inside a N_2 containing glove bag (acquired from Sigma Aldrich®).

---

[28] J.-Y. Luo, W.-J. Cui, P. He, Y.-Y. Xia. *Nat. Chem.* 2010, **2**, 760-765. “Raising the cycling stability of aqueous lithium-ion batteries by eliminating oxygen in the electrolyte.”

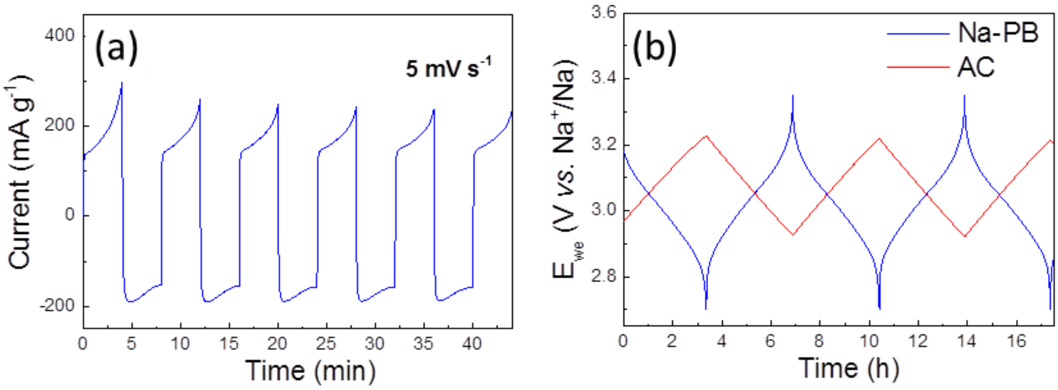

Figure 2.23. a) Five first cycles of a cyclic voltammetry at 5 mV·s^{-1} in a voltage range of 1.2 V for a symmetrical supercapacitor using activated carbon (AC) Norit DLC super30 as electrodes. The resultant capacitance was 70 F·g^{-1}. b) Cathode and anode galvanostatic curves at C/5 of a Na-PB (sodium Prussian Blue)/Norit DLC super30 (AC) cell with a mass ratio of 1: 12.

In addition, and for comparative purposes, two-electrode Swagelok organic cells were built (Figure 2.17). Working electrodes were prepared as mentioned in the following paragraph and metallic Na was used as reference and counter electrode. 1 M $NaPF_6$ in EC: PC: FEC in a ratio 49:49:2 was the electrolyte deployed. All organic half-cells were assembled in an argon-filled dry glove box (MBRAUN®).

Glass fiber (Whatman®, Grade D), impregnated with the aqueous or organic electrolyte, was used as separator for all measured cells.

Preparation of electrodes

Working electrodes were composed of 85 wt% active material, 10 wt% of conductive additive carbon (Super® C65, TIMCAL) and 5 wt% of binder (PvdF, Solef®). The mixture was solubilized in NMP (99.5% anhydrous, Sigma Aldrich) for 1h. An aliquot of 200 µL of the resultant slurry was deposited on a stainless steel (ss) current collector disk. Afterwards, electrodes were dried overnight at 120 °C under vacuum, pressed at 5 t·cm^{-2} for few seconds and dried again at 120 °C under vacuum until its utilization for assemble the cell.

Self-standing AC (Norit DLC super30), was used as counter electrode. AC electrodes were prepared dispersing 95 wt% of AC with 5% PTFE (60 wt% in H_2O) in ethanol.

Chapter 3

Synthesis and structural, morphological and physico-chemical characterization of the Prussian Blue phases

3 .-) Synthesis and structural, morphological and physico-chemical characterization of the Prussian Blue phases

This chapter describes both the synthesis and the structural, morphological and physico-chemical characterization of the different Prussian Blue type materials that are under study along this doctoral thesis. Mainly, purely iron-based Prussian Blue ($A_{1-x}Fe[Fe(CN)_6]\cdot yH_2O$ (A = Na/ K, $0 \leq x \lesssim 1$)) and their reduced phases Prussian White ($A_{2-x}Fe[Fe(CN)_6]$ ($x \sim 0.5$)) constitute the set of compounds in which the research focuses, with the exception of titanium PBA ($A_{1-x}Ti[Fe(CN)_6]\cdot zH_2O$ or $Ti[Fe(CN)_6]\cdot H_2O$) that is also subject of investigation, mostly concerning its syntheses.

The structure of the chapter is divided in 3 main sections as listed in Table 3.1. The first section is dedicated to the titanium Prussian Blue derivative $A_{1-x}Ti[Fe(CN)_6]\cdot zH_2O$ or $Ti[Fe(CN)_6]\cdot zH_2O$ and results in an extensive study as a consequence of the numerous synthetic routes attempted. In the experiments where a couple of fractions are obtained in a route of synthesis (x), the first fraction (labelled as x_1f) always refers to the precipitate forming which is obtained by filtration, while the second fraction (x_2f) corresponds to the resultant solid isolated after evaporating the solvent of the filtrate. Powder X-ray diffraction was essentially the main characterization technique used to verify the achievement of the desired materials. The second section details the synthesis of the sodium and potassium Prussian Blue (ideally $AFe[Fe(CN)_6]\cdot yH_2O$ (A = Na, K)) by co-precipitation and its wide structural characterization through several techniques (PXRD, IR, TGA, AAS, elemental analysis (H, C, N), SEM, etc.). Finally, the last section addresses the synthesis of the analogous reduced phases of Prussian Blue, i.e. both the sodiated and the potassiated Prussian White (ideally $A_2Fe[Fe(CN)_6]\cdot yH_2O$ (A = Na, K)), and its thorough characterization, including a comparison with the Prussian Blue systems.

Table 3.1. Prussian Blue materials studied along this chapter.

Section	Metals	Alkali content	Ideal composition	Label
3.1	FeTi	A_{1-x} (A = Na/K)	$ATi[Fe(CN)_6]H_2O$*	Ti-PBA
3.2	FeFe	Na_{1-x}	$NaFe[Fe(CN)_6]\cdot yH_2O$	Na-PB
3.2	FeFe	K_{1-x}	$KFe[Fe(CN)_6]\cdot yH_2O$	K-PB
3.3	FeFe	Na_{2-x}	$Na_2Fe[Fe(CN)_6]$	Na-PW
3.3	FeFe	K_{2-x}	$K_2Fe[Fe(CN)_6]$	K-PW

*or $Ti[Fe(CN)_6]H_2O$

3.1 Titanium Prussian Blue Analogue (Ti-PBA)

3.1.1 Scope

Among the materials investigated as anodic component for SIB, those based on titanium chemistry represent a large number. NASICON type compound $NaTi_2(PO_4)_3$[1] or $Na_2Ti_3O_7$[2] are some of the most representative examples that have proved their feasibility for sodium intercalation. Since the presence of titanium in the structure allows reaching low voltage values and sodium intercalation requires larger cavities compared to Li, the concept of using Ti-PBA as potential low-voltage anode for SIB was conceived.

3.1.2 Synthesis

The titanium Prussian Blue derivative, abbreviated as Ti-PBA, stands for $Ti[Fe(CN)_6]$, $ATi[Fe(CN)_6]$ or $AFe[Ti(CN)_6]$ (A = Alkali cation). Several synthetic routes have been attempted with the aim of achieving the Ti-PBA and the following scheme gathers all these different options:

1.) **Solid state synthesis** (direct synthesis)

1a.) $TiCl_3 + K_3[Fe(CN)_6] \xrightarrow[325^\circ C]{12\ days} Ti[Fe(CN)_6]\ (s) + 3\ KCl\ (s)$ **(3.1)**

1b.) $TiCl_3 + K_4[Fe(CN)_6]\cdot 3H_2O \xrightarrow[325^\circ C]{12\ days} KTi[Fe(CN)_6]\ (s) + 3\ KCl\ (s)$ **(3.2)**

2.) **Synthesis in organic media** (direct synthesis)

2a.) $TiCl_3 + K_3[Fe(CN)_6] \xrightarrow[24h,\ R.T.]{DMSO} Ti[Fe(CN)_6] \downarrow + 3\ KCl$ **(3.3)**

2b.) $TiCl_3 + K_4[Fe(CN)_6]\cdot 3H_2O \xrightarrow[96h,\ R.T.]{DMSO} KTi[Fe(CN)_6] \downarrow + 3\ KCl$ **(3.4)**

3.) **Solvothermal synthesis** (direct synthesis)

3a.) $TiCl_3 + K_3[Fe(CN)_6] \xrightarrow[24h,\ 100^\circ C]{anh.\ CH_3CN} Ti[Fe(CN)_6] + 3\ KCl$ **(3.5)**

3b.) $TiCl_3 + K_4[Fe(CN)_6]\cdot 3H_2O \xrightarrow[24h,\ 100^\circ C]{anh.\ CH_3CN} KTi[Fe(CN)_6] + 3\ KCl$ **(3.6)**

3c.) $TiBr_4 + K_3[Fe(CN)_6] \xrightarrow[20h,\ 120^\circ C]{anh.\ CH_3CN} Ti[Fe(CN)_6]Br + 3\ KBr$ **(3.7)**

3d.) $TiBr_4 + Na_4[Fe(CN)_6]\ ]\cdot 10H_2O \xrightarrow[24h,\ 100^\circ C]{anh.\ CH_3CN} Ti[Fe(CN)_6] + 4\ NaBr$ **(3.8)**

---

[1] S. I. Park, I. Gocheva, S. Okada, J. Yamaki, *J. Electrochem. Soc.* 2011, **158**, A1067. "Electrochemical Properties of $NaTi_2(PO_4)_3$ Anode for Rechargeable Aqueous Sodium-Ion Batteries".

[2] P. Senguttuvan, G. Rousse, V. Seznec, J.-M. Tarascon, M. R. Palacín. *Chem. Mater.* 2011, **23**, 4109 – 4111. "$Na_2Ti_3O_7$: Lowest Voltage Ever Reported Oxide Insertion Electrode for Sodium Ion Batteries".

4.) **Aqueous synthesis** (direct synthesis)

4a.) $\mathrm{TiCl_4 + K_4[Fe(CN)_6]\cdot 3H_2O \xrightarrow[1h,\ 80^\circ C]{1M\ HCl} Ti[Fe(CN)_6]\downarrow + 4\ KCl}$ **(3.9)**

4b.) $\mathrm{TiCl_4 + Na_4[Fe(CN)_6]\cdot 10H_2O \xrightarrow[1h,\ 80^\circ C]{1M\ HCl} Ti[Fe(CN)_6]\downarrow + 4\ NaCl}$ **(3.10)**

5.) **Precursor´s synthesis route** (indirect synthesis)

5a.) $\mathrm{3\ Bu_4NClO_4 + K_3[Fe(CN)_6] \xrightarrow[72h,\ R.T.]{MeOH\ dry} (Bu_4N)_3[Fe(CN)_6] + 3\ KClO_4\downarrow}$ **(3.11)**

$\mathrm{(Bu_4N)_3[Fe(CN)_6] + TiCl_3 \nrightarrow Ti[Fe(CN)_6]\downarrow + 3\ Bu_4NCl}$

5b.) $\mathrm{3\ Et_4NBF_4 + K_3[Fe(CN)_6] \xrightarrow[18h,\ R.T.]{H_2O} (Et_4N)_3[Fe(CN)_6] + 3\ KBF_4}$ **(3.12)**

$\mathrm{(Et_4N)_3[Fe(CN)_6] + TiCl_3 \nrightarrow Ti[Fe(CN)_6]\downarrow + 3\ Et_4NCl}$

5c.) $\mathrm{3\ Me_4NI + K_3[Fe(CN)_6] \xrightarrow[ii)\ EtOH]{i)\ H_2O,\ 2h,\ R.T.} (Me_4N)_3[Fe(CN)_6]\downarrow + 3\ KI}$ **(3.13)**

$\mathrm{(Me_4N)_3[Fe(CN)_6] + TiCl_3 \xrightarrow[48h,\ R.T./\ 24h,\ 100^\circ C]{CH_3CN} Ti[Fe(CN)_6]\downarrow + 3\ Me_4NCl}$

5c.) $\mathrm{3\ AgNO_3 + K_3[Fe(CN)_6] \xrightarrow[2\text{-}4h,\ R.T.]{H_2O} Ag_3[Fe(CN)_6]\downarrow + 3\ KNO_3}$ **(3.14)**

$\mathrm{Ag_3[Fe(CN)_6] + TiCl_3 \xrightarrow[72h,\ R.T./\ 24h,\ 100^\circ C]{CH_3CN} Ti[Fe(CN)_6] + 3\ AgCl}$

6.) **Trifluoroacetate synthesis route** (indirect synthesis)

6a.) $\mathrm{TiCl_3 + 3\ CF_3COOK \xrightarrow[48h,\ 60^\circ C]{anh.\ CH_3CN} Ti(OOCCF_3)_3 + 3\ KCl\downarrow}$ **(3.15)**

$\mathrm{Ti(OOCCF_3)_3 + 6\ ACN \xrightarrow[72h,\ R.T.]{anh.\ CH_3CN} A_3[Ti(CN)_6]\downarrow + 3\ AOOCCF_3}$ (A = K, Na)

$\mathrm{A_3[Ti(CN)_6] + FeX_2 \nrightarrow AFe[Ti(CN)_6] + 2\ AX}$ ($\mathrm{X = SO_4^{2-}, NO_3^-}$)

6b.) $\mathrm{TiCl_3 + 3\ CF_3COOK \xrightarrow[48h,\ 60^\circ C]{anh.\ CH_3CN} Ti(OOCCF_3)_3 + 3\ KCl\downarrow}$ **(3.16)**

$\mathrm{Ti(OOCCF_3)_3 + A_4[Fe(CN)_6]\cdot xH_2O \xrightarrow[1\ week,\ R.T.]{anh.\ CH_3CN} ATi[Fe(CN)_6]\downarrow + 3\ AOOCCF_3}$

(A = K, Na and x= 3 or 10, respectively for K and Na).

(X illustrates the impossibility of making that step of reaction, as a result of not obtaining the desired material in the previous step).

We can classify the different approaches of synthesis in direct (solid state, organic, solvothermal and aqueous) and indirect (precursors and trifluoroacetate). Direct synthesis is referred to a type of synthesis in which all reactants are commercially available and the desired product can be simply obtained in a one-step reaction, whereas indirect synthesis implies that, at least, a two-step reaction is required.

Although direct routes are preferred for obvious reasons, the indirect synthesis is the recourse against the non-viability of the former.

The incoming considerations apply througout this section (3.1) of the chapter. As the Ti-PBA materials were expected to be air- and H_2O-sensitive, the X-ray data collection was done using Kapton® film to cover and protect them from the real atmosphere. The utilization of this kapton-tape however entails the appearance of some broad reflections at angles below $2\Theta = 25^\circ$, as it is observed in the resulting diffractograms. The only exceptions to the use of kapton include the materials prepared by aqueous route and those attained in the first step of the precursor route, that is, the synthesis of the so-called precursors.

In general, to facilitate analysis of the X-ray data obtained, the experimental diffractograms of the compounds obtained were plotted along with those of the reactants and the expected products. The next criterion was employed: X-ray diffractograms of the experimental products are presented in different colors at the top of the figures accompanied with a label corresponding to the route attempted (and the fraction investigated, in cases where there are distinction). Below, delineated in grey, the patterns of the reactants are displayed. If the diffractograms of the reactants have already been shown previously in other figure and there is no trace of their reflections in the diffraction pattern of the product, these will not be displayed for clarity. Finally, at the bottom, the diffractograms of the corresponding byproduct and the "desired" product are exposed. The diffraction pattern of the byproduct is only plotted the first time it appears and, in posterior diffractogram analyses, its reflections will appear marked in the products with asterisks. Note that, although $Ti[Fe(CN)_6]$ or $ATi[Fe(CN)_6]$ is the desired product, $Ti_3Cl[Fe(CN)_6]_2$ will be considered as standard for the titanium derivative of the Prussian Blue type structure[3] and it is drawn in blue at the bottom in every comparative figure.

3.1.2.1 *Solid state synthesis*

The starting point fell on the solid state synthesis (route 1). The absence of solvent makes this methodology the more attractive among those above proposed for its simplicity. The reactions (equations (3.1) and (3.2)) were performed in glass ampoules (see Figure 3.1) that were filled with the appropriate amount (0.24 mmols) of $TiCl_3$ and $K_3[Fe(CN)_6]$ or $K_4[Fe(CN)_6]\cdot 3H_2O$, in a stoichiometric ratio 1:1, inside the glove box. Subsequently, the ampoules were closed using a vacuum key to avoid exposure to air of $TiCl_3$. $TiCl_3$ is known to violently react with O_2 and H_2O to form $TiOCl_2$ (oxotitanium chloride), that evolves to form TiO_2.[4] Then, the ampoules were taken out of the glove box and were sealed using an N-butane and isobutane gas welding torch (BUTSIR®) while keeping them under vacuum. Finally, they were placed in a CARBOLITE furnace ELF 11/6b® and heated from room temperature (RT) to 325 °C with a ramp rate of 1 $^\circ C\cdot min^{-1}$ and kept in isotherm at 325 °C for 12 days. Lower reaction times and temperatures were previously tried out with no success. Elapsed this time,

---

[3] M. Ávila, C. Vargas, H. Yee-Madeira, E. Reguera. *Z. Anorg. Allg. Chem.* 2010, **636** (11), 1968-1973. "Titanium^{3+} Hexacyanometallates(II): Preparation and Porous Framework".

[4] B. Tan, Y. Zhang, M. Long. *Nanoscale Research Lett.* 2014, **9**, 190. "Large-scale preparation of nanoporous TiO_2 film on titanium substrate with improved photoelectrochemical performance".

the ampoules were opened inside the glove box using a diamond-tipped tool and a single a solid fraction was obtained.

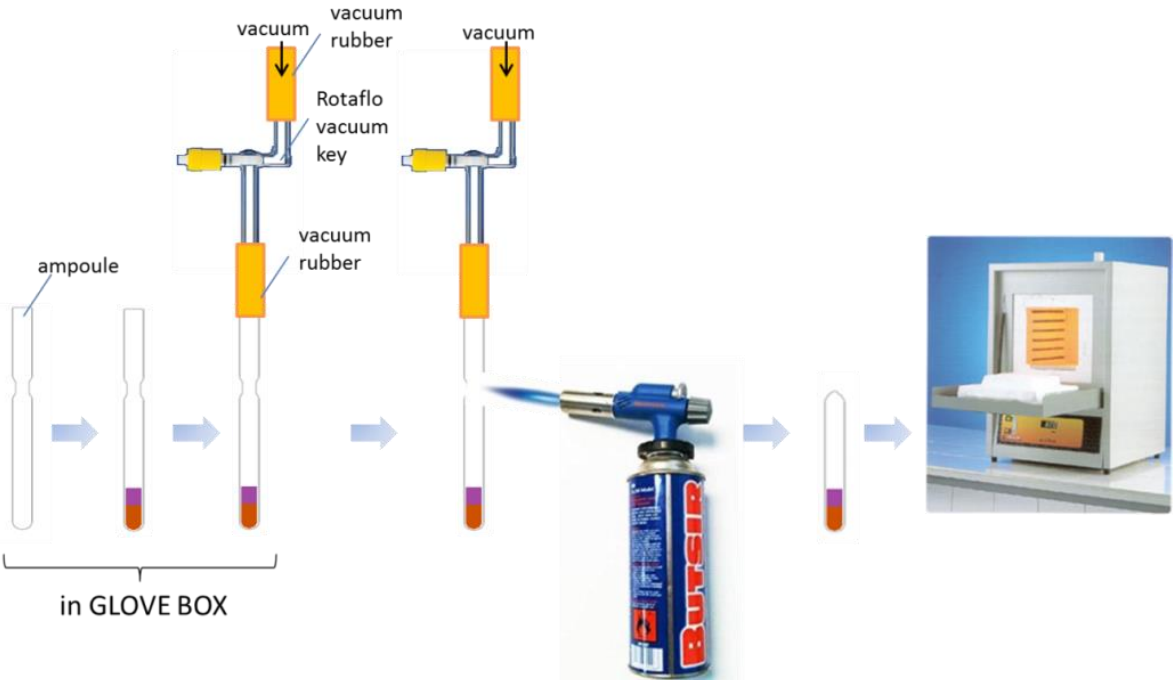

Figure 3.1. Illustration of the solid state synthesis procedure step by step.

A dark redish colour powder intermixed with white particles was attained when following route **1a**, that uses potassium ferricyanide ($K_3[Fe(CN)_6]$) as precursor. Analysis of its X-ray diffractogram (Figure 3.2) revealed that the reaction was completed and no starting materials remained. A few sharp reflections marked with dashed cyan lines in the pattern (Figure 3.2.) reveal the presence of the reaction byproduct KCl, consistent with getting some white particles. Therefore, it was assumed that Ti-PBA had also formed, and this was confirmed by the partial coincidence of some broad reflections with those assigned to the titanium derivative $Ti_3Cl[Fe(CN)_6]_2$ reported in the literature (dashed blue lines), what suggests that only nanoparticles would have formed. Other artefacts, below 2ϴ = 25, are attributed to kapton film.

Unlike the previous reaction, the bright grey material achieved through the synthesis **1b** turned out to be mainly unreacted titanium trichloride ($TiCl_3$) (see also Figure 3.2).

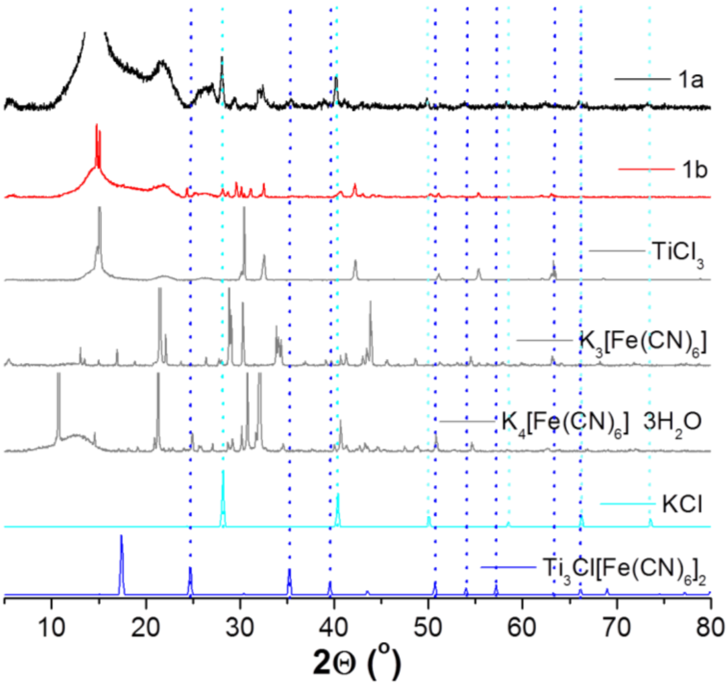

Figure 3.2. Comparison of the powder X-ray diffractograms of: the products **1a** (in black) and **1b** (in red), the starting reagents ($TiCl_3$, $K_3[Fe(CN)_6]$ and $K_4[Fe(CN)_6]\cdot 3H_2O$ - in gray), the byproduct KCl (in cyan) and the standard $Ti_3Cl[Fe(CN)_6]_2$ (in blue)).

Although one possibility that could be envisaged to ensure a complete reaction through **1b** would be to increase the temperature of synthesis, the melting points for $K_3[Fe(CN)_6]$ and $K_4[Fe(CN)_6]\cdot 3H_2O$ are 300 ˚C and 70 ˚C accordingly,[5, 6] and at such temperatures of reaction both materials decompose.[7] Meanwhile, $TiCl_3$ melts and also decomposes at 425 ˚C.[8] The decomposition of the reactants is not beneficial for the evolution of the reaction and, in general, it is advisable to apply temperatures under 80% of the melting points. In addition, typical values for Prussian Blue decomposition oscillates around 350 - 370 ˚C.[9] As a result, temperatures no higher than 325 - 350 ˚C must be deployed since, even if the product is formed, the possibility of degrading it does exist. The application of temperatures well above the decomposition temperature of $K_4[Fe(CN)_6]\cdot 3H_2O$ is probably the reason why $TiCl_3$ does not react forming Ti-PBA. On the other hand, at lower reaction temperatures $TiCl_3$ may not react either.

The fact that Ti-PBA seemed to be achieved through methodology **1a**, was encouraging to further proceed in the synthesis of this phase. However, the coexistence of Ti-PBA with the byproduct KCl, which is not soluble in any organic solvent and only soluble in H_2O,[7] makes impossible the isolation of

---

[5] P.K. Gallagher (edited by Richard L. Cohen). Applications of Mössbauer spectroscopy. Elsevier, 2012, 220.

[6] i) Dale L. Perry, Handbook of Inorganic Compounds, 2nd Ed., CRC Press. Boca Raton (Florida) – USA, 2011, pp. 322. ISBN 9781439814611. ii) SDS - $K_4Fe(CN)_6\cdot 3H_2O$ (Sigma Aldrich).

[7] D. R. Lide, W. M . Haynes, CRC Handbook of Chemistry and Physics (Internet version), 90th Ed., CRC press. Boca Raton (Florida) – USA, 2010, pp. 4 – 82 (731).

[8] D. R. Lide, W. M . Haynes, CRC Handbook of Chemistry and Physics (Internet version), 90th Ed., CRC press. Boca Raton (Florida) – USA, 2010, pp. 4 – 96 (745).

[9] P. K. Gallagher, B. Prescott. *Inorg. Chem.* 1970, **9** (11), 2510–2512. "Further studies on the thermal composition of europium hexacyanoferrate (III) and ammonium europium hexacyanoferrate (II)".

Ti-PBA without hydrolyzing it, and thus called for alternative synthesis methods which could enable the preparation of Ti-PBA as single phase.

3.1.2.2 *Synthesis in organic media*

The solid state reactions were reproduced in organic medium (route 2). In solution, an easier contact between the molecules of the reactants is evident, what favors the evolution of the reaction, even though the temperature applied was necessarily lower than that used in the solid state route. Besides, a different solubility of the desired product and byproduct could enable the isolation of Ti-PBA, making this methodology promising.

Originally, CH_3CN was the solvent chosen in the synthetic routes **2a** and **2b**. Regrettably $K_3[Fe(CN)_6]$ and $K_4[Fe(CN)_6]\cdot 3H_2O$ were the compounds predominantly encountered through them respectively, indicating the absence of reaction. After conducting solubility tests with the starting materials, CH_3CN was replaced by DMSO. Especially, $TiCl_3$ showed a better, although far from complete, solubility in DMSO. Similar behavior was observed for the ferricyanide, $K_3[Fe(CN)_6]$, although no change was accused in the ferrocyanide, $K_4[Fe(CN)_6]\cdot 3H_2O$.

For the organic route (see Figure 3.3), a suspension of 0.456 mmols in 25 mL of DMSO was prepared separately for each reactant. After being stirred and heated at 60˚C for a couple of hours, both suspensions $K_3[Fe(CN)_6]$ and $TiCl_3$ for route **2a** (see equation (3.3)), and $K_4[Fe(CN)_6]\cdot 3H_2O$ and $TiCl_3$ for route **2b** (see eq.(3.4)) were mixed by dropwise addition and were kept at RT for 24 and 96 h, respectively.

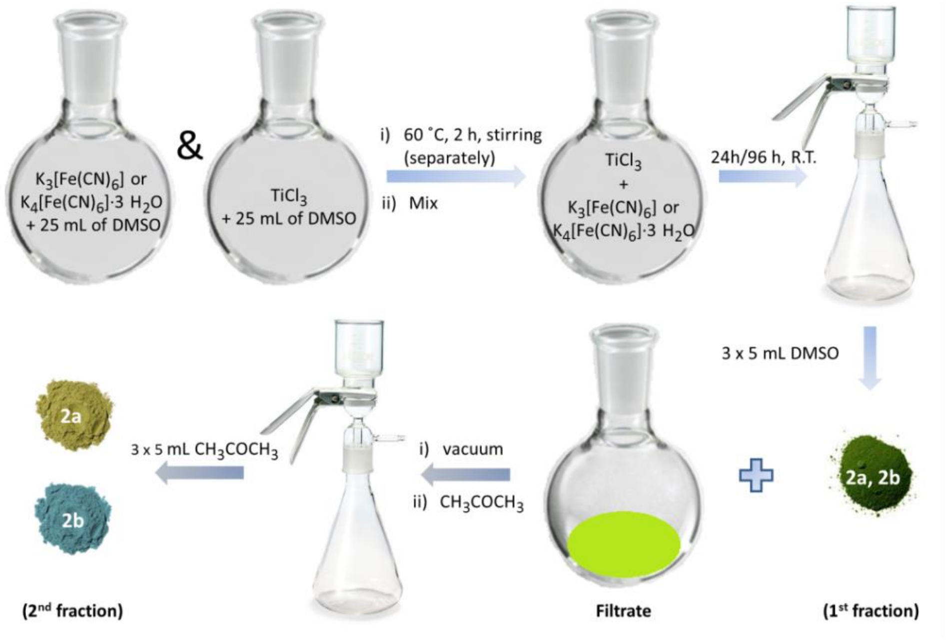

Figure 3.3. Synthesis procedure followed in route 2 – synthesis in organic media. All the steps were performed inside an argon-filled glove box.

Two fractions were collected for the two variants (**2a** and **2b**). The first fraction (**2a_1f** and **2b_1f**) is a billiard green precipitate resultant after reacting, which is picked up by filtering and subsequent washing with some DMSO (3 x 5 mL). The second fraction (**2a_2f** and **2b_2f**) proceeds from the remaining lime yellow filtrate that is vacuumed to remove the solvent and later on is forced to precipitate with CH_3COCH_3. Respectively, an olive green and a turquoise powder compounds were isolated as second fractions of **2a** and **2b**, after filtering and washing several times with acetone (3 x 5 mL).

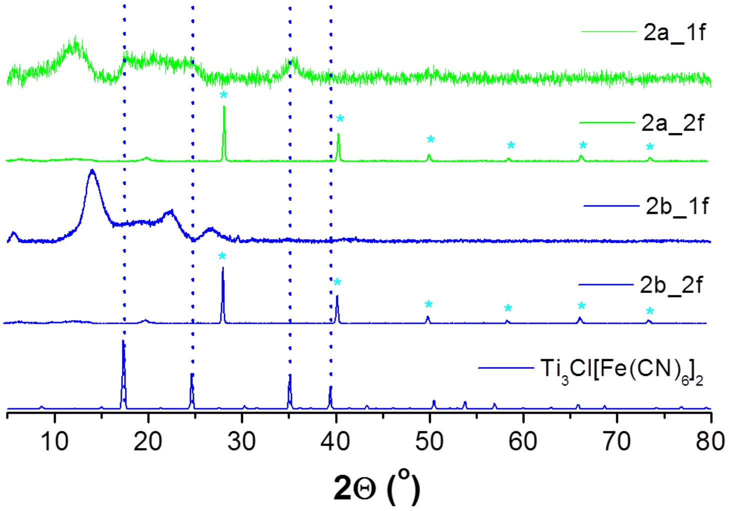

Figure 3.4. Comparison of the powder X-ray patterns of the products **2a_1f**, **2a _2f** (in green) and **2b_1f**, **2b_2f** (in blue)and the desired product $Ti_3Cl[Fe(CN)_6]_2$ (in blue). KCl reflections have been highlighted in **2a_2f** and **2b_2f** with asterisks colored in cyan.

Figure 3.4 includes the PXRD data corresponding to the compounds synthesized through routes **2a** (in green) and **2b** (in blue). No trace of starting materials was noted in them (see Appendix, Figure A3.1). Indeed, a strong evidence that the reaction had taken place was the absolute coincidence of the peaks of the second fractions (**2a_2f** and **2b_2f**) with the reflections of the KCl byproduct. As pointed out in the solid state route, once the byproductis attained, the formation of Ti-PBA is also expected. The most intense reflections of Ti-PBA can be easily distinguished in **2a_1f**. However, no signal apart from those of the Kapton® film is guessed in **2b_1f**, suggesting a very small particle size.

Even though no signals of Ti-PBA are appreciated by PXRD in **2b_1f**, the presence of a characteristic cyano (-C≡N) band at 2076 cm^{-1} in the IR spectrum (see Figure 3.5) could be indicative of the formation of a Prussian Blue type structure. The absence of $K_4[Fe(CN)_6]\cdot 3H_2O$, which is typically highly crystalline, in the X-ray pattern of the compound could rule out the possibility that such band was related to the starting cyanide, thus sustaining the achievement of Ti-PBA. A more determinant evidence is the position of the -C≡N band, that is shifted with respect to that of $K_4[Fe(CN)_6]\cdot 3H_2O$ observed at 2044 cm^{-1}.[10, 11]

---

[10] V. Caglioti, G. Sartori, M. Scrocco. *J. Inorg. Nucl. Chem*. 1958, **8**, 87-92. "Infrared spectra of hexacoordinated cyanide complexes".

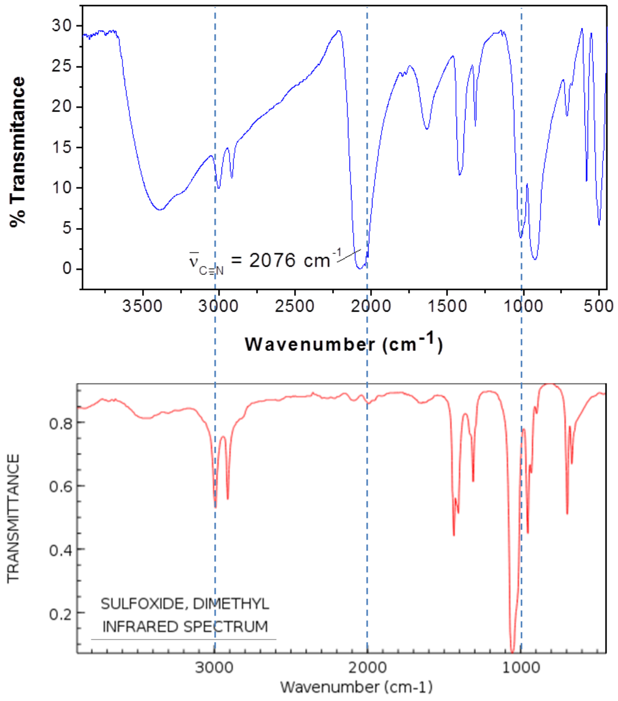

Figure 3.5. Top) IR spectrum of the product **2b_1f**, highlighting the cyano (-C≡N) band. Bottom) IR spectrum of DMSO.[12]

The IR spectrum of **2b_1f** also showed other bands, the majority of which can be associated with the DMSO solvent. In fact, EDX analysis of **2b_1f** corroborated the presence of sulfur and oxygen in the compound. Other elements present in the material were K, Ti, Fe, C and N, where the Ti: Fe ratio was *ca*. 1:0.8 (as shown Figure 3.6a), suggesting that Ti-PBA had been formed and that DMSO could be trapped in the cubic cavities or coating the titanium derivative. The existence of a 5.46 Å interplanar distance observed in the TEM (Figure 3.6b) agress with the formation of Ti-PBA.

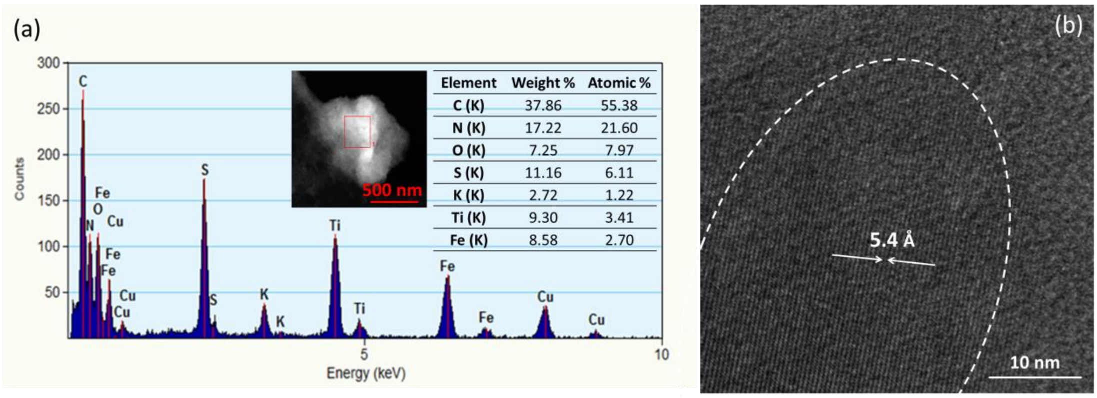

Element	Weight %	Atomic %
C (K)	37.86	55.38
N (K)	17.22	21.60
O (K)	7.25	7.97
S (K)	11.16	6.11
K (K)	2.72	1.22
Ti (K)	9.30	3.41
Fe (K)	8.58	2.70

Figure 3.6. a) EDX analysis and b) Interplanar distances of **2b_1f**.

---

[11] L. Xia and R. L. McCreery. *J. Electrochem. Soc*. 1999, **146** (10), 3696-3701. "Structure and Function of Ferricyanide in the Formation of Chromate Conversion Coatings on Aluminum Aircraft Alloy".

[12] http://webbook.nist.gov/cgi/cbook.cgi?ID=C67685&Type=IR-SPEC&Index=2 (National Institute of Standards and Technology)

It can be concluded that Ti-PBA was successfully prepared by the organic route as a single isolated fraction and, unlike the previous solid state methodology, without any impurity. Therefore, these materials were further characterized to determine its suitability as electrode materials for Na-ion batteries, as will be discussed in Chapter 4.

3.1.2.3 *Solvothermal synthesis*

With the purpose of optimizing the precedent reactions and decrease the amount of time invested on them, solvothermal synthesis were performed (routes 3a, b) using autoclaves. Besides, new reactions with $TiBr_4$ as titanium source instead of $TiCl_3$ and $Na_4[Fe(CN)_6]\cdot10H_2O$ were carried out (routes 3c, d). The use of $TiBr_4$ would generate KBr and NaBr as byproducts, which can be more easily eliminated than KCl. KBr is slightly soluble in $(CH_3CH_2)_2O$,[13] soluble in EtOH when heating at 80˚C and partially soluble in CH_3COCH_3,[7, 14] whereas NaBr is soluble in EtOH.[15]

The autoclave (see Figure 3.7) is a closed stainless steel vessel with an internal cup and lid made of Teflon (PTFE). When the instrument is charged with reagents, there must always be an adequate free space above the charge in the bomb before closing the system. For inorganic samples which do not generate gases, at least 33% of the capacity of the cup should be left as free space. Under external heating, the contents will be raised to higher temperatures and pressures than within an unsealed container. These devices are specifically designed for harsh chemicals, high temperatures and high pressures.[16]

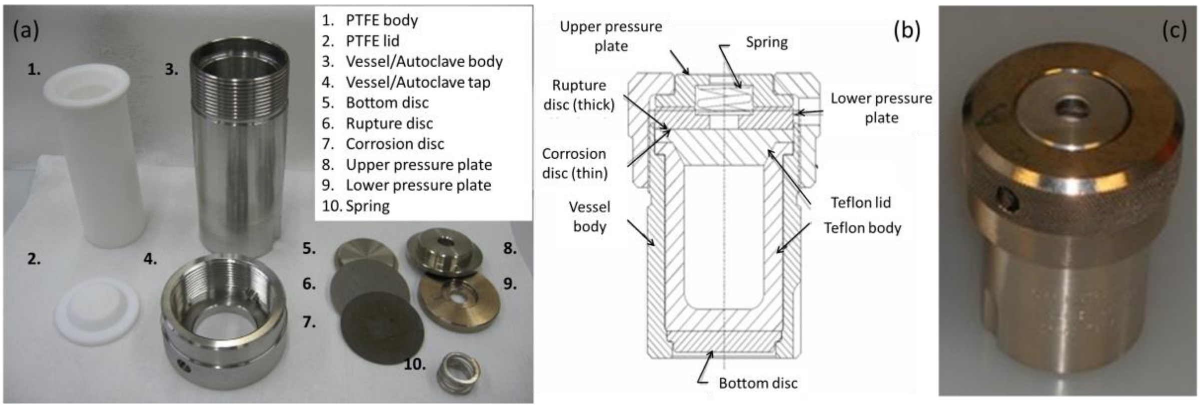

Figure 3.7. a) Autoclave components, b) Schema of the solvothermal autoclave configuration[16] and c) final aspect of the autoclave, once it is closed.

---

[13] http://www.ispoptics.com/admuploads/file/msds_kbr.pdf

[14] http://periodic-table-of-elements.org/SOLUBILITY/potassium_bromide

[15] D. R. Lide, W. M . Haynes, CRC Handbook of Chemistry and Physics (Internet version), 90th Ed., CRC press. Boca Raton (Florida) – USA, 2010, pp. 4 – 82 (738).

[16] Standard Operating Procedure (SOP): Use of Autoclaves for Hydrothermal Experiments (see 1.0), Oregon State University, Department of Chemistry.
http://chemsafety.chem.oregonstate.edu/content/osp-autoclave-hydrothermal-experiments

Under inert atmosphere, inside an argon-filled glove box, *ca*. 0.3 mmols of each starting reagent was deposited inside a 32 mL capacity PTFE body of the autoclave in powder form and *ca.* 20 mL of anhydrous CH_3CN were added (Figure 3.8). DMSO was not considered as solvent fearing not being able to totally remove it, which would thus hinder the Na^+ insertion, as will be discussed in chapter 4 (section 4.1.2). Then, the autoclave was closed and transferred into an oven at the appropriate temperature (100 or 120 ˚C) for the specified time (20 - 24 h), as listed in Eq. (3.5) to (3.8). The reaction conditions were the same for every solvothermal synthesis attempted (100˚C for 24 h), except for the methodology **3d** (Eq. (3.8)). At 100 ˚C, only starting material was obtained for 3d. Consequently, the temperature was raised from 100 ˚C to 120 ˚C and the time was decreased in 4 h. After this time, the autoclave was taken out from the oven and it was allowed to cool down naturally on a heat-resistant plate. Then, the autoclave was placed again inside the glove box, where it was carefully opened and its content was filtered and washed with CH_3CN (3 x 5 mL).

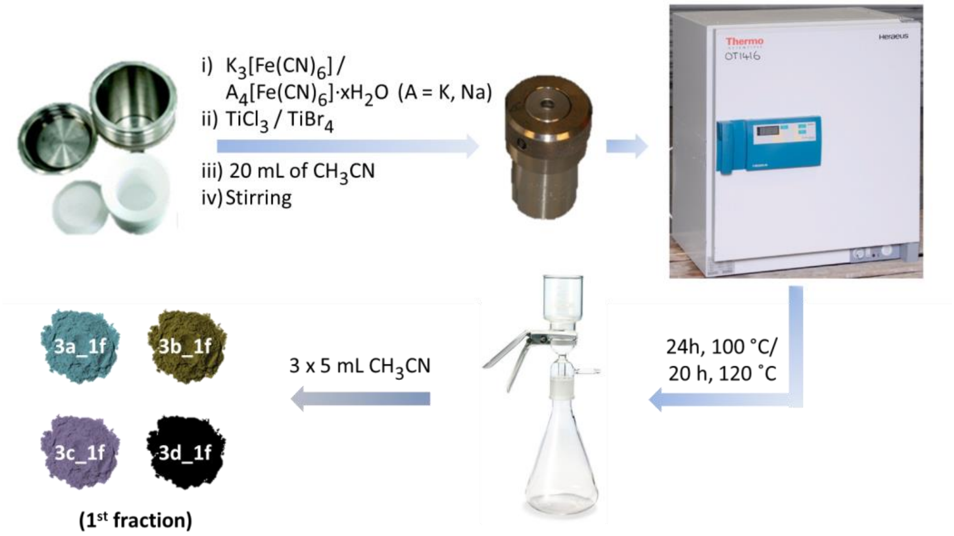

Figure 3.8. Solvothermal synthesis procedure (route 3) specified step by step.

Just a single first fraction, petrol blue and dark green color, was isolated in routes **3a** and **3b,** since the colorless filtrate resultant (likely CH_3CN) was eliminated.

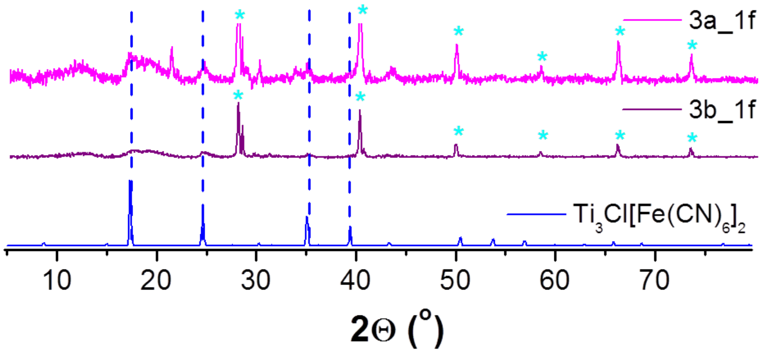

Figure 3.9. Comparison of the powder X-ray diffractograms of products **3a_1f** (in pink), **3b _1f** (in purple) and the desired product $Ti_3Cl[Fe(CN)_6]_2$ (in blue). KCl reflections have been highlighted in **3a_1f** and **3b_1f** with asterisks colored in cyan.

No starting materials were detected in the X-ray patterns of fractions **3a_1f** and **3b_1f** (Figure 3.9), except some residual signals from the cyanide $K_3[Fe(CN)_6]$ in **3a_1f** (see Appendix, Figure A3.2). On the other hand, the reflections corresponding to the byproduct KCl appear together with those ascribed to the titanium Prussian Blue, as it can be observed in Figure 3.9.

Through routes **3c** and **3d,** with $TiBr_4$, a purple-brownish color precipitate (**3c_1f**) and a blackish precipitate (**3d_1f**) were obtained, accordingly. In these cases, the second fraction of **3c** and **3d** possessed an orange-brownish color. To intend isolating them, the flasks containing them were vacuumed and the acetonitrile solvent evaporated. The final products were oily and gummy and they couldn´t be extracted from the container. Some solvents, including CH_3COCH_3, were added to try to recover the material with no success. The powder X-ray diffractograms of precipitates **3c_1f** and **3d_1f** are shown in Figure 3.10 (olive green and orange, respectively). The peaks of the byproducts, KBr and NaBr, can be distinguished in both as well as some traces of the corresponding starting cyanides ($K_3[Fe(CN)_6]$ (see Appendix, Figure A3.3) and/or $Na_4[Fe(CN)_6]\cdot 10H_2O$). As already discussed, the presence of the byproduct and absence of other phases, suggests that the main product Ti-PBA has also been generated, although much less crystalline. Actually, in **3c** the four main reflections of Prussian Blue are perceptible. Conversely, no trace of the Ti-PBA is guessed in **3d**.

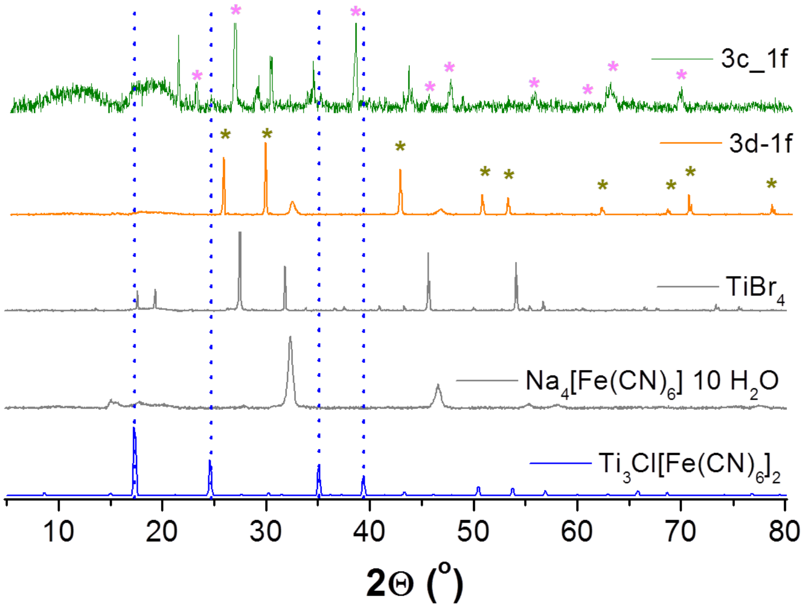

Figure 3.10. Comparison of the powder X-ray diffractograms of the products **3c_1f** (in olive green), **3d _1f** (in orange), the starting reagents ($TiBr_4$ and $Na_4[Fe(CN)_6]\cdot 10H_2O$ - in gray), the byproducts (KBr (whose reflections have been highlighted in 3c_1f with asterisks in coral) and NaBr (whose reflections have also been highlighted in 3d_1f with asterisks in dark yellow)) and the desired products $Ti_3Cl[Fe(CN)_6]_2$ (in blue).

The Ti-PBA has thus been attained by routes **3a**, **3b** and **3c**. Unfortunately, the product is mixed with some remaining starting cyanide and the corresponding byproduct (KCl or KBr). As it was discussed on route **1**, KCl cannot be removed without hydrolyzing the Ti-PBA. On the other hand, KBr is slightly soluble in $(CH_3CH_2)_2O$,[17] soluble in EtOH when heating at 80°C and partially soluble in CH_3COCH_3.[7, 18]

---

[17] http://www.ispoptics.com/admuploads/file/msds_kbr.pdf

However, the starting cyanides cannot be eliminated from the mixture. Since Ti-PBA here obtained are not pure, no electrochemical test was executed.

3.1.2.4 *Aqueous synthesis*

Obtaining of Ti-PBA by means of aqueous synthesis (route 4) had already been reported in the literature.[19, 20] The synthesis in aqueous media had been left on the sidelines to avoid having H_2O in the material, which is known to be detrimental for the electrochemistry, and mostly to avoid using acidic conditions. The preparation methodology was repeated with slight variations (see equations (3.9) and (3.10)).

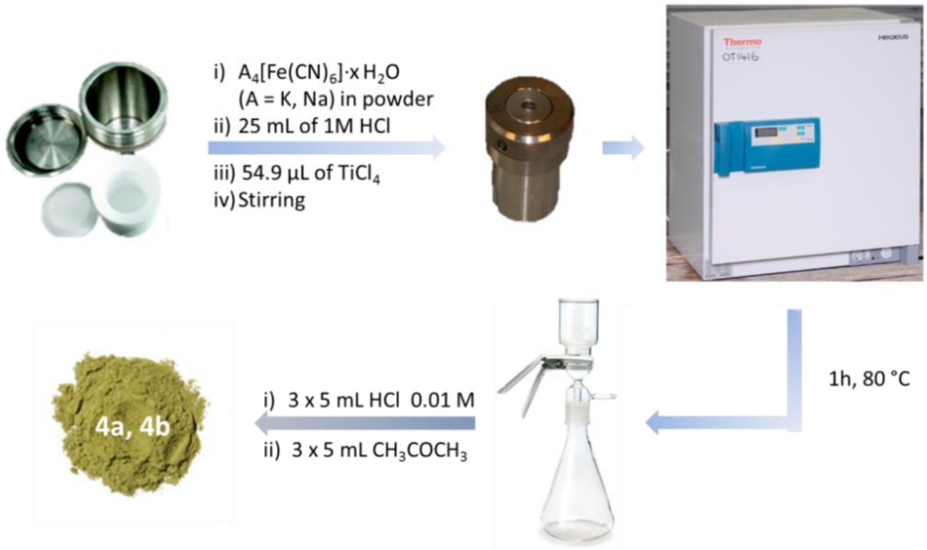

Figure 3.11. Detailed procedure for preparing Ti-PBA by aqueous synthesis (route 4).

In the teflon body of an autoclave, 25 mL of 0.02 M aqueous $TiCl_4$ solution (that is 54.9 μL) were added to a 25 mL of 0.02 M aqueous $A_4[Fe(CN)_6]\cdot xH_2O$ solution (A = K, Na and x= 3 (A= K), 10 (A = Na)) which contains 1M HCl. For security reasons, the whole procedure was developed in a chemical fumehood, using a gas respirator equipped with filters ABEK1 and also a CN^- detector Dräger pac7000®. The addition of HCl has the aim to prevent the hydrolysis of both $TiCl_4$ and $A_4[Fe(CN)_6]\cdot xH_2O$ and of the product that will be formed. The mixture was stirred for a couple of minutes and, then, the autoclaves were sealed and moved into a Thermo Scientific Heraeus® oven at 80 °C for 1h. Finally, a billiard green-brownish suspension was formed. It was filtered and the

---

[18] http://periodic-table-of-elements.org/SOLUBILITY/potassium_bromide

[19] M. Hu and Y. Yamauchi. *Chem. Asian J*. 2011, **6**, 2282 – 2286. "Synthesis of a Titanium-Containing Prussian-Blue Analogue with a Well-Defined Cube Structure and Its Thermal Conversion into a Nanoporous Titanium–Iron-Based Oxide".

[20] E. S. Zakaria, I. M. Ali and H. F. Aly. *Adsorption* 2004, **10**, 237-244. "Adsorption Behaviour of ^{134}Cs and ^{22}Na Ions on Tin and Titanium Ferrocyanides".

resultant olive green color precipitate was washed three times with 5 mL of diluted HCl (0.01 M) and three times more with 5 mL of acetone (Figure 3.11).

Several times ranges were tested with the objective of reducing the starting time used in the synthesis (that was of 24 h). Figure 3.12 compares the X-ray diffractograms of the compounds obtained with the K precursor (route 4a) at different times of reaction (from 1h to 18h). As it can be observed, all of them show the reflections belonging to the Prussian Blue type structure. Although the peaks broaden as the time of reaction is shortened, indicating a smaller particle size, it could be concluded that 1 h is enough time to achieve the Ti-PBA material. The same study was performed for the sodium precursor (route 4b) yielding similar results (see Annex A3.4).

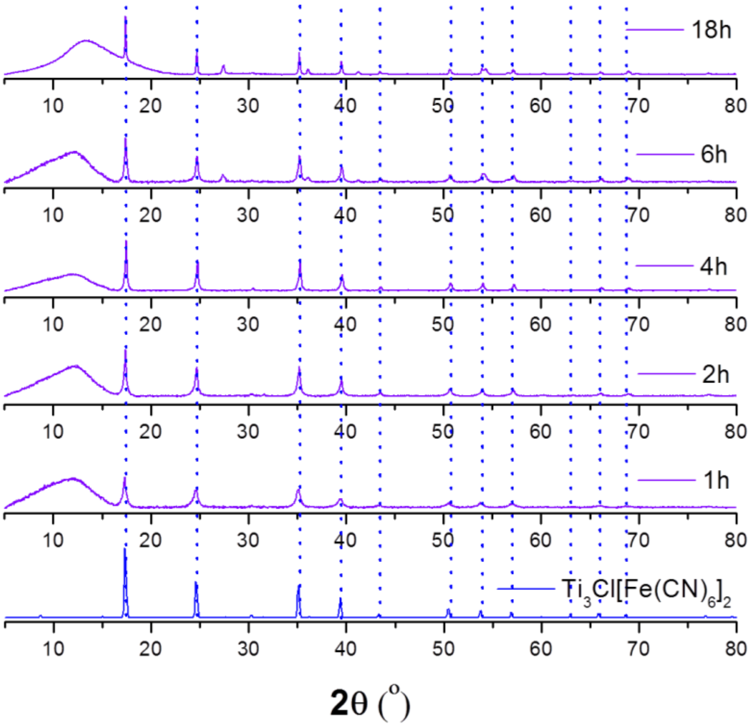

Figure 3.12. PXRD patterns of Ti-PBA prepared in aqueous media through route **4a**, using different times of reaction.

An advantage of this aqueous route, with regard to the previous methods, is the formation of more crystalline and thus unequivocally pure Ti-PBA. As it can be observed in Figure 3.12, the pattern perfectly matches with that reported for $Ti_3Cl[Fe(CN)_6]_2$. Besides, there is no trace of the reactants (see Annex A3.5) and, the byproducts generated in each case, KCl and NaCl, remained in the aqueous solution after filtering. Only the desired material, Ti-PBA, is obtained. However, highly acidic conditions, not recommended in presence of cyanides, are required and, as mentioned before, some H_2O could remain trapped in the structure interfering in its electrochemical behaviour.

To sum up, it can be concluded that *direct syntheses have yielded the targeted material Ti-PBA*. Through the solid state and solvothermal synthetic routes (**1a**, **3a**, **3b** and **3c**), Ti-PBA was achieved alongside the byproduct (KCl, KBr). Also some remaining starting cyanide is encountered following route 3. The mixed nature of these materials and the impracticability of removing the impurities preclude their electrochemical study. On the other hand, pure Ti-PBA was obtained following the organic and aqueous synthetic routes (**2a**, **2b**, **4a** and **4b**). The reaction yield of **2a** was extremely low, impeding its electrochemical test. Meanwhile, the formation of Ti-PBA through **2b** was not evident by PXRD, but other techniques (IR, TEM) allowed proving it. In the case of the materials obtained in aqueous media (**4a** and **4b**), it has been demonstrated that Ti-PBA has been unequivocally achieved. Consequently, the electrochemical properties of the materials attained by routes **2b**, **4a** and **4b** will be investigated in the next chapter (Chapter 4, section 4.1.2).

3.1.2.5 *Precursors route*

An alternative approach to prepare the Ti-PBA avoiding the presence of H_2O and byproduct impurities is by means of a two-step reaction by using a precursor. The strategy consisted of synthesizing first a precursor containing an organic counteranion. Later, when reacted with a titanium salt in an organic solvent, it would form a precipitate containing Ti-PBA and, ideally, a soluble organic salt that would remain in the filtrate. That is, Ti-PBA and the organic salt would have opposite solubility in the solvent deployed.

Among the ferrocyanide derivates reported in the literature, $(Et_4N)_3[Fe(CN)_6]$[21], $(Me_4N)_3[Fe(CN)_6]$[22] and $Ag_3[Fe(CN)_6]$[23, 24] were selected as the desired precursors. In addition, a new related precursor, $(Bu_4N)_3[Fe(CN)_6]$, was conceived and prepared.

3.1.2.5.1 *Step 1. Synthesis and characterization of the precursors*

In a fumehood and at room temperature, 0.5 mmols of potassium ferricyanide $K_3[Fe(CN)_6]$ was mixed with 1.5 mmols of an organic salt (Bu_4NClO_4, Et_4NBF_4, Me_4NI or $AgNO_3$) in 25 mL of H_2O (except in route **5a** that MeOH dry was used instead) for 2-72 h, as stipulated in Eq. 3.11-3.14. In routes **5a** and **5b**, the reaction was conducted under N_2 atmosphere.

A first fraction spontaneously precipitated in the media of **5a** and **5d**, while in routes **5b** and **5c**, it was necessary to force the precipitation by the addition of EtOH. In all the cases, the suspension was filtered. Through the procedures **5a**, **5c** and **5d**, a yellow-orange compound (**5a_1f**), a fine yellow powder (**5c_1f**) and an orange-redish complex (**5d_1f**) were accordingly obtained. The filtrates derived from the filtering process were reduced in the rotavapor and, once the volume was minimum, some ethylic ether (Et_2O) was added to recover the second fraction, again by filtration. The

---

[21] P. K. Mascharak. *Inorg. Chem.* 1986, **25** (3), 245-247. “Convenient synthesis of tris(tetraethylammonium) hexacyanoferrate(III) and its use as an oxidant with tunable redox potential”.

[22] M. Armand, M. S. Whittingham, R. A. Huggins. *Mat. Res. Bull.* 1972, **7**, 101-108. “The iron cyanide bronzes”.

[23] A. Bellomo, A. Casale, D. De Marco. *Talanta* 1973, **20** (3), 335-338. “Formation of ferricyanides-I silver(I), copper(II) and cadmium(II)”.

[24] A. L. Goodwin, D. A. Keen, M. G. Tucker, M. T. Dove, L. Peters, J. S. O. Evans. *J. Am. Chem. Soc.* 2008, **130** (30), 9660-9661. “Argentophilicity-dependent colossal thermal expansion in extended prussian blue analogues”.

colour of the compounds yielded were lemon yellow (**5a_2f**), beige (**5c-2f**) and white-cream (**5d_2f**), respectively (see Figure 3.13).

Just a single fraction was achieved following the procedure **5b**. The addition of EtOH only provided the formation of few miligrams (less than 5 mg) of a green powder in suspension. To reduce the volume and promote the precipitation of the compound, the turbid solution was rotary evaporated in the rotavapor. As soon as it was dried, few mL of Et_2O were added to collect the material. A green-lime powder was attained (**5b_1f**).

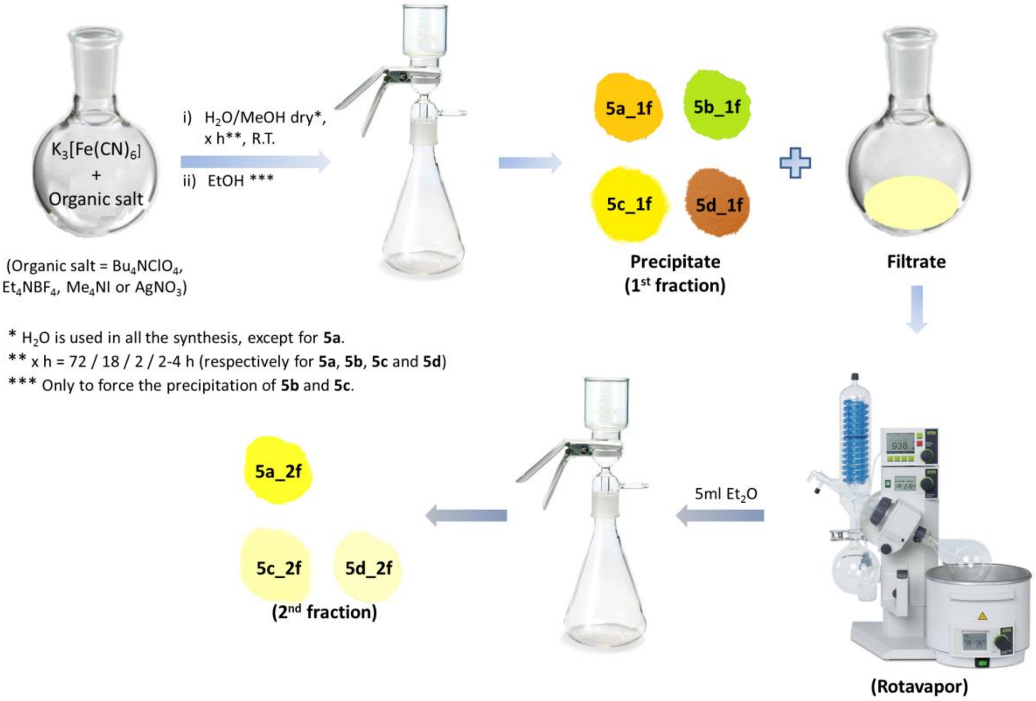

Figure 3.13. General schematic representation of the precursor synthesis (**5a**, **5b**, **5c** and **5d**).

3.1.2.5.1.1 ***$(Bu_4N)_3[Fe(CN)_6]$***

The recipe followed to intend synthesizing $(Bu_4N)_3[Fe(CN)_6]$ is identical to that reported in the literature for obtaining $(Et_4N)_3[Fe(CN)_6]$,[21] but using Bu_4NClO_4 instead of Et_4NClO_4. If the mixture is allowed to react for only 24 h, a blend of $K_3[Fe(CN)_6]$ and the byproduct $KClO_4$ precipitates (1st fraction, **5a_1f**), as Figure 3.14 illustrates. New reflections at 2Θ = 7.5, 15.45, 17.0, 17.3, 18.7, 25.8 and 31.8 ˚ are found in the X-ray pattern of the second fraction along with the reflections from unreacted $K_3[Fe(CN)_6]$ and Bu_4NClO_4 (Figure 3.14). Since the new reflections noticed in **5a_2f** do not fit to any of the reactants nor the byproduct $KClO_4$, they were assigned to the formation of the desired precursor $(Bu_4N)_3[Fe(CN)_6]$.

No difference is observed when the mixture is heated at 50 ˚C. Even if the reaction is extended in time up to 72 h, the same composition is achieved in both fractions (see Figure 3.14). A plausible explanation to the presence of unreacted reagents in **5a_2f** could be that a mixed ferrocyanide, such as $(Bu_4N)_{3-x}K_x[Fe(CN)_6]$, is being formed instead of $(Bu_4N)_3[Fe(CN)_6]$.

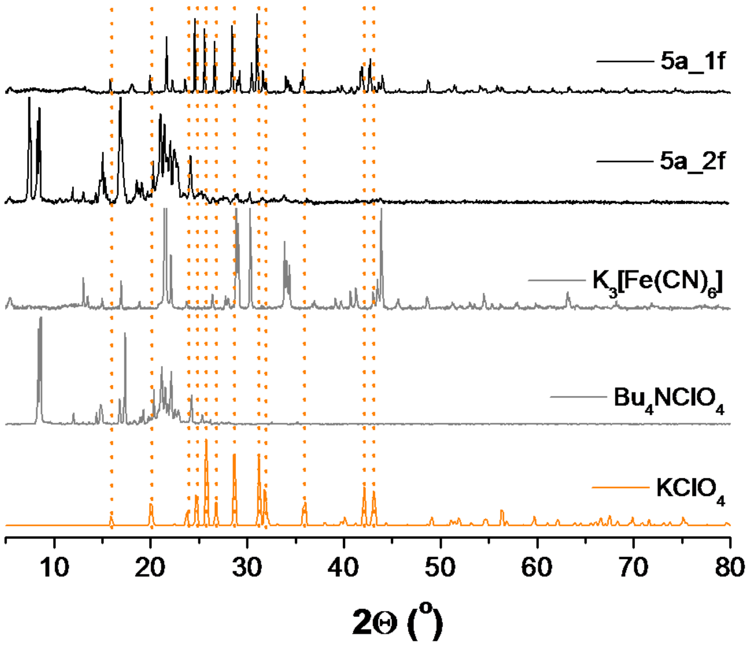

Figure 3.14. Powder X-ray diffractograms of the products **5a_1f** and _**2**f (in black), the starting reagents ($K_3[Fe(CN)_6]$ and Bu_4NClO_4 - in gray) and the byproduct ($KClO_4$ - in orange).

With the aim of removing the starting materials and isolate the precursor $(Bu_4N)_3[Fe(CN)_6]$, the second fraction **5a_2f** was washed with H_2O and isopropanol. The solvents were chosen based on a solubility test of the main impurity, Bu_4NClO_4, and the byproduct **5a_2f**.

When the second fraction is placed in H_2O, an insoluble white precipitate, that is allocated to Bu_4NClO_4, and a yellow solution can be distinguished. After filtering, the precipitate is eliminated and the filtrate is rotatory evaporated and recovered as a yellow powder with Et_2O. Despite the efforts to remove Bu_4NClO_4, the Cl-O stretching vibrational bands of ClO_4^- (1093 and 623 cm^{-1}) are still present in the IR spectrum of the yellow filtered fraction, indicating the permanence of Bu_4NClO_4 (see Figure 3.15, **5a_2f - H_2O_2f**). The cyanide (-C≡N) vibration of $K_3[Fe(CN)_6]$ can also be guessed at 2117 and 2076 cm^{-1}. Even though the reactants couldn´t be totally removed, the -C≡N band at 2097 cm^{-1} becomes more prominent. This band is attributed to the precursor $(Bu_4N)_3[Fe(CN)_6]$ (or $(Bu_4N)_{3-x}K_x[Fe(CN)_6]$), what agrees with the presumption made from PXRD.

If isopropanol is used as solvent, a green precipitate and a yellow filtrate are generated. The treatment of the filtrate was the same as that utilized with H_2O. Although Bu_4NClO_4 is expected in the precipitate, the fact that it presents a green color makes reconsider this possibility. The collected IR spectra data of both fractions (see Figure 3.15, **5a_2f – iPrOH_1f** and **5a_2f – iPrOH_2f**) shed light on the results. The green precipitate provided an IR spectrum pretty similar to that of the starting cyanide $K_3[Fe(CN)_6]$ but with different proportion in the intensity of the -C≡N bands. The second fraction, however, can be assigned to a mixture of the precursor $(Bu_4N)_3[Fe(CN)_6]$ (or $(Bu_4N)_{3-x}K_x[Fe(CN)_6]$) and the undesired Bu_4NClO_4.

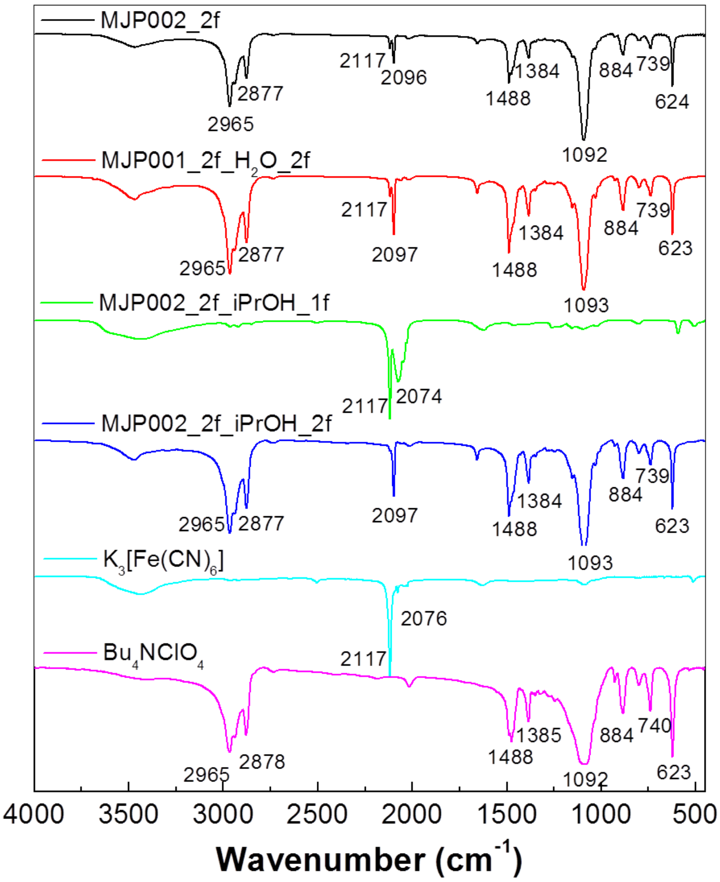

Figure 3.15. IR spectra of the product **5a_2f**, and the compounds resultant from washing it with H_2O (**5a_2f-H_2O_2f**) or isopropanol (**5a_2f_iPrOH_1f** and **5a_2f_iPrOH_2f**). IR of Bu_4NClO_4 and the starting cyanide $K_3[Fe(CN)_6]$ are also presented, for facilitating the comparison.

Table 3.2. Principal IR bands observed in **5a_2f**, **5a_2f-H2O_2f**, **5a_2f_iPrOH_1f**, **5a_2f_iPrOH_2f**, $K_3[Fe(CN)_6]$and Bu_4NClO_4.

	IR bands (cm^{-1})				
Fraction	ν(C-H), Bu_4N^+	ν(C≡N), $[Fe(CN)_6]^{3-}$	ν(C-C), Bu_4N^+	ν(Cl-O), ClO_4^-	ν(C-N), Bu_4N^+
5a_2f	2965, 2877	2117, **2096**	1488, 1384	1092, 624	884, 801, 793
5a_2f_H_2O_2f	2965, 2877	2117, **2097**	1488, 1384	1093, 623	884, 800, 793
5a_2f_iPrOH_1f		2117, 2074			
5a_2f_iPrOH_2f	2965, 2877	**2097**	1488, 1384	1093, 623	884, 800, 739
$K_3[Fe(CN)_6]$		2117, 2076			
Bu_4NClO_4	2965, 2878		1488, 1385	1092, 623	884, 800, 740

Table 3.2 collects the values at which the principal IR bands of all the fractions of route 5a shown in Figure 3.15. Although it has not been reflected in Table Table 3.2, the wide band centered at ca. 3500 cm^{-1}, also indicates the presence of H_2O in the structure of compound **5a_2f** and its derivatives.

Since the precursor $(Bu_4N)_3[Fe(CN)_6]$ was not achieved as a pure and single phase, the second stage of the reaction was not carried out.

3.1.2.5.1.2 $(Et_4N)_3[Fe(CN)_6]$

For preparing $(Et_4N)_3[Fe(CN)_6]$, the procedure of Mascharak[21] couldn´t be utilized, due to the unavailability of Et_4NClO_4. Instead, that reported by M. Armand for obtaining $(Me_4N)_3[Fe(CN)_6]$ was adapted.[22] The utilization of Et_4NI analogous to Me_4NI, provided only unreacted products (see Annex, figure A3.6), and it was decided to replace it with Et_4NBF_4. As it was mentioned above (Section 3.1.2.5.1) only a single fraction (**5b**) was obtained.

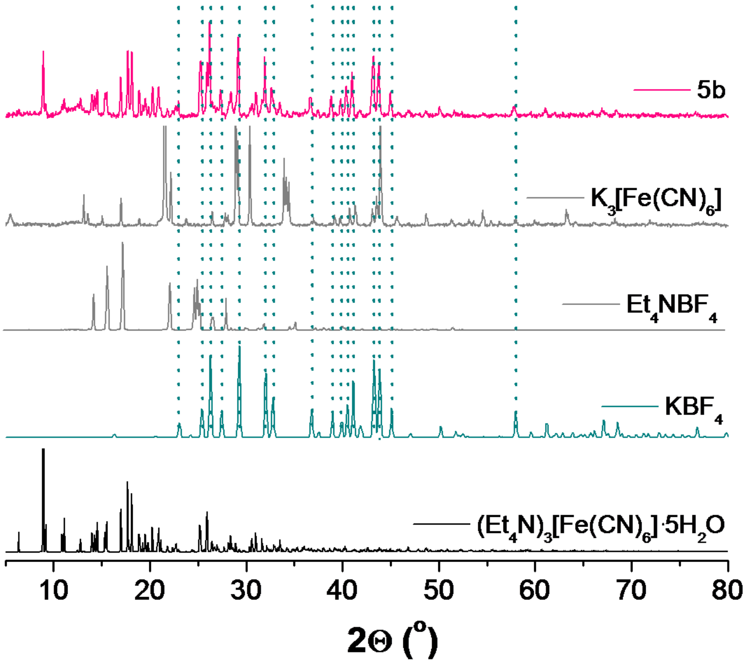

Figure 3.16. Powder X-ray diffractograms of product **5b** (in pink), the starting reagents ($K_3[Fe(CN)_6]$ and Et_4NBF_4 - in gray), the byproduct (KBF_4 - in green) and the desired precursor $(Et_4N)_3[Fe(CN)_6]$. The $(Et_4N)_3[Fe(CN)_6]$ X-ray diffractogram was simulated from the .cif file acquired from the CSD (Cambridge Structural Database).[25]

X-ray data showed no footprint of the starting materials in the precipitate (**5b**), as Figure 3.16 illustrates. The reflections of the byproduct KBF_4 appeared however intermixed along with other peaks belonging to a new phase, which is assumed to be the precursor $(Et_4N)_3[Fe(CN)_6]$. The contrast of its X-ray profile with that of the $(Et_4N)_3[Fe(CN)_6]$ obtained in the literature further confirmed it, [25] as Figure 3.16 displays. Almost all the reflections up to 2ϴ = 25˚ are coincident between **5b** and $(Et_4N)_3[Fe(CN)_6]$, although the intensity ratio varies. From 25˚ onwards, the peaks observed in **5b** are mainly due to the byproduct KBF_4.

As a consequence of the poor solubility of KBF_4, that is slightly soluble in EtOH and Et_2O,[26] the isolation of $(Et_4N)_3[Fe(CN)_6]$ from **5b** is very difficult. Even though **5b** was obtained after collecting it with Et_2O, in which KBF_4 is slightly soluble, we still observed the presence of this byproduct.

3.1.2.5.1.3 $(Me_4N)_3[Fe(CN)_6]$

The synthesis of $(Me_4N)_3[Fe(CN)_6]$ was performed according to the procedure described by M. Armand *et al.*[22] Tetramethyl ammonium Fe(III) cyanide was attained by mixing aqueous solutions of $K_3[Fe(CN)_6]$ and Me_4NI under N_2 atmosphere, and precipitating by alcohol.

No trace of the reactants and no residues of KI are visible in the X-ray diffractogram of **5c_1f** (see Figure 3.17). The signals of this first fraction are assigned to the pure phase of the precursor $(Me_4N)_3[Fe(CN)_6]$. On the other hand, the pattern of **5c_2f** is a blend of KI and unreacted Me_4NI.

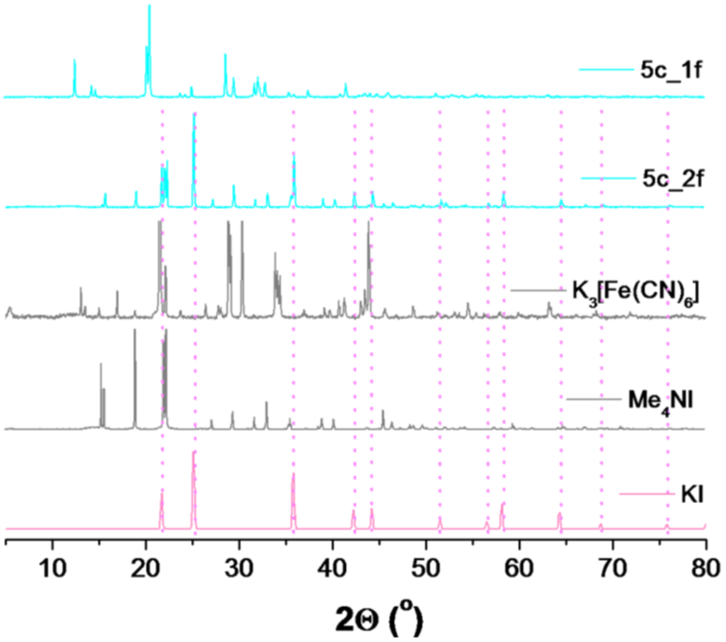

Figure 3.17. Powder X-ray diffractograms of the products **5c_1f** and **_2f** (in cyan), the starting reagents ($K_3[Fe(CN)_6]$ and Me_4NI - in gray) and the byproduct (KI - in soft pink).

To the best of our knowledge, the crystal structure of $(Me_4N)_3[Fe(CN)_6]$ has not been published yet and, consequently, cannot be compared with **5c_2f**. Several exhaustive searches were

---

[25] L. Ouahab, S. Bouhebour, J. P. Auffredic, D. Grandjean. J. Solid State Chem. 1989, 82, 139-145.” Tris-(tetraethylammonium) hexacyanoferrate (III): Stability of its hydrates and X-ray structure of the pentahydrate”.

[26] http://stage.cmc.com/msds/app/Default.aspx (Safety Data Sheet - potassium fluoroborate).

conducted in CSD and ICSD Karlsruhe, with 0 results. Nevertheless, it is believed that $(Me_4N)_3[Fe(CN)_6]$ or a new phase of stoichiometry $(Me_4N)_{3-x}K_x[Fe(CN)_6]$ has been obtained by this method.

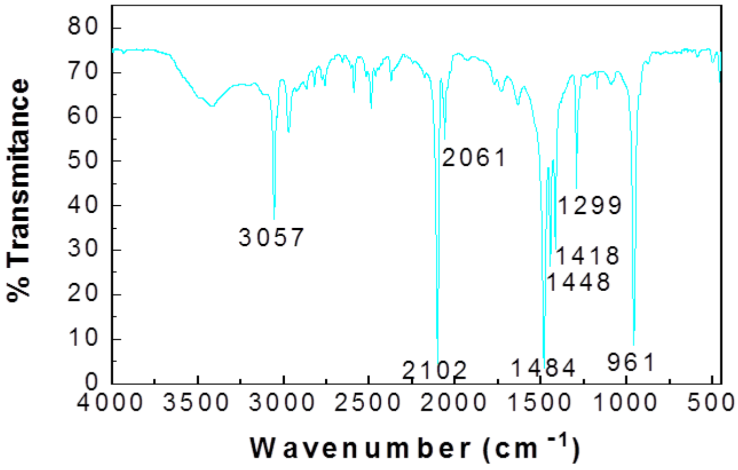

Figure 3.18. IR spectra of the product **5c_1f**, supposedly $(Me_4N)_3[Fe(CN)_6]$.

The infrared spectrum of **5c_1f,** presented above (Figure 3.18), confirmed the presence of the vibrational C-H bands and C-N bands of Me_4N^+ at the same position that they appear in the spectrum of Me_4NI. Besides, the shift of the -C≡N band from 2117 and 2076 cm^{-1} in the starting cyanide $K_3[Fe(CN)_6]$ to 2102 and 2061 cm^{-1} in **5c_1f** evinced the formation of a new cyanide species (see Table 3.3). EDX analysis conducted in the SEM revealed the presence of K (see Appendix, Figure A3.7), supporting the formation of a mixed ferrocyanide $(Me_4N)_{3-x}K_x[Fe(CN)_6]$ instead of $(Me_4N)_3[Fe(CN)_6]$.

Table 3.3. Principal IR bands observed in **5c_1f**, Me_4NI and $K_3[Fe(CN)_6]$.

	IR bands (cm^{-1})			
Fraction	ν(C-H), Me_4N^+	ν(C≡N), $[Fe(CN)_6]^{3-}$	δ(C-H), Me_4N^+	ν(C-N), Me_4N^+
5c_1f	3057	**2102,** 2061	1484, 1448, 1418	961
$K_3[Fe(CN)_6]$		2117, 2076		
Me_4NI[27]	3103		1484, 1403	946

3.1.2.5.1.4 $Ag_3[Fe(CN)_6]$

The last precursor that was attempted to prepare was $Ag_3[Fe(CN)_6]$. For this purpose, an aqueous solution containing 1 mmol of $K_3[Fe(CN)_6]$ was mixed with 3 mmols of $AgNO_3$ following the recipe described by Goodwin *et al.*[24]

---

[27] Spectral Database for Organic Compounds (SDBS). SDBS number – 3984 (Tetramethyl ammonium iodide).

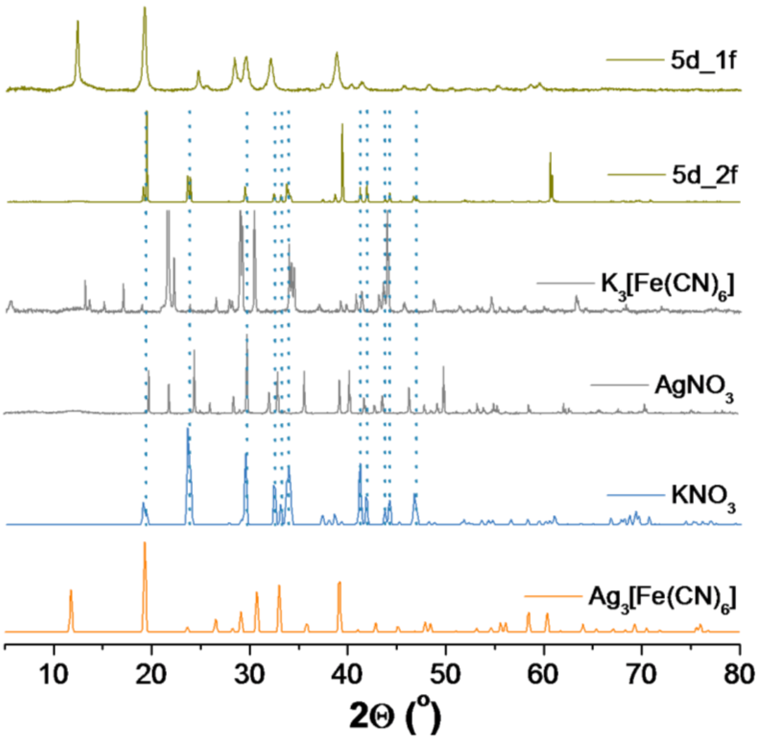

Figure 3.19. PXRD of the products **5d_1f** and **_2f** fraction (in dark yellow) the starting reagents (K$_3$[Fe(CN)$_6$] and AgNO$_3$ - in gray), the byproduct (KNO$_3$ - in blue) and the desired precursor Ag$_3$[Fe(CN)$_6$]. The Ag$_3$[Fe(CN)$_6$] X-ray diffractogram was simulated from the .cif file acquired from the ICSD Karlsruhe.[24]

No sign of the reactants was appreciated in the X-ray diffractograms of **5d_1f** and **5d_2f** (Figure 3.19). Although some signals are missing and new additional peaks are observed instead, the main reflections of **5d_1f** fitted mainly with those reported for Ag$_3$[Fe(CN)$_6$] by Goodwin,[24] as Figure 3.19 displays. The partial coincidence of the diffraction patterns led to think that, either a new compound different from Ag$_3$[Fe(CN)$_6$] had been obtained, or that the space group of the precursor here prepared was different from the trigonal *P* -3 1 *m* (162) described for Ag$_3$[Fe(CN)$_6$].[24] Meanwhile, the second fraction **5d_2f** was basically KNO$_3$, as demonstrated the matching reflections of both in Figure 3.19.

After drying the material at 80 ˚C under vacuum, its IR spectrum (see Figure 3.20) only presented a couple of -C≡N bands at 2168 and 2097 cm^{-1}, different from those of the cyanide precursor. This corroborated the formation of a new cyanide, most likely Ag$_3$[Fe(CN)$_6$], as the posterior EDX analysis carried out in the SEM seemed to confirm (see Annex A3.8).

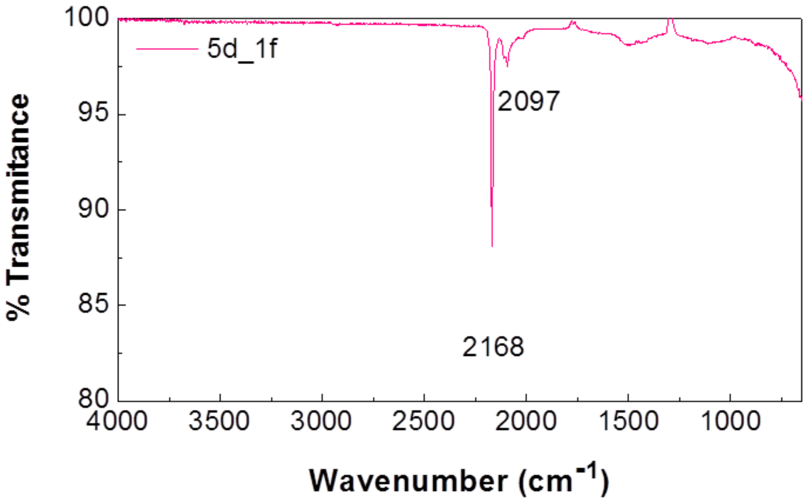

Figure 3.20. IR spectra of the product **5d_1f**, supposedly $Ag_3[Fe(CN)_6]$.

Summarizing the results of the precursor synthesis (step 1), it can be concluded that precursors $(Me_4N)_3[Fe(CN)_6]$ (actually $(Me_4N)_{3-x}K_x[Fe(CN)_6]$) and $Ag_3[Fe(CN)_6]$ prepared through routes **5c** and **5d** have been achieved as pure phases and could be used to go ahead with the second step of the reaction.

3.1.2.5.2 *Step 2. Synthesis and characterization of Ti-PBA*

Unlike step 1, all the reactions in the step 2 take place inside the glove box, as the resulting Ti-PBA is expected to be air- and H_2O-sensitive.

A couple of reaction conditions, at *R.T.* and in solvothermal conditions, were tested for both $(Me_4N)_3[Fe(CN)_6]$ (actually $(Me_4N)_{3-x}K_x[Fe(CN)_6]$) and $Ag_3[Fe(CN)_6]$ precursors.

3.1.2.5.2.1 Step 2. Reaction of the precursor $(Me_4N)_3[Fe(CN)_6]$

Synthesis in organic media

The addition of 0.23 mmol of $(Me_4N)_3[Fe(CN)_6]$ to 0.23 mmol of $TiCl_3$ in 25 ml of CH_3CN generated a greenish precipitate after 48 h of reaction at room temperature. The suspension was filtered and the precipitate was washed with CH_3CN and, subsequently, several times with MeOH with the purpose of eliminating the Me_4NCl byproduct. Finally, the product was dried under vacuum. The absence of color in the filtrate suggests that the second fraction was CH_3CN and thus it was eliminated. The X-ray diffractogram of the single fraction obtained, **5c_1f_step 2_organic**, is displayed in Figure 3.21.

Solvothermal synthesis

In the teflon body of a solvothermal autoclave, 0.23 mmol of $(Me_4N)_3[Fe(CN)_6]$ was mixed with 0.23 mmol of $TiCl_3$ in 20 mL of CH_3CN. The autoclave was then closed and transferred to an oven at 100˚ C. Elapsed 24 h, the autoclave was taken out from the oven, it was let to cool down naturally and was transferred again inside the glove box. After filtering the resultant suspension, washing the precipitate several times with CH_3CN and MeOH and finally drying it, a brown powder (**5c_1f_step 2_solvothermal**) was attained. Its X-ray diffraction pattern is shown in Figure 3.21.

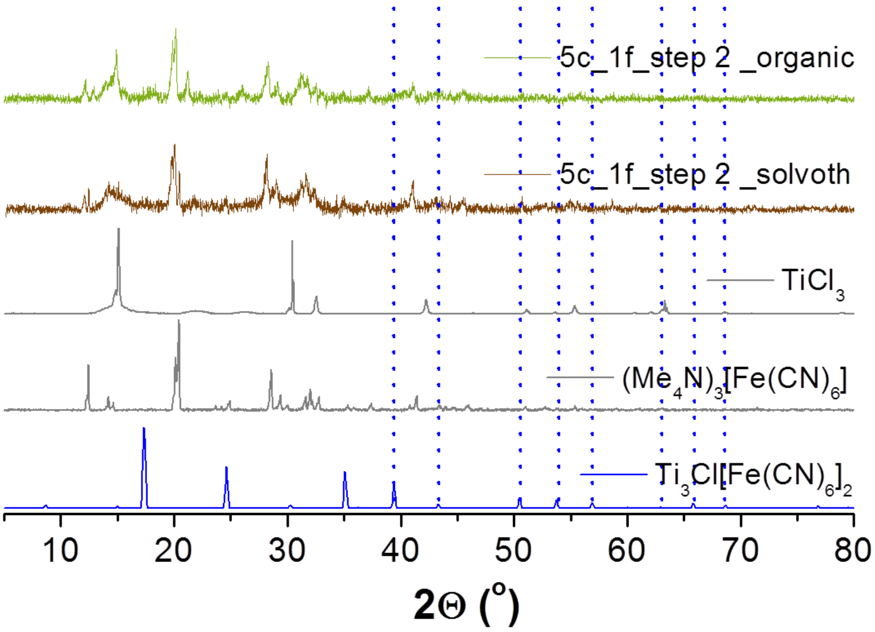

Figure 3.21. PXRD of the product **5c_1f_step 2_organic**, **5d_1f_step 2_solvoth**, the starting materials ($TiCl_3$ and $(Me_4N)_3[Fe(CN)_6]$ (actually $(Me_4N)_{3-x}K_x[Fe(CN)_6]$) and the product Ti-PBA. The diffractogram of the expected byproduct Me_4NCl is not here included, since it could not be found in the database.

The diffraction patterns of the materials obtained in this second step of reaction look similar, as it can be observed in Figure 3.21. Although some additional peaks can be observed, the diffractograms of **5c_1f_step 2_organic** and **_solvothermal** revealed mainly the presence of starting materials, $(Me_4N)_3[Fe(CN)_6]$ (actually $(Me_4N)_{3-x}K_x[Fe(CN)_6]$) and $TiCl_3$, indicating an incomplete reaction.

3.1.2.5.2.2 Step 2. Reaction of the precursor $Ag_3[Fe(CN)_6]$

Synthesis in organic media

For the synthesis performed in organic media with the silver precursor, 0.28 mmol of $Ag_3[Fe(CN)_6]$ were added to a solution of 0.28 mmol of $TiCl_3$ in 25 mL of CH_3CN. After reacting at

RT for 72 h, a green turquoise precipitate appeared in the medium. The compound was filtered, washed several times with CH_3CN and dried under vacuum. The absence of color in the filtrate suggests that the second fraction was CH_3CN and thus it was eliminated. The X-ray pattern of the single fraction **5d_1f_step 2_organic** (Figure 3.22) matches the reflections of the byproduct AgCl, showing no trace of starting reagents (see Annex A3.9). Since the AgCl salt is a white powder, the turquoise color should proceed from the formation of another phase, like Ti-PBA presumably. Nevertheless, no Prussian Blue reflection can be identified in the diffractograms. Conversely, there are broad reflections at 2Θ = 23.5, 30.27 and 40.96 ˚, that could not be assigned.

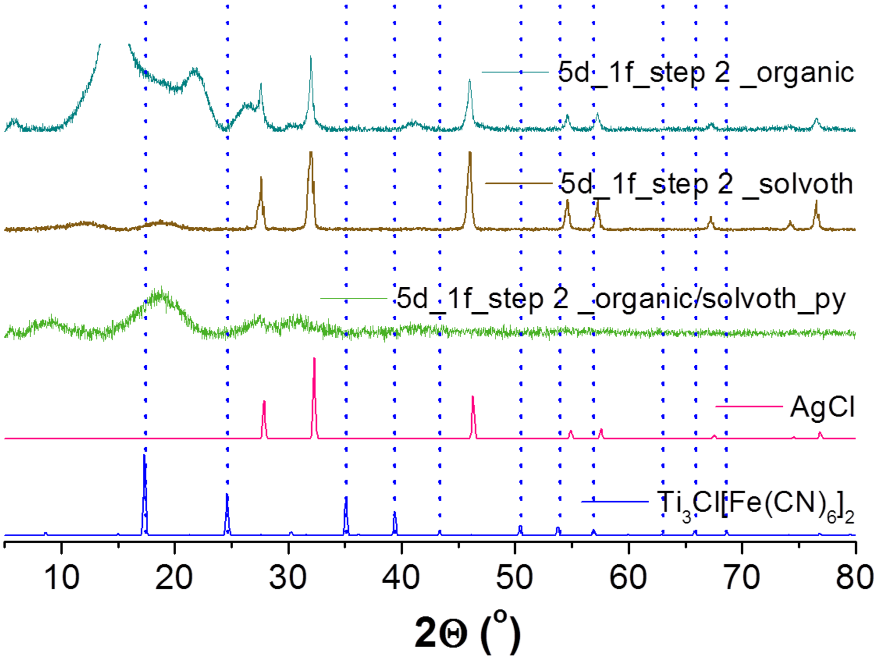

Figure 3.22. PXRD of the product **5d_1f_step 2_organic**, **5d_1f_step 2_solvoth**, **5d_1f_step 2_organic/solvoth_py** and the products AgCl and Ti-PBA.

Solvothermal synthesis

The reaction was also intended via solvothermal synthesis. In the teflon body of a solvothermal autoclave, 0.375 mmol of $Ag_3[Fe(CN)_6]$ is mixed with 0.375 mmol of $TiCl_3$ in 20 mL of CH_3CN. The autoclave is then closed and transferred to an oven at 100˚ C, in which the reaction occurred for 24 h. After this time, the device was taken out, was let to cool down and was transferred again inside the glove box. After filtering, washing several times with CH_3CN and drying, a brown precipitate is attained. Analysis of its X-ray data (see Figure 3.22, **5d_1f_step 2_solvoth**) also displays reflections coincident with those of AgCl.

To try to make sure that the formation of Ti-PBA is real and that its X-ray peaks are not hidden by the intensity of the crystalline AgCl or do not go unnoticed by its nanometric size, the materials (**5d_1f_step2_organic** and **5d_1f_step2_solvoth**) were washed several times with pyridine (py). AgCl is soluble in pyridine,[28] while Prussian Blue is not expected to dissolve in it. Only kapton signals are evident in the X-ray diffractogram of the resultant material, **5d_1f_step2_organic/solvoth_py**, as reveals Figure 3.22. EDX analysis acquired in the SEM suggested the formation of Ti-PBA, although also revealed the presence of AgCl (see Appendix, Figure A3.10).

3.1.2.6 *Trifluoroacetate route*

The last route intended to prepare Ti-PBA in organic media was based on the synthesis of the hexacyanotitanate (III) rather than the hexacyanoferrate used in the precedent routes (see equations (3.15) and (3.16)). The recipe was adapted from that described by Entley for the synthesis of $[Et_4N]_3[Ti^{III}(CN)_6]\cdot 4MeCN$.[29] In this case, all the steps were performed inside an argon-filled glove box (see Figure 3.23).

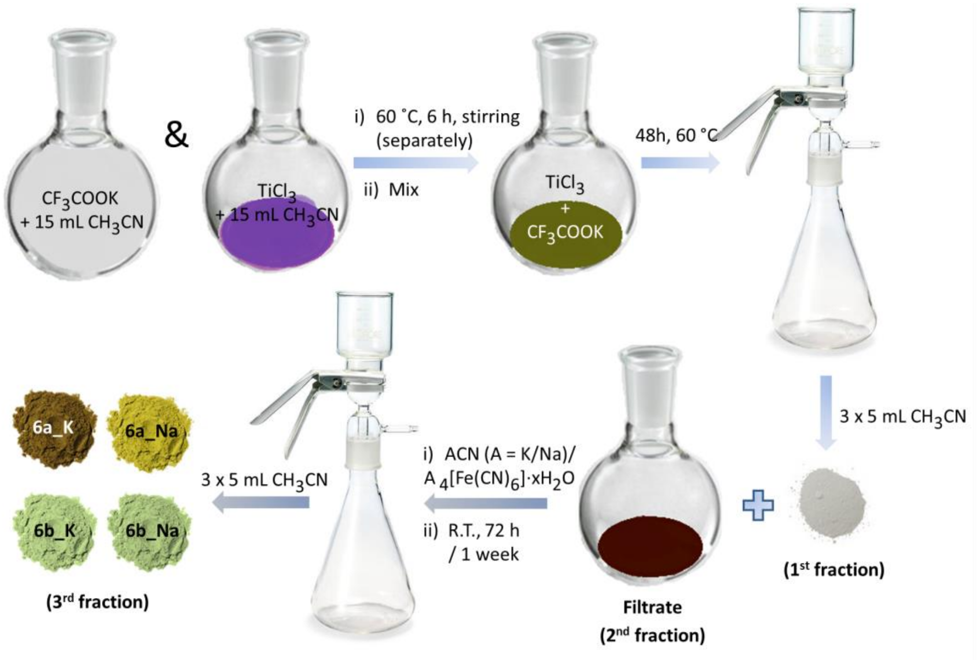

Figure 3.23. General schematic representation of the "trifluoroacetate" methodology for preparing the complexes **6a_K**, **6a_Na, 6b_K** and **6b_Na**.

In two different flasks, 0.43 mmol of $TiCl_3$ and 1.3 mmol of CF_3COOK are respectively dissolved in 15 mL of anhydrous CH_3CN. To favor the solubility of $TiCl_3$ was heated at 60 ˚C for 6h. Then, the consequent dark blue-violet suspension was mixed with the colorless transparent solution of CF_3COOK and was let to react during 48 h at 60 ˚C. The green-brownish suspension resultant was filtered, providing a white-greyish precipitate and a dark brown color filtrate. The white powder was

---

[28] http://periodic-table-of-elements.org/SOLUBILITY/silver_chloride

[29] W. R. Entley, C. R. Treadway, S. R. Wilson, G. S. Girolami. JACS 1997, 119, 6251 – 6258. "The Hexacyanotitanate Ion: Synthesis and Crystal Structure of $[NEt_4]_3[TiIII(CN)_6]\cdot 4MeCN$".

associated with the formation of KCl, as later confirmed by PXRD. Despite the efforts, the second fraction corresponding to the filtrate could not be isolated. Nevertheless, the reaction was continued by adding the theoretical stoichiometric amount of cyanide ACN or $A_4[Fe(CN)_6]\cdot xH_2O$ (A = K, Na; x = 3 (if A = K), 10 (if A = Na)) to the filtrate, also in anhydrous CH_3CN. The mixture was kept at room temperature for 72 h or 1 week, accordingly, for ACN or $A_4[Fe(CN)_6]\cdot xH_2O$. Finally, the suspension was filtered and the precipitate was washed with anhydrous CH_3CN and dried under vacuum. Depending on the cyanide utilized, the color of the material obtained varied. A green-brownish precipitate (**6a_K**) was achieved if KCN was used. When NaCN was chosen, a brown-yellowish powder (**6a_Na**) was attained. While a pale green precipitate (**6b_K** and **6b_Na**) is obtained if a ferrocyanide is deployed. In all the cases, the filtrate was colorless and transparent, thereby attributed to soluble CF_3COOA (A= K, Na).

Figure 3.24 collects the diffraction patterns of the final products obtained in the reactions referred as **6a_K** and **6a_Na**. The analysis of the patterns belonging to **6a_K** and **6a_Na** shows no presence of any of the reactants ($TiCl_3$, CF_3COOK, KCN or NaCN) in them.

The main reflections of **6a_K** (Figure 3.24) appear at 2ϴ = 26.95, 27.77, 38.60, 40.03, 45.76, 47.80, 49.64, 55.77, 58.02, 63.54, 66.00, 73.35 ˚ and those for **6a_Na** do it at 29.81, 30.38, 31.20, 43.09, 44.89, 51.07, 53.32 and 55.97 ˚. Both products (**6a_K** and **6a_Na)** were expected to be $A[Ti(CN)_6]$ (A = K, Na), but due to the non-availability of the crystalline structure for these complexes, it couldn´t be checked.

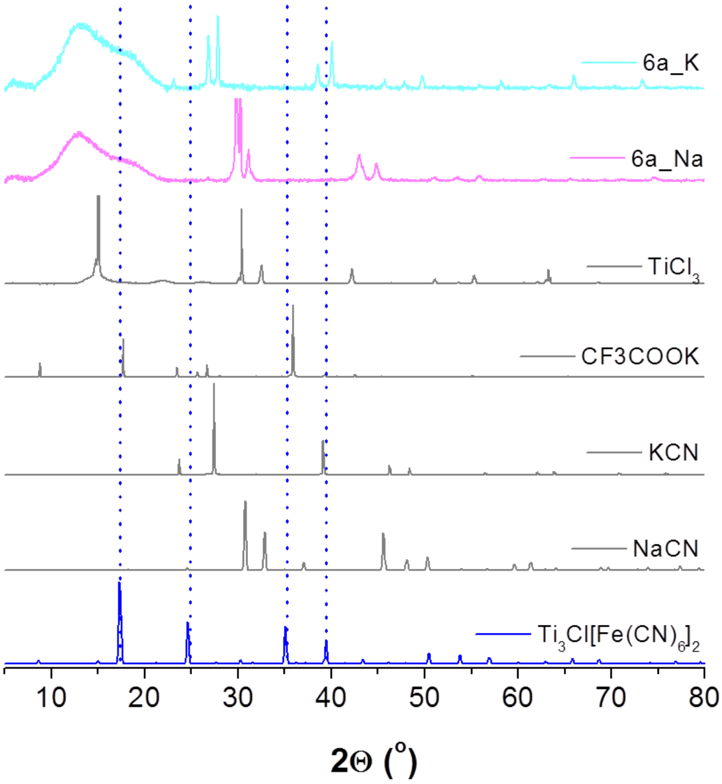

Figure 3.24. X-ray diffractograms of the products **6a_K** (pale blue), **6a_Na** (pale pink) and the starting reagents ($TiCl_3$, CF_3COOK, KCN and NaCN - in gray).

The powder X-ray diffractograms of the final products achieved through reactions **6b_K** and **6b_Na** are displayed in Figure 3.25. No trace of any of the reactants is encountered in **6b_K**. In contrast, the reflections of **6b_Na** perfectly fitted to $Na_4[Fe(CN)_6]\cdot 10H_2O$, indicating an absolute lack of reaction between the filtrate (presumably $Ti(OOCCF_3)_3$ and $Na_4[Fe(CN)_6]\cdot 10H_2O$). On the other hand, the compounds **6b_K** and **6b_Na** supposedly would provide Ti-PBA. However, the reflections of a Prussian blue type structure are not present in the diffractogram of **6b_K** and, as it have just been mentioned, **6b_Na** corresponds to unreacted $Na_4[Fe(CN)_6]\cdot 10H_2O$. EDX analysis performed in the SEM, revealed that no Ti is present in the material **6b_K** (see Annex A3.11). Therefore, we can sentence that Ti-PBA is not reached when ferrocyanides are used.

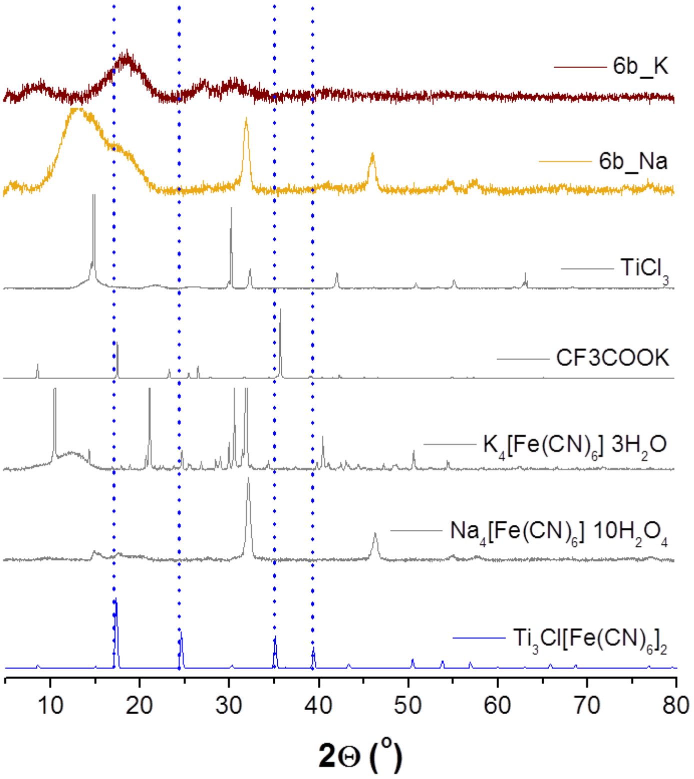

Figure 3.25. X-ray diffractograms of products **6b_K** (wine), **6b_Na** (mustard) and the starting reagents ($TiCl_3$, CF_3COOK, $K_4[Fe(CN)_6]\cdot 3H_2O$ and $Na_4[Fe(CN)_6]\cdot 10H_2O$ - in gray).

The IR absorption spectra partially unveiled the doubt regarding the formation of $A[Ti(CN)_6]$ compound in routes **6a_K** and **6a_Na**. As Figure 3.28 reveals, there is no -C≡N band in any of the complexes **6a_K** and **6a_Na**, suggesting that the species $A[Ti(CN)_6]$ have not been generated. It could happen that the -C≡N band was not visible in IR and it was only perceptible through Raman spectroscopy. However, the presence of a couple of bands at ca. 1650 and 1090 cm^{-1} discard this option. The band at 1650 cm^{-1} is usually related to the vibrational mode of a carbonyl group (–C=O) and the band at 1086 cm^{-1} could be associated with the -C-O stretching band, what leads to think that **6a_K** and **6a_Na** still contain the trifluoroacetate phase $Ti(OOCCF_3)_3$. Since the diffractograms of both materials do not coincide, it cannot be the same species ($Ti(OOCCF_3)_3$) as it was suspected, but other species containing this $–COO^-$ fragment.

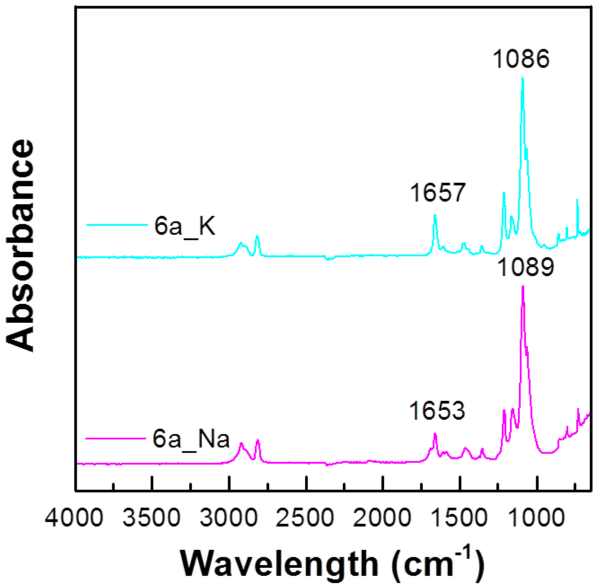

Figure 3.26. IR spectra of **6a_K** and **6a_Na** in the range of 4000 - 650 cm^{-1}. Unlike the previous, the IR measurements here presented were collected in absorption mode using a spectrometer placed inside an argon-filled glove box.

EDX analyses of the samples suggests that **6a_K** could be most likely composed of a mixture of $(CF_3COO)_3Ti$ and KCl residual (see Appendix, Figure A3. 12), whereas the composition of **6a_Na** is not so clear (see Appendix, Figure A3.11).

To conclude the indirect synthesis section, it can be stated that Ti-PBA could not be achieved via the trifluoroacetate route. Instead, it could be obtained by using $Ag_3[Fe(CN)_6]$ as precursor. Regrettably, the Ti-PBA phase was contaminated with AgCl, what discards it for electrochemical purposes.

3.2 Prussian Blue (Na-PB and K-PB)

3.2.1 Scope

For practical and simplistic reasons, that includes easiness of synthesis, low price and abundance of the element that composes it, the more appealing Prussian Blue phase is the Prussian Blue itself. It is ideally formulated as $KFe[Fe(CN)_6]\cdot xH_2O$ (abbreviated as K-PB hereinafter) and it is a compound based purely on iron, making it the most sustainable and environmentally benign among all the PBA. Apart from K-PB, and with the objective of avoiding a possible competition between the cations in the insertion/extraction process when it is cycled vs. Na, the K^+ cation located in the cavities would also be substituted by Na^+. Consequently, $AFe[Fe(CN)_6]$ (A = Na, K) was established as the target material. These materials will have a dual purpose. On the one hand, to serve as a comparison with the Ti-PBA in the anodic range. On the other hand, to explore the competitiviness of the sodiated compound at high voltages in NIB.

3.2.2 Synthesis

The synthesis of sodium/potassium Prussian Blue (abbreviated as A-PB from now on) was carried out by co-precipitation method, following the general recipe described by Weiser as early as 1942.[30] All chemicals were of analytical reagent and ACS grade and were used without further purification. The preparation of A-PB (A = Na, K) is straightforward. In a typical experiment, 100 mL of a freshly prepared pale yellow $K_4[Fe(CN)_6]\cdot 3H_2O$ or $Na_4Fe(CN)_6\cdot 10H_2O$ (40mM) aqueous solution was mixed with 100mL of a yellow-orange $FeCl_3\cdot 6H_2O$ (40 mM) aqueous solution. Deionized water was used in both cases.

As soon as the two solutions came in contact, a blue ink color suspension containing A-PB was formed in excess of sodium or potassium ions according to the reaction of equations (3.17) and (3.18). The small $A_{1-x}Fe^{3+}_{1+(x/3)}[Fe^{II}(CN)_6]\cdot yH_2O$ (A = Na, K) particles resisted centrifugation at 4000 rpm during 10 min and it was necessary to force its precipitation by adding ethanol and centrifuging again at higher speed for longer time (10000 rpm, 15´). Finally, after filtering for 6-12 hours, washing with ethanol (3 x 10 mL) and drying, dark blue crystal-like aggregates of “soluble” Prussian Blue[31] were obtained (see Figure 3.27).

$$(1 + (x/3))\ FeCl_3 + Na_4[Fe(CN)_6]\cdot 10H_2O \xrightarrow[R.T.]{H_2O} Na_{1-x}Fe^{3+}_{1(x/3)}[Fe^{II}(CN)_6]\cdot yH_2O + (3 + x)\ NaCl \qquad \textbf{(3.17)}$$

$$(1 + (x/3))\ FeCl_3 + K_4[Fe(CN)_6]\cdot 3H_2O \xrightarrow[R.T.]{H_2O} K_{1-x}Fe^{3+}_{1(x/3)}[Fe^{II}(CN)_6]\cdot yH_2O + (3 + x)\ KCl \qquad \textbf{(3.18)}$$

It is important to mention that, unlike the Ti-PBA, the A-PB materials (A = Na, K) are air-stable, what facilitates its handling.

---

[30] H. B. Weiser, W. O. Milligan, J. B. Bates. *J. Phys. Chem.* 1942, **46** (1), 99-111. “Thermal decomposition of Prussian blue under inert atmosphere”.

[31] K. Itaya, I. Uchida. *Acc. Chem. Res.* 1986, **19**, 162-168. “Electrochemistry of polynuclear transition metal cyanides: Prussian blue and its analogues”.

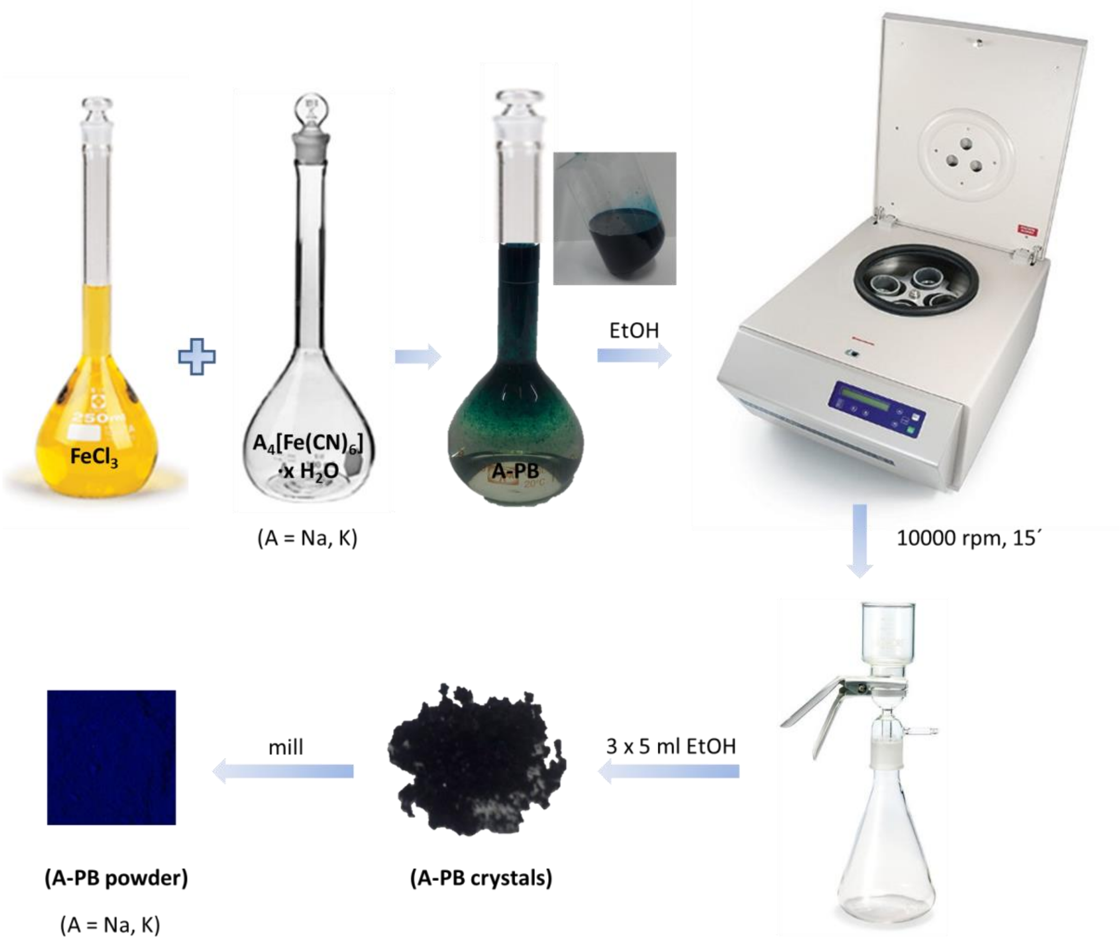

Figure 3.27. Schematic synthesis procedure for preparing A-PB, $A_{1-x}Fe^{3+}_{1+(x/3)}[Fe^{II}(CN)_6]\cdot yH_2O$ (A = Na, K).

3.2.3 Structural, morphological and physico-chemical characterization

3.2.3.1 *Powder X-ray diffraction*

The formation of A-PB (A = Na, K) was confirmed by PXRD, as Figure 3.28 illustrates. The patterns of A-PB are absolutely coincident to the Prussian Blue structure reported in the literature[30] and so it is corroborated by the Rietveld refinement of the PXRD data of A-PB shown in Figure 3.29. Both compounds crystallize in space group *Fm*-3*m* and the fitting results in a lattice parameter a = 10.2227(1) Å for Na-PB and a = 10.19(2) Å for K-PB. These values are close to the 10.21 Å reported for high quality Na-PB[32] and the 10.151 Å typically observed for K-PB[33]. Agreement factors were, respectively, R_B = 2.92, R_F = 3.88 and x^2 = 16.4 for Na-PB and R_B= 26.98, R_F= 24.86 and χ^2=11.1 for K-PB (see Appendix, Tables A3.1 and A3.3 for further details). The broadening of the reflections suggests the formation of nanoparticles or large

---

[32] Y. You, X-L. Wu, Y-X. Yin, Y-G. Guo. Energy Environ. Sci. **2014**, 7, 1643-1647. “High-quality Prussian blue crystals as superior cathode materials for room-temperature sodium-ion batteries”.

[33] W. Lu, L. Wang, J. Cheng and J. B. Goodenough. Chem. Comm. **2012**, 48, 6544-6546. “Prussian blue: a new framework of electrode materials for sodium batteries”.

strains, being the former most likely as a consequence of the fast nucleation occurring when the reaction takes place instantaneously at room temperature. A crystallite size of 13.5 for Na-PB and 6.5 nm for K-PB can be deduced from the refinement of the PXRD data.

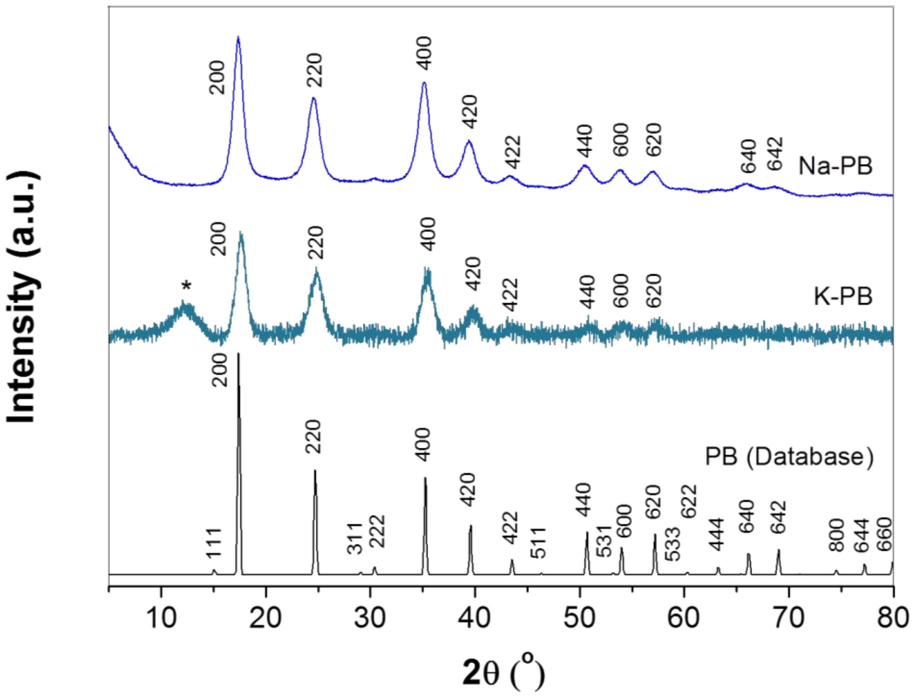

Figure 3.28. PXRD patterns of the synthesized Na-PB and K-PB and its comparative with the Prussian Blue $KFe^{3+}[Fe^{II}(CN)_6]$ (PB) listed in ICSD Karlsruhe Database (nº 162081). The Kapton® film peak has been marked with an asterisk (*).

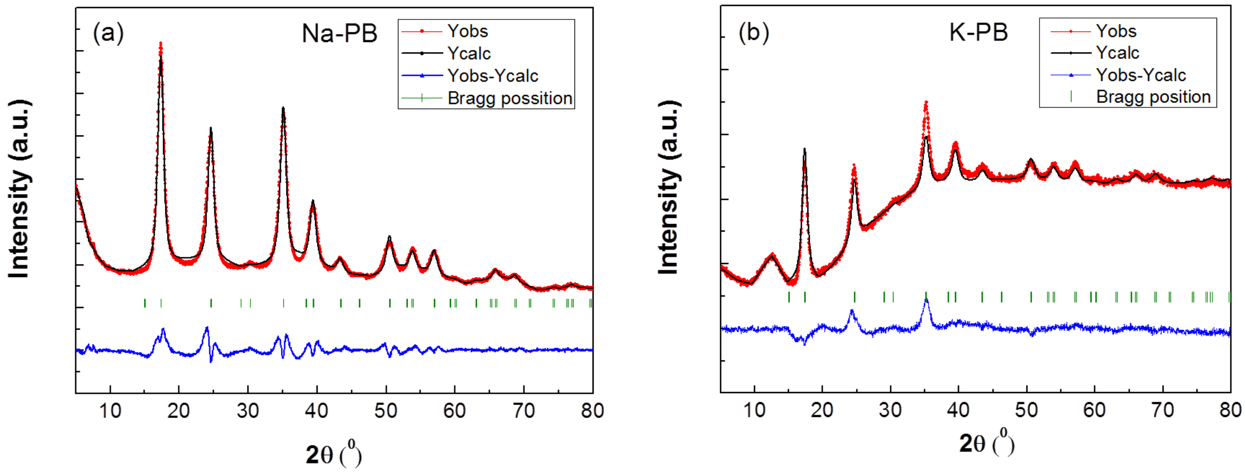

Figure 3.29. Rietveld refinement fitting the X-ray diffractogram of Na-PB (a) and K-PB (b) to the PXRD pattern of the Prussian blue reported in the literature, listed in ICSD Karlsruhe Database (nº 160281).[34] Experimental (black) and calculated (red) patterns are shown along with the difference curve (blue) and the Bragg positions (green).

---

[34] Bueno P.R., Ferreira F. F., Giménez-Romero D., setti G. O, Faria R. C., Gabrielli C., Perrot H., García-Jareño J. J., Vicente F. *J. of Physical Chemistry C* 2008, **112**, 13264-13271. "Synchrotron Structural Characterization of Electrochemically Synthesized Hexacyanoferrates Containing K^+: A Revisited Analysis of Electrochemical Redox".

3.2.3.2 *Infrared Spectroscopy*

Infrared data were collected in absorption mode. The spectra (see Figure 3.30 a, b) exhibited a strong characteristic cyanide stretching band ν(-C≡N) that appears at 2076 cm^{-1} for Na-PB and at 2074 cm^{-1} for K-PB, whose values are shifted with respect to the cyanide precursors position (Table 3.4). Moreover, the IR spectra reveal no trace of residual EtOH from washing the material, since no C-H vibration bands are observed. Instead, H_2O presence is appreciated, as reflects the wide stretching vibrational band ν(-O-H) centered at ~ 3450 cm^{-1} and the deformation band δ(-O-H) at 1615-1610 cm^{-1}.

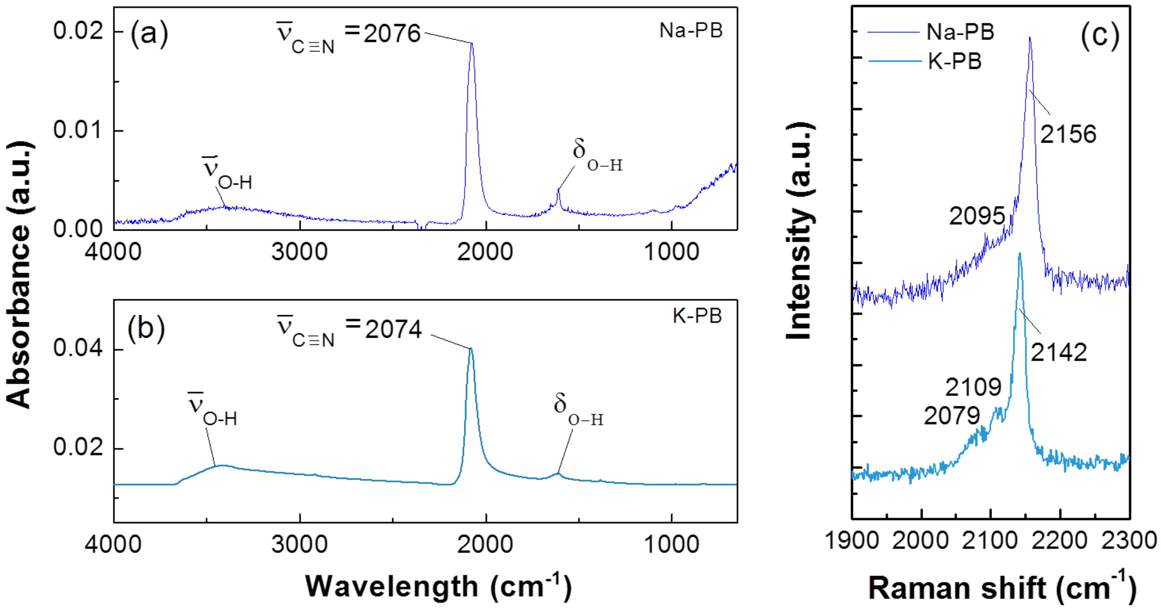

Figure 3.30. Infrared spectra of Na-PB (a) and K-PB (b), labelling the most characteristic absorption bands and c) Raman spectra of Na-PB and K-PB.

Table 3.4. Principal IR bands observed in Na-PB, K-PB and their corresponding cyanide precursors, $Na_4[Fe(CN)_6]\cdot 10H_2O$ and $K_4[Fe(CN)_6]\cdot 3H_2O$.

Compound	**IR bands (cm^{-1})**
Na-PB	3450 ν(O-H), 1610 δ(O-H) – H_2O **2076** ν(-C≡N) – $NaFe[Fe(CN)_6]$
K-PB	3400 ν(O-H), 1615 δ(O-H) – H_2O **2074** ν(-C≡N) – $NaFe[Fe(CN)_6]$
$Na_4[Fe(CN)_6]\cdot 10H_2O$[35]	2020, 2000 ν(-C≡N) – $[Fe(CN)_6]^{2-}$
$K_4[Fe(CN)_6]\cdot 3H_2O$[36]	2043 ν(-C≡N) – $[Fe(CN)_6]^{2-}$

---

[35] F. A. Miller, C. H. Wilkins. *Anal. Chem.* 1952, **24** (8), 1253–1294 - page 1258. “Infrared Spectra and Characteristic Frequencies of Inorganic Ions”.

[36] L. Xia, R.L. McCreery, *J. Electrochem. Soc.* 1999, **146**, 3696-3701. “Structure and Function of Ferricyanide in the Formation of Chromate Conversion Coatings on Aluminum Aircraft Alloy”.

3.2.3.3 Raman Spectroscopy

Raman spectra of pristine Na-PB and K-PB, collected in the characteristic region of the -C≡N stretching band, is depicted in Figure 3.30c. A main band is clearly distinguished at 2156 cm^{-1} along with a shoulder that emerge at 2095 cm^{-1} in the spectrum of Na-PB. In the case of K-PB, a main band at 2142 cm^{-1} and a couple of shoulders at 2109 and 2079 cm^{-1} are observed. This distinctive profiles resemble those that have already been detailed for Prussian blue.[37] The change of alkali results however in different scattering frequency position and relative intensities. Red shift on the bands when contrasting Na-PB to K-PB agrees with IR results and could be indicative of the C≡N bond softening due to the larger ionic radii of K ions.

3.2.3.4 Thermogravimetric analysis

To calculate the water content present in both compounds, thermogravimetric curves up to 325°C were measured in N_2 atmosphere heating at a speed of 10 C·min^{-1} (see Figure 3.31). For Na-PB, two different losses, amounting 18% of the total mass, were observed at 80˚C and 210˚C. These losses corresponded to 2.7 H_2O and 0.7 H_2O molecules which could be respectively ascribed to removable physisorbed and interstitial zeolitic water, [38] resulting in a total of 3.4 H_2O detected in the structure of Na-PB. In the case of K-PB, two different losses were appreciated at 80 ˚C and 125 ˚C, equivalent to 1 H_2O and 1.73 H_2O molecules associated to physisorbed and zeolitic water, similarly to Na-PB.[38] The total water amount present in the structure of K-PB was therefore of 2.73 H_2O molecules.

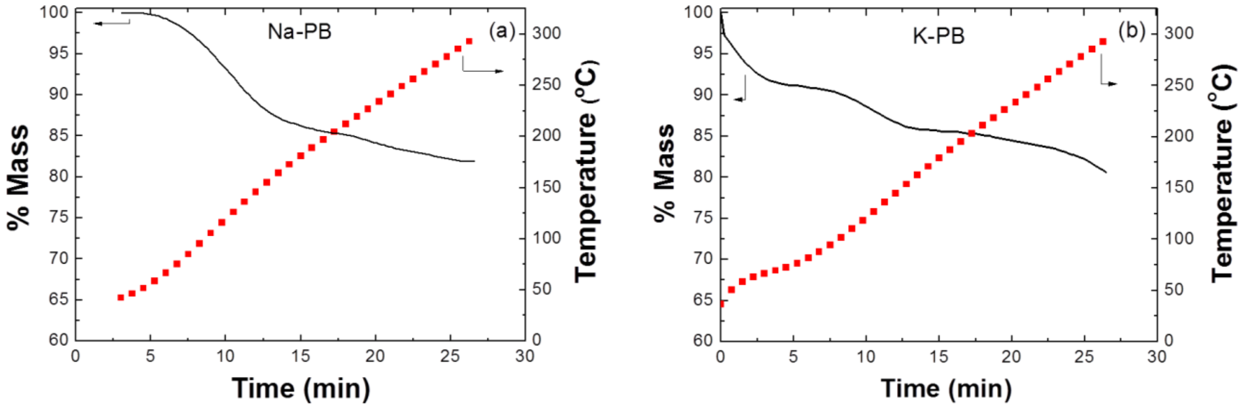

Figure 3.31. Thermogravimetric analysis of pristine a) Na-PB and b) K-PB, scanned from 30 to 325 °C using N_2 atmosphere and a temperature step of 10 C·min^{-1}.

---

[37] R. Mazeikiene, G. Niaura, A. Malinauskas. *J. Electroanalytical Chemistry* 2011, **660**, 140–146. "Electroanalytic reduction of hydrogen peroxide at Prussian blue modified electrode: An in situ Raman spectroelectrochemical study".

[38] N. Imanishi, T. Morikawa, J. Kondo, Y. Takeda, O. Yamamoto, N. Kinugasa, T. Yamagishi. *J. Power Sources* 1999, **79**, 215-219. "Lithium intercalation behavior into iron cyanide complex as positive electrode of lithium secondary battery"

3.2.3.5 *Electron microscopy (SEM, TEM)*

SEM images showed a non-homogeneous particle size distribution in both materials. In Na-PB (Figure 3.32a), it varies from ca. 500 nm to 30 µm, in contrast to the 13.5 nm calculated by the Debye-Scherrer equation from the width of the PXRD reflections. An average value of 272 nm was obtained by measuring the size of a representative number of samples (100 particles) taken from a SEM picture. The resulting histogram is collected in Figure 3.32b. The particle size of K-PB however ranges between approx. 1 µm and 50 µm (Figure 3.32c). In any case, aggregation of nanocrystalline domains into larger microparticles seemed to occur in the two Prussian Blue phases, as proven by TEM. HRTEM images revealed the presence of ca. 5 nm crystalline domains in K-PB (Figure 3.32c), what agrees with the particle size deduced from the refinement of the PXRD data. These nanoparticles exhibited lattice fringes of 5.05 Å corresponding to half of the unit cell (a = 10.19(2) Å). Besides, the rings in the electron diffraction pattern (Figure 3.32d) perfectly fitted to the main crystallographic planes of the Prussian Blue structure: 200, 220, 222 and 400.

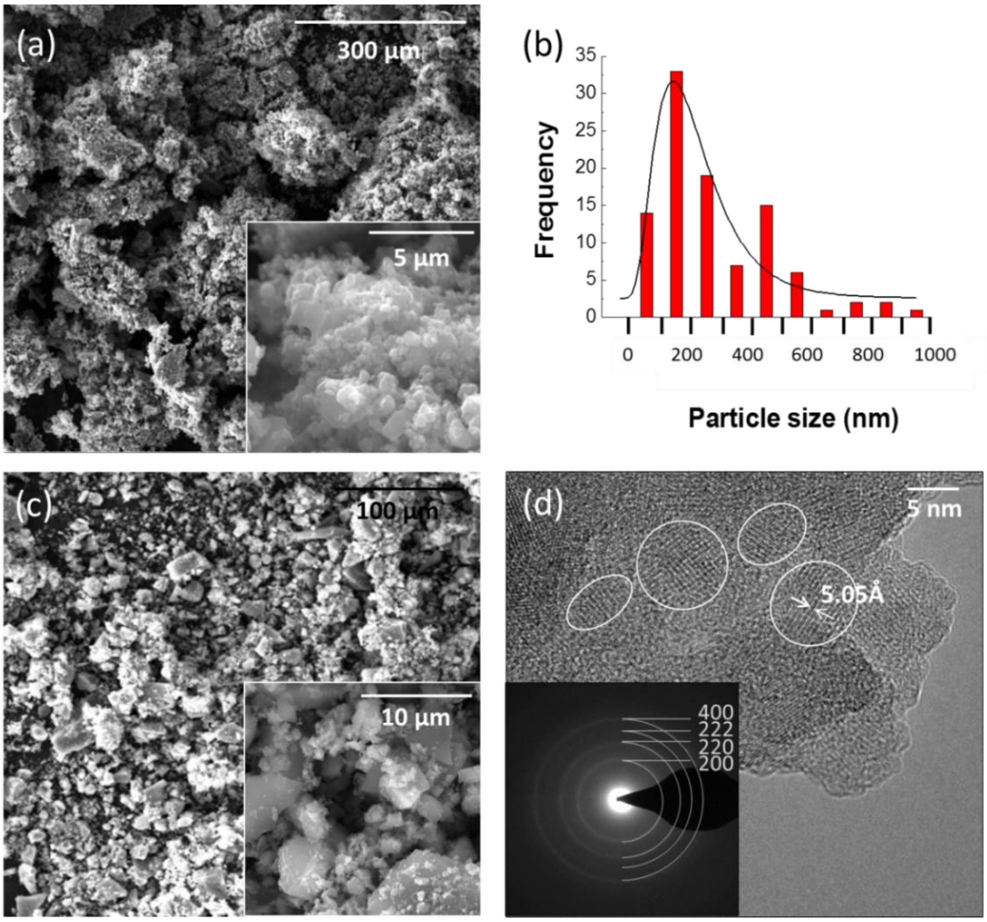

Figure 3.32. SEM images of a) Na-PB at 2 different magnifications (note the different scale in the SEM inset micrograph) and b) histogram of the Na-PB particle size distribution of a representative sample (100 particles). SEM images of c) K-PB at 2 different magnifications and d) TEM image of K-PB domains and (inset) electron diffraction pattern of K-PB nanocrystals with crystallographic planes indexed.

3.2.3.6 *Determining the materials composition.*

Semi-quantitative EDX analysis provided an estimated 1:2 A: Fe ratio for A-PB (A = Na, K). A chemical formula ca. $Na_{0.81}Fe[Fe(CN)_4]$ was calculated for Na-PB while $KFe[Fe(CN)_6]$ was yielded for K-PB, assuming a C/N ratio of one. As example, K-PB EDX analysis is here shown in Figure 3.33. As a consequence of making the analysis using a lacey carbon film on which the particles are held, the carbon signal is enhanced and only the nitrogen signal can be quantified as coming from K-PB. In addition, some residual chlorine (Cl) is detected (Cl: K ≈ 0.1) in K-PB but no trace of it is encountered in Na-PB, what let to assert that the products obtained are A-PB and discard the formation of a chlorine containing derivative, as for example $A_2Fe[Fe(CN)]_6Cl{\cdot}yH_2O$.

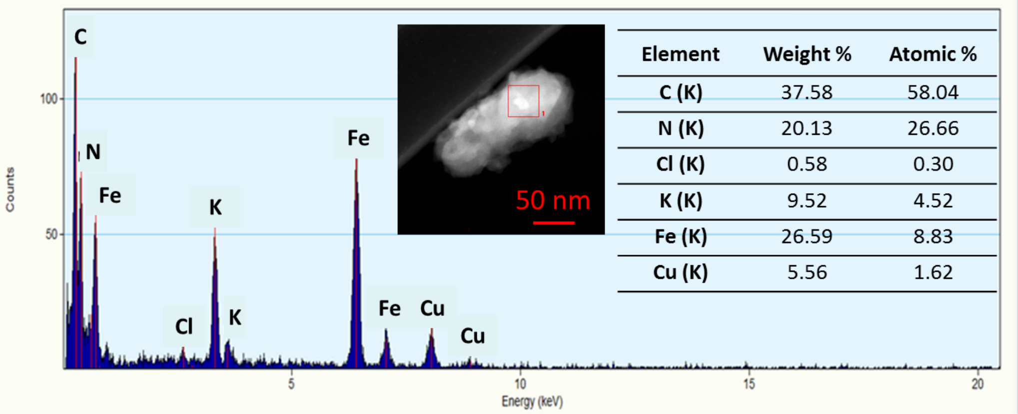

Element	Weight %	Atomic %
C (K)	37.58	58.04
N (K)	20.13	26.66
Cl (K)	0.58	0.30
K (K)	9.52	4.52
Fe (K)	26.59	8.83
Cu (K)	5.56	1.62

Figure 3.33. EDX analysis of pristine K-PB.

The exact composition of the materials, nevertheless, was determined by atomic absorption spectroscopy (AAS) or atomic emission spectroscopy (AES) and was further confirmed by elemental analysis (H, C, N). AAS provided a Na: Fe ratio of 0.7187: 2 or, according to the terminology presented, Na: Fe equal to 0.75: 2.08 (see Table 3.5). The molecular formula achieved was thus $Na_{0.75}[Fe_{2.08}(CN)_6]{\cdot}3.4H_2O$. On the other hand, AES afforded a K: Fe ratio of 0.86: 2 or, according to the terminology used above, of 0.88: 2.04 (see Table 3.6). Therefore, the molecular formula attained was $K_{0.88}[Fe_{2.04}(CN)_6]{\cdot}2.7H_2O$. In both cases, the elemental analysis (H, C, N) supported the formulas obtained (see Table 3.7).

Table 3.5. AAS results of the sample Na-PB.

Compound	**Na** (mg/L)	**RSD (%)**	**Fe** (mg/L)	**RSD (%)**
Na-PB	2.9	9.4	19.6	2.5

Table 3.6. AES results of the K-PB sample.

Compound	**K** (mg/L)	**RSD (%)**	**Fe** (mg/L)	**RSD (%)**
K-PB	5.4	7.4	17.9	0.9

Table 3.7. Elemental analysis (H, C, N) of A-PB (A = Na, K). Experimental values are presented first while theoretical values are included in parentheses

Compound	% N	% C	% H
Na-PB	20.18 (21.53)	18.96 (18.46)	2.80 (2.32)
K-PB	21.44 (21.18)	17.95 (18.15)	1.80 (1.83)

3.2.3.7 *X-ray Photoelectron Spectroscopy (XPS)*

XPS analysis at the Fe 2p edge was performed on A-PB (A = Na, K) and their spectra are shown in Figure 3.34. The Fe 2p region has two split orbit components $2p_{3/2}$ and $2p_{1/2}$ with maxima at 709 and 722 eV, coincident with those previously reported for low spin Fe^{II} of $[Fe(CN)_6]^{4-}$ in Prussian Blue species.[39, 40] The presence of a small peak at ca. 713 eV in K-PB has been assigned in the literature either to high spin Fe^{3+},[40, 41] despite the intensity is not as large as that of the Fe^{II} signal, or to Fe^{2+} bonded to oxygen,[42] as a consequence of the presence of water molecules.

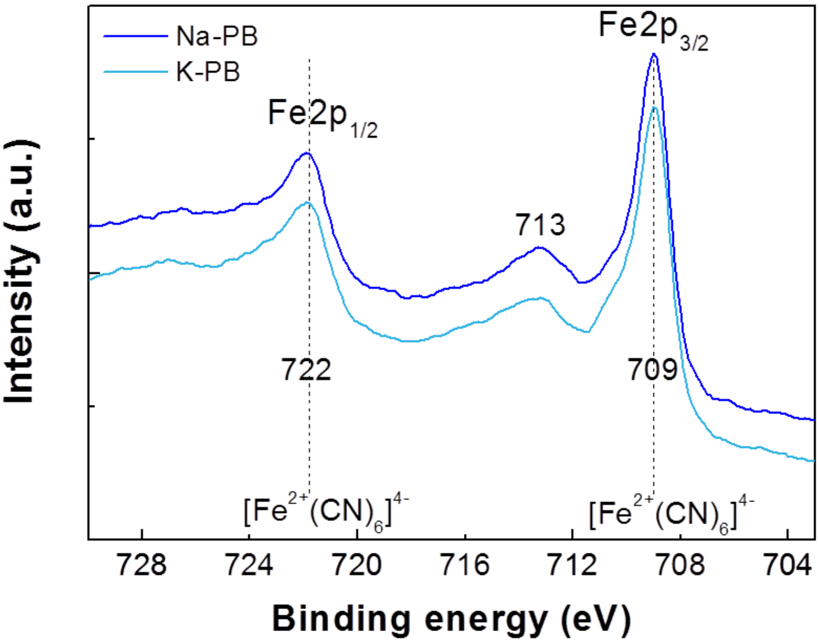

Figure 3.34. XPS spectra of Na-PB and K-PB at the Fe 2p edge.

---

[39] M. Datta, A. Datta. *J. Phys. Chem*. 1990, **94**, 8203–8207. "In situ FTIR and XPS studies of the hexacyanoferrate redox system".

[40] Q. Wu, G. Wu, L. Wang, W. Hu, H. Wu. *Mat. Sci. in Semicond. Process* 2015, **30**, 476-481. "Facile synthesis and optical properties of Prussian Blue microcubes and hollow Fe_2O_3 microboxes".

[41] E. Desimoni, B. Brunetti. *Chemosensors* 2015, **3**, 70-117. "X-Ray Photoelectron Spectroscopic Characterization of Chemically Modified Electrodes Used as Chemical Sensors and Biosensors: A Review".

[42] X. Li, J. Liu, A. I. Rykov, H. Han, C. Jin, X. Liu. *App. Catalysis B Environm.* 2015, **179**, 196-205. "Excellent photo-Fenton catalysts of Fe–Co Prussian blue analogues and their reaction mechanism study".

3.2.3.8 *Mössbauer Spectroscopy*

Mössbauer spectra of A-PB (A = Na, K) was registered at room temperature (see Figure 3.35). Each spectrum could be deconvoluted into a singlet absorption peak and a doublet absorption peak, which were respectively attributed to the low spin (LS) Fe^{II} covalently bonded to C and the high spin (HS) Fe^{3+} bonded to N. Their isomer shift (δ) and quadrupolar splitting (Δ) values are reflected in Table 3.8 and are in good agreement with those reported in the literature.[43] The intensity ratio between the two kinds of iron Fe^{II} and Fe^{3+}, is also listed in the Table 3.8. The resulting ratio of Fe^{3+}/ Fe^{II} turned out to be 1.269 and 1.326 accordingly, for Na-PB and K-PB, which is very close to the expected 1.33 (considering a 25% of $[Fe(CN)_6]^{4-}$ defects).[34]

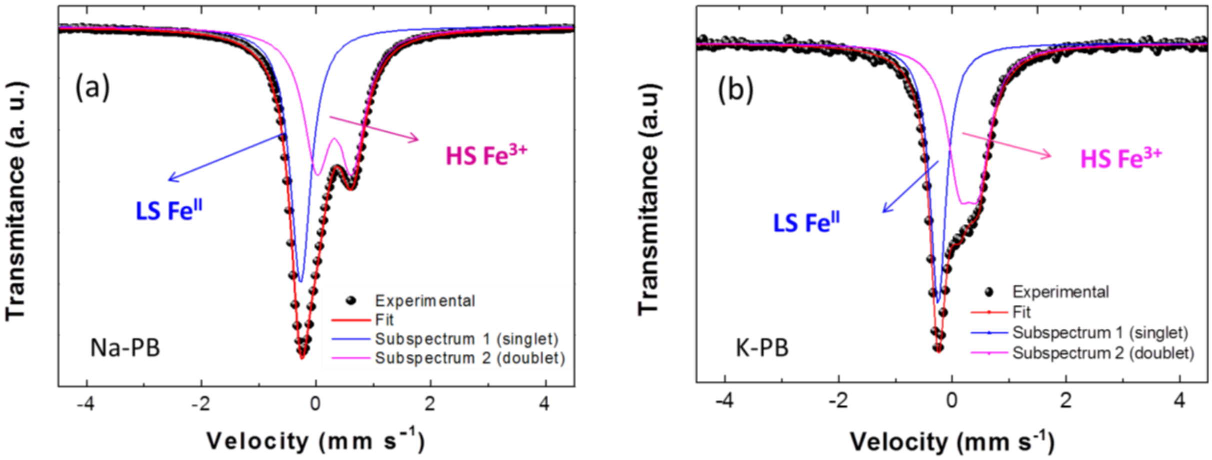

Figure 3.35. Mössbauer spectra of a) Na-PB and b) K-PB. Experimental (black dots) and fitting (red line) are shown along with the blue and pink solid lines that represent the LS Fe^{II} and HS Fe^{3+} spectral components, respectively.

Table 3.8. Values of parameters **δ**, **Δ** and **Fe ratio** extracted from the Mössbauer fitting for iron in K-PB **(δ** = isomer shift relative to Fe bcc, **Δ** = quadrupolar splitting).

Compound	Assignation	Isomer Shift, δ ($mm{\cdot}s^{-1}$)	Quadrupolar, Δ ($mm{\cdot}s^{-1}$)	Fe ratio
$Na_{1-x}Fe^{3+}_{(x+1/3)}[Fe^{II}CN_6]$	LS Fe^{II}	-0.116(1)	0	44.08 %
	HS Fe^{3+}	0.422(1)	0.619(1)	55.92 %
$K_{1-x}Fe^{3+}_{(x+1/3)}[Fe^{II}CN_6]$	LS Fe^{II}	-0.255(1)	0	42.99 %
	HS Fe^{3+}	0.397(4)	0.340(3)	57.01 %

It has been demonstrated through several characterization techniques (PXRD, IR, TEM, Raman, XPS and Mössbauer) that A-PB (A = Na, K) here obtained are pure phases. Consequently, both of them will be electrochemically studied to determine its suitability as electrodic materials.

---

[43] L. Samain, F. Granjean, G. J. Long, P. Martinetto, P. Bordet and D. Strivay. *J. Phys. Chem C* 2013, **117** (19), 9693. "Relationship between the Synthesis of Prussian Blue Pigments, Their Color, Physical Properties, and Their Behavior in Paint Layers".

3.3 Prussian White (Na-PW and K-PW)

3.3.1 Scope

In previous section, the synthesis and characterization of purely iron based Prussian Blue phases (A-PB, A = Na, K) have been described. Even of more technological importance is its reduced alkali-rich phase Prussian White, $A_2M[M'(CN)]_6$ (A = alkali ion, M and M´= transition metals, M´ = typically Fe, sometimes M = M´) and so it has been evidenced by several PW phases investigated as low-cost cathode materials for SIB, in parallel with the development of this work. Unlike PB, PW has all the cubic cavities occupied by alkali ions thereby preventing first cycle inefficiencies and the need of providing an additional source of alkali ions in the anode. This section will address a new synthetic method to attain A-PW (A = Na, K), as well as a thorough physico-chemical characterization of both materials.

3.3.2 Synthesis

3.3.2.1 *Initial attempts*

In first instance, A-PW (A = Na, K) was prepared following the methodology reported by Jiang *et al*. to produce K-PW from a single $K_4Fe(CN)_6$ source. In a typical procedure (see Figure 3.36), either $K_4[Fe(CN)_6]\cdot 3H_2O$ or $Na_4[Fe(CN)_6]\cdot 10H_2O$ (40 mmol) was added to 25 mL of deaerated distilled water to form a homogeneous solution. The solution was then transferred into the teflon body of a stainless steel autoclave, that was sealed and maintained at 160 ˚C for 48 h.[44] Elapsed this time, the resultant suspension was filtered. The reddish precipitate obtained was washed with H_2O (3 x 5 mL) and CH_3COCH_3 (3 x 5 mL), and finally dried in a vacuum oven at 60˚C for 12 h.

Figure 3.36. Schematic synthesis procedure for preparing A-PW (A = Na, K), $A_{2-x}Fe^{2+}_{1+(x/2)}[Fe^{II}(CN)_6]\cdot yH_2O$, by hydrothermal method, following Jiang´s methodology.

As its name indicates, the Prussian White phase should present a white color. The fact that the precipitate presents a reddish color indicate the possible presence of impurities. If Jiang´s procedure is reproduced straightforward, the formation of some iron oxides is observed by PXRD together with the

---

[44] M. Hu, J. S. Jiang. *Mat. Res. Bull.* 2011, **46**, 702–707. “Facile synthesis of air-stable Prussian White Microcubes via hydrothermal method.”

desired A-PW (see Figure 3.37). The reflections due to iron oxides impurities have been labelled with red asterisks within the patterns.

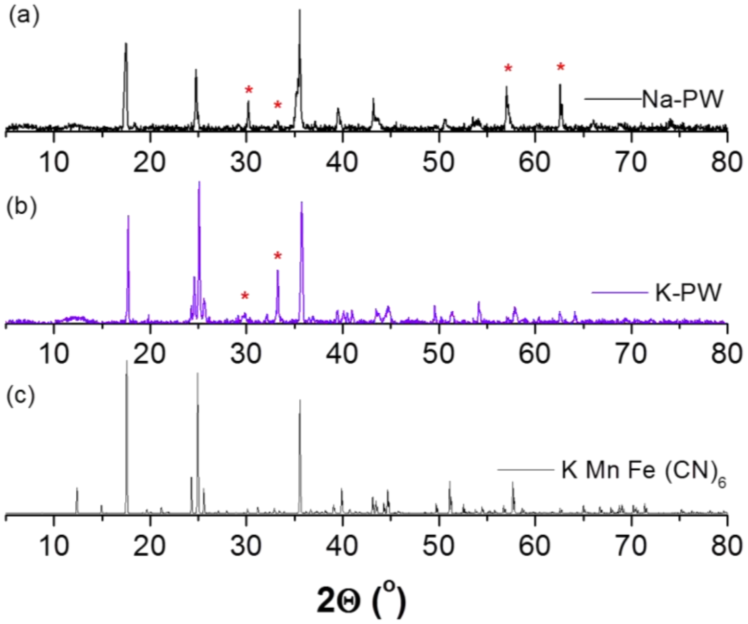

Figure 3.37. X-ray diffractograms of Na-PW (a) and K-PW (b) prepared reproducing Jiang´s methodology and its comparison with (c) the monoclinic potassium Prussian White pattern used by Jiang et al to confirm the formation of this phase (JCPDS 51-1896).

The presence of iron oxides impurities is further confirmed through Mössbauer measurements (Figure 3.38). In addition to the LS Fe^{II} and HS Fe^{2+} signals associated to the PW phase, the spectra also manifests the presence of a magnetic component in K-PW, and a couple of them in Na-PW. The magnetic components appear as a sextet and are ascribed to the formation of some Fe^{3+}. The Mössbauer parameters of Na-PW and K-PW phases obtained following Jiang´s method are collected, respectively, in Table 3.9 and Table 3.10.

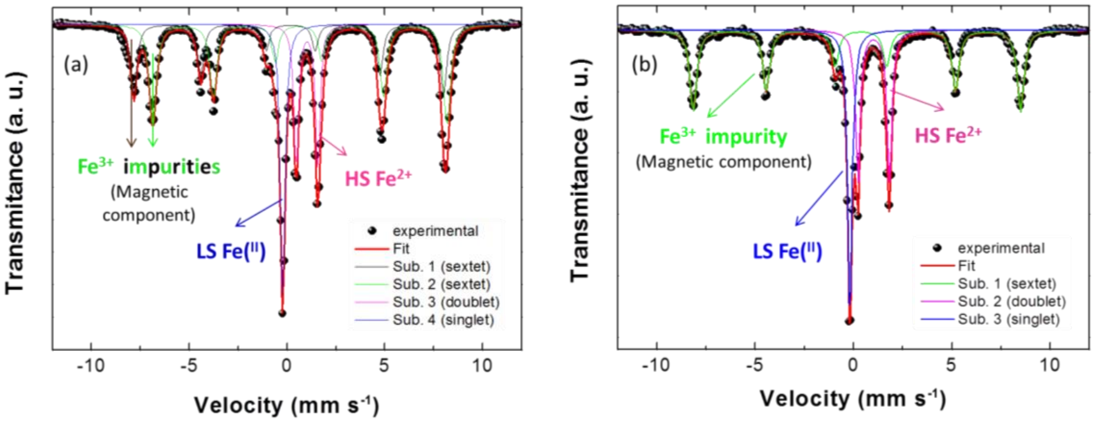

Figure 3.38. Mössbauer spectra of Na-PW (a) and K-PW (b) synthesized following Jiang´s methodology. Experimental (black dots) and fitting (red line) are shown along with the blue, green and pink solid lines that represent the LS Fe^{II}, HS Fe^{2+} and Fe^{3+} impurity spectral components, respectively. In addition, Na-PW, displays a 4th spectral component (solid line in black) also corresponding to an Fe^{3+} impurity.

Table 3.9. Values of parameters **δ**, **Δ** and **Fe ratio** extracted from the Mössbauer fitting for iron in Na-PW obtained by Jiang´s procedure (**δ** = isomer shift relative to Fe bcc, **Δ** = quadrupolar splitting).

		Isomer Shift, δ (mm·s^{-1})	**Quadrupolar, Δ** (mm·s^{-1})	**Fe ratio**
NaFe^{2+}[Fe(^{II})CN$_6$]	LS Fe^{II}	-0.103(1)	0	17.66 %
	HS Fe^{2+}	1.126(1)	1.091(1)	17.98 %
Impurity	Fe^{3+}	0.238(1)	-0.088(2)	24.99 %
Impurity	Fe^{3+}	0.729(1)	0.072(2)	39.36 %

Table 3.10. Values of parameters **δ**, **Δ** and **Fe ratio** extracted from the Mössbauer fitting for iron in K-PW obtained by Jiang´s procedure (**δ** = isomer shift relative to Fe bcc, **Δ** = quadrupolar splitting).

		Isomer Shift, δ (mm·s^{-1})	**Quadrupolar, Δ** (mm·s^{-1})	**Fe ratio**
KFe^{2+}[Fe(^{II})CN$_6$]	LS Fe^{II}	-0.08	0	28.08 %
	HS Fe^{2+}	1.13	1.61	25.42 %
Impurity	Fe($^{3+}$)	0.38	-0.20	46.50 %

Under these circumstances, the procedure described by Jiang *et al.* had to be slightly modified. Ascorbic acid is known to be a reducing agent and it has been previously utilized to prevent the oxidation of Fe^{2+} to Fe^{3+} in the synthesis of $LiFePO_4$.[45] With the aim of hindering the generation of iron oxides, certain amount of ascorbic acid was added in the preparation of A-PW via hydrothermal synthesis. This way, pale gray precipitates were attained and PXRD of these compounds are shown below (Figure 3.39).

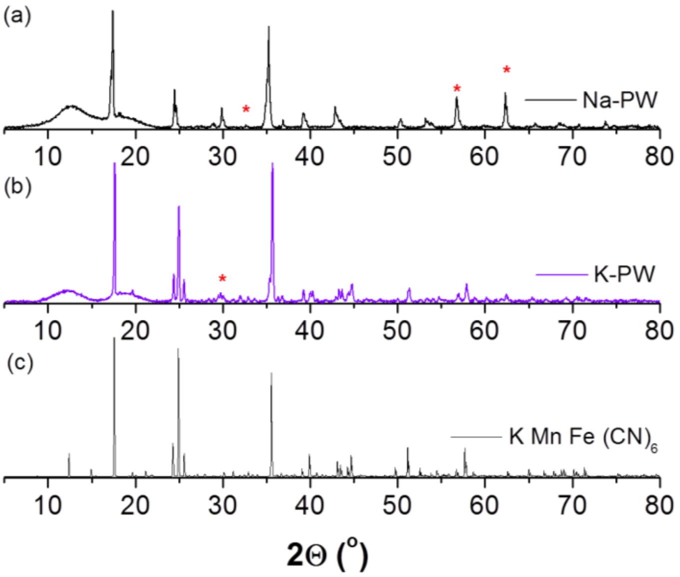

Figure 3.39. X-ray diffractograms of Na-PW (a) and K-PW (b) prepared modifying Jiang´s methodology by adding ascorbic acid as reducing agent and its comparison with c) (see c) from Figure 3.37).

---

[45] B. Jin, H-B. Gu. *Solid State Ionics* 2008, **178**, 1907–1914. "Preparation and characterization of $LiFePO_4$ cathode materials by hydrothermal method."

Practically no change is appreciated in the Na-PW pattern with regard to that synthesized in absence of ascorbic acid, since some iron oxides impurities (labelled with asteriks) still remains in it. On the contrary, almost no residue of iron oxides is observed in the K-PW diffractogram.

Images collected by SEM (Figure 3.40) mainly display a slightly distorted cubic morphology of the materials and a non-homogeneous particle size distribution.

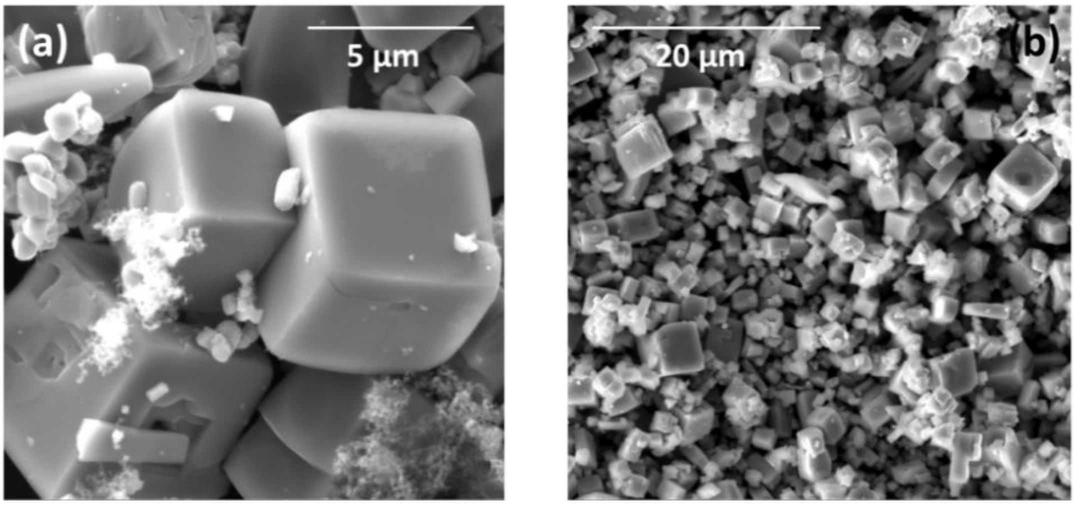

Figure 3.40. SEM images of Na-PW (a) and K-PW (b) synthesized via acuothermal synthesis (Jiang´s methodology) in the presence of ascorbic acid.

The presence of impurities in both A-PW synthesized through modified Jiang´s methodology and the lack of signal coming from Na in EDX analysis of Na-PW (as shown Figure A3.14, Appendix), led to further modify the synthesis strategy. This way, a new procedure was developed for the synthesis of A-PW (A = Na, K). The new synthetic route is described below.

3.3.2.2 *Development of a new synthetic route for A-PW (A = Na, K)*

A-PW (A = Na, K), ideally $A_2Fe^{2+}[Fe^{II}(CN)_6]\cdot xH_2O$, were obtained using a single step method. In inert atmosphere, 100 mL of a pale yellow $Na_4[Fe(CN)_6]\cdot 10H_2O$ or $K_4[Fe(CN)_6]\cdot 3H_2O$ 40 mM aqueous solution were directly mixed with 100 mL of a pale yellowish $FeCl_2$ 40 mM aqueous solution, forming a light blue or light green suspension, according to the reaction described in equations (3.19 and (3.20. To preserve the Prussian White and hinder the evolution towards Prussian Blue, a small amount (approximately 2 mg) of ascorbic acid was added in the solution. Then, the suspension was mixed with an excess of ACl (A = Na or K) to favor an increase in the alkali content (Na or K) present in the structure. After heating ca. 4 h at 60˚C under N_2 flow, the mixture was filtered. The precipitate obtained was washed with H_2O (3 × 10 ml) and acetone (3 × 10 ml) and dried under vacuum. Pale blue crystal-like aggregates of A-PW, $Na_{2-x}Fe^{2+}_{1+(x/2)}[Fe^{II}(CN)_6]\cdot yH_2O$ (see eq. (3.19)) or $K_{2-x}Fe^{2+}_{1+(x/2)}[Fe^{II}(CN)_6]\cdot yH_2O$ (see eq. (3.20)), were achieved (see Figure 3.41).

$$(1 + (x/2))\ FeCl_2 + Na_4[Fe(CN)_6]\cdot 10H_2O \rightarrow Na_{2-x}Fe^{2+}_{1+(x/2)}[Fe^{II}(CN)_6]\cdot yH_2O + (2 + x)\ NaCl\ (aq.) \tag{3.19}$$

$$(1 + (x/2))\ FeCl_2 + K_4[Fe(CN)_6]\cdot 3H_2O \rightarrow K_{2-x}Fe^{2+}_{1+(x/2)}[Fe^{II}(CN)_6]\cdot yH_2O + (2 + x)\ KCl\ (aq.) \tag{3.20}$$

Unlike other methodologies reported for K-PW and Na-PW, the materials here described were synthesized under mild conditions. Only 60 ˚C were here applied for 4h, in contrast to the 160 ˚C during 48 h used by Jiang[44] or the 140˚C for 20 h deployed by Goodenough,[46] and no acidification of the media was required, which is an improvement compared to the synthesis referred by Guo[47]. These soft conditions thus make more convenient and scalable this route of preparation.

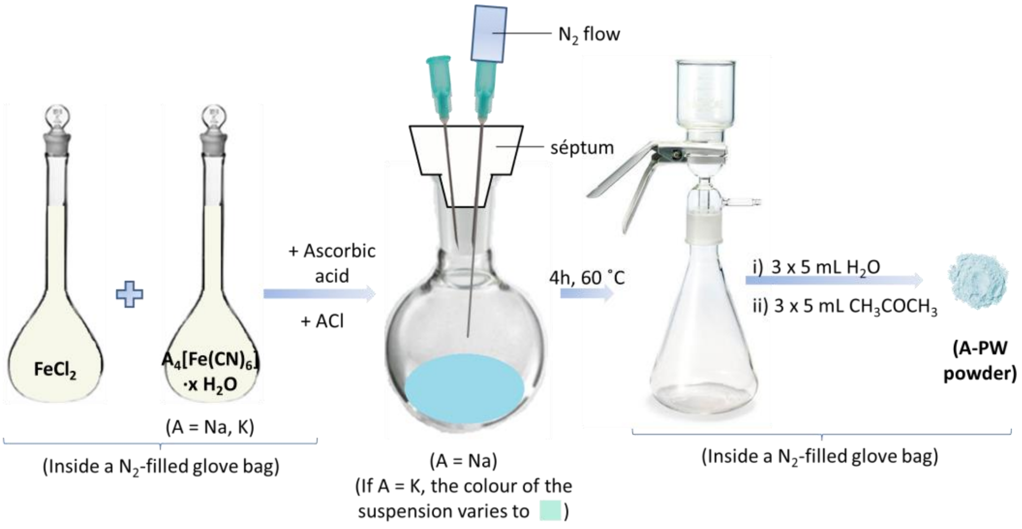

Figure 3.41. Schematic procedure for preparing A-PW (A = Na, K), $A_{2-x}Fe^{2+}_{1+(x/2)}[Fe^{II}(CN)_6]\cdot yH_2O$, using the new synthetic method developed in this thesis work.

An exhaustive characterization of the materials obtained through this new methodology is presented in subsequent sections.

3.3.3 Structural, morphological and physico-chemical characterization

3.3.3.1 *Powder X-ray diffraction*

The powder X-ray diffractograms of Na-PW and K-PW are illustrated in Figure 3.42a and b. The broad reflections evidence that samples obtained by this new synthetic method are less crystalline than

---

[46] L. Wang, J. Song, R. Qiao, L.A. Wray, M.A. Hossain, Y.-D. Chuang, W. Yang, Y. Lu, D. Evans, J.-J. Lee, S. Vail, X. Zhao, M. Nishijima, S. Kakimoto, J.B. Goodenoug. *J. Am. Chem. Soc.* 2015, **137**, 2548-2554. "Rhombohedral prussian white as cathode for rechargeable sodium-ion batteries".

[47] Y. You, X.-Q. Yu, Y.-X. Yin, K.W. Nam, Y.-G. Guo, *Nano Res.* 2015, **8**, 117-128. "Sodium iron hexacyanoferrate with high Na content as a Na-rich cathode material for Na-ion batteries".

those achieved by the other methodologies, probably as consequence of the lower temperature of reaction deployed (60 ˚C). This widening also suggests a nanoparticle nature of the materials. As opposed to the rhombohedral lattice (*R* -3) reported in the literature for purely iron based sodium Prussian White[46, 47] (Figure 3.42c), or to the monoclinic unit cell ascribed to the potassium analogue[44] (Figure 3.42d), the materials synthesized through the new methodology seem to present a cubic structure profile.

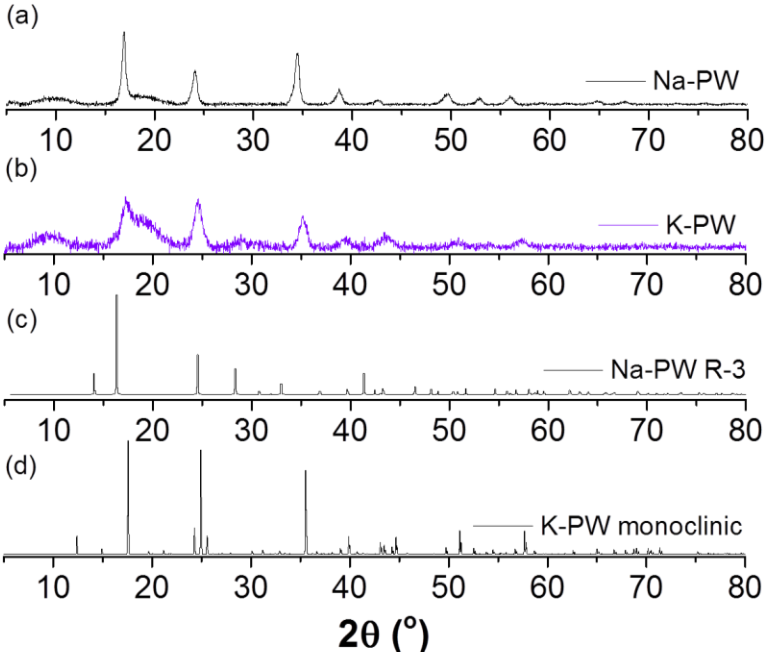

Figure 3.42. X-ray diffractograms of Na-PW (a) and K-PW (b). To compare the experimental patterns obtained with that already reported for Na-PW, a profile with lattice parameters and space group R-3 from ref.[48] was simulated (c). Monoclinic K-PW profile (d) was also included (JCPDS 51-1896, taken from ref. 44).

Indeed Rietveld refinement (Figure 3.43) have been performed refining lattice parameters, atomic positions and occupancies of a starting cubic Prussian blue model (space group (*Fm*-3*m*)) and results in a lattice parameter a = 10.350(5) Å for Na-PW and a = 10.117(6) Å for K-PW. Agreement factors were, R_B= 32.5, R_F= 24.9 and χ^2=3.61 for Na-PW and R_B= 37.1, R_F= 41.1 and χ^2=2.06 for K-PW. Despite R_B and R_F values are higher than desired, the χ^2 reached is acceptable for both materials, especially considering the possible nanoparticle nature of the materials, the use of kapton foil and the low counting times to avoid materials oxidation. Conversely, in the fittings attempted with the rhombohedral *R*-3 space group, the values of χ^2 were larger and the fittings to the experimental profile were poorer.

---

[48] J. Song, L. Wang, Y. Lu, J. Liu, B. Guo, P. Xiao, J.-J. Lee, X.-Q. Yang, G. Henkelman, J.B. Goodenough. *J. Am. Chem. Soc.* 2015, **137**, 2658-2664. “Removal of Interstitial H_2O in Hexacyanometallates for a Superior Cathode of a Sodium-Ion Battery”.

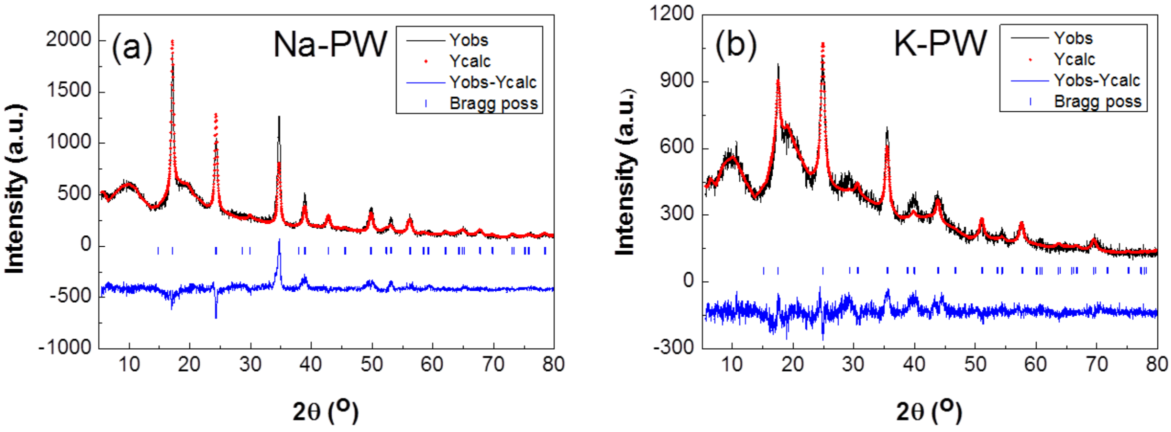

Figure 3.43. Rietveld fitting plot of Na-PW (on the left) and K-PW (on the right). Experimental (black) and calculated (red) patterns are shown along with the difference curve (blue).

So far, it might be think that cubic Prussian Blue has been obtained instead of the alkali-rich phase Prussian White. To corroborate the formation of Prussian White by this new methodology (section 3.3.2.2) and rule out the obtaining of cubic Prussian Blue, other spectroscopic and diffraction techniques were exploited.

3.3.3.2 *Infrared Spectroscopy*

IR spectra of Na-PW and K-PW (Figure 3.44) show the characteristic cyanide (-C≡N) vibrational band at 2068 and 2067 cm^{-1}, respectively.

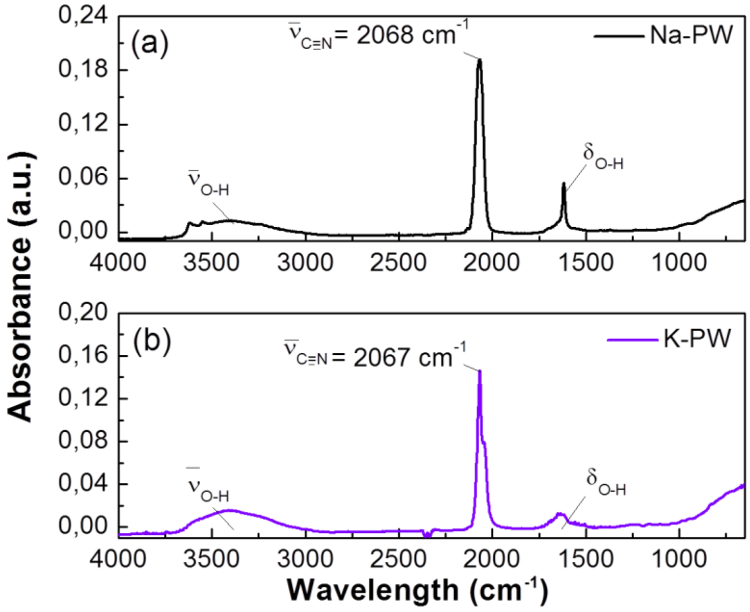

Figure 3.44. IR spectra of Na-PW (a) and K-PW (b), highlighting the more significant bands (-C≡N (cyanide) stretching vibrational band and O-H (hydroxyl) stretching vibrational and deformation band).

Compared to Prussian Blue, whose -C≡N vibration appears at ca. 2078 cm^{-1},[36] the position of the band is red-shifted in PW. This deviation towards lower wavenumbers implies longer C≡N distances when the two iron atoms approach to oxidation state 2^+ in PW. The above analyzed shift is consistent with the results presented by Takachi[49] and Wu[40], who observed a higher wavenumber of the -C≡N band when iron oxidation state increases in a Prussian blue structure. Other bands, such as the ν(O-H) and the δ (O-H), were also distinguished in the IR spectra, unveiling the presence of a small amount of water in both pristine materials. Table 3.11 collects all IR absorption peaks observed in A-PW (A = Na, K).

Table 3.11. Principal IR bands observed in Na-PW and K-PW.

Compound	IR bands (cm^{-1})
Na-PW	3400 ν(O-H), 1618 δ(O-H) – H_2O **2068** ν(-C≡N) – Na-PW
K-PW	3400 ν(O-H), 1630 δ(O-H) – H_2O **2067** ν(-C≡N) – K-PW

3.3.3.3 *Raman Spectroscopy*

Additional techniques were deployed to further characterize the Prussian White phases. Raman spectra of A-PW (A = Na, K) were collected in the wavenumber range 1900-2300 cm^{-1}, so as to evaluate the -C≡N stretching band (Figure 3.45). A couple of distinctive bands are clearly differentiated at 2116 and 2148 cm^{-1} for Na-PW, and at 2090 and 2131 cm^{-1} for K-PW. Besides, a shoulder at lower wavenumber can also be guessed at ca. 2060 - 2075 cm^{-1}. The change of alkali results in different scattering frequency position and relative intensities. Red shift on the bands when contrasting Na-PW to K-PW agrees with IR results and could be indicative of the C≡N bond softening. Deconvolution of Raman spectra for both Na-PW and K-PW unequivocally permits to assign 3 peaks, attributed to C≡N vibrations, for each compound (Figure 3.45b and c). Although the presence of three bands in the Raman spectra is usually found in rhombohedral Fe-based PW, the values obtained in this case are slightly different from those observed in previous works for Na-PW at 2070, 2110 and 2135 cm^{-1}.[47, 48] This fact suggests that, despite the average crystal structure is cubic as determined from PXRD and electron diffraction, local rhombohedral or monoclinic distortions might be present in both compounds.

---

[49] M. Takachi, T. Matsuda, Y. Moritomo. *Jpn J. Appl. Phys.* 2013, **52**, 090202. “Structural, Electronic, and Electrochemical Properties of $Li_xCo[Fe(CN)_6]_{0.90}2.9H_2O$”.

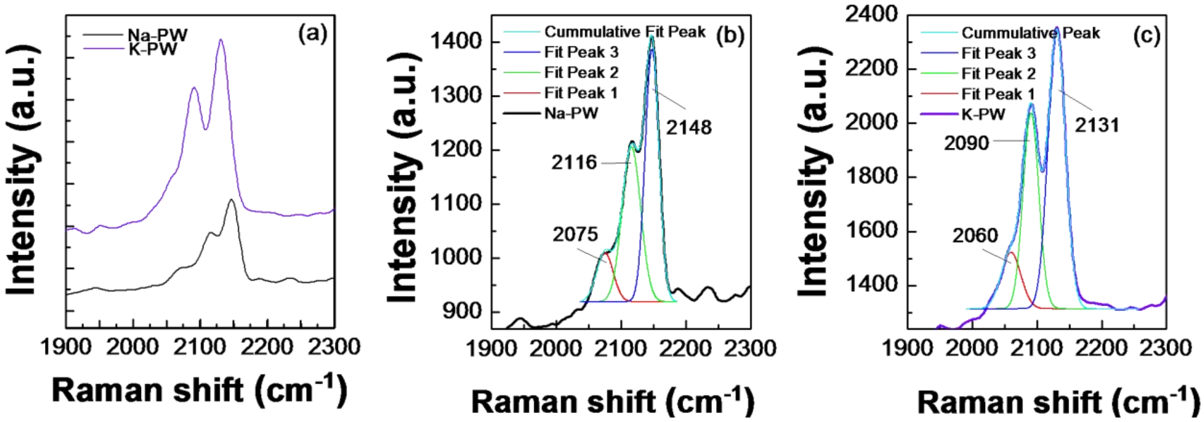

Figure 3.45. Raman spectra focusing on the cyanide band region (a) of Na-PW (black) and K-PW (purple) and its corresponding deconvolution b) Na-PW, c) K-PW.

3.3.3.4 *Thermogravimetric analysis*

To obtain the accurate amount of H_2O present in each material, TGA measurements were performed under N_2 atmosphere (see Figure 3.46). A negligible H_2O content is calculated both in Na-PW and K-PW, as it is appreciated by their almost invariable mass up to 300 ˚C. A single mass loss of 1.05 for Na-PW and 1.36% in K-PW corresponds, respectively, to 0.19 and 0.26 H_2O molecules. This low H_2O content, beneficial for electrochemistry purposes, represents and advantage over the Prussian Blue structures.

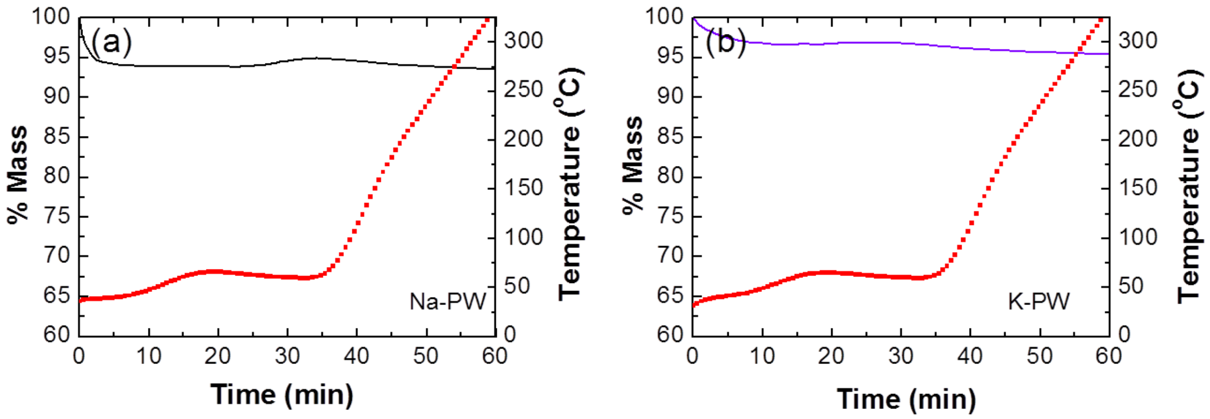

Figure 3.46. TGA curves of a) Na-PW and b) K-PW. Initially, the temperature was raised up to 60°C with a temperature step of 2°C·min^{-1} and was kept in isotherm for 20 minutes. Later on, the sample was heated up to 325°C at 10°C·min^{-1}.

3.3.3.5 *Electron microscopy (SEM, TEM) and chemical composition*

The morphology of both PW was determined by SEM. As Figure 3.47a and b, show, the materials present a heterogeneous particle size distribution that ranges from few micrometers (2-5 µm) to 100 µm. The particles are however composed of aggregates of smaller grains, showing crystalline domains of 35-40 nm for Na-PW and 20 nm for K-PW (Figure 3.47c and d), as observed by high resolution TEM. This is in agreement with the very broad reflections displayed in PXRD. To study a possible rhombohedral or monoclinic distortion, electron diffraction patterns were recorded on individual particles in the TEM. Indexation of the ring-type electron diffraction patterns shown by the nanocrystals of Na-PW (Figure 3.47e) and K-PW (Figure 3.47f) confirmed however the cubic structure (*Fm*-3*m*), previously observed by PXRD, in both materials. The diffraction rings matched the main crystallographic planes of the cubic Prussian Blue structure: 200, 220, 222, 400, 440 and so on. The poorer resolution for Na-PW images and diffraction pattern, observed in Figure 3.47, can be explained by the higher sensitivity exhibited by this sample under the electron beam, as already observed in A-PB samples.

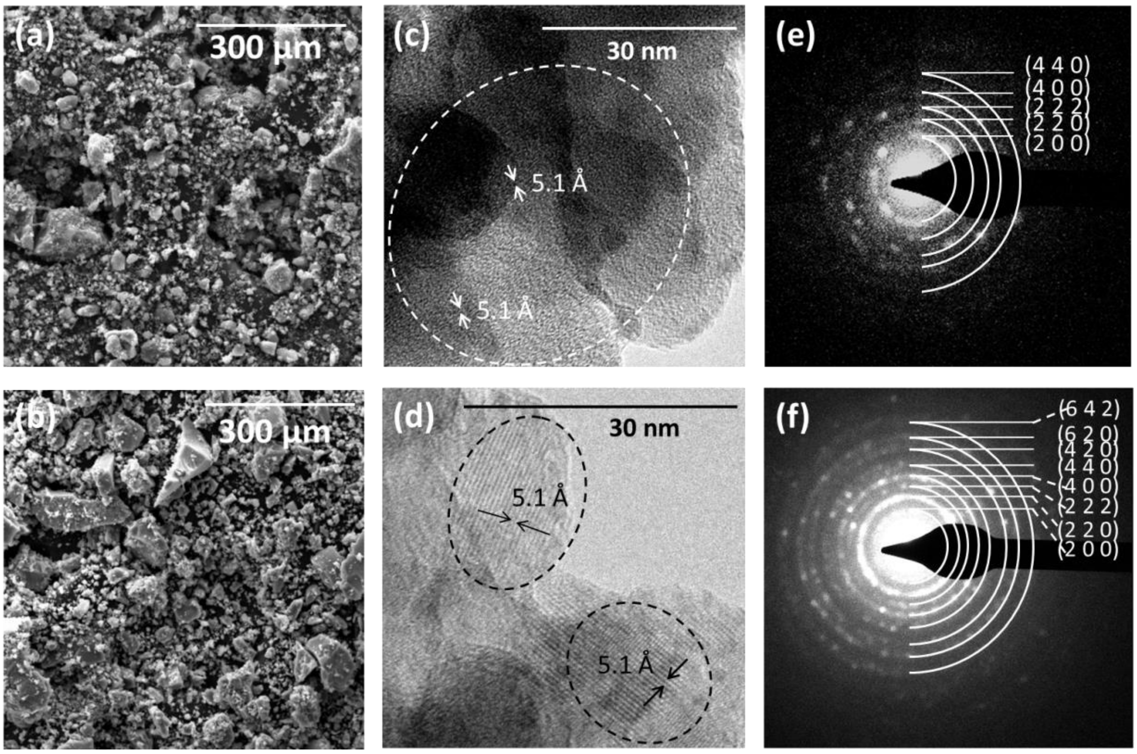

Figure 3.47. SEM images of Na-PW (a) and K-PW (b) morphology. Electron diffraction patterns of Na-PW (c) and K-PW (d).

EDX of the individual crystallites analyzed by electron diffraction yielded approximate Na: Fe and K: Fe proportions of 1.3: 2 and 1.6: 2, but more accurate ratios were calculated using atomic absorption and emission spectroscopy respectively (see Table 3.12 andTable 3.13). The exact chemical formula turned out to be $Na_{1.70}Fe_{2.15}(CN)_6$ for Na-PW and $K_{1.59}Fe_{2.20}(CN)_6$ for K-PW. Such chemical compositions were further confirmed with the H, C, N analyses (see Table 3.14).

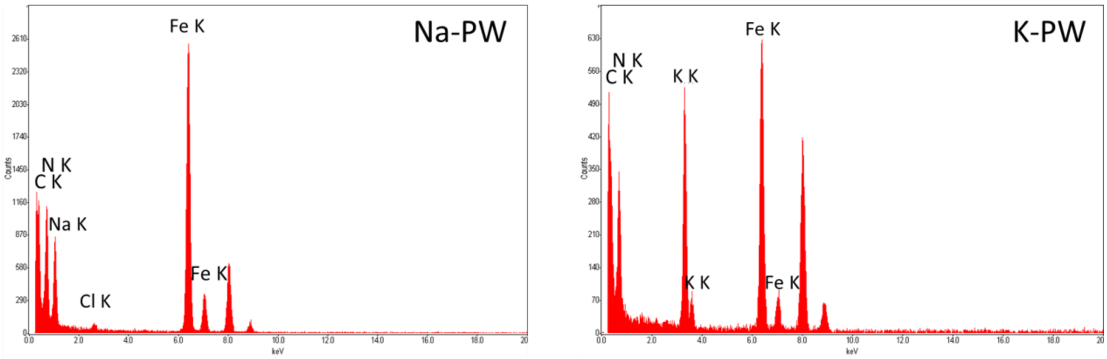

Figure 3.48. EDX spectra of Na-PW and K-PW.

Table 3.12. Atomic Absorption Spectroscopy (AAS) results of the Na-PW sample.

Compound	**Na** (mg/L)	**RSD (%)**	**Fe** (mg/L)	**RSD (%)**
Na-PW	9.90	0.2	30.47	2.1

Table 3.13. Atomic Emission Spectroscopy (AES) results of the K-PW sample.

Compound	**K** (mg/L)	**RSD (%)**	**Fe** (mg/L)	**RSD (%)**
K-PW	15.31	0.1	30.62	1.2

Table 3.14. Elemental analysis (H, C, N) of Na-PW and K-PW. Both values experimental and theoretical, the latter one in brackets, are here presented. The %N, C and H of Na-PW, was calculated considering ca. 3 H_2O molecules that probably were adsorbed by air-exposure.

Compound	**% N_{exp} (th)**	**% C_{exp} (th)**	**% H_{exp} (th)**
Na-PW	20.62 (20.82)	18.22 (17.85)	1.87 (1.89)
K-PW	21.44 (21.86)	18.98 (18.76)	1.02 (0.2)

The cubic symmetry that A-PW (A = Na, K) presents is attributed to an alkali content inferior to 2 (see Table 3.12 and Table 3.13), what agrees with other compositions described in the literature. For example, Guo et al. have observed the change in the crystal structure from cubic $Na_{1.24}Fe_{1.89}(CN)_6$ to rhombohedral $Na_{1.63}Fe_{1.89}(CN)_6$, suggesting that the PB framework tends to form lower symmetry structures the greater the amount of Na it contains.[47] Also, the phase transition from cubic to rhombohedral is known to occur at $\delta \leq 0.3$ in the Mn-based PW $Na_{2-\delta}Mn[Fe(CN)_6]$.[50] The molecular formula of the Na-PW here synthesized, $Na_{1.70}Fe_{2.15}(CN)_6$ (equivalent to $Na_{1.58}Fe_2(CN)_6$), is very close to that of Guo´s rhombohedral phase but still on the cubic side of the transition. On the other hand, the fully potassiated K-PW phase is reported to be monoclinic, while the PW here reported retains the cubic symmetry as well.[44] Consequently, despite having obtained alkali rich PW phases, the alkali

---

[50] L. Wang, Y. Lu, J. Liu, M. Xu, J. Cheng, D. Zhang, J. B. Goodenough. *Angew. Chem. Int. Ed.* 2013, **52**, 1-5. "A superior low-cost cathode for a Na-ion battery".

content in these new synthesized compounds did not reach the full site occupancy of 2 and thus they maintain the cubic structure.

3.3.3.6 *X-ray photoelectron spectroscopy*

The XPS spectra survey of the pristine Na-PW and K-PW are depicted in Figure 3.49a and show the presence of Fe, C, N and Na or K in the structure (see Table 3.15). Almost no O content is detected, supporting the low water content present in the samples.

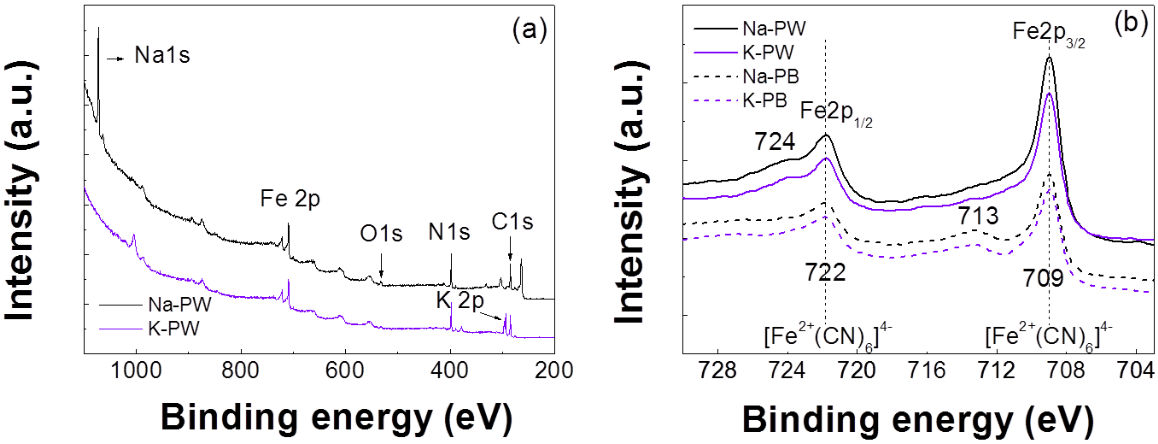

Figure 3.49. XPS spectra of Na-PW (in black) and K-PW (in violet) showing the Fe 2p edge, O 1s edge, N 1s edge, C 1s edge and Na 1s edge or K 2p edge. XPS at the Fe 2p edge (b) of Na-PW (black) and K-PW (purple). XPS spectra of Na-PB (dashed line, in balck) and K-PB (dashed line, in violet) are also included in Figure 3.30b.

Table 3.15. Atomic edge values encountered in the XPS spectra of the A-PW samples.

	Na-PW	**K-PW**
Na 1s edge	1071 eV	-
Fe 2p edge	709, 722, 724	709, 722, 724
N 1s edge	398 eV	398 eV
K 2p edge	-	293 eV
C 1s edge	285 eV	285 eV

Focusing on the region of interest (Fe 2p edge) to detect possible changes in the oxidation state of the redox active specie -iron- between different samples, it can be concluded that the Fe 2p edge XPS spectra of Na-PW and K-PW are virtually identical (see Figure 3.49b, continuous lines). This similarity is indicative of the same electronic configuration of the iron in both materials. With a comparative purpose, XPS analyses of the Prussian Blue phases A-PB (A = Na, K) are also included (see Figure 3.49b, dashed lines). Analogously, both Na- and K-PB spectra are identical between them as well. Thus, the shape of the Fe 2p spectra remains unalterable in both types of materials, regardless the substitution of the alkali metal (Na by K). For all the phases, A-PW and A-PB (A= Na, K), the Fe 2p region has two split orbit components 2p$_{3/2}$ and 2p$_{1/2}$ with maxima at 709 and 722 eV, coincident with those previously reported for low spin Fe^{2+} of [Fe(CN)$_6$]$^{4-}$ in Prussian Blue species.[39, 40] The satellite pattern, however, varies from PW to PB. The presence of a small peak at ca. 713 eV in PB has been assigned in the literature either to high spin Fe^{3+},[40, 41] even though the intensity is not as large as that of the Fe^{2+} signal, or to Fe^{2+} bonded to oxygen[42] ergo attributed to the presence of water molecules. Conversely, the peak at 713 eV is not observed for PW, what agrees with the absence of high spin Fe^{3+} and much lower content of H_2O (as can be observed in Figure 3.49a). Instead, another satellite at ca. 724 eV, which could be related to the high spin state of the Fe^{2+} ions, can be observed for the PW species. Therefore, the PB and PW phases can be distinguished by the Fe 2p data obtained from XPS, providing a determinant evidence of the formation of Prussian White phases distinct from Prussian Blue.

3.3.3.7 *Mössbauer spectroscopy*

The Mössbauer spectra of A-PB (A = Na, K) were registered at room temperature (see Figure 3.50). Each spectrum could be deconvoluted into a singlet absorption peak and a doublet absorption peak, which were respectively attributed to the LS Fe^{II} covalently bonded to C and theHS Fe^{2+} bonded to N. Their isomer shift (δ) and quadrupolar splitting (Δ) values are reflected in Table 3.16 and are in good agreement with those reported in the literature. [44, 47] Additionally, a doublet component assigned to HS Fe^{3+} is observed in both spectra. This component can be explained by the air-exposure of the material while collecting the Mössbauer spectrum, that could induce surface oxidation.

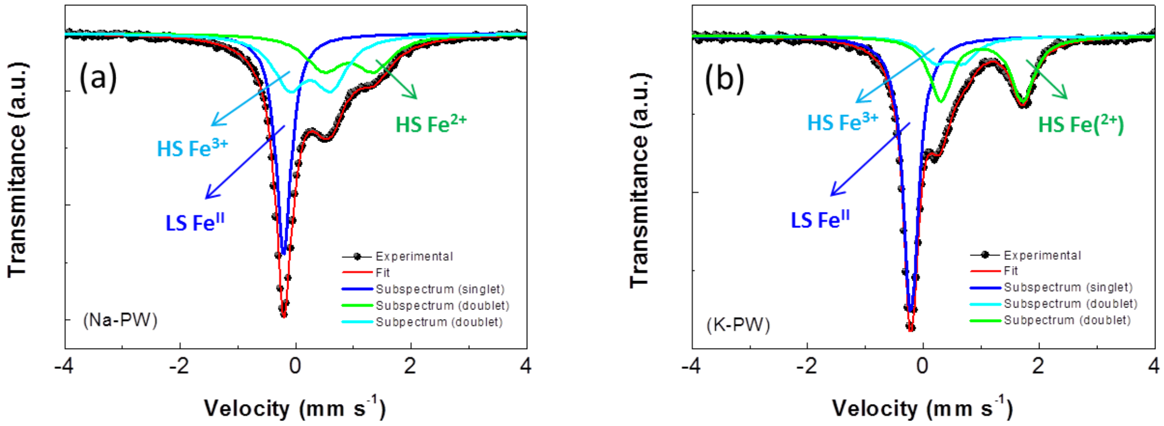

Figure 3.50. Mössbauer spectra of a) Na-PW and b) K-PW. Experimental (black dots) and fitting (red line) are shown along with the blue and green solid lines that represent the LS Fe^{II} and HS Fe^{2+} spectral components, respectively. An additional HS Fe^{3+} contribution is also observed.

Table 3.16. Values of parameters **δ**, **Δ** and **Fe ratio** extracted from the Mössbauer fitting for iron in Na-PW and K-PW (**δ** = isomer shift relative to Fe bcc, **Δ** = quadrupolar splitting).

Compound	**Assignation**	**Isomer Shift, δ** (mm·s^{-1})	**Quadrupolar, Δ** (mm·s^{-1})	**Fe ratio**
$Na_{2-x}Fe^{2+}_{(x+1/3)}[Fe^{II}CN_6]$	LS Fe^{II}	-0.11(1)	-	36.9%
	HS Fe^{2+}	1.03(2)	0.87(4)	27.4%
	HS Fe^{3+}	0.35(1)	0.72(3)	35.7%
$K_{2-x}Fe^{2+}_{(x+1/3)}[Fe(^{II})CN_6]$	LS Fe^{II}	- 0.11(1)	-	50.5%
	HS Fe^{2+}	1.11(1)	1.42(1)	34.9%
	HS Fe^{3+}	0.55 (1)	0.49(2)	14.6%

It has been demonstrated through several characterization techniques (PXRD, IR, TEM, Raman, XPS and Mössbauer) that A-PW (A = Na, K) here obtained are pure phases. Consequently, both of them will be electrochemically studied to determine its suitability as electrodic materials.

Chapter 4

Prussian Blue phases as anodes in Na-ion and Li-ion batteries

4.-) Prussian Blue phases as anodes in Na-ion and Li-ion batteries

This chapter describes the results obtained in the investigation of the electrochemical properties of the Prussian blue materials synthesized as single phases, when operating as anodes or negative electrodes. Firstly, the electrochemical behavior of the titanium derivative, $Ti[Fe(C)N)_6]$ (Ti-PBA), in NIB is addressed. Secondly, the sodium Prussian blue analogue $Na_{0.75}Fe_{1.08}[Fe(CN)_6]\cdot 3.4H_2O$ (Na-PB) is explored, also for NIB. Finally, the performance of potassium Prussian Blue $K_{0.88}Fe_{1.04}[Fe(CN)_6]\cdot 3.4H_2O$ (K-PB) is studied for LIB. The latter section, provided interesting results of the K-PB performance *vs*. Li^+/Li that could not be explained with the typical intercalation reaction. In order to find a reasonable explanation to the mechanism occurring, several *ex-situ* measurements, including XRD, IR, EM and synchrotron XAS, were performed. Additionally, an electrochemical *in-situ* Mössbauer study, using an *in-situ* Mössbauer cell specifically developed along this thesis work for such purpose, has been made to complement the information obtained in the *ex-situ* experiments.

As mentioned in chapter 2, the following table (Table 4.1) summarizes the formulation of the electrodes prepared for the electrochemical studies of the anodes under study along this chapter.

Table 4.1. Electrode composition of the electrodes tested as anodes within this chapter.

Electrode	Active material	Conductive Carbon	Binder	Proportion (a.m.: c.c.: b)*	Drying T (˚C)	Electrolyte
Ti-PBA (powder)	Ti-PBA (2b_1f, 4a, 4b)	Super C-65		80: 20: 0	120	$NaClO_4$ in EC:DMC 50:50 % vol
Ti-PBA (laminate)	Ti-PBA (4a, 4b)	Super C-65	CMC	70: 10: 20	120	$NaPF_6$ in EC:PC:FEC 49:49:2 % vol
Na-PB (powder)	Na-PB	Super C-65		80: 20: 0	80	$NaClO_4$ in EC:DMC 50:50 % vol or $LiPF_6$ in EC:DMC 50:50 % vol
Na-PB (laminate)	Na-PB	Super C-65	PVDF	80: 10: 10	80	$NaPF_6$ in EC:PC:FEC 49:49:2 % vol
Na-PB (laminate) *Binder optimization*	Na-PB	Super C-65	PVDF/CMC/PTFE/EPDM	80: 10: 10	80	$NaPF_6$ in EC:PC:FEC 49:49:2 % vol
Na-PB (laminate) *Optimized formula*	Na-PB	Super C-65	CMC/SBR	85:10:5	80	$NaPF_6$ in EC:PC:FEC 49:49:2 % vol
K-PB (powder)	K-PB	Super C-65		80: 20: 0	80	$NaClO_4$ in EC:DMC 50:50 % vol or $LiPF_6$ in EC:DMC 50:50 % vol
K-PB (laminate)	K-PB	Super C-65	PVDF	80: 10: 10	80	$LiPF_6$ in EC:DMC 50:50 % vol
K-PB (laminate) *Optimized formula*	K-PB	Super C-65	CMC/SBR	85:10:5	80	$LiPF_6$ in EC:DMC 50:50 % vol

*a.m.: active material, c.c.: conductive carbon, b: binder.

4.1. Ti-PBA as anode vs. Na^+/Na

4.1.1. Scope

$Ti[Fe(CN)_6]$, hereinafter Ti-PBA, comprises two transition metals (Fe and Ti) with oxidation states Fe^{2+} and Ti^{4+}. No electrochemical activity is presumed for the iron metallic center, unless a conversion mechanism happens. Conversely, a reversible redox activity is assumed for titanium metallic center. Considering the low voltage plateau of the redox couple Ti^{4+}/Ti^{3+} observed for sodium intercalation in other titanium compounds, such as $NaTi_2(PO_4)_3$ [1] or $Na_2Ti_3O_7$ [2], an analogous behavior is expected for Ti-PBA. Besides, the requirement of larger cavities for facilitating sodium intercalation is amply fulfilled in the Prussian Blue structure. Therefore, the Ti-PBA phase was investigated as anode material for NIB.

4.1.2. Electrochemical characterization - results and discussion

As a summary reminder, the Ti-PBA derivative was obtained as pure material through the *direct syntheses* in organic media (**2a**, **2b)** and following the aqueous routes (**4a** and **4b**). Unfortunately, the reaction yield of **2a** was so extremely low that impeded its electrochemical test. Consequently, only the electrochemical properties of the materials attained by routes **2b**, **4a**, **4b** are here examined.

Galvanostatic measurements were conducted *vs*. Na^+/Na, using a Maccor® battery tester. Electrodes containing **2b_1f**, **4a** or **4b** were easily prepared in powder form as detailed in Chapter 2 (Section 2.2.4.2.1). In all the cases, the electrolyte deployed was 1 M $NaClO_4$ in EC: DMC 50:50 % vol. and the current density was fixed to C/10, considering $1C_{th}$, $Ti[Fe(CN)_6]$ = 103.18 mAh g^{-1} / $1Na^+$ insertion / f.u.

Figure 4.1.a displays the galvanostatic voltage profile of **2b_1f**. When the Ti-PBA **2b_1f** is cycled *vs*. Na^+/Na, a pair of pseudo-plateaus between 0.6-0.9 V are observed along the first discharge. In Figure 4.1.b, the specific capacity of **2b_1f** is plotted *vs*. cycle number. On the order of 144 mAh g^{-1} of irreversible capacity and only 26 mAh g^{-1} of reversible capacity are achieved during the first cycle, as Figure 4.1b illustrates. Although the irreversibility is mainly attributed to the formation of a solid electrolyte interface (SEI layer) in the surface of the anode,[3, 4] the extremely low reversible capacity value suggests that this compound possesses a poor electrochemical activity. Taking into account that conductive carbon super C-65 exhibits 80 mAh g^{-1} of reversible capacity when cycled *vs*. Na^+/Na in the anodic range (as shown the inset of Figure 4.1b), it is determined that 16 of the 26 mAh g^{-1} obtained by Ti-PBA **2b_1f** in the first charge are due to the addition of 20% of the conductive carbon in the mixture, corroborating the poor redox activity of the material.

---

[1] S. I. Park, I. Gocheva, S. Okada, J. Yamaki, *J. Electrochem. Soc.* 2011, **158**, A1067. "Electrochemical Properties of $NaTi_2(PO_4)_3$ Anode for Rechargeable Aqueous Sodium-Ion Batteries".

[2] P. Senguttuvan, G. Rousse, V. Seznec, J.-M. Tarascon, M. R. Palacín, *Chem. Mater.* 2011, **23**, 4109 – 4111. "$Na_2Ti_3O_7$: Lowest Voltage Ever Reported Oxide Insertion Electrode for Sodium Ion Batteries".

[3] M. B. Pinson, M. Z. Bazant. *J. Electrochem. Soc.* 2013, **160** (2), A243-250. "Theory of SEI formation in Rechargeable Batteries: Capacity Fading Accelerated Aging and Lifetime Prediction".

[4] P. Verma, P. Maire, P. Novák. *Echim. Acta* 2010, **55**, 6332-6341. "A review of the features and analysies of the solid electrolyte interphase in Li-ion batteries".

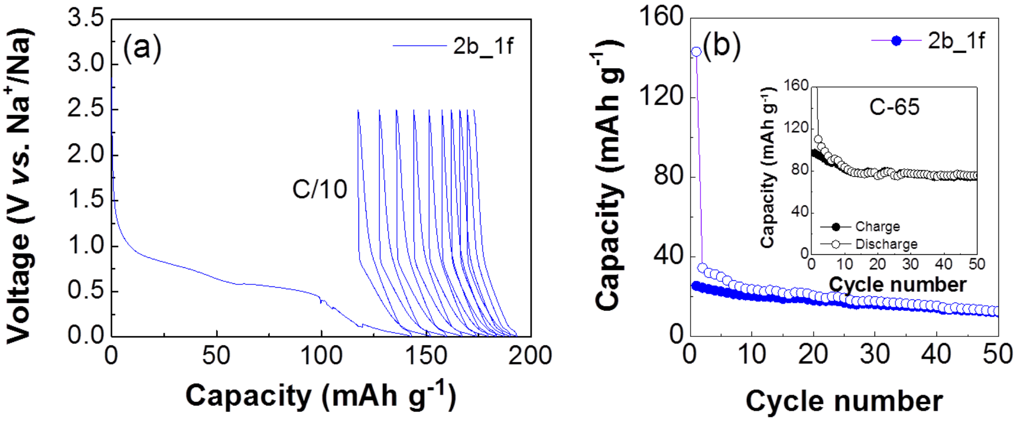

Figure 4.1. a) Voltage profile of the first 10 cycles and b) Capacity *vs*. cycle number of **2b_1f**, when cycled as powder in the voltage range from 5mV to 2.5 V *vs*. Na^+/Na. Inset) Capacity *vs*. cycle number of super **C-65®**, when cycled in the voltage range from 5mV to 2.5 V *vs*. Na^+/Na. 1M $NaClO_4$ in EC: DMC 1:1 % vol. was the electrolyte used.Filled circles represent charge capacity while empty circles refer to the discharge capacity.

In addition to the possible electrochemically inactive nature of the material, other reason behind the poor capacity encountered might be explained by the presence of DMSO molecules, as reflected the EDX data collected in the TEM showed in the previous chapter (Figure 3.6). On the one hand, DMSO molecules could be embedded in the structure. The big volume of the DMSO (422.2 Å^3) suggests that it could be occupying the position of the $[Fe^{II}(CN)_6]^{4-}$ vacancies, covering the zeolitic cavities destined for the alkali cation, and thus hindering the process of insertion and de-insertion of Na^+. On the other hand, the high viscosity of DMSO (1.991 cP at 20 ˚C)[5] makes difficult its complete removal from the compound. In this sense, the DMSO could be coating the material obstructing the diffusion process of Na^+ through it. In consequence, and as a preventive measure, the utilization of DMSO as solvent was avoided in posterior experiments and syntheses routes.

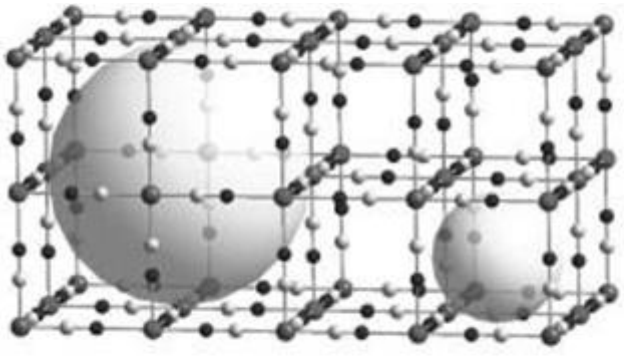

Figure 4.2. The porous framework of Prussian Blue is formed by: cavities of ca. 8.5 Å of diameter (represented by the big ball, on the left), as a result of the $[Fe(CN)_6]^{4-}$ vacancies; and interstitial spaces of 4 Å of diameter, known as zeolitic cavities, primarily destined to accommodate the alkali metals present in the structure.[6]

---

[5] http://www.gaylordchemical.com/65-2/literature/101b-dmso-physical-properties/#101-3

[6] B. Zamora, J. Roque, J. Balmaseda, E. Reguera. *ZAAC* 2010, **636** (15), 2574-2578. “Methane Storage in Prussian Blue Analogues and Related Porous Solids: Nature of the Involved Adsoprtion Forces”.

The galvanostatic voltage profiles of Ti-PBA **4a** and **4b** are pretty similar (see Figure 4.3a). Along the first discharge, a small plateau (3.5-5 mAh g^{-1}) at 2.75 V and other more defined (15-20 mAh g^{-1}) at 0.85-0.90 V can be distinguished for both materials. In the case of **4b**, a small additional pseudo plateau (5 mAh g^{-1}) is also appreciated at 2.25 V. Only *ca.* 40-45 mAh g^{-1} are invested in the formation of the SEI layer[3, 4] and the insertion of Na^+, suggesting a minimum intercalation of Na^+ into **4a** and **4b**. The subsequent charges and discharges thereby confirm it. No reversible capacity is exhibited by **4a** and **4b** (as Figure 4.3b displays), resulting in zero electrochemical activity of these materials. Either the little amount of Na^+ inserted seems to be blocked in the structure and thus cannot be extracted up to 2.0 V *vs.* Na^+/Na or no Na^+ was inserted during the first reduction.

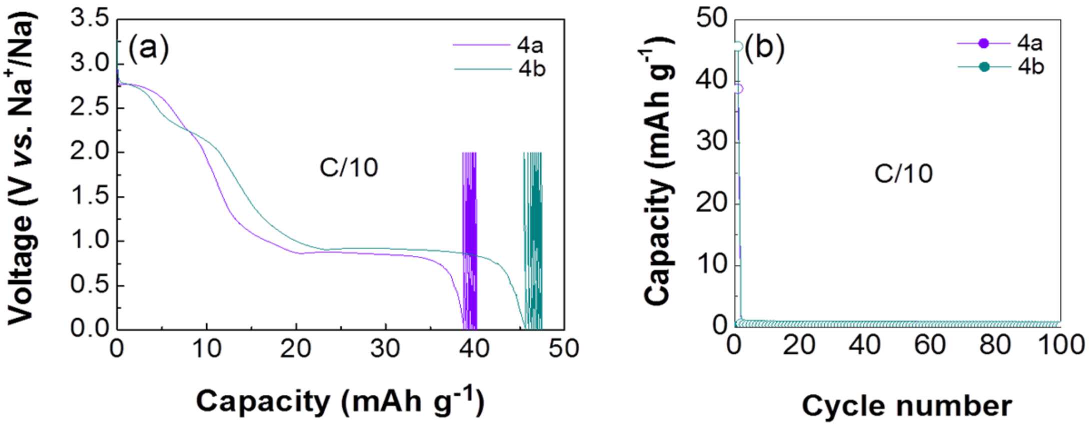

Figure 4.3. a) Voltage profile of the first 10 cycles and b) Electrochemical performance of **4a** (in violet color) and **4b** (in turquoise color), in the voltage window 5 mV – 2.0 V *vs.* Na^+/Na. For all the measurements, the electrolyte used was 1M $NaClO_4$ in EC: DMC 1:1 % vol. Filled circles represent charge capacity while the empty circles refer to the discharge capacity.

In an attempt to improve the electrochemical properties of the materials **4a** and **4b**, laminated electrodes were prepared, following the protocol described in chapter 2 (Section 2.2.4.2.1). Electrodes consisted of 70 wt. % of active material (4a or 4b) with 10% of Super C-65® and 20% of carboxymethyl cellulose (Na-CMC, MW ~ 250 000 g mol^{-1}), mixed with a solution of H_2O: EtOH (2:8). The electrolyte deployed was 1 M $NaPF_6$ in EC: PC: FEC (49:49:2 % vol.) and the current density was slowed down to C/20.

The reasons why CMC and 1M $NaPF_6$ in EC: PC: FEC (49:49:2) are deployed as binder and electrolyte will be explained in subsequent sections (Section 4.2.2) *Na-PB as anode vs. Na^+/Na* and section 5.1.2.1) *Na-PB as cathode vs. Na^+/Na in organic media,* respectively).

The voltage profiles of laminated electrodes of **4a** and **4b** are practically identical between them (see Figure 4.4a), although slightly different from those obtained in powder form (see Figure 4.3). Despite the small plateaus remain the same when compared with the batteries cycled with powder, at 2.75 V and ca. 2.25 V, the lower voltage plateau descends from 0.85-0.90 V to 0.61 and 0.72 V, respectively, for **4a** and **4b**. As can be seen in Figure 4.4b, no electrochemical activity is achieved. Even though the current density was decreased to half (ca. 51.6 mAg^{-1}) with respect to the measurements done with powder, just in case the problem was associated with the time needed to complete the redox process, no improvement was appreciated.

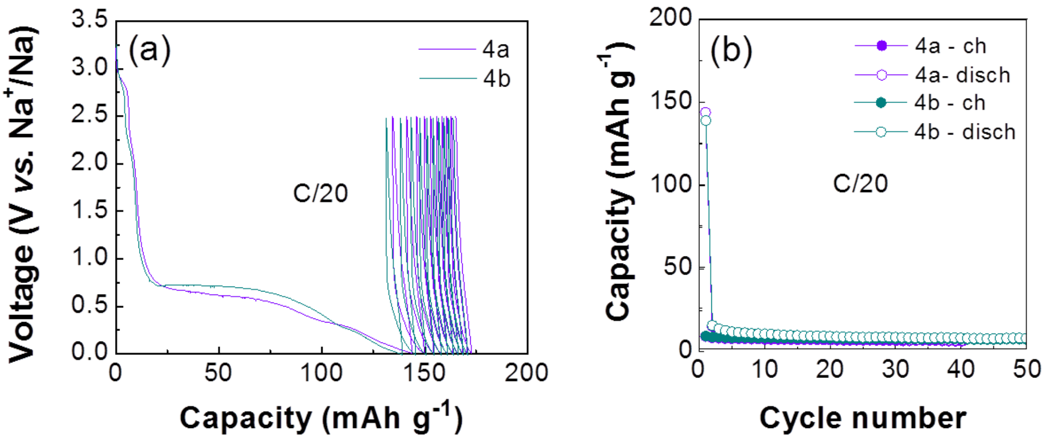

Figure 4.4. a) Voltage profile of the first 10 cycles and b) electrochemical performance (capacity *vs*. cycles) of **4a** (in violet color) and **4b** (in turquois color) laminated electrodes cycled in the voltage window of 5 mV – 2.5 V *vs*. Na$^+$/Na. The current density was fixed to C/20 (being C_{th}, Ti-PBA = 103.18 mAh g^{-1} / 1 Na$^+$ insertion / f.u.) and the electrolyte used was 1M $NaPF_6$ in EC: PC: FEC 49:49:2 % vol.

Consequently, it can be concluded that the material obtained through aqueous synthesis is not electrochemically active. At this stage, tree hypotheses are considered. On the one hand, the possibility that water molecules remain in the material as a result of having prepared the materials in aqueous medium. The effect of H_2O in the electrochemical process is known to be detrimental, since it reacts with the salt of the electrolyte and accelerates the decomposition of the latter.[7, 8] Despite the materials were dried under vacuum at 120˚C overnight releasing the zeolitic and surface adsorbed water, the chemically coordinated water cannot be removed without a lattice collapse.[9] On the other hand, it could be that Ti-PBA obtained using this adapted methodology,[10, 11] supposedly $A_{0.25}Ti[Fe_{0.875}(CN)_6]\cdot 6H_2O$ (A = Na, K), is electrochemically inactive at low potentials *vs*. Na$^+$/Na. Also, a third option could be that the Ti-PBA yielded by this synthesis is not the desired $A_{0.25}Ti[Fe_{0.875}(CN)_6]$ (A = Na, K) but the reported $Ti_3Cl[Fe(CN)_6]_2$.[12] $Ti_3Cl[Fe(CN)_6]_2$ is known to suffer from partial collapse of the structure and could hinder the electrochemical performance. However, EDX analysis of the materials revealed no presence of Cl (see Annex A4.1), and the latter option could be discarded.

---

[7] T. Kawamura, S. Okada, J-I Yamaki. *J. Power Sources* 2006, **156**, 547-554. "Decomposition reaction of $LiPF_6$-based electrolytes for lithium ion cells"

[8] W. Li, B. L. Lucht. *Echim. Solid State Lett.* 2007, **10** (4), A115-117. "Inhibition of the Detrimental Effects of Water Impurities in Lithium-Ion Batteries".

[9] N. Imanishi, T. Morikawa, J. Kondo, Y. Takeda, O. Yamamoto, N. Kinugasa, T. Yamagishi. *J. Power Sources* 1999, **79**, 215-219. "Lithium intercalation behavior into iron cyanide complex as positive electrode of lithium secondary battery".

[10] M. Hu and Y. Yamauchi. *Chem. Asian J.* 2011, **6**, 2282 – 2286. "Synthesis of a Titanium-Containing Prussian-Blue Analogue with a Well-Defined Cube Structure and Its Thermal Conversion into a Nanoporous Titanium–Iron-Based Oxide".

[11] E. S. Zakaria, I. M. Ali and H. F. Aly. *Adsorption* 2004, **10**, 237-244. "Adsorption Behaviour of ^{134}Cs and ^{22}Na Ions on Tin and Titanium Ferrocyanides".

[12] M. Ávila, C. Vargas, H. Yee-Madeira, E. Reguera. *ZAAC* 2010, **636**, 1968-1973. "Titanium^{3+} Hexacyanometallates (II): Preparation and Porous Framework ".

4.1.3. Concluding remarks of "Ti-PBA as anode *vs.* Na^+/Na"

To sum up, it can be concluded that the Ti-PBA materials obtained by the direct syntheses in organic and aqueous media, detailed in sections 3.1.2.2 and 3.1.2.4, turned out to beelectrochemically inactive as anodes in NIB. Thus, their utilization at low potential range for this type of technology should be discarded.

4.2. Na-PB as anode vs. Na^+/Na and vs. Li^+/Li. Optimization for NIB

4.2.1. Scope

Prussian Blue and its analogues are being extensively investigated as cathode materials both in LIB[13, 14, 15] and NIB[16], affording promising results. On the contrary, few efforts have been invested in exploring their electrochemical properties at low voltages. Solely three contemporaneous studies have been carried out with Mn- and Co-based PBA as anodes in LIB.[17, 18, 19] Therefore, it was considered interesting to analyze the performance of this kind of metalorganic framework as anode in NIB. For simplistic reasons, purely iron based Prussian Blue was the targeted material. With the objective of avoiding a possible competition between the cations in the insertion/extraction process when it is cycled *vs*. Na^+/Na, the sodium containing phase Na-PB (ideally $NaFe[Fe(CN)_6]$) was the material chosen to be explored. Since Na-PB had not been studied as anode neither for LIB, it was deemed appropiate to test it too.

4.2.2. Electrochemical characterization - results and discussion

Galvanostatic measurements were conducted both *vs*. Na^+/Na and *vs*. Li^+/Li, in the cut-off voltage of 5 mV - 1.6 V by using two-electrode coin-type cells (CR2032). All the measurements were performed at a current density of C/10, being $1C_{th}$, Na-PB = 92.18 mAh $g^{-1}/1A^+$ insertion per formula unit (A = Na, Li).

Electrodes of Na-PB were prepared in powder form (see procedure detailed in chapter 2, section 2.2.4.2.1) and the electrolytes deployed were respectively 1 M $NaClO_4$ in EC: DMC 50:50 % vol. *vs*. Na^+/Na and 1M $LiPF_6$ in EC: DMC 50:50 % vol. *vs*. Li^+/Li.

The first galvanostatic discharge of Na-PB displays a small plateau at 3.0 V (ca. 57 mAh·g^{-1}) and a plateau at ca. 0.5 V both *vs*. Na^+/Na and Li^+/Li, as shows Figure 4.5. The lower voltage plateau is better defined and shows larger capacity in the cells tested against lithium. Approximately twice the discharge capacity is obtained in the latter, i.e., about 1300 mAh·g^{-1} compared to the 650 mAh·g^{-1} in NIB. The material provided 74 and 292 mAh·g^{-1} of reversible capacity in the first charge, accordingly, *vs.* Na^+/Na and *vs.* Li^+/Li, giving evidence that Na-PB could eventually function as anode for both technologies.

---

[13] N. Imanishi, T. Morikawa, J. Kondo, Y. Takeda, O. Yamamoto, N. Kinugasa, T. Yamagishi. *J. Power Sources* 1999, **79**, 215–219. “Lithium intercalatino behavior into cyanide complex as positive electrode of lithium secondary battery”.

[14] L. Shen, Z. Wang, L. Chen. *Chem. Eur. J.* 2014, **20** (39), 12559-12562. “Prussian Blue as Cathode Material for Lithium Ion Batteries”.

[15] D. Asakura, M. Okubo, Y. Mizuno, T. Kudo, H. Zhou, K. Ikedo, T. Mizokawa, N. Kojima. *J. Phys. Chem. C* 2012, **116**, 8364. “Fabrication of a Cyanide-Bridge Coordination Polymer Electrode for Enhanced Electrochemical Ion Storage Ability”.

[16] Y. Lu, L. Wang, J. Cheng, J. B. Goodenough. *Chem. Comm.* 2012, **48**, 6544. “Prussian blue: a new framework of electrode materials for sodium batteries”.

[17] M. Shokouhimehr, S-H. Yu, D-C. Lee, D. Ling, T. Hyeon, Y-E. Sung. *NanoSci. and Nanotech. Lett.* 2013, **5**, 770-774. “Metal Hexacyanoferrate Nanoparticles as Electrode Materials for Lithium Ion Batteries”.

[18] P. Nie, L. Shen, H. Luo, B. Ding, G. Xu, J. Wang, X. Zhang. *J. Mater. Chem.* A, 2014, **2**, 5852. “Prussian blue analogues: a new class of anode materials for lithium ion batteries”.

[19] P. Xiong, G. Zeng, L. Zeng, M. Wei. *Dalton Trans.* 2015, **44**, 16746-16751. “Prussian blue analogues $Mn[Fe(CN)_6]_{0.6667}{\cdot}nH_2O$ cubes as an anode material for lithium-ion batteries”.

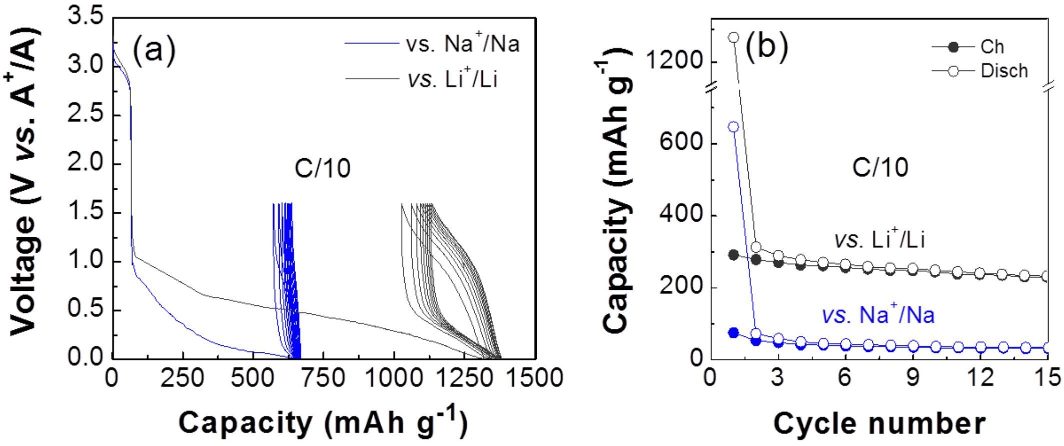

Figure 4.5. a) Voltage profile of the 10 first cycles and b) capacity *vs*. number of cycles plot of Na-PB when tested in powder *vs*. Na$^+$/Na (in blue) using 1M $NaClO_4$ in EC:DMC 50:50 % vol and *vs*. Li$^+$/Li (gray) using 1M $LiPF_6$ in EC:DMC 50:50 % vol/vol. Filled circles represent charge capacities while empty circles refer to the discharge capacities.

To enhance the electrochemical properties of the material, new cells were assembled using laminated electrodes, following the general procedure detailed in chapter 2 (section 2.2.4.2.1). In this occasion, the electrolyte utilized for sodium measurements was changed to 1 M $NaPF_6$ in EC: PC: FEC 49:49:2 % vol.

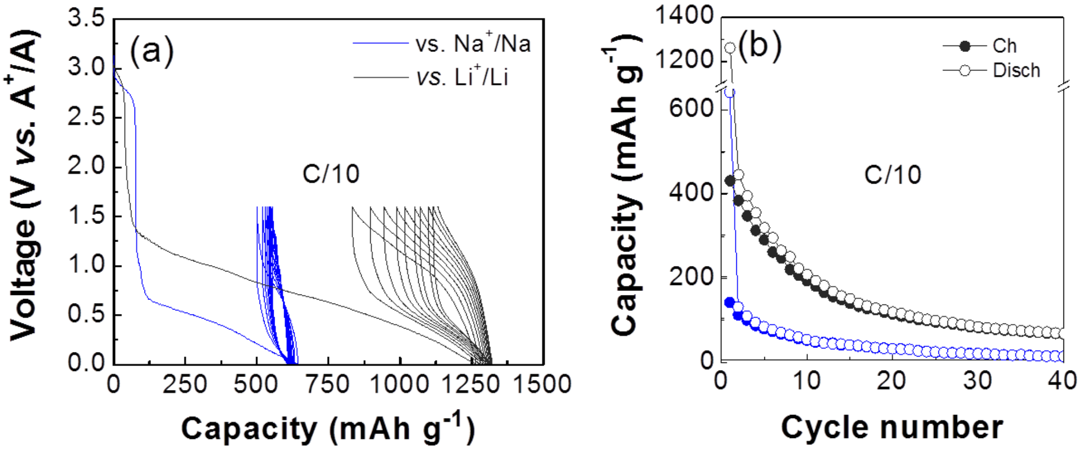

Figure 4.6. Left) Voltage profile of the 10 first cycles of Na-PB electrodes when tested *vs*. Na$^+$/Na (blue) using 1M $NaPF_6$ in EC: PC: FEC 49:49:2 % vol and *vs*. Li$^+$/Li (black) using 1M $LiPF_6$ in EC:DMC 50:50 % vol. Right) Capacity *vs*. number of cycles of Na-PB when tested for NIB (blue dots) and LIB (black dots).

The voltage profiles (see Figure 4.6) are quite similar to those obtained with Na-PB in powder. However, in cells assembled with electrodes, the lower voltage plateau becomes more defined in the sodium experiment and an increment from 0.5 to 0.75 V in the potential of the pseudo-plateau is observed *vs*. Li$^+$/Li. It is worth mentioning that the values of the irreversible capacity for the first discharge remains the same compared to powder while a marked improvement in the reversible capacities is achieved. Up to 143 and 430 mAh·g^{-1} of reversible capacity are achieved in the first charge, respectively, *vs.* Na$^+$/Na and *vs*. Li$^+$/Li. Nevertheless, the capacity retention is poor.

At this point, and because the priority of this work was to find materials for NIB, it was determined to concentrate the attention on the performance of Na-PB *vs.* Na^+/Na. The capacity fading observed could be explained by the formation of dendrites, which is known to occur at such a low voltage range due to the use of alkali metal as counter electrodes.[20] Given that Na metal is the anode used for testing new materials for NIB technology, the plating and stripping of sodium could not be avoided and it was necessary to contemplate other additive effects. Since the material is being tested as negative electrode, another plausible reason for the capacity fading is whether the SEI layer formed is stable enough. It is well known that SEI layer composition basically depends on the electrolyte deployed.[4] In this study, the electrolyte used was 1 M $NaPF_6$ in EC: PC: FEC 49:49:2 % vol. As will be discussed in the following chapter (Chapter 5, section 5.1), 1 M $NaPF_6$ in EC: PC: FEC 49:49:2 % vol resulted to be the optimum electrolyte among several combinations explored for Prussian Blue cathodes *vs*. Na^+/Na. Besides, the combination of 1M $NaPF_6$ in EC: PC has already been proposed as standard electrolyte for Na-ion batteries, as a result of the compendium of suitable features if offers.[21] Furthermore, the addition of a small percentage of FEC has also demonstrated to upgrade the capacity retention and the coulombic efficiency of anode materials in NIB.[22] Consequently, the choice of this electrolyte it is justified. Other parameter which has not been deeply investigated but that could also play an important role in the SEI formation is the binder component.[23]

4.2.2.1. Optimization of type of binder and % wt. of binder

For this purpose, the binders Solef® PVDF, sodium CMC (M.W. ca. 250000 g/mol, Sigma Aldrich), polytetrafluoroethylene (PTFE) and EPDM rubber were explored. The reasons that promote the election of these binders are explained below. PVDF is the universal binder used since the establishment of Li-ion batteries. EPDM is an organic binder that could provide a non-fluorinated alternative to PVDF. CMC is an aqueous-based binder considered as potential alternative to replace PVDF, which avoids the utilization of toxic NMP. The benefit of the utilization of PTFE, another aqueous-based binder, resides in its capacity of allowing prepare self-standing electrodes.

Electrodes were prepared by mixing Na-PB with amorphous carbon (Super C65) and the binder dissolved in their corresponding solvent in an 80:10:10 ratio, following the procedure described in section 2.2.4.2.1. Solef® PVDF was dissolved in NMP, sodium CMC was solubilized in a mixture ethanol/H_2O, polytetrafluoroethylene (PTFE) 60 wt. % in H_2O was dispersed in ethanol and EPDM rubber 50 wt. % was dissolved in cyclohexane. Typically, the slurries were then casted on Al foil and dried under vacuum at 80°C overnight, except for PTFE which provided self-standing electrodes. As usual, disc electrodes were punched, pressed and dried under vacuum again at 80°C overnight.

---

[20] D. I. Iermakova, R. Dugas, M. R. Palacín, A. Ponrouch. *J. Electrochem. Soc.* 2015, **162** (13), A7060-A7066. "On the Comparative Stability of Li and Na Metal Anode Interfaces in Conventional Alkyl Carbonate Electrolytes".

[21] A. Ponrouch, E. Marchante, M. Courty, J.-M. Tarascon, M.R. Palacín, *Energy Environ. Sci.* 2012, **5,** 8572–8583. "In search of an optimized electrolyte for Na-ion batteries".

[22] S. Komaba, T. Ishikawa, N. Yabuuchi, W. Murata, A. Ito, Y. Ohsawa. *ACS Appl. Mater. Interfaces* 2011, **3,** 4165–4168. "Fluorinated Ethylene Carbonate as Electrolyte Additive for Rechargeable Na Batteries".

[23] T. Jaumann, J. Balach, M. Klose, S. Oswald, U. Langklotz, A. Michaelis, J. Eckert, L. Giebeler. *Phys. Chem. Chem. Phys.* 2015, **17**, 24956. "SEI-component formation on sub 5 nm sized silicon nanoparticles in Li-ion batteries: the role of electrode preparation, FEC addition and binder".

It is necessary to highlight that, when Na-PB slurry is prepared with CMC as binder dissolving it in H_2O, the mechanical properties of the electrodes are not adequate. When the mixture is extended over the current collector foil, a total lack of wettability and adherence to the metal is observed. This fact is probably due to the apparent solubility of Na-PB in H_2O, which forms a colloidal suspension with high surface tension as a consequence of the small particle size. However, if the slurry is prepared using EtOH as solvent but adding few drops of H_2O, the previous problem is solved. It seems that EtOH, which was the solvent used to force the precipitation of Na-PB (see section 3.2.2), avoids the partial dissolution of Na-PB and electrodes completely glued to the foil are then achieved.

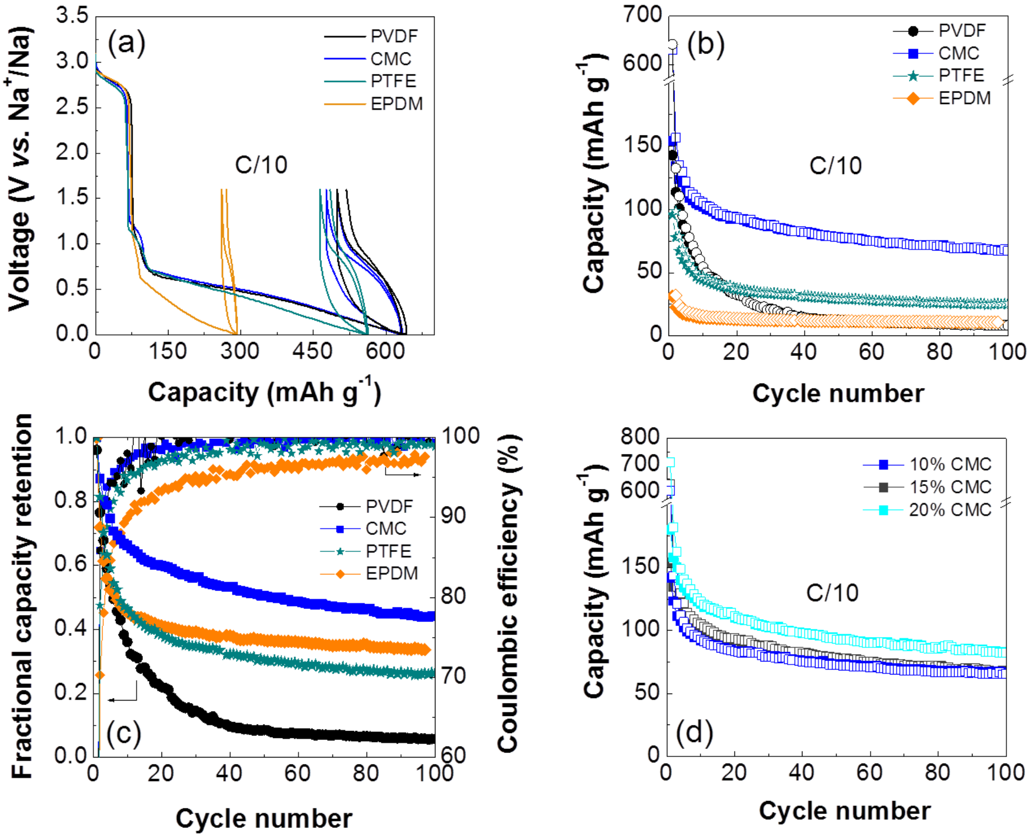

Figure 4.7. a) Voltage profile, b) capacity *vs.* cycle number and b) coulombic efficiency & fractional capacity retention *vs.* cycle number of Na-PB electrodes prepared using 10 % wt. of different binders (PVDF, CMC, EPCM or PTFE) and tested in NIB. d) Capacity vs. cycle number of Na-PB electrodes containing different % of CMC *vs.* Na^+/Na. The electrolyte deployed was 1M $NaPF_6$ in EC: PC: FEC 49:49:2 % vol/vol, in all the cases. Measurements were performed at a current density of C/10, being $1C_{th}$, Na-PB = 92.18 mAh $g^{-1}/1Na^+$ insertion per formula unit.

Figure 4.7a illustrates the voltage profile comparison of the Na-PB electrodes prepared with different binders, when cycled *vs.* Na^+/Na in the voltage range from 5 mV to 1.6 V. Clearly (see Figure 4.7b), the binder providing better capacity and cycle life to Na-PB as anode is CMC, while EPDM displayed the worst behavior, followed closely by PVDF. The CMC based Na-PB electrodes exhibited specific charges of up to 150 $mAh{\cdot}g^{-1}$, coulombic efficiencies of nearly 99% after 25 cycles and the higher capacity retention at the end of the galvanostatic test (after 100 cycles), as show Figure 4.7c. Surprisingly, PVDF and PTFE also presented fairly good capacity in the first cycle (respectively, ca. 140 $mAh{\cdot}g^{-1}$ and 100 $mAh{\cdot}g^{-1}$), although it drastically dropped just after few cycles. These results are consistent with those reported by Chou et al., who referred that some water based binders have proved to work better for anodes in contrast to PVDF.[24] Indeed, the replacement of PVDF, only soluble in toxic NMP, by environmentally friendly aqueousbased binders such as CMC or PTFE, is very convenient.

As it was suggested previously, one argument for the amelioration produced would be based in the influence of the binder in the SEI formation. It has already been demonstrated that the choice of the binder affects the chemical composition of the SEI and its thickness. In fact, the use of CMC as binder in NIB leads to the formation of a thinner passivation layer that homogeneously covers the surface of the active material. On the contrary, PVdF binder presents a more pronounced degradation of the electrolyte and thereby generates a thicker SEI layer.[25, 26,27]

After evidencing that CMC is the best binder among those here tested for Na-PB when acting as anode, different percentages of this component were assayed to determine the optimum value in the electrode. Three different percentages (10, 15 and 20% wt.) of CMC were evaluated, varying the amount of active material while keeping a 10% wt. of carbon C-65. Noting Figure 4.7d, there is no much difference between adding 10% or 15% of CMC, although the best capacity is reached with 20% CMC. Probably, the higher the amount of binder, the greater the stickness to the current collector and, consequently, the better capacity achieved. However, the usage of 20% of binder is non-viable, as habitual formulations in the market only contain 3-5 % of binder.

Consequently, some electrodes with a new formulation were prepared. The solution came by means of the utilization of styrene-butadiene rubber (SBR). This SBR copolymer is water resistance and is characterized by its strong adhesion. The SBR/CMC composite recipe is generally used in aqueous binders, with SBR as the primary binder and CMC as a thickening/setting agent.[28] Consequently, Na-PB electrodes were prepared in a mixture of EtOH/H_2O by mixing the active material (Na-PB), carbon (Super C65) and the binders (SBR/CMC) in a proportion 85:10:3:2. Na-PB laminated electrodes were then tested in the anodic range *vs*. Na^+/Na and 1M $NaPF_6$ in EC: PC: FEC 49.49:2 % vol was the electrolyte selected.

---

[24] S.-L. Chou, Y. Pan, Y.-Z. Wang, H.-K. Liu, S.-X. Dou, *Phys. Chem. Chem. Phys.* 2014, **1**6, 20347–20359. “Small things make a big difference: binder effects of the performance of Li and Na batteries”.

[25] M. Dahbi, T. Nakano, N. Yabuuchi, T. Ishikawa, K. Kubota, M. Fukunishi, S. Shibara, J-Y. Son, Y-T. Cui, H. Oji, S. Komaba. *Electrochem. Commun.* 2014, **4**4, 66-69. “Sodium carboxymethyl cellulose as potential binder for hard-carbon negative electrodes in sodium-ion batteries”.

[26] L. Bodenes, A. Darwiche, L. Monconduit, H. Martínez. *J. Power Sources*, 2015, **273**, 14-24. “The Solid Electrolyte Interphase a key parameter of the high performance of Sb in sodium-ion batteries: Comparative X-ray Photoelectron Spectroscopy Study of Sb/Na-ion and Sb/Li-ion batteries.”

[27] M. A. Muñoz-Márquez, M. Zarrabeitia, E. Castillo-Martínez, A. Eguía-Barrio, T. Rojo, M. Casas-Cabanas. *ACS Appl. Mater. Interfaces* 2016, **7** (14), 7801-7808. “Composition and Evolution of the Solid-Electrolyte Interphase in $Na_2Ti_3O_7$ Electrodes for Na-ion Batteries: XPS and Auger Parameter Analysis”.

[28] J-P. Yen, C-C. Chang, Y-R. Lin, X-T. Shen, J-L. Hong. *J. Electrochem. Soc*. 2013, **160** (10), A1811-A1818. “Effects of Styrene-Butadiene Rubber/Carboxymethylcellulose (SBR/CMC) and Polyvinylidene Difluoride (PVDF) Binders on Low Temperature Lithium Ion Batteries”.

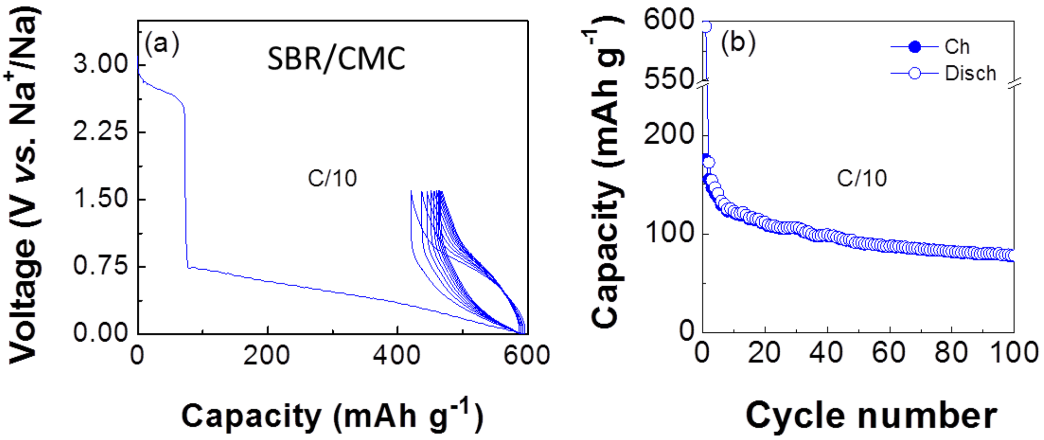

Figure 4.8. a) Voltage profile (10 first cycles) and b) Capacity *vs*. cycle number of Na-PB when tested for NIB using a SBR/CMC composite as binder. The electrolyte deployed was 1M $NaPF_6$ in EC: PC: FEC 49:49:2 % vol/vol, in all the cases. Measurements were performed at a current density of C/10, being $1C_{th}$, Na-PB = 92.18 mAh g^{-1}/1Na^+ insertion per formula unit.

The voltage profile of Na-PB is quite reproducible, as Figure 4.8a demonstrates. Nevertheless, the capacity values of the electrodes containing only 5% of the composite SBR/CMC are as good as (120 mAh·g^{-1} after 10 cycles) those obtained with 20% of CMC, what represents an effective improvement in the cost of materials and optimization of dead weight components of the battery.

4.2.3. Concluding remarks of "Na-PB as anode *vs.* Na^+/Na and *vs.* Li^+/Li. Optimization for NIB"

It is the first time that Na-PB has been investigated as anode both for NIB and LIB. Preliminary electrochemical results were encouraging, as Na-PB delivered *ca*. 140 mAh·g^{-1} *vs*. Na^+/Na and up to 430 mAh·g^{-1} *vs*. Li^+/Li of reversible capacity in the first charge. Further optimization of the electrode formulation was accomplished for NIB. The sodium CMC binder has demonstrated to act as the most suitable binder with Na-PB, among those here selected for testing. The definitive electrode composition results from a proportion 85: 10: 5 of active material (Na-PB): C-65: SBR/CMC, that provides 80 mAh·g^{-1} after 100 cycles at C/10.

4.3. K-PB as anode vs. Li$^+$/Li and vs. Na$^+$/Na. Mechanistic insights for LIB

4.3.1. Motivation

As mentioned before, Prussian Blue, ideally formulated as KFe[Fe(CN)$_6$]·xH$_2$O, is the more appealing system among the Prussian Blue derivatives by simplistic reasons of preparation, abundance of elements contained on it and cost. In parallel to the research in Na-PB, the study of the feasibility of K-PB as negative electrode for sodium and lithium ion batteries (NIB and LIB) was developed.

4.3.2. Electrochemical characterization - results and discussion

Similarly to its sodiated phase Na-PB, K-PB was investigated as anode material both *vs*. Na$^+$/Na and *vs*. Li$^+$/Li, in the cut-off voltage of 5 mV - 1.6 V.

Analogously to Na-PB, the material was first tested in powder form. In experiments for NIB, 1 M NaClO$_4$ in EC: DMC 50:50 % vol was used as electrolyte. Likewise, 1M LiPF$_6$ in EC: DMC 50:50 % vol was utilized for LIB.

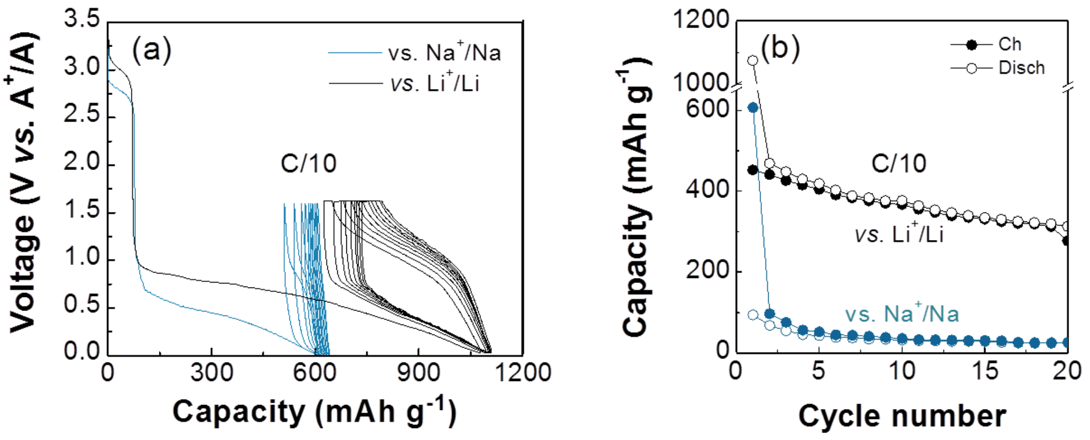

Figure 4.9. a) Voltage profile of the 10 first galvanostatic cycles of K-PB when tested in powder *vs*. Na$^+$/Na (blue) using 1M NaClO$_4$ in EC:DMC 50:50 % vol/vol and *vs*. Li$^+$/Li (black) using 1M LiPF$_6$ in EC:DMC 50:50 % vol. b) Capacity *vs*. number of cycles of K-PB when tested for NIB (blue) and LIB (black). Filled symbols always represent charge and empty symbols are associated to the discharge capacity values.

Figure 4.9 depicts the voltage profile of K-PB when cycled against Na$^+$/Na (plotted in blue) and Li$^+$/Li (plotted in black) at a current density of C/10, considering 1C$_{th}$, K-PB = 87.5 mAh g^{-1} / 1A$^+$ insertion (A = Na, Li) per formula unit. A couple of plateaus are appreciated along the first discharge, at 2.75 and 0.45 V *vs*. Na$^+$/Na and at 3.0 V and 0.6 V *vs*. Li$^+$/Li. The higher voltage plateau is attributed to the intercalation of Li$^+$ accompanied by the reduction of the ionic HS Fe^{3+} to HS Fe^{2+}, while the lower voltage plateau is the product of the combination of the formation of the SEI layer and additional redox processes that will be later discussed. As it happened with Na-PB, about half of the capacity is obtained along the first discharge when sodium experiment is contrasted with regard to the lithium. Also, reversible capacities equivalent to those displayed by Na-PB are achieved. K-PB roughly exhibits 95 mAh·g^{-1} in NIB and up to 450 mAh·g^{-1} in LIB, that fiercely decay to 33 mAh·g^{-1} and 375 mAh·g^{-1}, respectively, after only 10 cycles. It is worth mentioning the similarities encountered between the performance of K-PB and Na-PB vs. Na^{+}/Na, as well as the differences observed *vs.* Li^{+}/Li, such as the huge reversible capacity achieved with K-PB (450 mAh·g^{-1}) compared to the 300 mAh·g^{-1} obtained with the analogous Na-PB in the same conditions.

Since the results provided *vs.* Na^{+}/Na resembled those achieved with Na-PB in powder, and similar progress to that attained with Na-PB when using CMC as a binder can be presumed, no more efforts were invested in the study of K-PB as anode *vs.* Na^{+}/Na. Research was centered on the study of the K-PB operation as anode in LIB, given the improvement found in the reversible capacity of K-PB *vs.* Na-PB. In consequence, new experiments were performed incorporating the preparation of K-PB laminated electrodes.

Commercial (Solvionic) 1M LiPF$_6$ in EC: DMC was the electrolyte utilized. The current density was fixed at the following Crates: 20C, 10C, 2C, C, C/10 and C/100, based on the theoretical capacity aforementioned (1 C$_{th}$, K-PB = 87.5 mAh·g^{-1}). Typical cell loadings were 2-6 mg of active material per coin cell and reported data are single run for typical results.

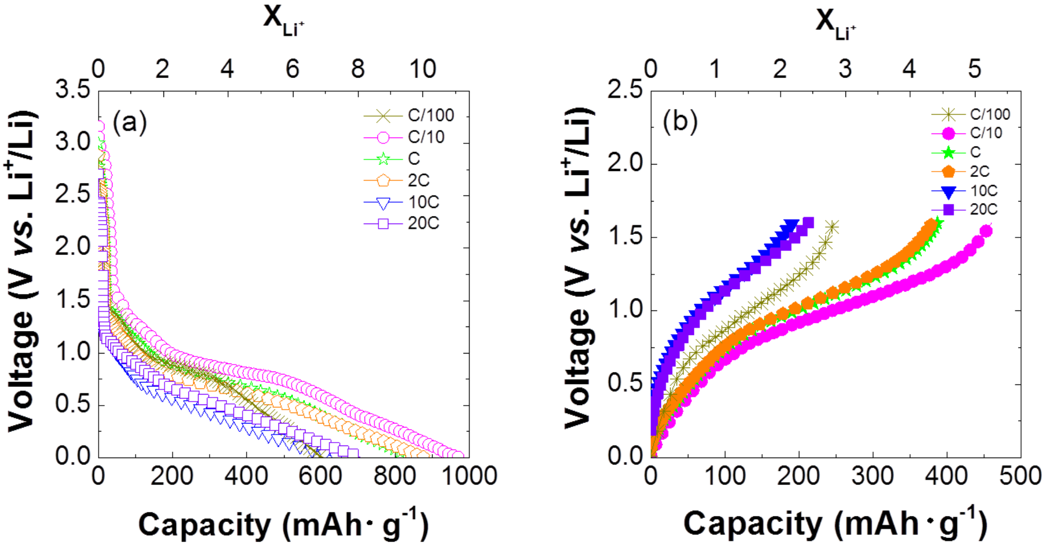

Figure 4.10. Galvanostatic first discharge (a) and first charge (b) curves of K-PB cells measured at different currents (from C/100 = 0.875 mA·g^{-1} to 20C = 1.750 A·g^{-1}) in the voltage range of 0.005 - 1.6 V *vs.* Li^{+}/Li.

Figure 4.10a shows the first galvanostatic discharge profiles of K-PB *vs.* Li^{+}/Li at several C-rates (20C, 10C, 2C, C, C/10 and C/100). A different cell was used for each current density. The discharge capacity is higher at low currents, as expected. However, this trend is not followed at C/100, maybe because of the electrolyte degradation, as the battery required one month to complete its first discharge. Several redox processes occur between 0.1 and 1.5 V. A couple of pseudo-plateaus between 0.8-0.9 V which are clearly observed at low (C/100 and C/10) and moderate (1C and 2C) rate capabilities, but fade out at higher current densities. Regardless of the rate deployed, a very large irreversible capacity is noted in the first cycle as a consequence of the SEI layer formation. Although this irreversibility varies between 600 - 1000 mAh·g^{-1} in function of the rate, the material possesses a fairly good reversible capacity. Up to 450 mAh·g^{-1} are observed in the first charge at C/10 (see Figure 4.10b) and even 200 mAh·g^{-1} at high current densities as 20C (1.75 A·g^{-1}), what makes this material a good candidate as anode for lithium ion batteries.

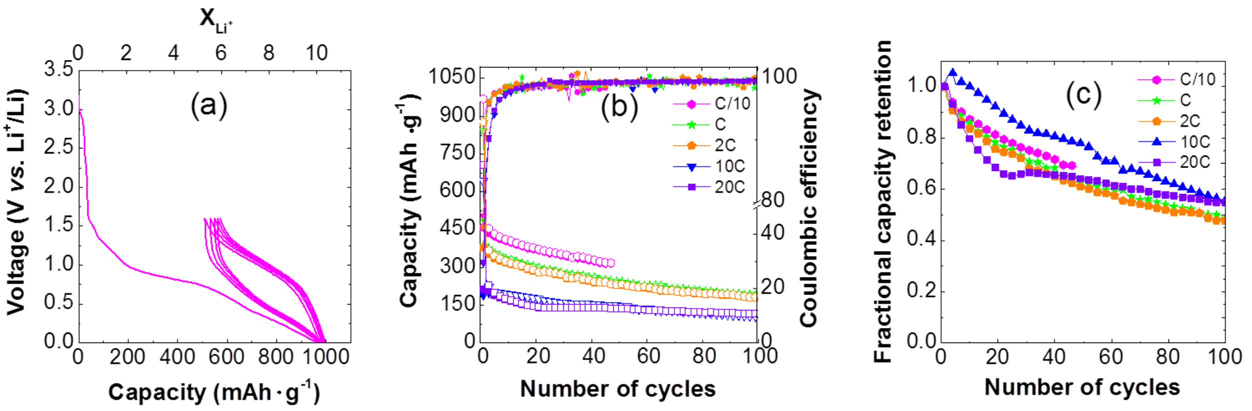

Figure 4.11. Electrochemical performance of K-PB when tested *vs*. lithium with $LiPF_6$ in EC: DMC. a) Voltage profile during the five first cycles of galvanostatic discharge and charge at C/10. b) Specific capacity of PB at different C-rates and their coulombic efficiency. c) Capacity retention *vs*. cycle number for different C-rates.

Besides, K-PB displays a nice cyclability that reversibly inserts and de-inserts about 5 Li^+/formula unit with a hysteresis of ca. 0.5 V, as observed in Figure 4.11a. Only after 20 cycles, the coulombic efficiency remains between 98-100% (Figure 4.11b), indicating that a stable SEI layer has been formed. Despite the reversible capacity increases when the C-rate decreases (Figure 4.11b), as usual, the capacity retention (Figure 4.11c) does not follow the opposite tendency, i.e., it does not diminish when the C-rate decreases. For instance, the retention at C/10 is slightly higher than at 1C or 2C. In any case, after 100 cycles all batteries showed between 50 and 60% of capacity retention, which is still far from optimum.

Comparable high capacities have only been reported by Sung and Zhang, who explored the properties of Co-based PBA in the 0.01-3.0 V range *vs*. Li^+/Li.[29, 30] No insights into the possible reaction mechanism were given by Sung while Zhang suggested the formation of Co^I once the cell is completely discharged, following the mechanism proposed by Cui for Mn-PBA as anode in an aqueous electrolyte battery.[31]

The large reversible capacity showed by the K-PB cannot be simply explained by the intercalation mechanism of 1 or 2 Li^+ atoms and, unlike Mn or Co, Fe(I) coordinated to CN ligand has not been reported. Intercalation and accompanying reduction of Fe(III) to Fe(II) is known to occur at voltages between 2.0 and 4.3 V *vs*. lithium or sodium with reversible capacities of 100-170 mAh·g^{-1}.[32, 33, 34, 35] Therefore, it seems very likely that a displacement or conversion reaction is taking place at voltages

---

[29] M. Shokouhimehr, S-H. Yu, D-C. Lee, D. Ling, T. Hyeon, Y-E. Sung. *Nanosci. Nanotechnol. Lett.* 2013, **5** (7), 770-774. "Methal Hexacyanoferrate Nanoparticles as Electrode Materials for Lithium Ion Batteries".

[30] P. Nie, L. Shen, H. Luo, B. Ding, G. Xu, J. Wang, X. Zhang, *J. Mater. Chem. A* 2014, 2, 5852-5857. "Prussian Blue analogues: a new class of anode materials for lithium ion batteries".

[31] M. Pasta, C.D. Wessells, N. Liu, J. Nelson, M.T.McDowell, R.A. Huggins, M.F. Toney, Y. Cui, *Nat. Commun.* 2014, 5. DOI: 10.1038.ncomms4007. "Full open-framework batteries for stationary energy storage".

[32] Y. Lu, L. Wang, J. Cheng, J.B. Goodenough, *Chem. Commun*. 2012, **48**, 6544-6546. "Prussian Blue: a new framework of electrode materials for sodium batteries".

[33] T. Matsuda, M. Takachi, Y. Moritomo, *Chem. Commun.* 2013, **49**, 2750-2752. "A sodium manganese ferrocyanide thin film for Na-ion batteries".

[34] Y. You, X.-L. Wu, Y.-X. Yin, Y.-G. Guo, *Energy Environ. Sci.* 2014, **7**, 1643-1647. "High-quality Prussian blue crystals as superior cathode materials for room-temperature sodium-ion batteries".

[35] N. Imanishi, T. Morikawa, J. Kondo, Y. Takeda, O. Yamamoto, N. Kinugasa, T. Yamagishi, *J. Power Sources* 1999, **79**, 215-219. "Lithium intercalation behavior into iron cyanide complex as positive electrode of lithium secondary battery".

below 2V, as it has been observed for many metal organic framework based materials.[36] In consequence, the reaction mechanism will be studied in detail in section 4.3.3.

4.3.2.1. The role of water. Prussian blue vs Prussian white.

Since intense O-H bands are visible in the IR spectra (as showed in Figure 3.30), it was interesting to determine whether water was playing a major role in the electrochemical performance of this compound. Previous studies revealed that hydration affects the activation energy of alkali ions diffusion, such as Li^+, $Na^{+,}$ or Mg^{2+}, improving its diffusion and interfacial transfer into the K-PB structure and resulting in a high power output.[37] Nevertheless, the reasoning behind it only applies to measurements in aqueous media. On the other hand, the presence of water has also been shown to be beneficial and even necessary for reactions in organic media. In the case of the performance of K-PB as positive electrode, removal of zeolitic water by heating up to 150 ˚C have little effect on the electrochemistry.[35] However coordinating water molecules, that will be lost at higher temperatures, are necessary for lithium intercalation into K-PB affecting strongly its electrochemical behaviour. This is also the case for the reversible Mg^{2+} electrochemical surface reaction in layered vanadium oxides.[38, 39]

To evaluate the role of water in K-PB operating as anode in organic media, the completely reduced form of K-PB, that is potassium Prussian White (K-PW) $K_2Fe_2(CN)_6$, was tested As expected and as confirmed by TGA (see Appendix, Figure A4.2), K-PW presented no zeolitic water present in the channels.

Electrochemical measurements on K-PW *vs*. Li^+/Li were done in the same conditions than for K-PB (Figure 4.12). The reversible capacity of K-PW is similar to that achieved for K-PB although the irreversibility of K-PW is much lower than the observed for K-PB (see Figure 4.12a). The reduction in the irreversible component at higher voltages is logical, as a result of the initial oxidation states of the transition metallic centers (K-PB begins reducing HS Fe^{3+} to HS Fe^{2+} while K-PW skip this step, since it starts from both iron in oxidation state II). Additional phenomena, may be contributing to the descent of the rest of the irreversible component, such as the cessation of reduction reaction of H_2O, which is in trace level in K-PW. However, the similar reversible capacity (350 $mAh \cdot g^{-1}$ after 10 cycles) and capacity retention observed in both phases seems to indicate that the presence of zeolitic water is not playing an important role in Li^+ diffusion, as previously suggested. Nevertheless, the electrochemistry of both materials cannot be directly compared because of the different particle size that both exhibit, being K-PW more crystalline and presenting larger particle size (as shown in Figure 3.40) than the aggregates of nanoparticles of K-PB.

---

[36] P. Tran-Van, K. Barthelet, M. Morcrette, M. Herlem, J.-M. Tarascon, A.K. Cheetham, G. Férey. *J. New Mater. Electrochem. Syst.* 2003, **6** (1), 29-31. "Reactivity of Lithium with a Microporous Phosphate".

[37] Y. Mizuno; M. Okubo, E. Hosono, T. Kudo, H. Zhow and K. Oh-ishi. *J. Phys. Chem. C* 2013, **117**, 10877-10882. "Suppressed Activation Energy for Interfacial Charge Transfer of a Prussian Blue Analog Thin Film Electrode with Hydrated Ions (Li^+, Na^+ and Mg^{2+})".

[38] P. Novak, W. Scheifele and O. Haas. *J. Power Sources* 1995, **54** (2), 479-482. "Magnesium insertion batteries – an alternative to lithium?".

[39] P. Novak, W. Scheifele, F. Joho and O. Haas. *J. Electrochem. Soc.* 1995, **142** (8), 2544-2550. "Electrochemical Insertion of Magnesium into Hydrated Vanadium Bronzes".

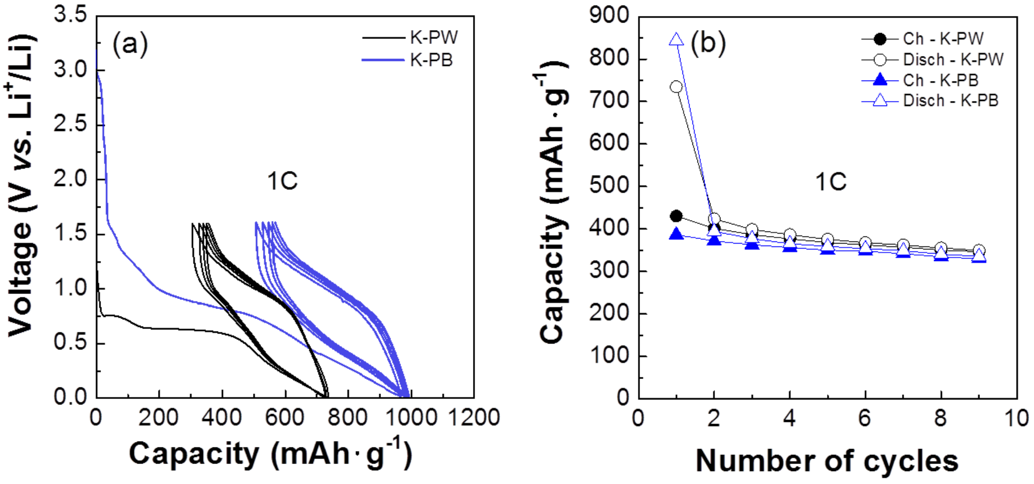

Figure 4.12. a) Electrochemical profile of K-PW (in black) compared to the corresponding profile of K-PB (in blue). b) Capacity vs cycles number of K-PW (black dots) and K-PB (blue triangles) *vs*. Li^+/Li, using $LiPF_6$ 1M EC: DMC as electrolyte, in a voltage window of 0.005 - 1.6V and cycled at 1C (being $C_{th,\ PW}$=77.5mAh/g per $1Li^+$/f.u.).

4.3.2.2. Prussian Blue binder optimization.

Similarly to Na-PB, K-PB electrodes were prepared also using SBR/CMC binder composite. K-PB laminated electrodes were prepared by mixing the active material (K-PB), carbon (Super C65) and the binders (SBR/CMC) in a proportion 85:10:3:2 in a mixture of EtOH/H_2O. For the new electrochemical test, 1M $LiPF_6$ in EC: DMC 1:1 % vol. was kept as electrolyte.

The performance of the electrodes containing SBR/CMC binder was explored in the voltage range of 5 mV – 1.6 V *vs*. Li^+/Li, at a current density of 1C (see Figure 4.12). Again, the voltage profile (Figure 4.13a) resembles those already observed for K-PB at low voltage range (as shown in Figure 4.9a, Figure 4.11a and Figure 4.12).

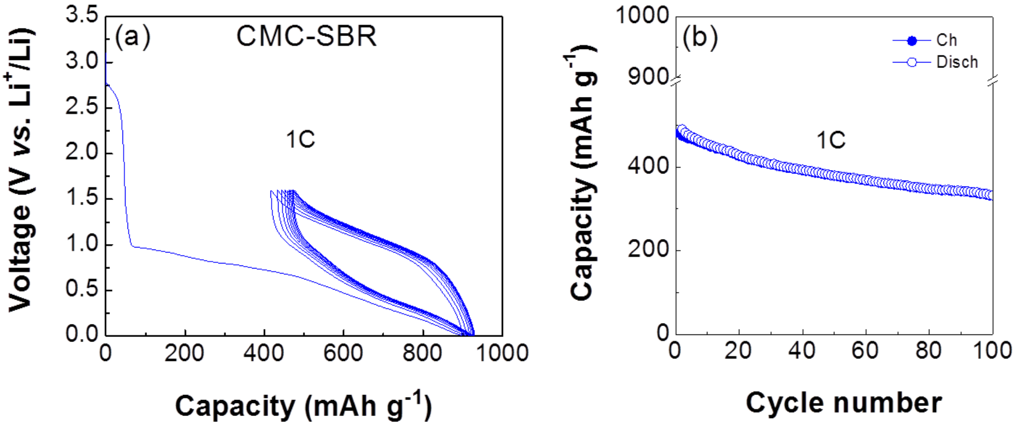

Figure 4.13. a) Voltage profile and b) capacity *vs*. cycle number of K-PB when tested for LIB using a SBR/CMC composite as binder. The electrolyte deployed was 1M $LiPF_6$ in EC: DMC 50:50 % vol. Measurements were performed at a current density of 1C, being $1C_{th}$, K-PB = 87.5 mAh $g^{-1}/1Na^+$ insertion per formula unit.

In light of the results obtained, it is necessary to draw the attention in the advantageous enhancement achieved. By using the mixture SBR/CMC, K-PB has reached reversible capacities of up to 480 mAh·g^{-1} at a current density of 1C, and it retains 330 mAh·g^{-1} after 100 cycles (Figure 4.13b). If these results are contrasted to the analogous obtained deploying PVDF as binder (375 mAh·g^{-1} were achieved in the first cycle at 1C and ca. 225 mAh·g^{-1} after 100 cycles), one can see the convenient boost in terms of capacity. Thus, for the first time, it has been demonstrated the impressive optimization achieved for K-PB as anode in LIB when SBR/CMC replace PVDF as binder. In addition, it is believed that the use of this SBR/CMC binder can be extended to other PBA and also to other systems operating as anodes for NIB.

4.3.3. Elucidation of the reaction mechanism of K-PB *vs.* Li^+/Li

To understand if a displacement reaction could be responsible for the observed electrochemical behaviour of Na-PB and K-PB *vs*. Li^+/Li, *ex-situ* XRD and IR data of cycled K-PB electrodes after stopping and opening them at different stages of the first discharge and charge were collected (see Figure 4.14a).

The XRD diffractogram of the initial K-PB electrode (Figure 4.14.b.i) exhibits the most intense reflections of Prussian Blue (at 2Θ =17.41, 24.72, 35.24 and 39.57°). When the electrode is reduced only to 1.6 V (Figure 4.14.b.ii), no clear structural changes are observed as K-PW formed is expected to have all iron reduced to Fe^{2+} while keeping the framework structure and all cavities filled by alkali cations ($K_{1-x}Fe_{1+(x/3)}{}^{3+}[Fe^{II}(CN)_6]\cdot yH_2O \rightarrow Li_{1+(x/3)}K_{1-x}Fe_{1+(x/3)}{}^{2+}[Fe^{II}(CN)_6]$). However, once K-PW is fully discharged down to 0.005 V (Figure 4.14.b.iii), all reflections belonging to K-PB disappear at the same time that another, corresponding to $LiPF_6$ from imbibing solvent, appears at 2Θ=25.14°. This suggests cleavage of the crystalline lattice which commonly occurs in displacement reactions.[40] In addition, new reflections at 32.5 and 35.7° can be guessed in the completely discharged electrode (Figure 4.14.b.iii). Following the hypothesis of the displacement reaction, these peaks can be attributed to the formation of Fe_2O_3, as a result of the oxidation, during the eventual exposure to air while collecting XRD, of nanometric metallic Fe that would have been formed along the reduction process. During the following charge up to 1.6 V (Figure 4.14.b.iv) only a broad band at 2Θ=19.41°, assigned to the Kapton® protection. Finally, the diffractogram from the fully charged cell (Figure 4.14.b.v) displays a new reflection due to KPF_6 which suggests that Li^+ has replaced K^+ in the electrolyte. The absence of additional reflections indicates that the Prussian blue long range structure is not restored upon oxidation.

---

[40] H. Li, P. Balaya, J. Maier. *J. Electrochem. Soc.* 2004, **151** (11), A1878-A1885. "Li-storage via Heterogeneous Reaction in Selected Binary Metal Fluorides and Oxides".

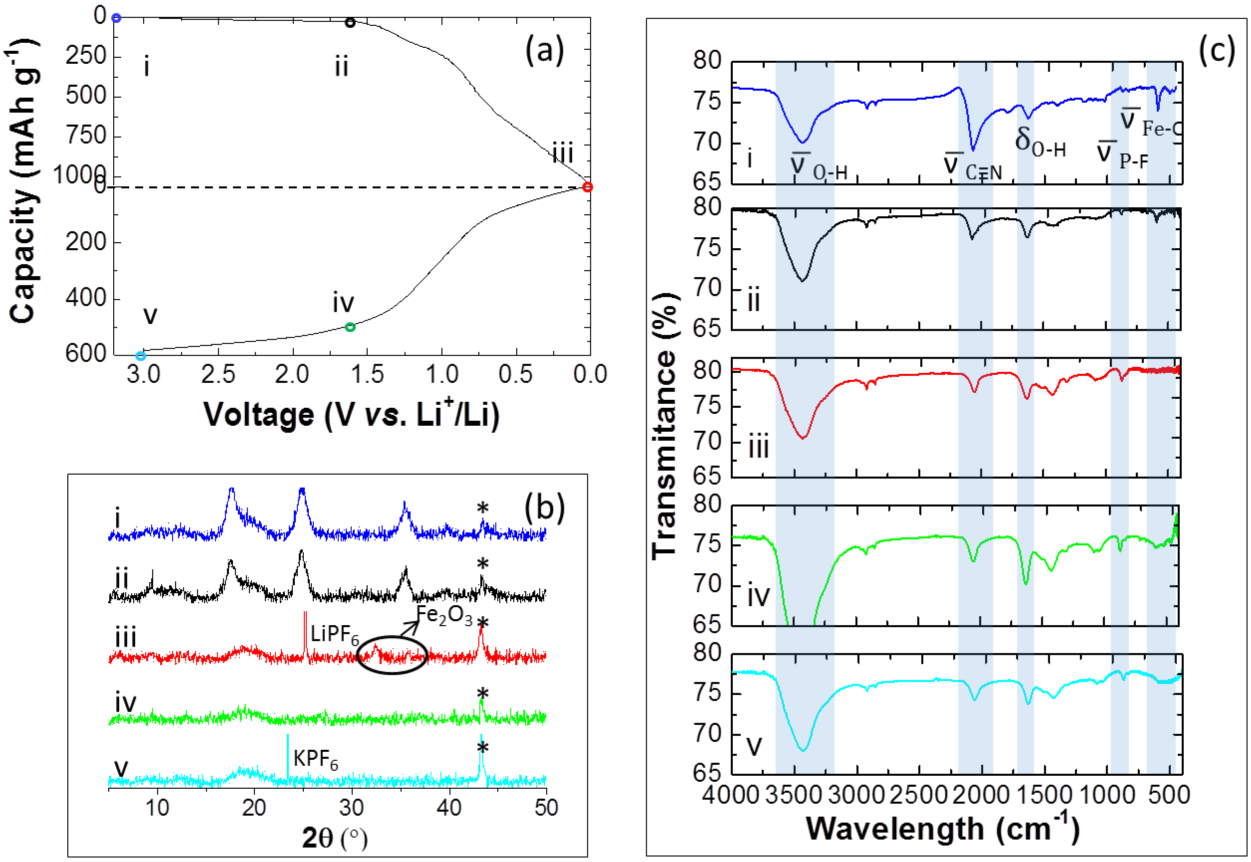

Figure 4.14. a) First discharge and charge profile of K-PB/lithium cell at RT in a voltage range of 0.005 - 3.2 V. b) XR diffractograms of the electrodes stopped at different points (i, ii, iii, iv, v) of the galvanostatic curve of a. The reflections due to the Cu-foil are marked with an *. c) IR spectra of the electrodes in the different points (i, ii, iii, iv, v) of the galvanostatic curve (a).

The FTIR spectra of the electrodes shown in Figure 4.14.c demonstrate the presence of absorption bands corresponding to the stretching of hydroxyl ($\bar{\boldsymbol{\nu}}_{\mathbf{O-H}}$), cyanide ($\bar{\boldsymbol{\nu}}_{\mathbf{C\equiv N}}$), P-F bonds ($\bar{\boldsymbol{\nu}}_{\mathbf{P-F}}$) and Fe-C bonds ($\bar{\boldsymbol{\nu}}_{\mathbf{Fe-CN}}$), as well as the bending of hydroxyl ($\boldsymbol{\delta}_{\mathbf{O-H}}$), that are highlighted with shading. When the electrode gets discharged (see Figure 4.14c, i-iii), the intensity of the cyanide band decreases and it is partially recovered once it is fully charged (see Figure 4.14c, iii-v). If the reduction in intensity of this band was related to the cleavage of C≡N, the 2080 cm^{-1} absorption band would disappear, which is not the case. Besides, the sharp Fe-C band from the Fe-C≡N bond at 592 cm^{-1} disappears when the electrode is reduced and seems to reappear as a broad band when it gets oxidized again. Since the Fe-C bond breaks while the C≡N bond remains, other metal cyanide, likely LiCN or KCN, must be forming and the reduction of intensity of the CN band can be attributed to the partial solubility of LiCN or the formed cyanide in the electrolyte. Comparison of FTIR spectra of fresh electrolyte, electrolyte in contact with K-PB and the glass fiber of a fully discharged battery of PB confirm this hypothesis (see Figure 4.15).

Figure 4.15a presents the FTIR spectrum of the commercial electrolyte, 1M LiPF$_6$ EC: DMC. Whereas the FTIR of the electrolyte mixed with K-PB (Figure 4.15b) displays no trace of the C≡N band and a very similar profile to that obtained for the pure electrolyte, C≡N vibrations are clearly observed at 2188 and 2076 cm^{-1} in the FTIR spectra of DMC in contact with the glass fibre separator of the discharged battery (Figure 4.15c). Therefore, we can state that K-PB is not soluble in LiPF$_6$ 1M EC: DMC and that the discharge products have higher solubility in the electrolyte than K-PB. Despite having CN^- ions in solution, the basicity of the electrolyte under these reducing conditions prevent the formation of risky compounds.

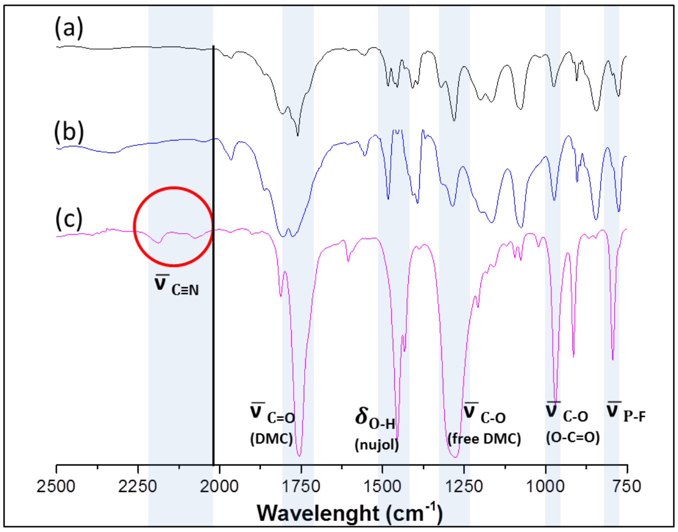

Figure 4.15. FTIR spectra of a) the electrolyte (1 M $LiPF_6$ in EC: DMC 1:1 % vol), b) the electrolyte in contact with PB and c) the glass fiber of a fully discharged battery washed with DMC.

Lower lattice energy is expected for LiCN with respect to other alkali metal cyanides such as KCN, which are highly ionic salts.[41] Because of this low lattice energy, a high solubility is expected for LiCN, as it is observed in DMF.[42] However the only reported measurements of solubility of LiCN in carbonate electrolytes correspond to a very low value. A solubility = 10^{-5} g/l in PC was deduced from titration of a solution containing Et_4NCN and Et_4NClO_4 with $LiClO_4$.[43] These low values might result from its possible association into soluble non-ionic complexes. Solubility of 0.24 g/l was on the other hand reported for KCN in pure PC.[44] In the case of the discharged electrode, the presence of dissolved CN^- in the glass fiber separator suggests a high solubility of LiCN, which is partially dissolved even in the presence of high concentration and high activity solutions of 1M $LiPF_6$ in carbonates electrolytes.[45]

Besides the confirmation of the formation of cyanide species different from K-PB, SEM-STEM and bright field TEM images of the totally discharged electrode (Figure 4.16) manifest the presence of bright and dark nanoparticles, which could be ascribed to iron containing nanoparticles. By SEM-STEM microscopy, it is possible to obtain images in which the contrast is directly related to the atomic number (Z). The STEM images of the pristine material (Figure 4.16a, b) show a homogeneous contrast all along the particles which represents a more homogeneous iron distribution. Bright spots (marked by dashed ovals) within a darker matrix were however observed in the discharged electrodes (Figure 4.16c, d). These bright spots,

---

[41] D. F. C. Morris. *Acta Cryst.* 1961, **14**, 547-548. “Crystal radius of the cyanide ion”.

[42] T. J. Markley, B. H. Toby, R. M. Pearlstein and D. Ramprasad. *Inorg. Chem.* 1997, **36**, 3376-3378. “New Synthesis Routes to Lithium and Cesium Cyanide Salts”

[43] T. Nakamura and K. Izutsu. *Anal. Sci.* 1991, **7**, 1677-1679. “The Fluoride and Cyanide ions-selective sensor for use in nonaqueous solution based on the membrane of polyacrylamide coupled to phthalocyanine cobalt”.

[44] M. J. Blandamer, J. Burgess and A. J. Duffield. *Dalton Trans.* 1980, **1**, 1-6. “Solubitliy of potassium cyanide in mixed aqueous and non-aqueous media; Gibbs free energies of transfer of the cyanide ion”.

[45] L. O. Valoen, J. N. Reimers. *J. Electrochem. Soc.* 2005, **152**, A882-A891. “Transport properties of $LiPF_6$-Based Li-ion Battery Electrolytes”.

not observed in the pristine electrodes (Figure 4.16a, b) were related to Fe containing nanoparticles formed during the discharge process.

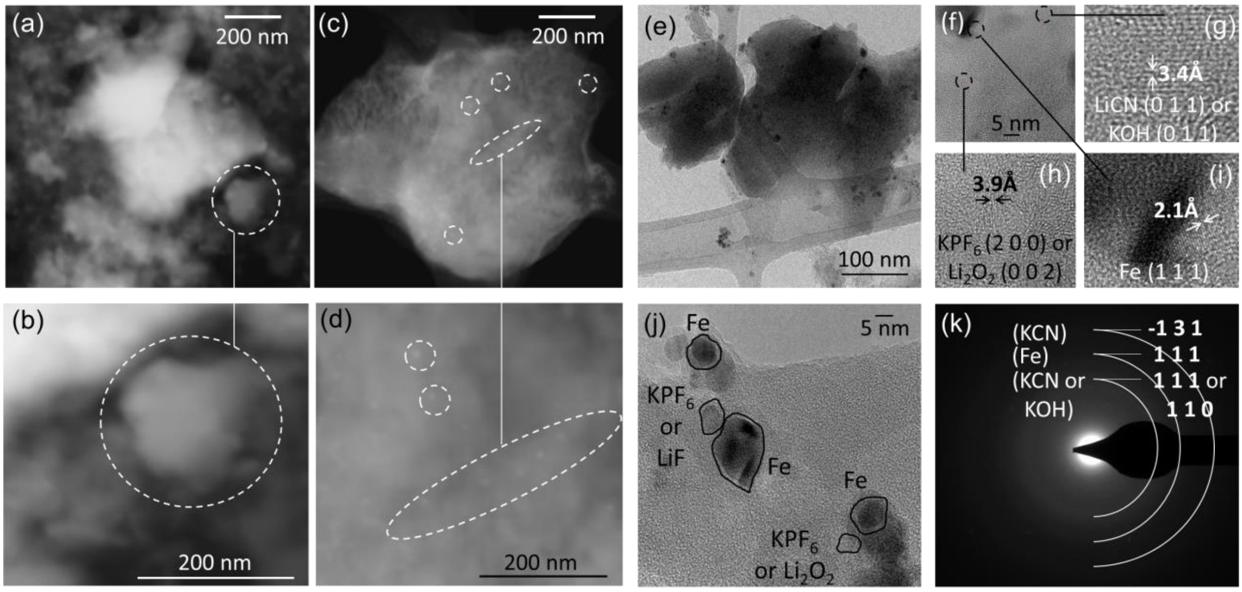

Figure 4.16. SEM-STEM images of the pristine material K-PB (a), the material completely discharged (c), and zoomed zones of both of them, respectively (b, d). e) Bright field TEM image of the material from a fully discharged half battery, f) TEM image of a completely discharged battery displaying several domains, and their magnifications (g, h and i). j) Different domains observed in a completely discharged battery, possibly containing Fe, LiF and KPF_6. k) Electron diffraction pattern of another area of the same fully discharged battery. White lines schematically indicate the broad diffraction rings with the crystallographic planes of possible reaction compounds.

These iron containing nanoparticles can also be observed in bright field TEM, but in this case as very small dark nanoparticles (of ca. 5 nm) (Figure 4.16e). In Figure 4.16f, the darker domains can be assigned to elemental Fe, since the 2.1 Å interplanar distance could belong to the (1 1 1) lattice plane, as observed in Figure 4.16i. Likewise, other interplanar spacings can be observed as weak contrast within the matrix. Lattice fringes of 3.4 Å could be assigned to the (0 1 1) crystallographic plane of LiCN or KOH (Figure 4.16g). Interplanar distances of 3.9 Å distances could be attributed to the (2 0 0) crystallographic plane of KPF_6 (Figure 4.16h) or to the (0 0 2) of Li_2O_2. However, Li_2O_2 is unlikely to form in such reducing conditions. In Figure 4.16j, the domain allocations have been done again based on the interplanar distances measured and how they coincided with the different compounds listed as possible components of the matrix. In agreement with these TEM images, the electron diffraction rings (Figure 4.16k) can be allotted to the interplanar spacings of metallic Fe (2.1 Å) and KCN or KOH.From these TEM results, it can therefore be concluded that interplanar spacing close to those of metallic Fe (2.1 Å) are found in these particles (Figure 4.16i). These nanoparticles are embedded into a matrix of less crystalline material which shows interplanar distances that could belong to KOH, KCN and LiCN, LiF and KPF_6 or Li_2O_2 (Figure 4.16g, h, i, j, k).

Based on the above PXRD, FTIR, SEM and TEM experiments on cycled electrodes, the idea of a displacement reaction is reinforced. The proposed mechanism thought to take place during discharge involves the complete reduction of $Fe^{III/II}$ into metallic Fe^0 nanoparticles along with an unrecoverable loss of structure of PB with Fe-C bond cleavage and possible formation of Li-CN bond (in the form of LiCN) or Li-O bond (in the form of LiOH) that compose an amorphous matrix. In addition, K^+ from the PB structure may also form the corresponding potassium salts. Upon oxidation, some Fe-O bonds seem to be formed, in agreement with the recovery of the stretching band at *ca*. 592 cm^{-1} in the IR (Figure 4.14c, iv and v), justifying the stable capacity. The suggested reduction reaction is described in equation Eq. 4.1, being x = 0.12, as shown by the results of Atomic Absorption Spectroscopy (AAS) (section 3.2.3.6, Table 3.6).

$$K_{1-x}Fe^{3+}_{1+(x/3)}[Fe^{II}(CN)_6]\cdot yH_2O \xrightarrow[+(1+(x/3))\ e^-]{+(1+(x/3))\ Li^+} Li_{1+(x/3)}K_{1-x}Fe^{2+}_{1+(x/3)}[Fe^{II}(CN)_6]\cdot yH_2O$$

$$\xrightarrow[+2\cdot(2+(x/3))\ e^-]{+2\cdot(2+(x/3))\ Li^+} 2+(x/3)\ Fe^0 + (5+x)LiZ + (1-x)KZ\ \ (Z= CN-, OH-, F-,\dots) \qquad \textbf{(Eq. 4.1)}$$

To determine unequivocally whether Fe^0 nanoparticles were generated during the electrochemical reduction, XAS and Mössbauer measurements were additionally performed.

Ex-situ XAS synchrotron measurements were carried out in electrodes cycled and stopped at different stages of the electrochemical curve, as in the *ex-situ* experiments above described but extending the number of points studied (see Figure 4.17a). Sample preparation was detailed in chapter 2 (section 2.1.10).

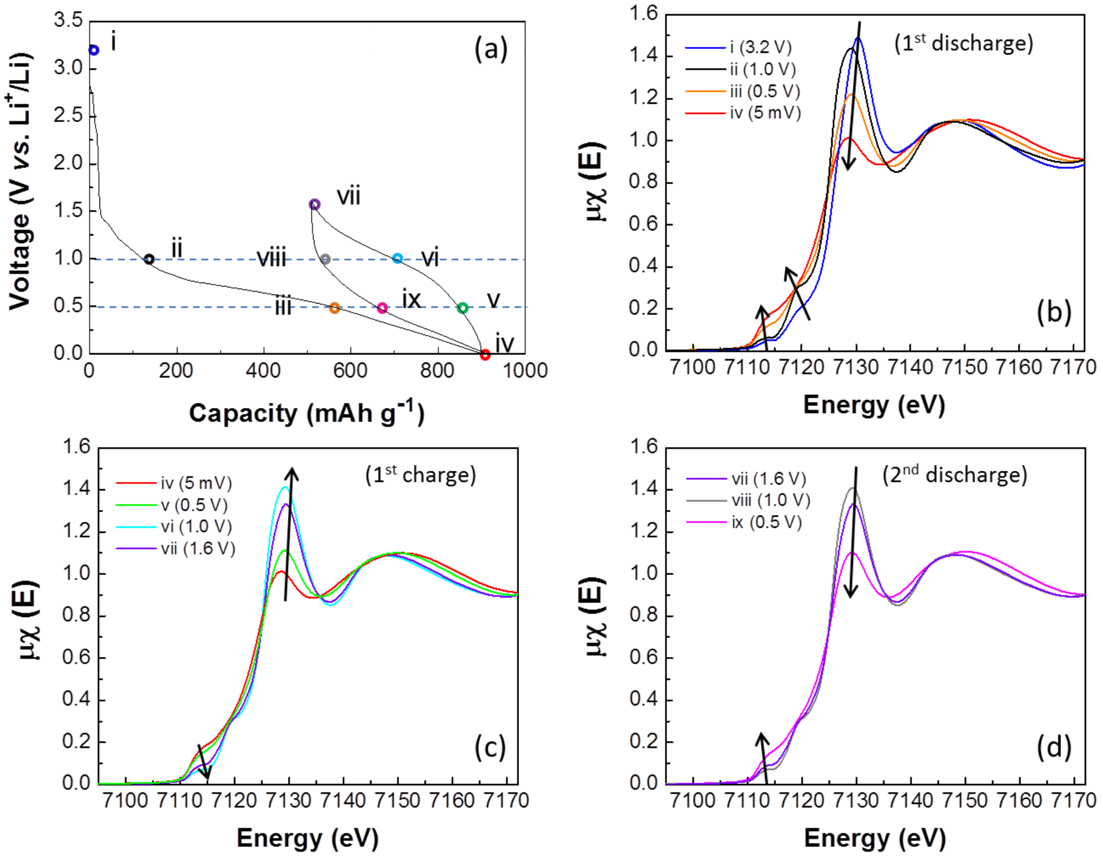

Figure 4.17. a) First discharge-charge profile and second discharge of K-PB *vs*. Li$^+$/Li at RT in a voltage range of 0.005 - 3.2 V. X-ray absorption spectra of K-PB at the Fe K-edge in the XANES region, respectively along the first discharge (a), first charge (b) and second discharge (d).

The XAS spectra of the first Li-insertion processes are shown in Figure 4.17b. A clear shift in the peak at 7130 eV (mixture of Fe^{2+}-Fe^{3+}) towards lower energy is observed along the reduction process. This shift down to 7128 eV is assigned to Fe^{2+} state and it is accompanied with the reduction in its peak intensity, which translates as a decline in its population. At the end of the reduction (point "iv") conversely, the peak at 7113.7 eV has augmented thus confirming the formation of Fe^{0} at the totally discharged state. Fitting of the spectrum "iv" with an iron metal standard and other spectrum "ii" indicated that at least 58% of the iron was reduced to Fe^{0}. The value referred to metallic iron sounds reasonable, accounting the data reported for FeF$_3$ conversion cathode in LIB in the totally discharged state.[46]

The trend is reverted, that is the population of Fe^{2+} increases and that of Fe^{0} decreases, when the first charge occurs (Figure 4.17c) and it is again recovered in the subsequent discharge (Figure 4.17d), providing an idea of the reversibility of the process. Indeed, the XANES profile of spectra ii, vi and viii are identical between them and, the same way, spectra iii, v and ix too.

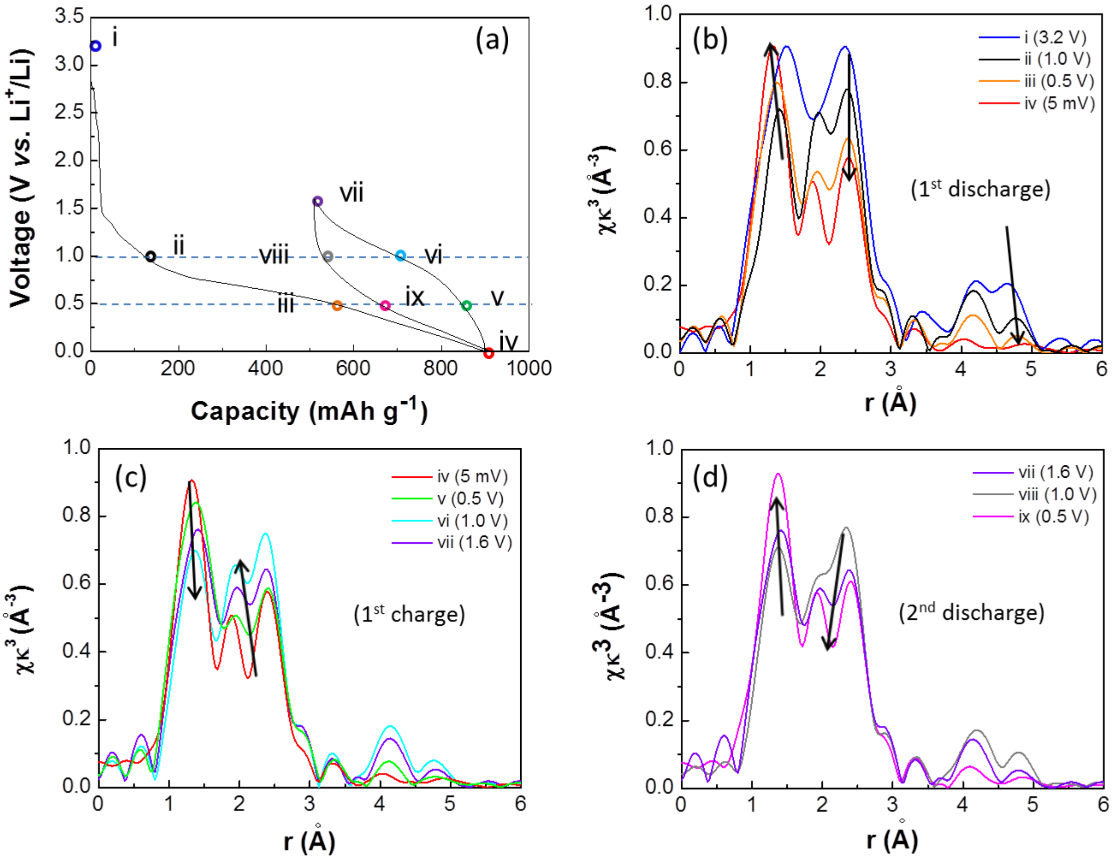

Figure 4.18. a) First discharge and charge profile of K-PB/Li cell at RT in a voltage range of 0.005 - 3.2 V. X-ray absorption spectra of K-PB at the Fe K-edge in the EXAFS region, respectively along the first discharge (b), first charge (c) and second discharge (d).

EXAFS interpretation resulted more complicated (see Figure 4.18). The Fe-C (1.92 Å), Fe-N (2.03 Å) distances are too close to be able to distinguish between them and, additionally, the two EXAFS of the

---

[46] A. Pohl, M. Faraz, A. Schrörder, M. Baunach, W. Schabel, A. Guda, V. Shapovalov, A. Soldatov, V. S. k. Chakravadhanula, C. Kübel, R. Witte, H. Hann, T. Diemant, R. J. Behm, H. Emerich, M. Fichtner. *Journal of Power Sources*, 2016, **313**, 213-222. "Developments of water based process for stable converstion cathodes on the basis of Fe$_3$F."

two iron sites interfere in a complicated manner. What is certain is that the longer-range Fe-Fe distances at ca. 4.5 - 5 Å disappear along the first discharge, and it is not recovered in the subsequent cycle, thus indicating the rupture of the Prussian Blue structure and reinforcing the theory of the conversion/displacement mechanism.

In-situ Mössbauer spectra were continuously acquired all along the different cycling stages. The *in-situ* Mössbauer cell (prototype III) used for these measurements was developed in this thesis work, as already described in chapter 2 (section 2.2.4.1.1). The electrode preparation is also detailed in chapter 2 (section 2.2.4.2.1). As Figure 4.19 illustrates, the electrochemical performance obtained with prototype III is comparable to that observed using coin cells. However, in this measurement 260 mAh·g^{-1} of reversible capacity was obtained in the first cycle at a current density of 1C, compared to the 375 mAh·g^{-1} typically reached in a coin cell CR2032. This difference is probably due to the different electrode preparation method followed and the high-rise mass loading (39.158 mg *vs*. 2.0 mg of active material).

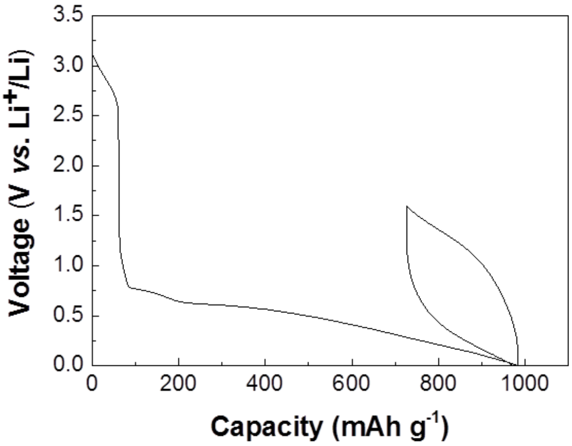

Figure 4.19. Electrochemical performance of K-PB against Li$^+$/Li at the anodic range from 5 mV to 1.6 V when cycled using the *in-situ* Mössbauer cell (prototype III). 1M $LiPF_6$ was the electrolyte deployed.

Mössbauer spectra collected along the first discharge are displayed in Figure 4.20. The spectrum of the initial material (3.2 V) is similar to that already shown in chapter 3 (see section 3.2.3.8, Figure 3.35b). It can be fitted using two main components: a singlet typical for a low spin LS Fe^{II} covalently linked to C (blue line) and a doublet assigned to a high spin HS Fe^{3+} ionically bonded to N (pink line). Below 2.78 V, a third component, attributed to the formation of HS Fe^{2+} as a consequence of the reduction of Fe($^{3+}$) ionic, appears as a doublet (green line). As it can be observed in the reduction from 2.78 V to 0.79 V, the population of the new HS Fe^{2+} increases as long as the HS Fe^{3+} is consumed. Indeed, at 0.79 V, the K-PB has completely evolved into K-PW and almost no trace of the initial Fe^{3+} is appreciated. From 0.68 V downwards, a new doublet component can be defined (orange line). According to some papers reported in the literature, the hyperfine parameters of this doublet can be ascribed to the formation of paramagnetic Fe^0 nanoparticles, usually observed at the end of the lithiation of conversion materials.[47,48] It is clear anyway that the proportion of Fe^0 augments when the voltage is reduced from 0.62 to 0.55 V at

---

[47] J. L. Tirado, P. Lavela, C. Pérez Vicente, B. León, C. Vidal-Abarca. *Hyperfine Interact.* 2012, **207**, 53-59. "Unfolding the role of iron in Li-ion conversión electrode materials by 57Fe Mössbauer spectroscopy".

[48] M. T. Sougrati, A. Darwiche, X. Liu, A. Mahmoud, R. P. Hermann, S. Jouen, L. Monconduit, R. Dronskowski, L. Stievano. *Angew. Chem. Intern. Ed.* 2016, **55**, 5090-5095. "Transition-Metal Carbodiimides as Molecular Negative Electrode Materials for Lithium- and Sodium-Ion Batteries with Excellent Cycling Properties."

the expense of the depletion of the HS Fe^{2+} (plotted in green). Finally, at 0.48 V, almost no HS Fe^{2+} remains. At this point of the electrochemical curve, an additional doublet makes an appearance (in purple). The formation of this new type of iron is subject to the consumption of the LS Fe^{2+}, which was invariant/intact until then. The parameters of the new iron generated, could not be matched to any known iron and it is tentatively assigned to the formation of Fe^0 with different structural environment to that precedent from the HS Fe^{2+}.

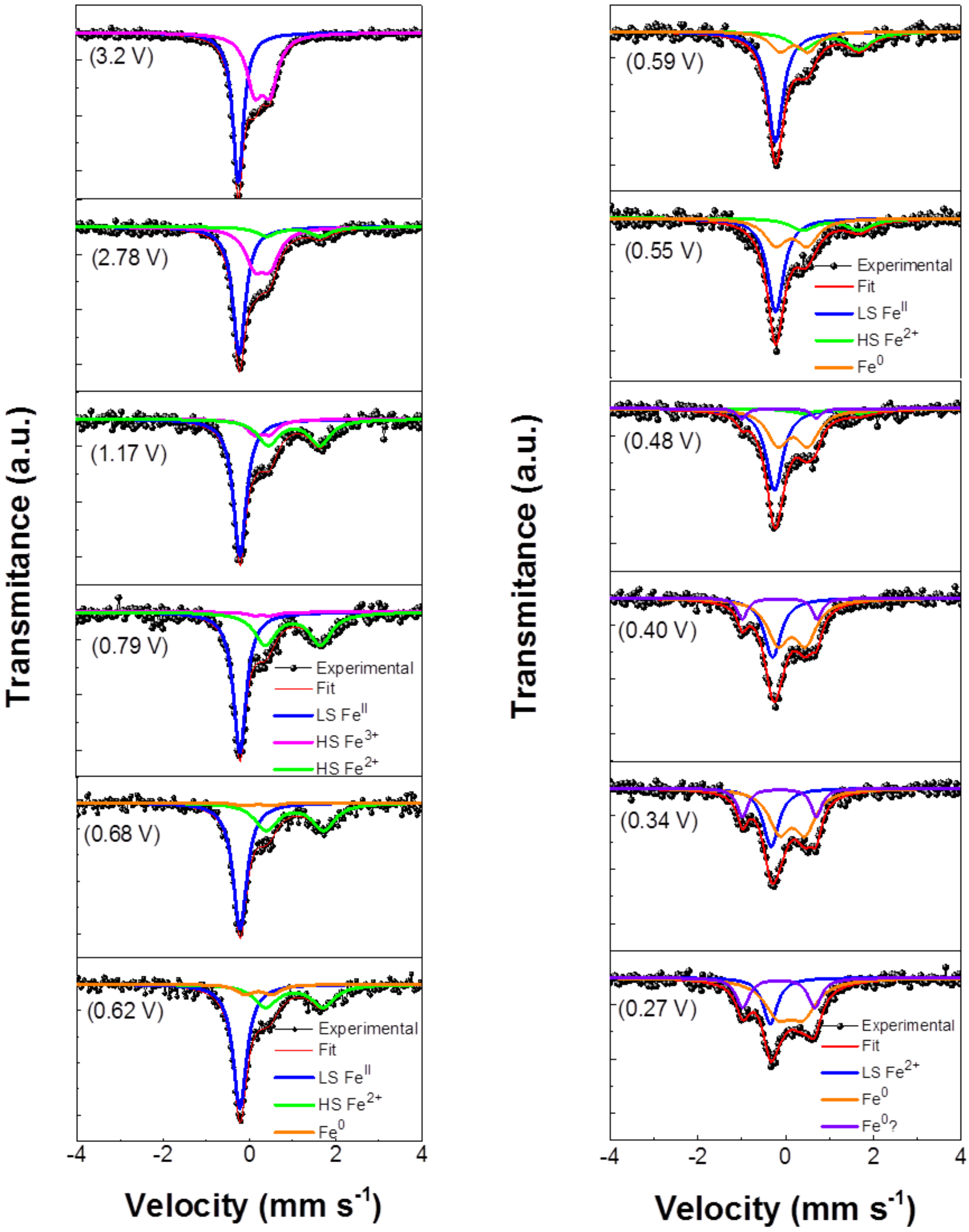

Figure 4.20. Mössbauer spectra obtained at different points of the electrochemical curve of K-PB *vs.* Li^+/Li, along the discharge, when using the in-situ Mössbauer cell here developed. Experimental (black dots) and fitting (red line) are shown along with the blue, pink, green, orange and purple solid lines that represent the LS Fe^{II}, HS Fe^{3+}, HS Fe^{2+}, Fe^0 and Fe^0? spectral components, respectively.

The hyperfine parameters of the different irons formed and its variation along the reduction are collected in the following table (Table 4.2):

Table 4.2. Hyperfine parameters **δ**, **Δ** and **WID** extracted from the Mössbauer fitting for ^{57}Fe in K-PB along the discharge curve (**δ** = isomer shift relative to Fe bcc, **Δ** = quadrupolar splitting, **WID** = width at half hight).

Voltage*	**Assignation**	**Isomer Shift, δ** (mm·s^{-1})	**Quadrupolar, Δ** (mm·s^{-1})	**WID** (mm·s^{-1})
0.5 V	l.s. Fe($^{2+}$)	- 0.12(2)	0	0.43(4)
0.76 V	h.s. Fe($^{3+}$)	0.42(2)	0.36(3)	-
0.68 V	h.s. Fe($^{2+}$)	1.14(2)	1.27(7)	0.66(6)
	Fe(0)	0.27(3)	0.64(6)	0.56(9)
	Fe(0)?	0.24(2)	1.68(4)	0.28(2)

*voltage down to what this type of iron is stable.

If not the totality of the mechanism occurring along the discharge was unveiled, the formation of Fe^0 nanoparticles was unequivocally confirmed by the *in-situ* Mössbauer experiments. In addition to XAS data, Mössbauer results undoubtedly vouch the conversion reaction mechanism that we previously proposed for the K-PB performance at low voltages in LIB.

Insights in the charge mechanism are still on-going. So far, it can be assure that a LS Fe^{2+} is formed at the totally oxidation state (that is 1.6 V), but the nature of the other iron (tentatively Fe^0) is still unknown.

4.3.4. Concluding remarks of "K-PB as anode *vs.* Li$^+$/Li and *vs.* Na$^+$/Na. Mechanistic insights for LIB"

It is the first time that purely iron-based K-PB has been investigated as anode for LIB. Preliminary electrochemical results were greatly successful, the material exhibiting comparable capacities to those presented by graphite. Since the huge reversible capacity obtained (up to 450 mAh·g^{-1}) could not be explained by a simple intercalation mechanism, a conversion reaction was proposed instead, as several evidences suggested (*ex-situ* experiments in cycled electrodes, including XRD, IR, SEM and TEM). Further investigations to elucidate the reaction mechanism were conducted by *ex-situ* XAS and *in-situ* Mössbauer, endorsing the formation of metallic Fe. As mentioned in chapter 2, the *in-situ* Mössbauer cell deployed in the measurements has been entirely developed in this thesis work. Additionally, the optimization of the electrochemical properties of K-PB has been performed by using SBR/CMC as binder, what constitutes another innovation.

Chapter 5

Prussian Blue phases as cathodes in Na-ion batteries

5.-) Prussian Blue phases as cathodes in Na-ion batteries

This chapter presents the electrochemical results achieved with Na-PB ($Na_{0.75}[Fe_{2.08}(CN)_6]\cdot 3.4H_2O$), Na-PW ($Na_{1.70}[Fe_{2.15}(CN)_6]\cdot 0.19H_2O$) and K-PW ($K_{1.59}Fe_{2.20}(CN)_6\cdot 0.26H_2O$) when evaluated as cathodes in NIB. It is divided in 3 main sections. The first section details a systematic study of the operability of sodium Prussian Blue (Na-PB) in organic media, by means of optimizing the electrolyte composition and type of binder deployed. Afterwards, the exploration of Na-PB as material for aqueous NIB and its comparison with the performance in organic media is discussed. The third and last part of this chapter is devoted to the assessment of the performance of the Prussian White reduced phases K-PW and Na-PW in organic Na-ion cells and the understanding of their different voltages of intercalation/ de-intercalation.

As mentioned in chapter 2, a table (Table 5.1) summarizing the formulation of the electrodes prepared for the electrochemical investigation as cathodes within this chapter is presented below.

Table 5.1. Electrode composition of the electrodes tested as cathodes within this chapter.

Electrode	Active material	Conductive Carbon	Binder	Proportion (a.m.: c.c.: b)*	Drying T (°C)	Electrolyte
Na-PB (laminate) Electrolyte optimization	Na-PB	Super C-65	PVDF	80: 10: 10	80	*see Table 5.2.*
Na-PB (laminate) *Binder optimization*	Na-PB	Super C-65	PVDF/CMC/PTFE/EPDM	80: 10: 10	80	$NaPF_6$ in EC:PC:FEC 49:49:2 % vol
Na-PB (laminate) *Aqueous study*	Na-PB	Super C-65	PVDF	85: 10: 5	120	$NaPF_6$ in EC:PC:FEC 49:49:2 % vol
A-PW (powder) (A = Na, K)	A-PW (A= Na, K)	Ketjen black	-	80: 20: 0	80	$NaPF_6$ in EC:PC:FEC 49:49:2 % vol
A-PW (laminate) (A = Na, K)	A-PW (A= Na, K)	Ketjen black	PVDF	70: 10:10	80	$NaPF_6$ in EC:PC:FEC 49:49:2 % vol

*a.m.: active material, c.c.: conductive carbon, b: binder.

5.1. Na-PB as cathode vs. Na^+/Na in organic media

5.1.1. Scope

As it was pointed in the introduction, Na-PB and its analogues have proved their feasibility as positive electrode materials in sodium-ion batteries. The aim of this study is to determine the optimum electrolyte and binder for Na-PB when used as cathodic electrode in NIB, with the intention of establishing them as standards for future studies with Prussian Blue related materials (PBA, PW, BG). Thus, different carbonate based electrolyte formulations and binder compositions were tested.

5.1.2. Electrochemical characterization - results and discussion

For testing the electrochemical properties of Na-PB *vs.* Na^+/Na, galvanostatic rate capabilities measurements were conducted at room temperature in the voltage window of 2.4 - 4.2 V in two-electrode coin-type half cells (CR 2032 type). Current densities were fixed to C/10, 1C, 10C and C/10, based on the theoretical capacity of 1C = C_{th}, Na-PB = 92.2 mAh· g^{-1} calculated considering the insertion of 1 Na^+/f.u.

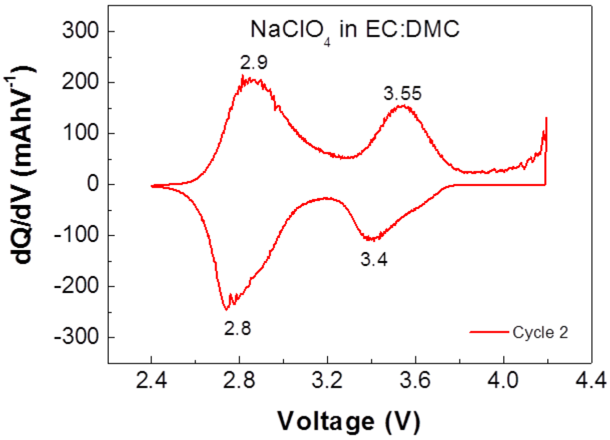

Figure 5.1. dQ/dV *vs.* voltage profile of the 2nd cycle at C/10 of Na-PB laminated electrode in the cut-off 2.4-4.2 V *vs.* Na^+/Na, using $NaClO_4$ in EC: DMC 50: 50 % vol.

The characteristic dQ/dV profile of Na-PB when cycled at C/10 along the cathodic range above mentioned is depicted in Figure 5.1. As expected, two plateaus are easily distinguished. Each plateau is associated to a different redox process, the lower voltage process (~2.8 V *vs.* Na^+/Na) corresponding to the reduction of Na-PB to Na-PW and the upper voltage plateau (~3.3 V) to the oxidation of Na-PB to BG, from the perspective/point of view of the Na-PB evolution, as shown (Eq. 5.1.).

$$\underset{\text{(Na-PW)}}{Na_{2-x}Fe_{1+x/3}^{2+}[Fe^{II}(CN)_6]\cdot yH_2O} \leftrightarrow \underset{\text{(Na-PB)}}{Na_{1-x}Fe_{1+x/3}^{3+}[Fe^{II}(CN)_6]\cdot yH_2O} \leftrightarrow \underset{\text{(BG)}}{Fe_{1+x/3}^{3+}\,[Fe_x^{III}(CN)_6]\cdot yH_2O} \qquad \textbf{(Eq. 5.1)}$$

5.1.2.1. Electrolyte election

For the election of the electrolyte, positive laminated electrodes were prepared according to the procedure described in chapter 2 (section 2.2.4.2.1). Common cell loadings were 1.5 - 3 mg of active material per coin cell. The data here displayed are single run for typical results.

To determine the most appropriate electrolyte for Na-PB, several carbonate mixtures (ethylene carbonate: propylene carbonate (EC: PC), ethylene carbonate: dimethyl carbonate (EC: DMC), ethylene carbonate: diethyl carbonate (EC: DEC)) containing either $NaClO_4$ or $NaPF_6$ as salt both with and without a 2% of fluorinated ethylene carbonate (FEC) as electrolyte additive were tested. All combinations deployed are listed in Table 5.2.

Table 5.2. Summary of the electrolytes tested for selecting the most optimal for Na-PB in NIB. Percentages are referred in % vol.

1M $NaClO_4$	**1M $NaPF_6$**
EC:PC (50:50)†	EC:PC (50:50)†
EC:PC:FEC (49:49:2)	EC:PC:FEC (49:49:2)†
ED:DMC (50:50)	ED:DMC (50:50)
EC:DMC:FEC (49:49:2)†	EC:DMC:FEC (49:49:2)
ED:DEC (50:50)	ED:DEC (50:50)
EC:DEC:FEC (49:49:2)	EC:DEC:FEC (49:49:2)
	PC:FEC (98:2)

Other sodium salts, different from $NaClO_4$ or $NaPF_6$, such as NaTf (sodium triflate), NaFSI (sodium bis(fluorosulfonyl) imide) or NaTFSI (sodium bis(trifluoromethanesulfonyl) imide), were not considered in this study as a result of the corrosion problem they present with the aluminum current collector.[1] The option of using Ionic liquids (IL) was neither contemplated due to their exorbitant cost of production and their impossibility of obtaining them without impurities, what alters their response and degrades their selectivity.[1]

The first galvanostatic discharge and the second galvanostatic charge profiles of Na-PB *vs*. Na^+/Na at C/10 are illustrated in Figure 5.2 The first charge is not shown given that the initial phase only contains 0.75 Na and less than one sodium can thus be de-inserted in the first oxidation of Na-PB to form BG (ideally $Fe_2(CN)_6$). As expected, two plateaus are easily distinguished in the voltage profile both in charge at ca. 2.9 and around 3.55 V *vs*. Na^+/Na and in discharge at ~ 2.8 and ~ 3.4 V. Table

---

[1] A. Ponrouch, D. Monti, A. Boschin, B. Steen, P. Johansson, M.R. Palacín, *J. Mater. Chem. A* 2015, **3**, 22-42. "Non-aqueous electrolytes for sodium-ion batteries."

5.3 collects the specific discharge values obtained for each electrolyte, where a significant difference of 22.85% is observed between the electrolytes providing the highest and lowest specific charge at C/10.

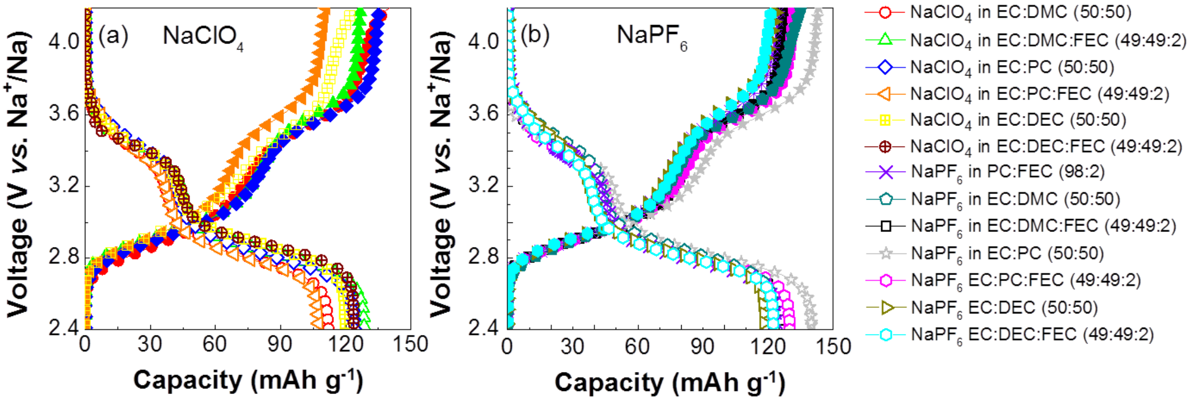

Figure 5.2. First discharge (empty symbols) and second charge (filled symbols) of the Na-PB when cycled *vs.* Na$^+$/Na using different electrolytes in the voltage window 2.4–4.2 V. Data of electrolytes containing $NaClO_4$ (a) or $NaPF_6$ (b) salts are plotted separately for clarity.

Table 5.3. First reversible specific discharges of Na-PB cycled using different electrolytes in the voltage window of 2.4-4.2 V.

	1M $NaClO_4$	**1M $NaPF_6$**
EC:PC (1:1)	**124 mAh·g^{-1}**	**140 mAh·g^{-1}**
EC:PC:FEC (49:49:2)	108 mAh·g^{-1}	**130 mAh·g^{-1}**
ED:DMC (1:1)	112 mAh·g^{-1}	123 mAh·g^{-1}
EC:DMC:FEC (49:49:2)	**129 mAh·g^{-1}**	127 mAh·g^{-1}
ED:DEC (1:1)	120 mAh·g^{-1}	118 mAh·g^{-1}
EC:DEC:FEC (49:49:2)	123 mAh·g^{-1}	123 mAh·g^{-1}
PC:FEC (98:2)	-	124 mAh·g^{-1}

Figure 5.3 compares the dQ/dV *vs*. V profiles of Na-PB electrodes cycled using the electrolytes 1M $NaPF_6$ in EC: PC (50: 50) and 1M $NaClO_4$ in EC: PC: FEC (49:49:2), which showed the highest and lowest reversible capacities among this series, respectively. No major change is observed in the redox processes from cycle 2 to cycle 5, suggesting that no electrode degradation is taking place and that Na-PB remained stable along cycling, regardless the electrolyte deployed. In addition, the area covering both redox processes when using $NaPF_6$ in EC: PC is bigger than the observed for $NaClO_4$ in EC: PC: FEC, as a result of the highest and lowest reversible specific charge reached, respectively.

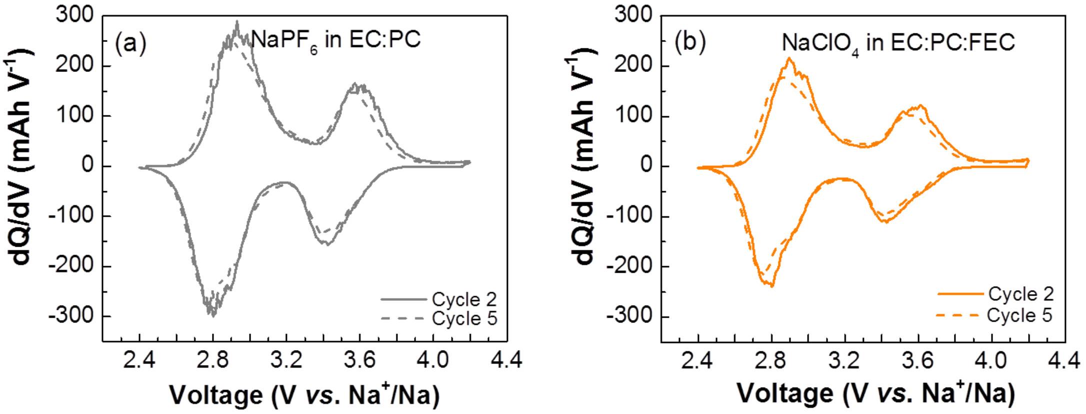

Figure 5.3. dQ/dV *vs*. V of 2nd and 5th cycle of Na-PB electrodes tested *vs.* Na^+/Na at C/10, when using a) 1M $NaPF_6$ in EC: PC (50:50) and b) 1M $NaClO_4$ in EC: PC: FEC (49:49:2).

Rate capability tests, consisting of 10 cycles at each of the following current densities: C/10, 1C, 10C and again C/10, were conducted for Na-PB. The results are displayed in Figure 5.4a and b. For the $NaClO_4$ based electrolytes, the largest reversible specific discharge for every C-rate was achieved with EC: PC 50:50 and EC: DMC: FEC 49:49:2. Both solvent mixtures approximately exhibited 125 mAh·g^{-1} at C/10, 100 mAh·g^{-1} during the following 10 cycles run at 1C and about 55 mAh·g^{-1} when cycled at 10C (922 mA·g^{-1}). Even 120 mAh·g^{-1} and 110 mAh·g^{-1} were recovered by 1 M $NaClO_4$ in EC: DMC: FEC 49:49:2 and 1M $NaClO_4$ in EC: PC 50:50 when coming back to C/10. Although the mixture EC: DEC: FEC 49:49:2 achieved similar specific discharge to EC: PC along the first 10 cycles, the values attained at higher current densities (89.5 and 41.4 mAh/g at 1C and 10C, respectively) were not as good as with the latter. Regarding the electrolytes containing $NaPF_6$, EC: PC 50:50 and EC: PC: FEC 49:49:2 enabled Na-PB to reach specific discharge capacities up to 140 and 130 mAh·g^{-1}, respectively, when cycled at C/10. Even on the order of 110 mAh·g^{-1} at 1C and 65 mAh·g^{-1} at 10C were achieved by using 1 M $NaPF_6$ EC: PC 50:50.

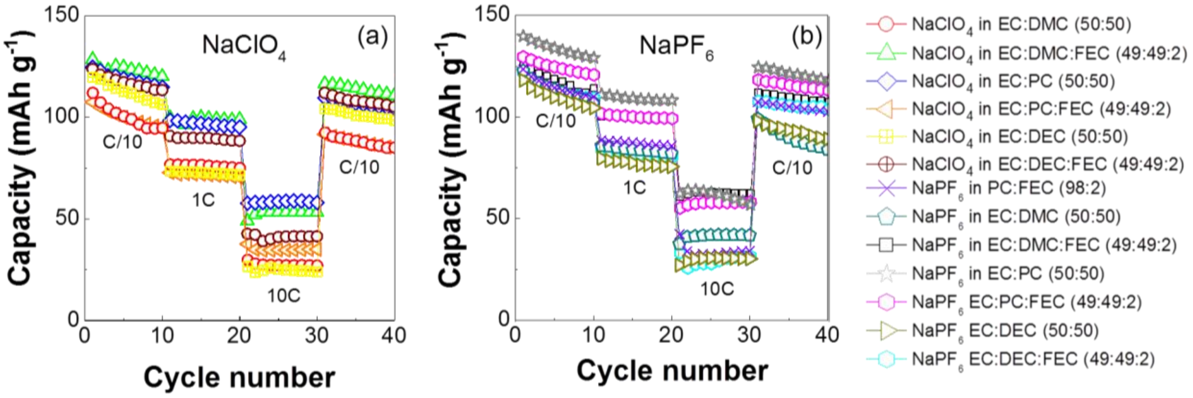

Figure 5.4. Electrochemical performance of the Na-PB tested at several C-rate capabilities (being C_{th}, Na-PB = 92.185 mAh·g^{-1} per 1Na^+ insertion/f.u.) using the electrolytes containing the $NaClO_4$ (a) salt or the $NaPF_6$ (b) salt. Only discharge capacities are showed in the figure.

In summary, the four electrolytes displaying the highest discharge specific capacities at the different C-rates were: 1 M $NaClO_4$ in EC: PC 50:50, 1 M $NaClO_4$ in EC: DMC: FEC 49:49:2, 1 M $NaPF_6$ in EC: PC 50:50 and 1 M $NaPF_6$ in EC: PC: FEC 49:49:2. They have been marked in Table 5.2 with the symbol † and their capacity values are highlighted in bold letter in Table 5.3.

Once established the best electrolytes in terms of capacity, other important parameters such as the coulombic efficiency (Figure 5.5a-e) and the capacity retention (Figure 5.6) were analyzed. For the four shortlisted electrolytes, coulombic efficiencies ≥97% are observed when cycled at C/10, except for $NaClO_4$ 1 M in EC: PC 50:50. For the latter, the efficiency (< 95%) is not appropriate for battery operation. The electrolyte $NaPF_6$ 1 M in EC: PC 50:50 also displayed low coulombic efficiencies (98% and 97%) at high rates of 1C and 10 C, which is still far from the satisfactory 99.5 and 99.85% displayed at 1C and 10 C by both $NaClO_4$ 1 M EC: DMC: FEC 49:49:2 and $NaPF_6$ 1 M EC: PC: FEC 49:49:2. In general, a better efficiency along with an improved capacity is appreciated for those electrolytes containing FEC as electrolyte additive (Figure 5.5), resulting in a stabilization enhancement between the charge and discharge processes during cycling. Thus, the two electrolytes that showed the highest capacities and coulombic efficiencies for Na-PB are 1 M $NaClO_4$ in EC: DMC: FEC 49:49:2 and 1 M $NaPF_6$ in EC: PC: FEC 49:49:2.

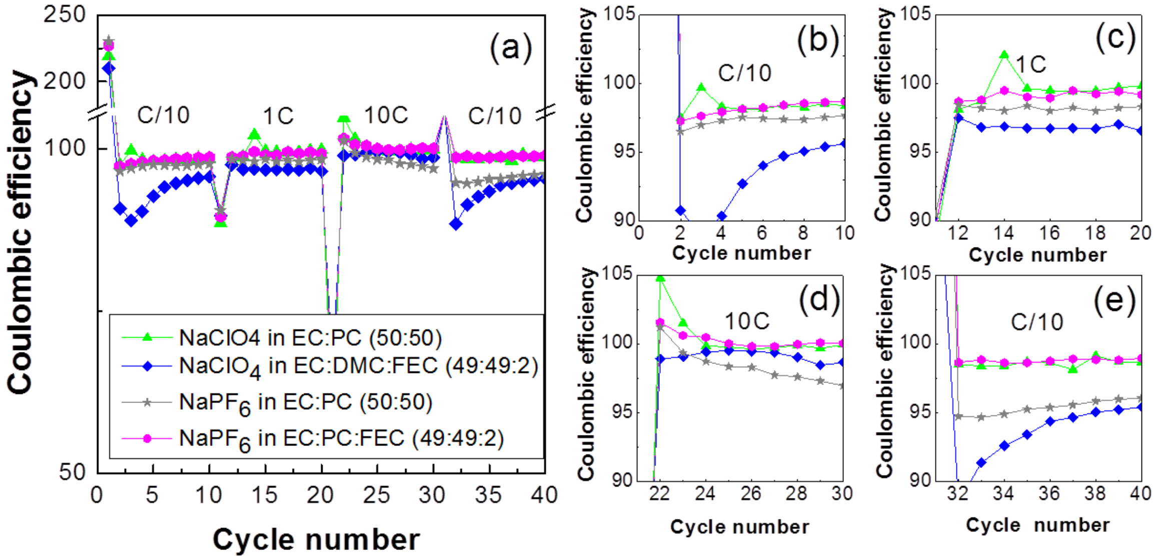

Figure 5.5. a) Coulombic efficiency of the Na-PB cycled in the voltage window from 2.4 to 4.2 V *vs.* Na^+/Na using the following different electrolytes: 1 M $NaClO_4$ EC: PC 50:50 (blue rhombus), 1 M $NaClO_4$ EC: DMC: FEC 49:49:2 (green triangles), 1 M $NaPF_6$ EC: PC 50:50 (gray stars) and 1 M $NaPF_6$ EC: PC: FEC 49:49:2 (pink hexagons)). For better distinction, a zoom of each range of current densities (C/10, C, 10C and again C/10) has been performed as can be observed in graphs b), c), d) and e), respectively.

Focusing finally on the capacity retention (Figure 5.6) it should be noted that 1 M $NaPF_6$ in EC: PC: FEC 49:49:2 displays a more stable behavior at high C-rates, despite similar retention of the initial capacity is shown at low C-rates. Consequently, 1 M $NaPF_6$ in EC: PC: FEC 49:49:2 can be claimed as the most suitable organic liquid electrolyte for exploiting Na-PB as cathode in NIB.

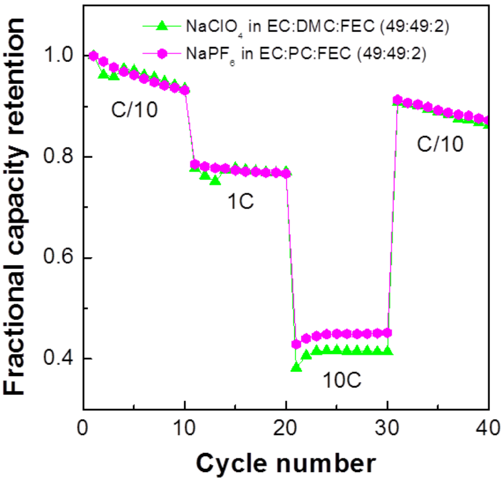

Figure 5.6. Fractional capacity retention *vs*. number of cycles for the two best electrolytes, 1 M $NaClO_4$ EC: DMC: FEC 49:49:2 (green triangles) and 1 M $NaPF_6$ EC: PC: FEC 49:49:2 (pink hexagons), at the indicated C-rates.

To further validate the previous statement and to correlate the different electrochemical features encountered among them, EIS experiments were performed with the four most promising electrolytes (signposted in Table 5.2 with the symbol ✝). Impedance measurements were carried out in three-electrode Swagelok cells configuration, as shown in chapter 2 (Figure 2.18b). The data were recorded in the frequency range from 100 KHz to 10 mHz with an amplitude of 10 mV. The electrochemical impedance spectra recorded at the end of discharge (EOD), i.e. at 2.4 V *vs*. Na^+/Na, after each of the first five cycles, is shown in Figure 5.7. At first sight, a clear difference between the cells tested with electrolytes containing both salts can be observed. Na-PB electrodes cycled in $NaClO_4$ based electrolytes (Figure 5.7a and b) exhibit impedance profiles which evolve upon cycling, whereas in those cycled using $NaPF_6$ based electrolytes (Figure 5.7c and d) the total impedance is more stable regardless of the presence of FEC additive. Undoubtedly, $NaPF_6$ in EC: PC: FEC presents the lowest impedance values.

The EIS spectra of Na-PB cycled in 1 M $NaClO_4$ in EC: DMC: FEC and 1 M $NaPF_6$ in EC: PC (Figure 5.7a and c, respectively) admitted fitting with only two RC elements. The other two samples using 1 M $NaClO_4$ in EC: PC and 1 M $NaPF_6$ in EC: PC: FEC (Figure 5.7b and d) were fitted with an equivalent circuit with three RC elements (see Figure 5.8 inset). The proposed equivalent circuit exhibited larger relative error but smaller statistical parameter χ^2 than the circuit with only two RC elements. Since the electrodes were all from the same laminate and were carefully chosen to have similar mass and thickness leaving the electrolyte as the only varying parameter, it was decided to maintain the same equivalent circuit (3 RC elements) for all samples (see Figure 5.8, inset). In all the analyzed spectra the χ^2 parameter was kept below $9 \cdot 10^{-4}$. Two semicircles appear at high frequency, which could be assigned to the presence of surface films, however the capacitances calculated are several orders of magnitude lower than expected (~ 5–10 $mF \cdot cm^{-2}$). Another possible explanation for the high frequency semicircle is the contact resistance between the electrode material and the Al current collector.[2] In this case, the only difference between samples is the electrolyte solvents and salt,

---

[2] M. Gaberscek, J. Moskon, B. Erjavec, R. Dominko, J. Jamnik, Electrochem. *Solid State Lett*. 2008, **11**, A170–A174. "The Importance of Interphase Contacts in Li Ion Electrodes: The Meaning of the High-Frequency Impedance Arc."

which could certainly affect the passivation of the Al current collector and the contact resistance. Notwithstanding, further investigations are needed to prove it.

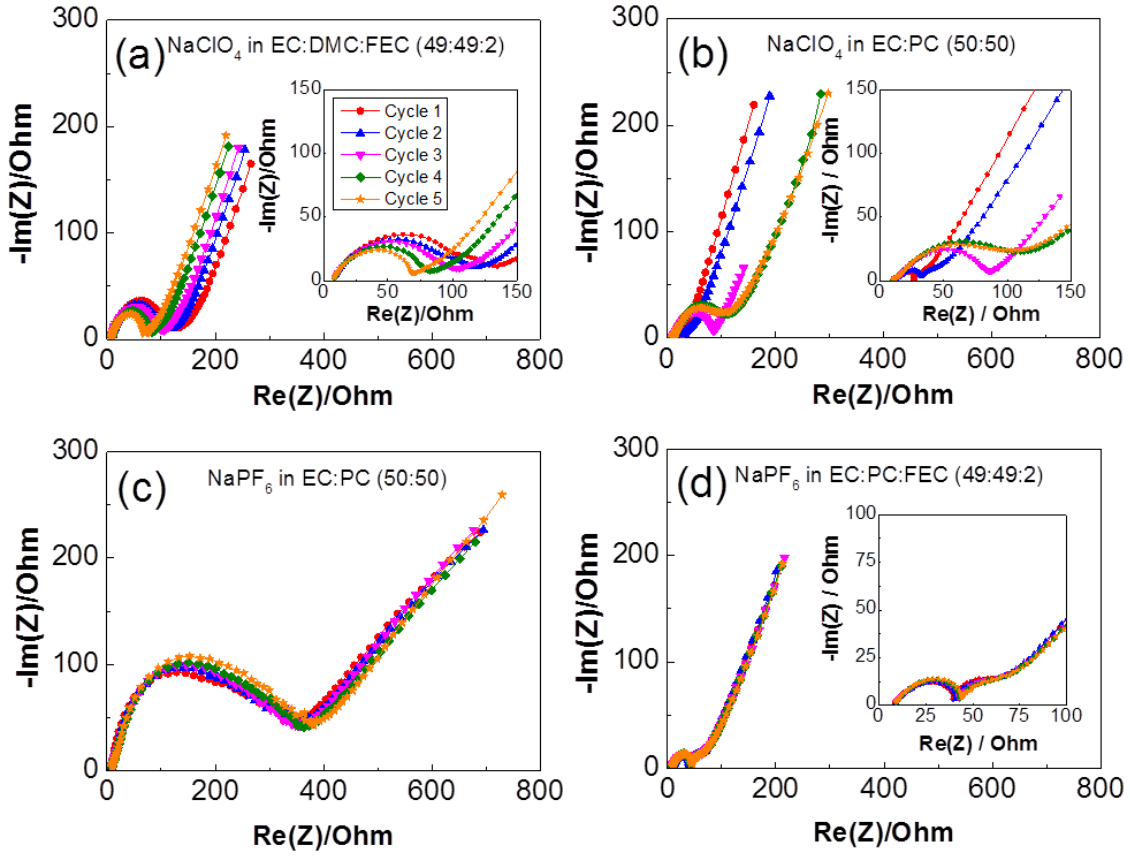

Figure 5.7. Nyquist diagrams of impedance measurements at the EOD for each one of the first 5 cycles of Na-PB *vs.* Na^+/Na at C/10 in a) 1 M $NaClO_4$ in EC:DMC:FEC (49:49:2), b) 1 M $NaClO_4$ in EC:PC, c) 1 M $NaPF_6$ in EC:PC and d) 1 M $NaPF_6$ in EC:PC:FEC. Inset in (b), (c) and (d) displays zoom in the high frequency range.

Since the origin of the high frequency response is unclear, all Na-PB samples are compared by their total resistivity, $R_1 + R_2 + R_{ct}$ (R_1: resistance component 1, R_2: Resistance component 2, R_{ct}: charge transfer resistance).[3] Figure 5.8 shows the total resistivity of the Na-PB samples cycled in the four studied electrolyte combinations. Na-PB cycled in $NaClO_4$ based electrolytes exhibited low resistivity and different behavior upon cycling. The 1 M $NaClO_4$ in EC: DMC: FEC electrolyte results in higher resistivity than in EC: PC but with more stable response. Indeed, the stronger fading of 1 M $NaClO_4$ in EC: PC and its worse capacity retention after the high C-rate capability test (Figure 5.4a) could be attributed to the increasing resistivity along the cycles. On the other hand, $NaPF_6$ based electrolytes exhibit great stability after 5 cycles, especially the 1 M $NaPF_6$ in EC: PC: FEC which shows much lower resistivity than without FEC additive. In principle, this seems to contradict the better cycling performance of 1 M $NaPF_6$ in EC: PC (Figure 5.4b). However at high C-rate (at 10C and afterwards) the specific discharge capacities of both become similar, the coulombic efficiency of the FEC-free electrolyte worsens while a more stable cycling can be obtained with FEC.

---

[3] D.I. Iermakova, R. Dugas, M.R. Palacín, A. J. Ponrouch. *J. Electrochem. Soc.* 2015, **162**, A7060–A7066. “On the Comparative Stability of Li and Na Metal Anode Interfaces in Conventional Alkyl Carbonate Electrolytes”.

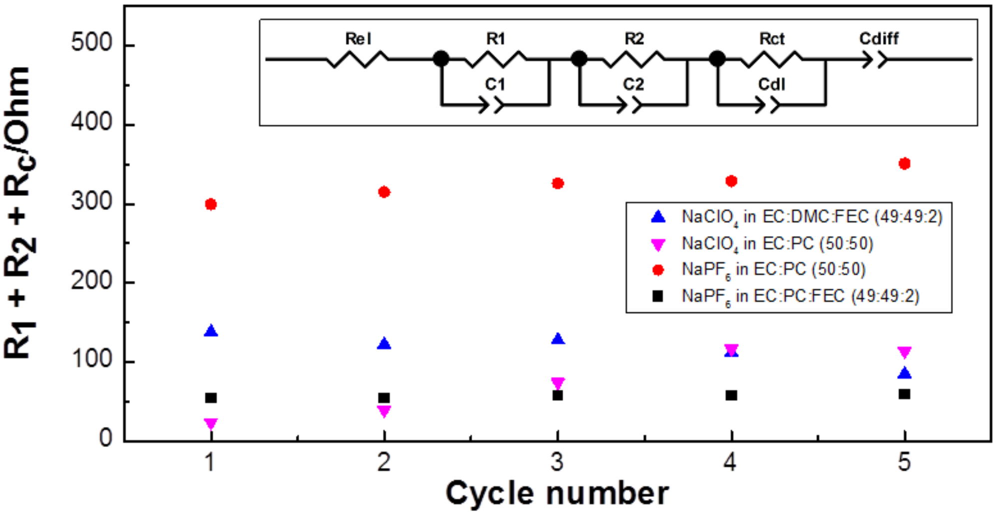

Figure 5.8. Comparison of the resistances for the 4 different electrolytes tested is here presented. Inset shows the equivalent circuit used to fit the data.

Therefore, 1M $NaPF_6$ in EC: PC: FEC 49:49:2 % vol. was corroborated as the most suitable electrolyte for Na-PB materials in NIB and was deployed for all the following experiments. These results are in good agreement with those described in the literature, that claim that PF_6^- anion is a more suitable salt for cathodic studies than ClO_4^-, as a consequence of its higher resistance to oxidation.[4] Such optimum electrolyte is also consistent with Palacin's report who established that $NaPF_6$ in EC: PC possessed all the features to be adopted as standard electrolyte for Na-ion batteries,[5] as a consequence of its superior thermal and electro-chemical stability among a wide variety of carbonate mixtures. Moreover, the addition of a small percentage of an additive, such as FEC, is assumed to enhance the capacity retention and the Qeff in anode materials for NIBs, as Komaba already demonstrated for hard carbons.[6,7] Although there are contradictory results related to hard carbons, other anode investigations revealed an ameliorated electrochemical stability when FEC is added.[8] Recent studies also proved an improvement in the cycling stability of cathodes in LIB when using FEC, as a result of the formation of SEI components on the cathode surface or SPI (solid polymer interface). This surface is abundant in polycarbonate components that enhance the ionic conductivity of the SPI film and reduces the electrode/electrolyte interfacial impedance.[9, 10] Thus, the

---

[4] J.M. Tarascon, D. Guyomard, *Solid State Ionics* 1994, **69**, 293–305. "New electrolyte compositions stable over the 0 to 5 V voltage range and compatible with the $Li_{1+x}Mn_2O_4$/carbon Li-ion cells."

[5] A. Ponrouch, E. Marchante, M. Courty, J.-M. Tarascon, M.R. Palacín, *Energy Environ. Sci.* 2012, **5**, 8572–8583. "In search of an optimized electrolyte for Na-ion batteries."

[6] S. Komaba, T. Ishikawa, N. Yabuuchi, W. Murata, A. Ito, Y. Ohsawa, *ACS Appl. Mater. Interfaces* 2011, **3**, 4165–4168. "Fluorinated Ethylene Carbonate as Electrolyte Additive for Rechargeable Na Batteries."

[7] I.A. Shkrob, J.F. Wishart, D.P. Abraham*, J. Phys. Chem. C* 2015, **119**, 14954– 14964. "What Makes Fluoroethylene Carbonate Different?"

[8] X. Chen, X. Li, D. Mei, J. Feng, M.Y. Hu, J. Hu, M. Engelhard, J. Zheng, W. Xu, J. Xiao, J. Liu, J.-G. Zhang, *Chem. Sus. Chem.* 2014, **7**, 549–554. "Reduction Mechanism of Fluoroethylene Carbonate for Stable Solid–Electrolyte Interphase Film on Silicon Anode."

[9] E. Markevich, G. Salitra, K. Fridman, G. Sharabi, A. Gershinsky, G. Garsuch, M.A. Schmidt, D. Aurbach, *Langmuir* 2014, **30**, 7414–7424. "Fluoroethylene Carbonate as an Important Component in Electrolyte Solutions for High-Voltage Lithium Batteries: Role of Surface Chemistry on the Cathode."

beneficial effect of FEC on cathode performance for NIB has been here demonstrated, leading to a decrease in the interfacial resistivity when it is added.

5.1.2.2. Binder election

Having defined the electrolyte providing the best electrochemical properties for Na-PB (1 M $NaPF_6$ EC: PC: FEC 49:49:2), the effect of the binder was investigated *vs*. Na^+/Na in the same voltage window, ΔV = 2.4 - 4.2 V. The binders tested in this study were: PVDF (Solef®), sodium CMC (M.W. ca. 250000 g/mol, Sigma Aldrich), PTFE (60 % wt. dispersed in H_2O, Sigma Aldrich) and EPDM rubber (50% wt).

Positive laminated electrodes were prepared by mixing 80 wt % of Na-PB with 10 wt % of Super C65 and 10 wt % of binder in the appropriate solvent. Specifically, PVDF was dissolved in NMP, Na-CMC in a mixture EtOH/H_2O (see Chapter 4, section 4.2.2.1), PTFE was dispersed in H_2O/EtOH and EPDM was solubilized in cyclohexane. Disc-shaped electrodes were punched from the coated Al foil, except for PTFE which was self-standing. Common cell loadings were 1.5 - 3 mg of active material per coin cell. The data here displayed are single run for typical results.

Rate capability tests, consisting of 10 cycles at each of the following current densities: C/10, 1C, 10C and again C/10, were conducted for Na-PB, and are displayed in Figure 5.9a and b.

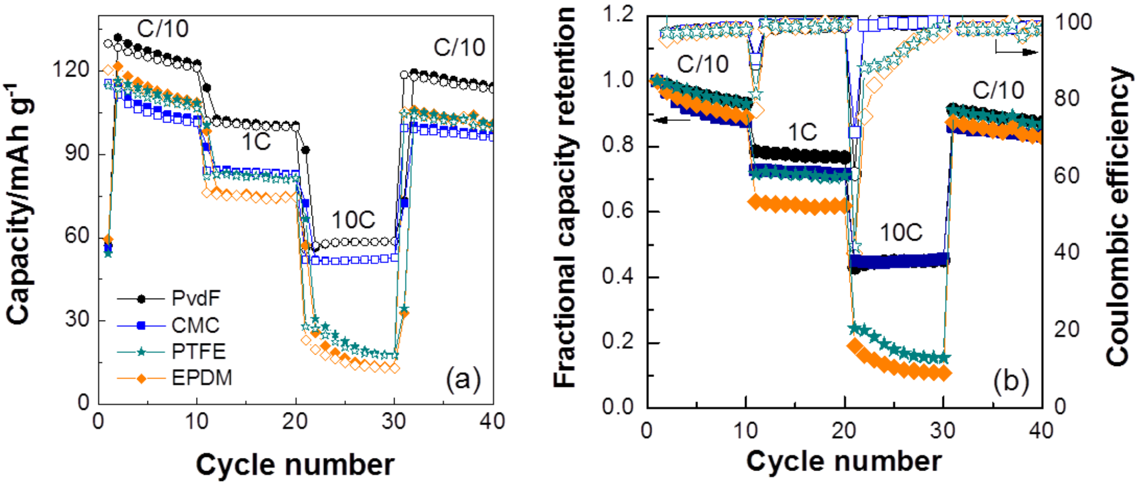

Figure 5.9. a) Specific capacity, b) capacity retention (filled symbols) and coulombic efficiency (empty symbols) of Na-PB electrodes prepared with different type of binder (PVDF in NMP, CMC in EtOH/H_2O, PTFE in H_2O and EPDM in cyclohexane) at different C-rates, when cycled against Na^+/Na in the cut-off voltage from 2.4 to 4.2 V, using 1M $NaPF_6$ in EC: PC: FEC 49:49:2.

By far, and regardless of the current densities analyzed, the highest capacities were achieved using PVDF as binder (see Figure 5.9). Electrodes based in PVDF exhibited specific discharge capacities of up to 130 mAh·g^{-1}, coulombic efficiencies of nearly 99% after 30 cycles and 87% of capacity retention

---

[10] P. Yeonju, H.-S. Su, H. Hoon, et al., *J. Molecular Structure* 2014, **1069**, 157–163. "Investigation of solid electrolyte interface (SEI) film on $LiCoO_2$ cathode in fluoroethylene carbonate (FEC)-containing electrolyte by 2D correlation X-ray photoelectron spectroscopy (XPS)."

at the end of the rate capability test (after 40 cycles). In contrast, CMC electrodes presented the lowest capacity (115 mA mAh·g^{-1}) and the higher capacity fading at low capabilities. Surprisingly, moderate values were observed at 1C and fairly good capacities were reached at high C-rates (ca. 53 mAh·g^{-1} at nearly 1 A·g^{-1}). In general, PTFE manifested an intermediate response and EPDM displayed the worst behavior, considering the electrochemical parameters here shown (specific capacity, coulombic efficiency and capacity retention).

Figure 5.10a reveals that there are no significant differences in the dQ/dV *vs*. V profiles among the binders deployed. It is noticeable however the splitting of the reduction redox process at 2.8 V when using PTFE, which suggests a 2-step reaction process. Meanwhile, Figure 5.10b and c contrasts the dQ/dV vs. V profiles corresponding to cycles 2 and 5 of Na-PB electrodes containing the best (PVDF) and worst (EPDM) binders. Both curves are similar except in the width/height of the redox processes. The larger area in PVDF corresponds to the higher capacity observed in Figure 5.9.

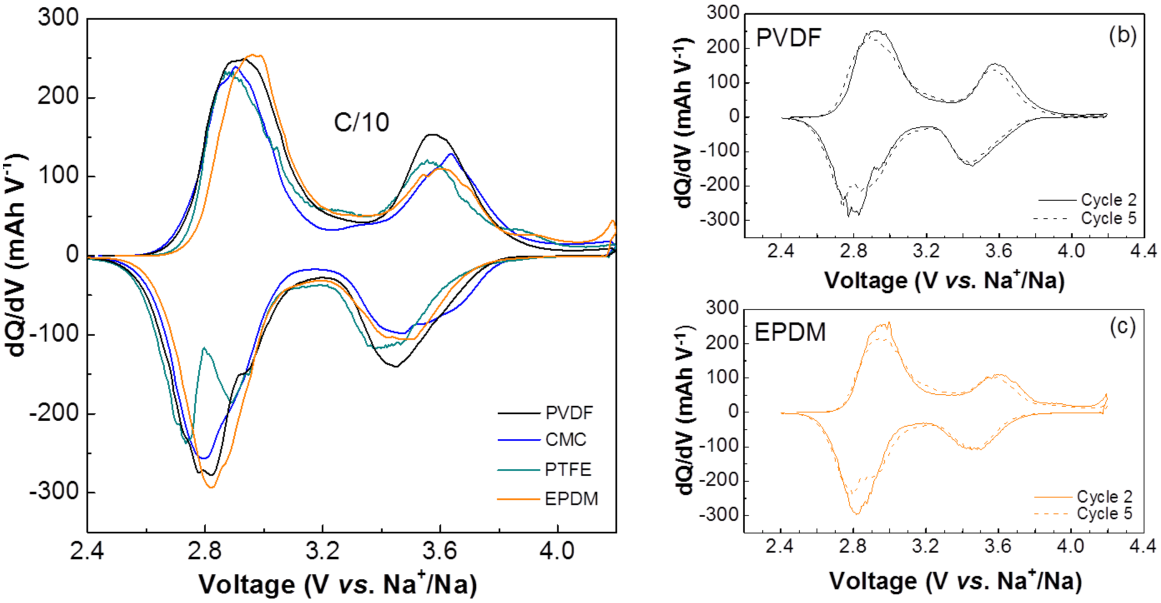

Figure 5.10. a) dQ/dV *vs*. V of the 2nd cycle of Na-PB *vs*. Na$^+$/Na, when electrodes containing different binders are tested at C/10 and b, c) dQ/dV *vs*. V of 2nd and 5th cycle of Na-PB electrodes tested *vs*. Na at C/10, when using PVDF (in grey) and EPDM (in pink) as binders.

In order to explain the different electrochemical behavior observed in function of the binder used, cross-section images of the electrodes were recorded by SEM. The study of the cross-section provides an idea of the adherence existent between the coating (electrode layer hereafter) and the current collector. The adherence is crucial for an adequate electrical contact and thus a good electron transport. Images of electrodes prepared with PVDF binder (Figure 5.11a and b) showed an approximately 25 µm thick electrode layer that seems to be perfectly glued to the Al foil, resulting in good electrical contact as so evidences its electrochemical results. When CMC is used as binder (Figure 5.11c and d), similar electrode layer thickness to PVDF is observed. The adherence of CMC electrodes is also good although at some points a small void space is distinguished between the coating and the current collector. PTFE (Figure 5.11e and f) was prepared as self-standing electrode, without using current collector. As mentioned before, its electrochemical behavior is intermediate, however, the larger thickness of this electrode (~ 200 µm) can explain its fading when cycling at high current densities as 1 A·g^{-1}. Finally, in EPDM-based electrodes (Figure 5.11g and h), 2 zones can be easily differentiated: a thinner layer of ~ 20 micron assigned to the electrode layer adhered to the current collector, and a thicker layer of ~ 40 micron clearly separated, revealing a lack of electrical contact, that would explain the low capacities exhibited at moderate and high current densities.

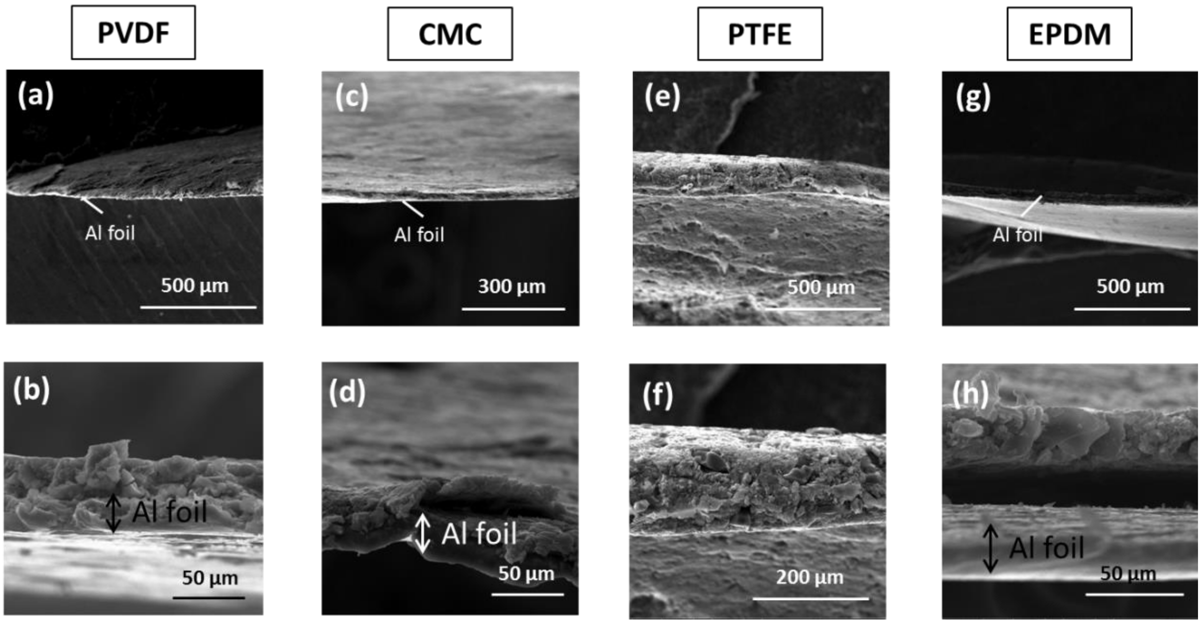

Figure 5.11. SEM images of the cross-section electrodes containing the different binders and their corresponding magnifications: PVDF (a and b), CMC (c and d), PTFE (e and f) and EPDM (g and h).

It is evident that comparing all the cross-section images of the binders, PVDF and EPDM are respectively those with best and worse contact, what agrees with their corresponding electrochemical performance. Apart from the adherence, the influence of the functional groups, present on the binders, and the thickness of the electrode films are also critical for the electrochemical behavior and would constitute an interesting study to develop in the future.

The results are consistent with those reported by Chou et al,[11] in which the replacement of PVDF by environmentally friendly aqueous based binders in cathodes, such as CMC or PTFE, presents some difficulties, unlike in the anodes. These facts could be related to the lack of stability of the cathode in water, as well as the slurry formulation, the control on the viscosity and the way of processing the film.[12] Notwithstanding, it is worth noting that the electrolyte-binder combination is crucial for achieving the optimum performance and therefore, if other electrolyte is used, another binder might outperform PVDF's results.

---

[11] Chou S-L., Pan Y., Wang Y-Z., Liu H-K., Dou S-X. *Phys. Chem. Chem. Phys.* 2014, **16**, 20347-20359. "Small things make a big difference: binder effects on the performance of Li and Na batteries."

[12] Magasinski A., Zdyrko B., Kovalenko I., Hertzberg B., Byrtovyy R., Huebner C. F., Fuller T. F., Luzinov I., Yushin G. *ACS Appl. Mater. Interfaces* 2010, **2**, 3004-3010. "Towar Efficient Binders for Li-Ion Battery Si-Based Anodes: Polyacrylic Acid."

5.1.3. Concluding remarks of "Na-PB as cathode *vs.* Na^+/Na in organic media"

Electrolytes containing $NaClO_4$ or $NaPF_6$ salts in carbonated mixtures (EC: PC, EC: DMC, EC: DEC), with and without a small amount of FEC as additive, have been electrochemically investigated for Na-PB as cathode material in NIB. The most suitable organic electrolyte turned out to be 1M $NaPF_6$ in EC: PC: FEC 49:49:2, exhibiting one of the highest reversible specific discharge capacities (130 $mAh·g^{-1}$), with 99.5% of Qeff and 87% of capacity retention after 40 cycles. Its optimal response was corroborated by EIS, owing to the lower interfacial resistance this mixture exhibited.

The effect of different binders (PVDF, CMC, PTFE and EPDM) on the electrochemical performance of Na-PB has also been explored. PVDF has clearly shown the best results (130 $mAh·g^{-1}$, nearly 99% of Qeff after 30 cycles and a capacity retention of 87% after 40 cycles.

The use of this electrolyte (1M $NaPF_6$ in EC: PC: FEC 49:49:2) and binder (PVDF) composition could be extended by analogy to other PBA and derived. Apart from contributing to homogenize the results facilitating the comparison among the different PBA, it is assumed that they will provide optima features. It could also be considered the possibility of using this combination for market applications and, as mentioned above, the extension to other SIB systems.

5.2. Na-PB vs. Na^+/Na as cathodes in aqueous media

5.2.1. Scope

The electrochemical behavior of Na-PB, $Na_{0.75}Fe_{2.08}(CN)_6 \cdot yH_2O$, as cathodic material in sodium-ion aqueous batteries was also considered of great interest. Aqueous batteries are even greener electrochemistry technology than the organic analogues, being one of the major benefits the utilization of a safe and cheap water based electrolyte. The main drawback resides, however, in the low energy density obtained using this devices, compared to the non-aqueous systems. The aim of this study was to discover whether purely iron-based Na-PB works similarly to those PBA already reported and contrast it with the response obtained in organic media. This work was developed in collaboration with the PhD student (now Dr.) Antonio Jesús Fernández Ropero and Dr. Montserrat Casas Cabanas.

5.2.2. Electrochemical characterization – results and discussion

Cyclic voltammograms and galvanostatic measurements were recorded in a Bio-Logic VMP3 Multi-Channel Potentiostast/Galvanostat. Three-electrode Swagelok aqueous cells and two-electrode Swagelok organic cells were built for this purpose (as specified in chapter 2, section 2.2.4.3).

Cyclic voltammogram (at 1 $mV \cdot s^{-1}$ scan rate) of Na-PB within the cut-off voltage from 1.5 to 4.75 V *vs.* Na^+/Na in non-aqueous electrolyte is shown in Figure 5.12a. Two main redox processes are observed at 3.25 and 3.95 V upon charge and at 2.5 and 3.1 V during discharge. Both processes are reversible and are ascribed respectively to the reduction from Na-PB to sodium Prussian White (Na-PW) and the oxidation from Na-PB to BG, in accordance with (Eq. 5.1) (see section 5.1.2.1).

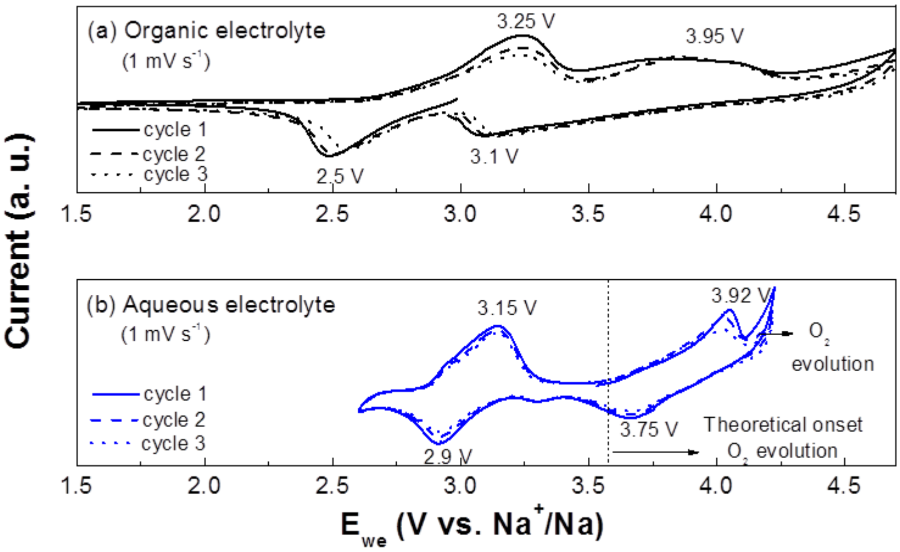

Figure 5.12. Cyclic voltammogram at $1 mV \cdot s^{-1}$ of the 3 first cycles of Na-PB in a) 1M $NaPF_6$ in EC: PC: FEC 49:49:2 % vol, in the voltage range of 1.5 - 4.75 V *vs.* Na^+/Na and b) 1M Na_2SO_4, in the voltage window of 2.6 - 4.2 V *vs.* Na^+/Na.

In aqueous electrolyte, the cyclic voltammogram of Na-PB from 2.6 to 4.2 V *vs*. Na^+/Na also exhibits two redox processes (Figure 5.12b). The cathodic peaks show up at 3.15 and 3.92 V and the anodic peaks at 2.83 and 3.63 V. In general, the average voltages at which processes occur in aqueous electrolyte, i.e. 3 V and 3.75 V *vs.* Na^+/Na, are moderately shifted towards higher values with respect to the average voltage of 2.9 V and 3.5 V observed in organic media. Additionally, a significant difference in the overpotential is also noticed when the two electrolytes are contrasted. In this case, a strong decrease in the overpotential for both redox processes, from ca. 0.75 - 0.8 V in organic electrolyte at around 0.17 - 0.25 V in aqueous electrolyte, has been observed.

The oxidation of Na-PB to BG partially overlaps with H_2O oxidation, as Figure 5.12b depicts. The theoretical O_2 evolution onset is 3.58 V *vs*. Na^+/Na at pH = 6.14,[13] but in practice it occurs at higher voltages. The instability of Na-PB in aqueous electrolyte at high potential was further demonstrated when the material was cycled at a low constant current such as C/5. Capacities around 80 mAh·g^{-1} were achieved even though the limiting upper potential (4.1 V) was never reached (Figure 5.13a). A continuous charge up to 3.55 V *vs*. Na^+/Na was observed (Figure 5.13b) only limited by time, what impeded to complete the second process making it inaccessible. Conversely, when Na-PB was cycled at a higher rate as 14C, the oxidation to BG was kinetically favored with respect to electrolyte decomposition and could be partially achieved (Figure 5.13c). However, the battery quickly self-discharged during relaxation periods and the voltage of the cell decreased to a value close to its initial OCV (3.165 V *vs*. Na^+/Na) in less than one hour (Figure 5.13c).

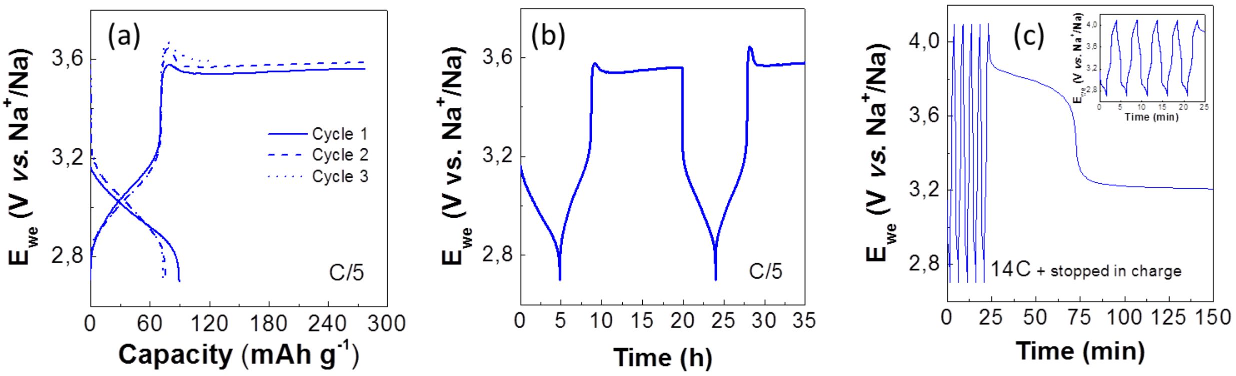

Figure 5.13. Galvanostatic tests of Na-PB cycled between 2.7 and 4.1 V *vs*. Na^+/Na in 1 M Na_2SO_4: individual center plot of the 3 first cycles at C/5 (a), voltage evolution of the material at C/5 (b) and 14C (c) and OCV variation of the charged battery (c inset: zoom of the 5 cycles).

At this point, it seems logical to assess whether the instability at high potential was due to material dissolution. Therefore, Na-PB and BG solubilities were tested by immersing 3 mg of Na-PB in powder or an electrode previously charged to BG in an organic half-cell (see Figure 5.14b) in 20 mL of electrolyte. As Figure 5.14a and c illustrates, both pristine Na-PB and the oxidized phase BG resulted insoluble in 1M Na_2SO_4. Notwithstanding, when the aqueous cells were disassembled, no active material was found on the current collector; while a blue solid, corresponding to Na-PB appeared in the separator (Figure 5.15a), as confirmed by IR (Figure 5.15b). This is indicative of the formation of colloidal particles of Na-PB, a

---

[13] W. Li, W. R. Mckinnon, J. R. Dahn, *J. Electrochem. Soc.* 1994, **141**, 2310-2316. “Lithium Intercalation from Aqueous Solution.”

process known as peptization that is common in this material.[14] The fact that this process becomes more apparent in the high voltage process might be due to repulsive effect of an overall positive charge on the surface coming from the oxidation and to bubble formation from electrolyte decomposition resulting in O_2 adsorption on the surface of Na-PB particles. In an attempt to observe O_2 formation on the electrode surface, new galvanostatic measurements were conducted in a beaker-typ cell, but these measurements led to inconclusive results. In any case, since peptization causes impractical cells involving electrode detachment and self-discharge, the voltage window was reduced to the lower voltage redox process (Na-PB ↔ Na-PW).

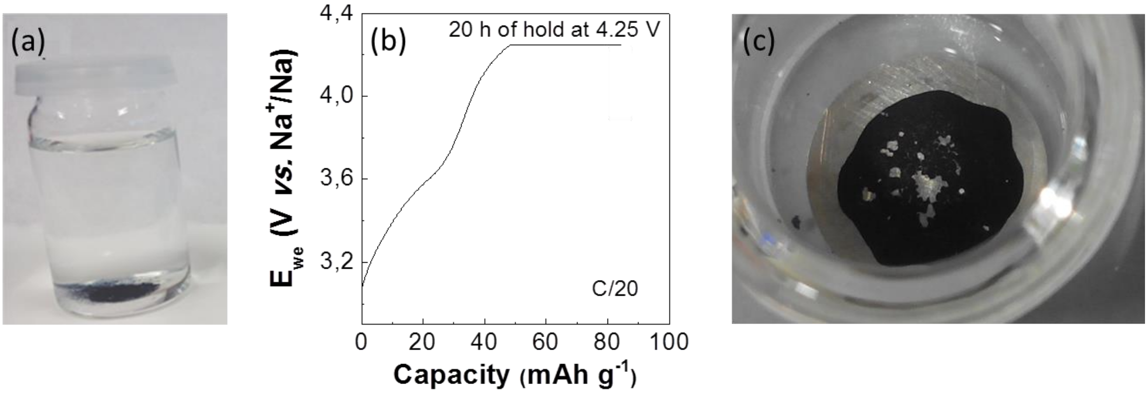

Figure 5.14. a) 3 mg Na-PB placed in 20 mL of 1 M Na_2SO_4 aqueous electrolyte, b) Voltage profile of the oxidation of Na-PB to BG at C/20 and subsequent hold for 20 hours at 4.25 V *vs*. Na^+/Na, c) Solubility test of BG electrode in 20 mL of 1 M Na_2SO_4.

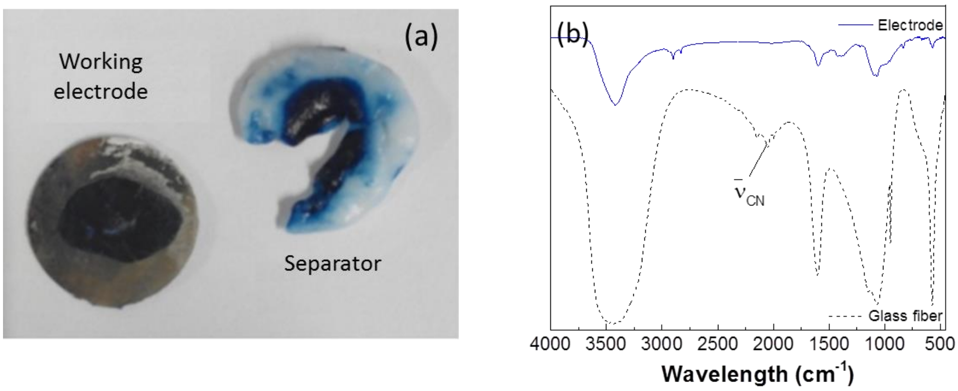

Figure 5.15. a) Working electrode and separator from the disassembly of the battery cycled at 14 C (represented in Figure 5.13c, b) IR spectra of the electrode and glass fiber presented in a).

Na-PB was tested within the voltage window from 2.6 to 3.45 V *vs*. Na^+/Na (Figure 5.16), exhibiting an enhanced stability. As expected, no trace of active material was found on the separator after cycling. The choice of this narrower window obviously results in a lower capacity, but such a trade-off is required for a better stability of the system, especially if long-cycling systems are required.

---

[14] C. G. Granqvist, Handbook of Inorganic Electrochemistry Materials, 1st Edition, Elsevier, Amsterdam 1995.

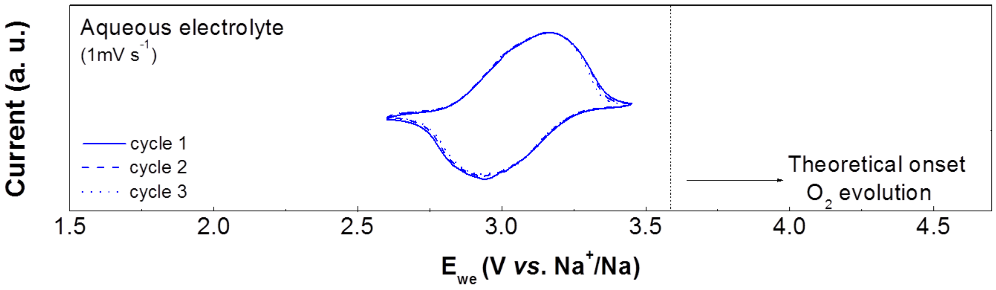

Figure 5.16. a) Cyclic voltammogram at 1mV·s^{-1} of the 3 first cycles of Na-PB in 1M Na_2SO_4, within the voltage window ΔV = 2.6-3.45 V *vs*. Na^+/Na.

Several ideas were put into practice to intend improving the results. The first idea consisted of the addition of some extra electrolyte, not only to avoid the total drying of the battery during the cycling but also to prevent the entrance of oxygen, since it could react with the material oxidizing it or promoting other side reactions. The capacity retention obtained with the extra electrolyte was mildly deteriorated, as shown in Figure 5.17a. Apparently, the device used to increase the electrolyte amount produced the opposite effect than expected, resulting in a less leak-proof system boosting the risk of O_2 diffusion.

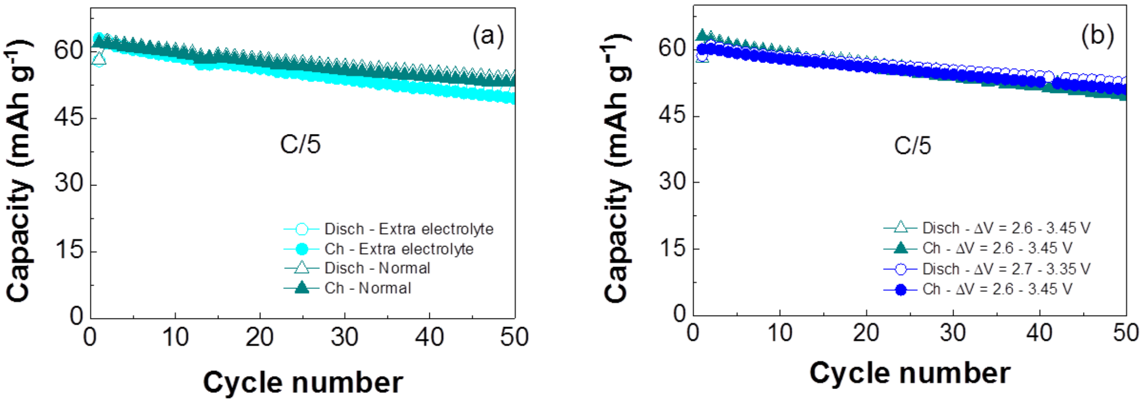

Figure 5.17. a) Comparison in the charge and discharge specific capacities observed in two different aqueous cells cycled between 2.6 to 3.45 V *vs*. Na^+/Na with the normal amount of electrolyte (blue) and adding extra amount of electrolyte (cyan). (b) Fractional capacity retention calculated for these same cells, based on the second discharge specific capacity value.

Additionally, it was decided to investigate a slightly shorter voltage window, ΔV = 2.7 - 3.35 V. As can be seen in Figure 5.17b, a better fractional capacity retention is obtained in this shorter range with a non-significant lost in the capacity.

Galvanostatic measurements carried out at C/5 and 1C in the voltage range from 2.7 to 3.35 V *vs*. Na^+/Na confirmed the good stability of the material. An initial reversible capacity of 61 mAh·g^{-1} (see Figure 5.18a), similar to those reported for other PBA such as CuHCF,[15, 16] NiHCF[15, 17, 18] and MnHCF[16], was

---

[15] C.D. Wessells, S. V. Peddada, M. T. McDowell, R. A. Huggins, Y. Cui. *J. Electrochem. Soc.* 2012, **159**, A98-A103. "The Effect of Insertion Species on Nanostructured Open Framework Hexacyanoferrate Battery Electrodes."

reached by Na-PB at C/5 and roughly 87% of capacity was retained after 50 cycles. At higher current densities, such as 1C (Figure 5.18b), the initial reversible capacity was 50 mAh·g^{-1} and 43 mAh·g^{-1} were maintained after 150 cycles. About 87% of the capacity was retained at the end of the test (calculated regarding the 2nd discharge capacity value). This capacity obtained is far from the *ca*. 125 mAh·g^{-1} reported by Wu *et al.* (), since they addressed the 2 redox processes[19] and here only the lower redox voltage process was investigated. Nevertheless, improved coulombic efficiencies close to 100% at 1C (Figure 5.18b) are achieved when the O_2 evolution is avoided, compared to the 80% obtained by Wu *et al.* at 1C when the voltage window was opened to reach the BG phase.[19]

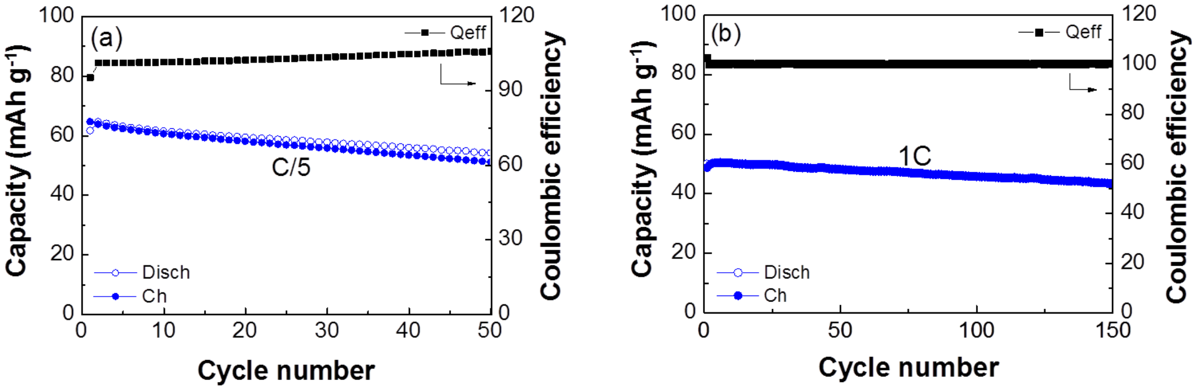

Figure 5.18. Charge and discharge specific capacities and coulombic efficiencies displayed by Na-PB when cycled in the voltage range of 2.7-3.35 V *vs*. Na$^+$/Na at a current density of a) C/5 and b) 1C.

Rate capability tests of Na-PB, consisting of 5 cycles at each of the following rates: C/5, C/2.5, 1C, 2C, 5C and 10C, were performed in the 2.7 to 3.35 V *vs*. Na$^+$/Na voltage range both in organic and aqueous media. To complete the discharge process, the voltage window in organic media had to be extended from 2.4 to 3.35 V *vs*. Na$^+$/Na, as a consequence of the larger overpotential observed in organic electrolyte (Figure 5.19a) in contrast to that in aqueous electrolyte (Figure 5.19b). Despite important differences are appreciated in terms of polarization, similar capacity values were achieved in both media. In organic electrolyte, capacities of 63, 50 and 39 mAh·g^{-1} were accordingly reached at C/5, 1C and 5C, while in aqueous electrolyte, 65, 52 and 34 mAh·g^{-1} were exhibited at the same C/5, 1C and 5C rates.

---

[16] M. Pasta, C. D.Wessells, N. Liu, J. Nelson, M. T. McDowell, R. A. Huggins, M. F. Toney, Y. Cui. *Nat. Commun.* 2014, **5**, 3007. “Full open-framework batteries for stationary energy storage.”

[17] C. D. Wessells, S. V. Peddada, R. A. Huggins, Y. Cui. *Nano Lett.* 2011, **11**, 5421-5425. “Nickel Hexacyanoferrate Nanoparticle Electrodes For Aqueous Sodium and Potassium Ion Batteries.”

[18] X. Wu, Y. Cao, X. Ai, J. Quian and H. Yang. *Electrochem. Commun.* 2013, **31**, 145-148. “A low-cost and environmentally benign aqueous rechargeable sodium-ion battery based on $NaTi_2(PO_4)_3$–$Na_2NiFe(CN)_6$ intercalation chemistry”

[19] X. Wu, Y. Luo, M. Sun, J. Quian, Y Cao, X Ai, H. Yang. *Nano Energy* 2015, **13**, 117-123. “Low-defect Prussian blue nanocubes as high capacity and long life cathodes for aqueous Na-ion batteries.”

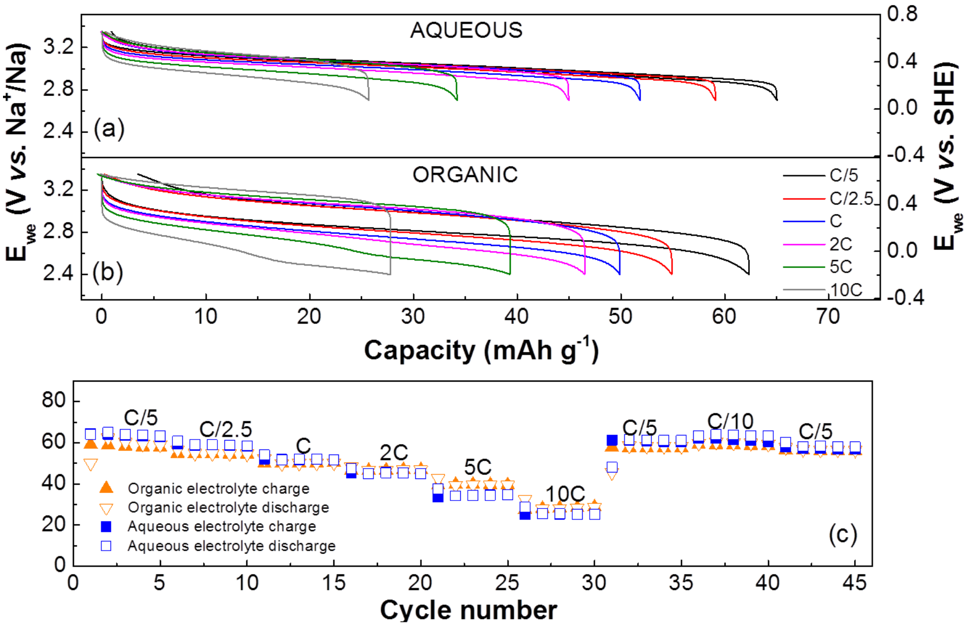

Figure 5.19. Voltage profiles of Na-PB at different C-rates (C/5, C/2.5, 1C, 2C, 5C and 10 C) cycled between a) 2.7 - 3.35 V *vs.* Na^+/Na in aqueous media, b) 2.4 – 3.35 V *vs.* Na^+/Na in organic media and c) C-rate capabilities of Na-PB tested both in the aqueous and organic electrolyte.

As previously highlighted, the main differences between both media were fundamentally observed in the overpotential values. In organic electrolyte, the overpotential was quite significant at all rates. Values of 0.178, 0.259 and 0.540 V were obtained at 0.2C, 1C and 10C, respectively. In aqueous electrolyte however the overpotential at C/5 and 1C was almost undetectable (0.018 and 0.046 V). At 10C, it increased up to 0.198 V but still lower than half of the value obtained in organic media. It is worth mentioning that, when the battery was cycled at lower rates after the rate capability tests, the initial capacity was still maintained after at least 45 cycles in both electrolytes (Figure 5.19c), indicating a good cycling stability.

The lower overpotential found in aqueous media has already been reported for other materials as $LiFePO_4$[20] in LIBs and $NaTi_2(PO_4)_3$[21], $NaFePO_4$[22] or $K_xNi[Fe(CN)_6]\cdot nH_2O$[23] for NIBs. Since the contribution of the conductivity of the electrolyte on the overall cell overpotential in Li-ion and Na-ion batteries is negligible (despite aqueous electrolytes have typically a higher ionic diffusion coefficient compared to organic electrolyte),[5, 24] this improvement can be explained by the easier desolvation of Na^+ in H_2O that results in a fast Na^+ charge transfer at the interface.[20]

---

[20] P. He, X. Zhang, Y. G. Wang, L. Cheng, Y. Y. Xia. *J. Electrochem. Soc.* 2008, **155** (2), A144–A150. "Lithium-Ion Intercalation Behavior of $LiFePO_4$ in Aqueous and Nonaqueous Electrolyte Solutions."

[21] S. Park, I. Gocheva, S. Okada, J. Yamaki. *J. Electrochem. Soc.* 2011, **158**, 1067–1070. "Electrochemical Properties of $NaTi_2(PO_4)_3$ Anode for Rechargeable Aqueous Sodium-Ion Batteries"

[22] A.J. Fernández-Ropero, D. Saurel, B. Acebedo, T. Rojo, M. Casas-Cabanas. *J. Power Sources* 2015, **291**, 40-45. "Electrochemical characterization of $NaFePO_4$ as positive electrode in aqueous sodium-ion batteries."

[23] Y. Mizuno, M. Okubo, E. Hosono, T. Kudo, H. Zhou, K. Oh-ishi. *J. Phys. Chem. C* 2013, **117**, 10877–10882. "Suppressed Activation Energy for Interfacial Charge Transfer of a Prussian Blue Analog Thin Film Electrode with Hydrated Ions (Li^+, Na^+ and Mg^{2+})".

[24] Y.J. Zhu, Y.H. Xu, Y.H. Liu, C. Luo, C.S. Wang. *Nanoscale* 2013, **5**, 780–787. "Comparison of electrochemical performances of olivine NaFePO4 in sodium-ion batteries and olivine $LiFePO_4$ in lithium-ion batteries."

5.2.3. Concluding remarks of "Na-PB *vs.* Na^+/Na as cathodes in aqueous media"

It has been demonstrated that Na-PB presents good electrochemical properties in aqueous NIB. Reversible capacities of 65 and 52 mAh·g^{-1} have been respectively obtained at C/5 and 1C when the voltage range is limited to the first redox process, avoiding peptization. The selection of the adequate voltage window allowed achieving noteworthy cycling stabilities with 87% and 97% of capacity retention after 50 cycles at C/5 and 1C, and remarkable coulombic efficiencies above 99%. Moreover, a very low overpotential (0.018 V at C/5), which results in an excellent round trip efficiency, is observed in aqueous media.

The promising performance of Na-PB (good round trip efficiency and excellent coulombic efficiency at all rates) along with the fact that it is a material easy to synthesize and made of low-cost earth-abundant elements, make it a very appealing candidate for aqueous systems able to compete with current stationary storage systems, despite Cu or Ni based PBA present higher voltages. Indeed, Na-PB is a material that complies with the most important requirements for stationary storage applications, where cost and efficiency prevail over energy density.

5.3. Prussian White as cathode vs. Na^+/Na in organic media

5.3.1. Scope

In previous sections, the good electrochemical properties of Na-PB as cathode material in NIB have been demostrated. As pointed out in Chapter 3, even of more technological importance is its reduced alkali-rich phase Prussian White, $A_2M[M'(CN)]_6$ (A = alkali ion, M and M´= transition metals, M´ = typically Fe, sometimes M = M´) and as so it has been evidenced by the several phases of PW investigated as low-cost cathode materials for NIB, in parallel with the development of this thesis. Unlike PB, PW has ideally all the cubic cavities occupied by alkali ions thereby preventing first cycle inefficiencies and the need of providing an additional source of alkali ions in the anode. This section will address the study of the electrochemical performance of cubic Na-PW and K-PW as cathode materials in organic NIB.

5.3.2. Electrochemical characterization – results and discussion

The electrochemical properties of Na-PW and K-PW were investigated for organic NIB in the voltage range of 2.25 - 4.25 V. Galvanostatic tests were performed in CR2032 coin cells using powder electrodes and laminated electrodes. Unlike routinely casted A-PB laminates, laminated PW electrodes were prepared by mixing 70 wt. % of active material (either Na-PW or K-PW) with 20 wt. % conductive C (Ketjen black® EC-600JD) and 10 wt. % PVDF® (Solef). The electrolyte deployed for both A-PW (A = Na, K) was 1M $NaPF_6$ in EC: PC: FEC 49:49:2 % vol, whose choice has already been discussed in a previous section (section 5.1.2.1).

The voltage profiles corresponding to the first galvanostatic charge-discharge of Na-PW and K-PW in a sodium half-cell are depicted in Figure 5.20. Typical OCV values oscillate from ca. 2.85-2.9 V *vs.* Na^+/Na for Na-PW to 2.9-2.95 V *vs.* Na^+/Na for K-PW. The lower OCV obtained compared to the usual 3.2 V observed in Prussian Blue evidences the higher alkali content in the PW phases and so supports the large first low voltage plateau, which indicates an almost complete filling of the alkali ion cavities in both cases.

In the profile of Na-PW (see Figure 5.20a, in black), a pair of sloppy plateaus centered at 3.0 and 3.3 V *vs.* Na^+/Na are observed along the charge. During the discharge, the higher voltage redox process keeps on occurring at 3.3 V whereas the reaction at lower voltage experiences a small shift from 3.0 to 2.8 V resulting in a 0.2 V polarization (see dQ/dV *vs*. V curve in the inset of Figure 5.20a), most likely due to the insulating character of the sodiated phase. These values are in between those reported for rhombohedral Na-PW by Guo-Guo *et al.*,[25] who showed mainly a single plateau at 2.8-2.9V *vs.* Na^+/Na, and those found by Goodenough *et al.*,[26] where a couple of plateaus are visible in the range from 3.0 to 3.3 V *vs.* Na^+/Na.

---

[25] Y. You, X.-Q. Yu, Y.-X. Yin, K.W. Nam, Y.-G. Guo, *Nano Res.* 2015, **8**, 117-128. “Sodium ion hexacyanoferrate with high Na content as a Na-rich cathode material for Na-ion batteries”.

[26] L. Wang, J. Song, R. Qiao, L.A. Wray, M.A. Hossain, Y.-D. Chuang, W. Yang, Y. Lu, D. Evans, J.-J. Lee, S. Vail, X. Zhao, M. Nishijima, S. Kakimoto, J.B. Goodenoug. *J. Am. Chem. Soc.* 2015, **137**, 2548-2554. “Rhombohedral prussian white as cathode for rechargeable sodium-ion batteries”.

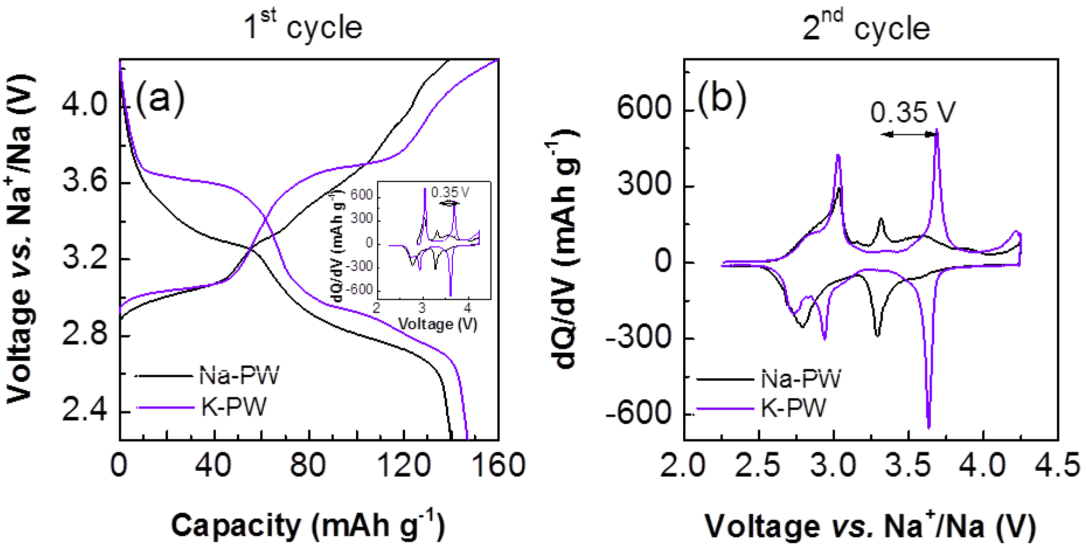

Figure 5.20. a) First cycle voltage profile, (inset) first cycle dQ/dV *vs.* voltage curves and b) second cycle dQ/dV *vs.* voltage curves of laminated Na-PW (in black) and K-PW (in violet) electrodes, when cycling *vs.* Na^+/Na at C/10 in the voltage range of 2.25-4.25 V, using 1M $NaPF_6$ in EC: PC: FEC 49:49:2 % vol. as electrolyte.

For K-PW, two plateaus are distinguished at 3.0 and 3.7 V *vs.* Na^+/Na along the oxidation curve. This time, both redox processes suffer from polarization while discharging and the plateaus appear respectively at 2.85 and 3.65 V. As expected, the lower voltage redox process again presents a higher polarization, following the tendency already observed for Na-PW.

When the dQ/dV curve of K-PW is compared to that of Na-PW (see inset of Figure 5.20a and/or Figure 5.20b), a significant gain of 0.35 V is noticed in the upper voltage plateau, even though both materials were cycled *vs*. metallic sodium (Na^+/Na) using the same Na^+ containing electrolyte. In addition, dQ/dV plots show the complexity of the redox processes that are taking place in both materials, as well as the repeatability and reproducibility of these along cycling.

To explain the convenient voltage difference existing in the upper voltage redox process between Na-PW and K-PW, two hypotheses were considered:

a) The fact of having a different cation in the materials could be potentially responsible of the positive potential shift. The effect of the cation on increasing cell voltage, and as a result on the energy density, has already been reported for other systems such as quinones.[27] In our particular case, once K-PW is completely charged and thereby the lattice emptied of K^+, the alkali metal inserted when starting to discharge could be either Na^+ or K^+. Despite the amount of Na^+ present in the media is several fold higher with respect to K^+ (ca. 26.5 times bigger), the selectivity of the PB framework for K^+ is likely higher.[28] The bigger ionic size of K^+ probably stabilizes somehow the molecular structure of the metal-organic framework. The low voltage redox process of K-PW vs. Na^+/Na occurs however at similar voltage to that

---

[27] K. Hernández-Burgos, G. G. Rodríguez-Calero, W. Zhow, S. E. Burkhardt, H. D. Abruña. *J. Am. Chem. Soc.* 2013, **135**, 14532–14535. "Increasing the Gravimetric Energy Density of Organic Based Secondary Battery Cathodes Using Small Radius Cations (Li^+ and Mg^{2+})."

[28] V. Krishnan, A. L. Xidis, V. D. Neff. *Anal. Chim. Acta* 1990, **239**, 7-12. "Prussian blue solid-state films and membranes as potassium ion-selective electrodes."

observed for Na-PW electrodes, suggesting that either Na$^+$ insertion is taking place during this reaction or that the second K$^+$ intercalation happens at the same potential value of Na$^+$.

b) Structural variances in the lattice from Na-PW to K-PW could also be responsible of the difference in the potential of the upper voltage plateau.

In any case, the effect coming from the negative electrode can be ruled out, as the reduction potential of K$^+$ is more negative than that of Na$^+$, and thus the only redox equilibrium taking place corresponds to Na$^+$ + e$^-$ ⇔ Na°.

To investigate the first hypothesis and check whether the voltage difference between Na-PW and K-PW stems from the insertion of a different alkali metal, a new experiment was conducted. A K-PW laminated electrode was galvanostatically charged up to 4.2 V at C/10 and held at such potential for few hours with the aim of reaching the alkali-empty phase known as Berlin Green (BG). The cell was de-crimped, the electrode was carefully extracted and repeatedly washed with the corresponding carbonate solvent (PC) and, once dried, it was reassembled again with 1M NaPF$_6$ EC: PC: FEC vs. Na$^+$/Na. As illustrated in Figure 5.21a, the electrochemical performance of this BG phase is almost identical to that exhibited by Na-PW. This similarity therefore reinforces the assumption that K$^+$ is the alkali ion inserting and de-inserting into/from the structure when K-PW is directly cycled against Na$^+$/Na, or at least in the high voltage redox process. Consequently, it can be stated that the difference in the voltage value between Na-PW and K-PW can be attributed to the different alkali ions intercalated.

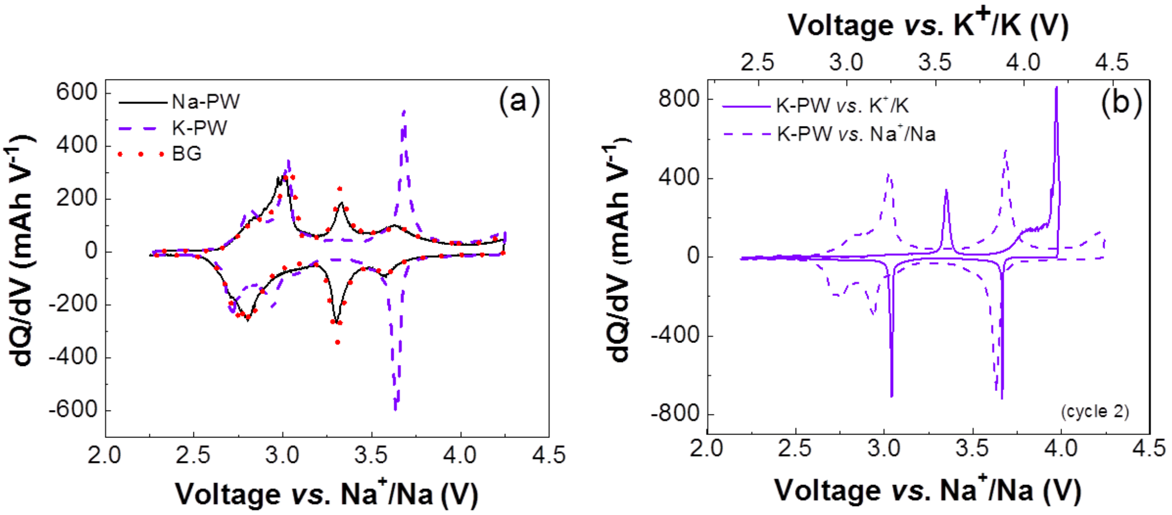

Figure 5.21. a) Comparative dQ/dV *vs.* V profile of laminated Na-PW (continuous line in black), K-PW (dashed line in purple) and BG (red dots) electrodes against Na$^+$/Na. As a reminder: BG is K-PW charged, washed with PC and cycled again *vs.* Na$^+$/Na. The electrolyte used was 1M NaPF$_6$ in EC: PC: FEC 49:49:2 % vol. in the three cases. b) dQ/dV profile comparative between the electrochemistry behavior of K-PW *vs.* K$^+$/K (continuous line in purple) and vs. Na$^+$/Na (dashed line in purple). The electrolyte used for KIB was 1M KPF$_6$ in EC: DMC 50:50 % vol. while 1M NaPF$_6$ in EC: PC: FEC 49:49:2 % vol. was the mixture selected for NIB.

In order to determine the nature of the lower voltage plateau and further corroborate the insertion of K$^+$ at the higher voltage process, K-PW was cycled *vs*. metallic potassium (K$^+$/K) using 1M KPF$_6$ in EC: DMC 50:50 % vol. as electrolyte. It is worth mentioning the excellent properties obtained when K-PW is tested vs. K$^+$/K (see Appendix, Figure A5.1), what proves its viability to be used as cathode in K-ion batteries, as Eftekhari[29] had already pointed out for potassium Prussian Blue in 2004. The dQ/dV *vs*. V curve of K-PW is plotted in Figure 5.21b along with the equivalent data obtained when the material was tested *vs*. Na$^+$/Na. The voltage shown by K-PW when cycled *vs.* Na$^+$/Na has been recalculated to facilitate comparison with that of K-PW cycled in a K-ion battery. The 0.211 V difference in the standard reduction potentials between Na$^+$/Na and K$^+$/K in aqueous solution[30] has been considered for the calculation, although this value may change in organic media. For clarity purposes, the voltage values are presented both *vs*. Na$^+$/Na and K$^+$/K. As it can be observed, the redox reduction peak is somehow coincident at the higher voltage plateau, which agrees with K$^+$ insertion previously described. Conversely, the redox process in the lower voltage plateau occurs at different potential value, revealing that the species inserted in the second reduction might be predominantly Na$^+$ or a mixture of both cations, Na$^+$ and K$^+$. The latter possibility is postulated as favorite since two redox peaks appear when cycling *vs*. Na$^+$/Na and only 1 peak when cycling *vs*. K$^+$/K. However, this fact should be verified.

To chemically confirm the hybrid nature of the cation insertion in K-PW, EDX analyses of 4 K-PW electrodes cycled *vs*. Na$^+$/Na and strategically stopped at certain points (a, b, c, d) of the electrochemical discharge curve (see Figure 5.22.a) have been performed. The electrolyte used in all the experiments was 1M $NaPF_6$ in EC: PC: FEC 49:49:2 % vol. Prior to the EDX collection, the electrodes were properly rinsed with PC several times (6-8 times) to remove any residual Na$^+$ trace that could remain from the electrolyte salt and, then, dried overnight at 80˚C under vacuum.

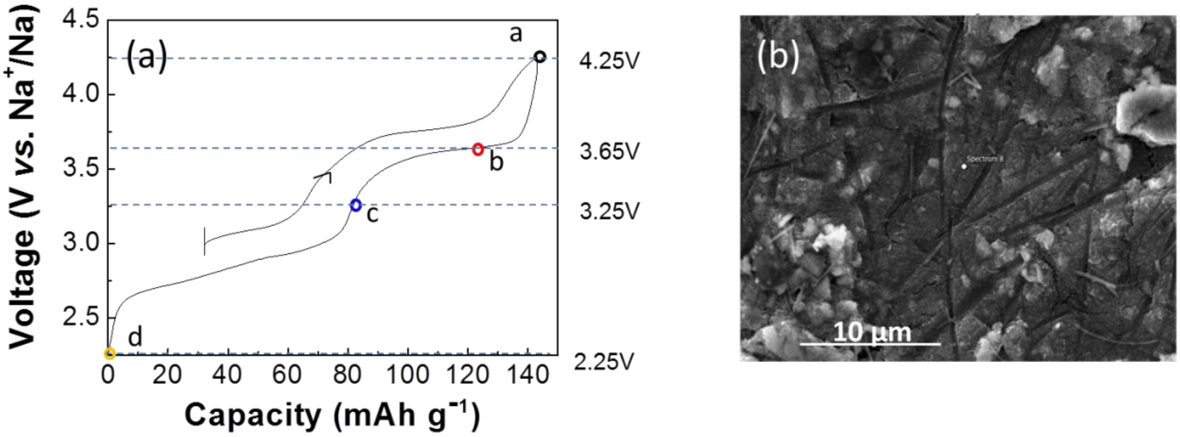

Figure 5.22. a) Electrochemical curve of K-PW when cycled vs. Na$^+$/Na at C/10. The different points at which the reaction was stopped are surrounded with a colored circle and are tagged in alphabetical order. b) SEM image of one of the cycled electrodes, showing the presence of fibers on it (see them in black).

No traces of K and Na should be found at the point "**a**" of the electrochemical curve since the totally charged phase Berlin Green (BG) is reached. However, a K/Na ratio of ca. 1 is observed at this point. The presence of the alkali content can be easily explained by the presence of Si in all the EDAX analyses, as a

---

[29] A. Eftekhari. *J. Power Sources* 2004, **126**, 221–228. "Potassium secondary cell based on Prussian blue cathode."

[30] D. R. Lide, W. M. Haynes. 2010 (Internet version), CRC Handbook of Chemistry and Physics, 90th Edition, page 8-22 (1212), Boca Raton (Florida) – USA, CRC press).

consequence of A_2SiF_6 (A = Na, K) formation. The source of Si is, without doubt, the glass fiber used as separator, as supported by the fibers encountered in the SEM picture of one of the electrodes (see Figure **5.22**b). The K/Na ratio evolution followed along the cycling (a, b, c, d) clearly indicates an increase in the K^+ content from Berlin Green (point "a") to the 25% of the discharge (point "b", in the middle of the PB formation process). This increment is even higher from "b" to "c", where "c" is equivalent to 50% of the discharge, i.e. once PB is completely achieved. Finally, the K/Na ratio, return to ca. 1, when the material reaches the PW phase at point "d". The K/Na ratios (summarized in Table 5.4) thus increase from BG to the PB phase and decrease from PB to PW, supporting our theory that K^+ is the metal being mainly inserted at the high voltage redox process and Na^+ is being the alkali mostly inserted at the low voltage plateau.

Table 5.4. K/Na ratio extracted at each point of the electrochemical curve.

	Electrode stopped in the electrochemical curve at the point			
	a	**b**	**c**	**d**
K/Na ratio	0.93	1.52	2.84	0.91

The hypothesis of structural variances in the lattice and/or different structural transformations upon cycling however is not discarded, since these effects could be additive to the cation effect already demonstrated. To determine whether structural variations are contributing, further work in understanding the mechanism behind should be carried out. In addition, a thorough study of the reaction mechanism could unravel the enigma of the cation (either Na^+ or a mixture of Na^+/K^+) which is being inserted/de-inserted in the lower voltage plateau of K-PW. If a mixed insertion was verified, this would add to the list of beneficial cooperative effects which have already been observed for other cation combinations, such as Li and Na[31, 32, 33] or Mg and Na.[34]

Figure 5.23a and b shows the C-rate capabilities of Na-PW and K-PW against metallic sodium (Na^+/Na). When cycled in powder form (Figure 5.23a), both materials exhibited reversible capacities up to 145-150 $mAh{\cdot}g^{-1}$ at C/10 (considering C_{th} = 85.4 $mAh{\cdot}g^{-1}$ per $1Na^+$ insertion per formula unit for Na-PW and 77.5 $mAh{\cdot}g^{-1}$ for K-PW) with coulombic efficiencies of ca. 95-97% and 97-99.4%, respectively. These specific discharge capacities are similar to those already reported in the literature for the rhombohedral purely iron based Na-PW.[25, 26] At moderate C-rate as 1C, capacities around 115-120 $mA{\cdot}g^{-1}$ were achieved by both PW phases while at 10C (nearly $1A{\cdot}g^{-1}$), the capacity retention displayed by Na-PW (75 $mAh{\cdot}g^{-1}$) was larger than that of K-PW (50 $mAh{\cdot}g^{-1}$). However, both materials demonstrated a good stability when cycled back at C/10.

---

[31] A. Kohandehghan, K. Cui, M. Kupsta, J. Ding, E. M. Lotfabad, W. P. Kalisvaart, D. Mitlin. *Nano Lett.* 2014, **14**, 5873–5882. "Activation with Li Enables Facile Sodium Storage in Germanium."

[32] W. Song, X. Ji, Z. Wu, Y. Zhu, F. Li, Y. Yao, C. E. Banks. *RSC Adv.* 2014, **4**, 11375-11383. "Multifunctional dual $Na_3V_2(PO_4)_2F_3$ cathode for *both* lithium-ion and sodium-ion batteries"

[33] L. Chen, Q. Gu, X. Zhow, X. Lee, Y. Xia, Z. Liu. *Sci. Rep.* 2013, **3**, 1946. "New-concept Batteries Based on Aqueous Li^+/Na^+ Mixed-ion Electrolytes."

[34] M. Walter, K. V. Kravchyk, M. Ibáñez, M. V. Kovalenko. *Chem. Mater.* 2015, **27**, 7452–7458. "Efficient and Inexpensive Sodium–Magnesium Hybrid Battery."

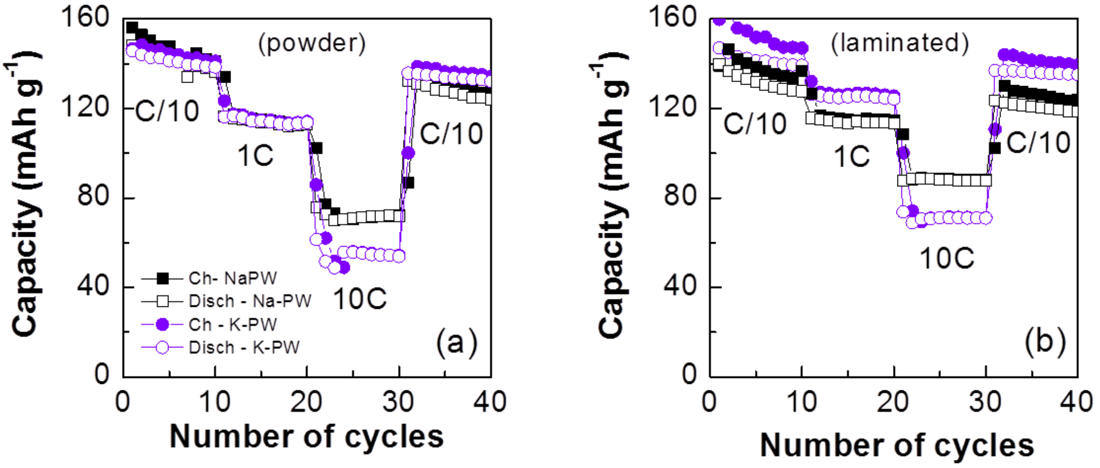

Figure 5.23. C-rate capabilities of Na-PW (black squares) and K-PW (violet circles) *vs.* Na$^+$/Na cycled in powder (a) and coated over Al current collector (b). 1M NaPF$_6$ in EC: PC: FEC 49:49:2 % vol. was used as electrolyte in all experiments.

C-rate capabilities of Na-PW and K-PW, when the materials are coated over Al current collector forming electrodes are displayed in Figure 5.23b. In this case, although the obtained specific capacities were similar to those achieved in powder, a negative effect in the coulombic efficiency is observed at low current densities, C/10. This non-desirable inefficiency is reduced, nonetheless, once the materials operate at moderate and higher capabilities, finding analogous values than in powder. Moreover, better capacity retention is noted when comparing to the powder form. Approximately 126 mAh·g^{-1} was achieved for K-PW at 1C, and 88 mAh·g^{-1} and 72 mAh·g^{-1} were respectively observed for Na-PW and K-PW at 10C. The adverse effect on the coulombic efficiency at low current densities could tentatively be attributed to Al current collector corrosion, though PF$_6^-$ usually protects the Al$_2$O$_3$ layer. The addition of ACl (A = Na, K) to synthesize the material, although beneficial to raise the alkali content, can imply the risk of corroding the Al used as substrate by the rests of Cl. Consequently, it is primordial to thoroughly rinse the material with H$_2$O to remove all the Cl$^-$. In our case, no Cl$^-$ presence was detected in pristine K-PW and only some traces in some isolated particles at Na-PW (as shown EDX spectra, in section 3.3.3.5, Figure 3.48).

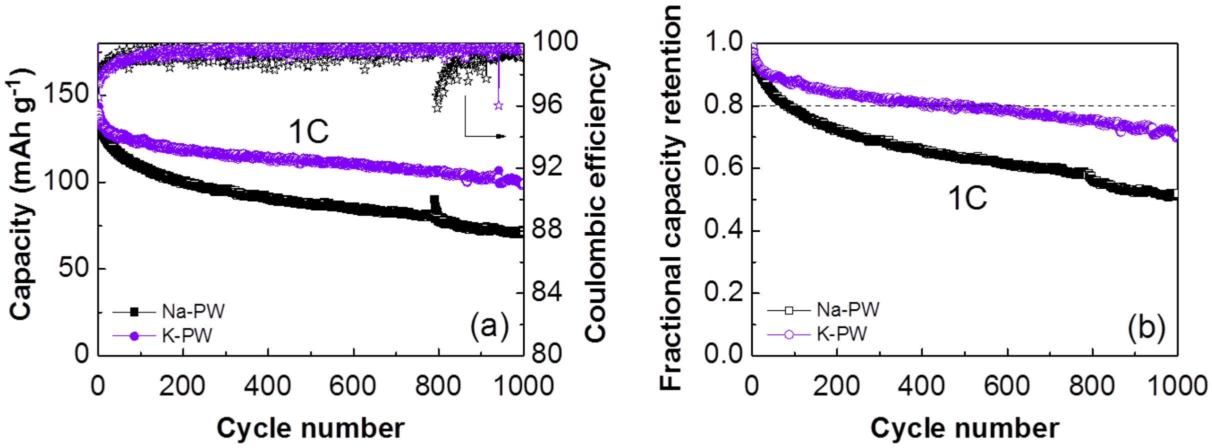

Figure 5.24. Long-term cyclabilities (a) capacities and coulombic efficiency values, b) fractional capacity retention) of Na-PW (black) and K-PW (violet) laminated electrodes when cycling *vs.* Na$^+$/Na in the cut off voltage ΔV= 2.25 – 4.25 V. 1M NaPF$_6$ in EC: PC: FEC 49:49:2 % vol. was the electrolyte utilized in all experiments here displayed.

The good performance of Na-PW and K-PW along the cycle-life at moderate current density (see Figure 5.24) is also remarkable. Roughly 140 mAh·g^{-1} were achieved during the first cycles at 1C. In addition, 63.4% of the initial capacity was retained after 500 cycles with > 98% of coulombic efficiency for Na-PW. Although the capacity retention obtained for the cubic Na-PW is lower than that presented by Goodengouh[26] and Guo-Guo[25], the coulombic efficiency is far superior. Besides, comparing cubic Na-PW with other Prussian White systems, such as those Mn-Fe,[35, 36] Co-Fe[37, 38] or Mn-Mn[39] based, the capacity retention and coulombic efficiency values are also higher. On the other hand, the hybrid K-PW exhibits enhanced properties compared to Na-PW when cycled *vs*. Na$^+$/Na. Exactly 80% of the initial capacity was retained after 500 cycles with > 97.5% of coulombic efficiency during the first 30 cycles and > 99.5% in cycle 500, evidencing a fairly good stability in a long-term cyclability of ca. 1000 h = 42 days of autonomy. The coulombic efficiency obtained, far from the optimum > 99.9%, could be fairly improved by simply assembling full cells. As mentioned in the introduction, the deployment of metallic Na as negative and counter electrode is known to react detrimentally with the electrolyte forming dendrites, resulting in inefficiency.[1, 3, 40, 41] Another option to bear in mind could be to change the Al current collector deployed in here by a carbon cloth current collector substrate frequently used in Prussian Blue systems.[39] These tasks will be addressed in the future.

5.3.3. Concluding remarks of "Prussian White as cathode *vs*. Na$^+$/Na in organic media"

Purely iron based Na-PW and K-PW have been synthesized following a new mild synthetic route, that allowed the formation of materials with cubic structure, as confirmed by XRD and Electron diffraction experiments in the TEM, unlike those reported previously in the literature. The benefit of obtaining cubic symmetry is important, since the species formed during the cycling process (PB and BG) are cubic as well, and no structural transitions, would be in principle required. Specific capacities above 140 mAh·g^{-1} at moderate current density (1C) with reasonably high coulombic efficiencies values (above 98%) were exhibited by Na-PW and K-PW when operating *vs*. Na$^+$/Na in the cathodic range from 2.25 to 4.25 V. To improve the good but limited coulombic efficiency obtained with Al current collector and the use of metallic Na as counter and reference electrode, full cell constructions and the use of carbon based

---

[35] M. Takachi, T. Matsuda, Y. Moritomo. *Chem. Commun.* 2013, **49**, 2750-2752. "A sodium manganese ferrocyanide thin film for Na-ion batteries."

[36] L. Wang, Y. Lu, J. Liu, M. Xu, J. Cheng, D. Zhang, J. B. Goodenough. *Angew. Chem. Int. Ed.* 2013, **52** (7), 1964-1967. "A superior low-cost cathode for a Na-ion battery"

[37] M. Takachi, T. Matsuda, Y. Moritomo. *Appl. Phys. Express* 2013, 6, 025802. "Cobalt Hexacyanoferrate as Cathode Material for Na+ Secondary Battery."

[38] X. Wu, C. Wu, C. Wei, L. Hu, J. Qian, Y. Cao, X. Ai, J. Wang, H. Yang. *ACS Appl. Mat. Interfaces* (2016). DOI: 10.1021/acsami.5b12620. "Highly Crystallized $Na_2CoFe(CN)_6$ with Suppressed Lattice Defects as Superior Cathode Material for Sodium-Ion Batteries"

[39] H.-W. Lee, R. Y. Wang, M. Pasta, S. W. Lee, N. Liu, Y. Cui. *Nat. Commun.* 2014, **5**, 5280. "Manganese hexacyanomanganate open framework as a high-capacity positive electrode material for sodium-ion batteries."

[40] A. Rudola, D. Aurbach, P. Balaya. *Electrochem. Commun.* 2014, **46**, 56. "A new phenomenon in sodium batteries: Voltage step due to solvent interaction."

[41] N. Weadock, N. Varongchayakul, J. Wan, S. Lee, J. Seog, L. Hu. *Nano Energy* 2013, **2**, 713. "Determination of mechanical properties of the SEI in sodium ion batteries via colloidal probe microscopy".

current collectors are recommended. Undoubtedly, the novelty and the greatest achievement obtained with these phases is the interesting boost in the gravimetric energy density observed in K-PW (for the first time tested as cathode in NIB) with respect to Na-PW, due to a raise of 0.35V in the potential at which the high voltage redox process occurs. The main reason is so far ascribed to the insertion and de-insertion of K^+ instead of Na^+. However, further studies on the reaction mechanism must be performed to either discard or confirm an additional effect due to a structural change and synergetic effects related to the presence of both cations in the medium. This higher voltage, along with the better capacity retention (80% after 500 cycles), makes K-PW an even more attractive cathode material than Na-PW for real market applications.

Chapter 6

Development of Na-ion full cells based on Prussian Blue and Prussian White materials

6.-) Development of Na-ion full cells based on Prussian Blue and Prussian White materials

This chapter focuses on the development of organic sodium-ion full cells, involving the utilization of sodium Prussian Blue, $Na_{0.75}[Fe_{2.08}(CN)_6]\cdot 3.4H_2O$, and Prussian White materials, ($Na_{1.70}[Fe_{2.15}(CN)_6]\cdot 0.19H_2O$ and $K_{1.59}Fe_{2.20}(CN)_6\cdot 0.26H_2O$), as positive electrodes. First, an evaluation of the materials to be used in the full cell is covered. Then, the following section of this chapter are intended to the build-up of a full cell using Na-PB or A-PW (A= Na, K) as cathodes. Finally, a comparison among all the full cells assembled is addressed.

6.1. Na-ion organic full cell development

6.1.1. Scope

Considering the fairly good performance of the Prussian Blue/White materials already studied in previous chapters for NIB, especially as cathodes in organic media, the development of a sodium-ion full cell based on them arose as the next step to follow.

Because the specific energy (also called gravimetric energy density) of a rechargeable battery is determined mainly by the specific capacities and operating voltages of the anodes and the cathode, the election of the electrodes is of paramount importance. The higher the specific capacities of the electrodes and the larger chemical potential difference between the two electrodes, the greater the energy that will be stored in and released by the battery[1, 2] (see (Eq. 6.1).

$$Specific\ Energy\ (Wh \cdot Kg^{-1})\ = \int Capacity\ (Ah \cdot kg^{-1}) \cdot\ Voltage\ (V) \qquad \textbf{(Eq. 6.1)}$$

being the voltage of the cell the voltage difference between the cathode and the anode (Voltage (V) = Voltage cell = $V_{cathode} - V_{anode}$) at any given point of the charge-discharge curve of the full battery. Graphically, the specific energy is the area under the voltage *vs*. specific capacity curve resultant of cycling the full cell (as shown Figure 6.1).

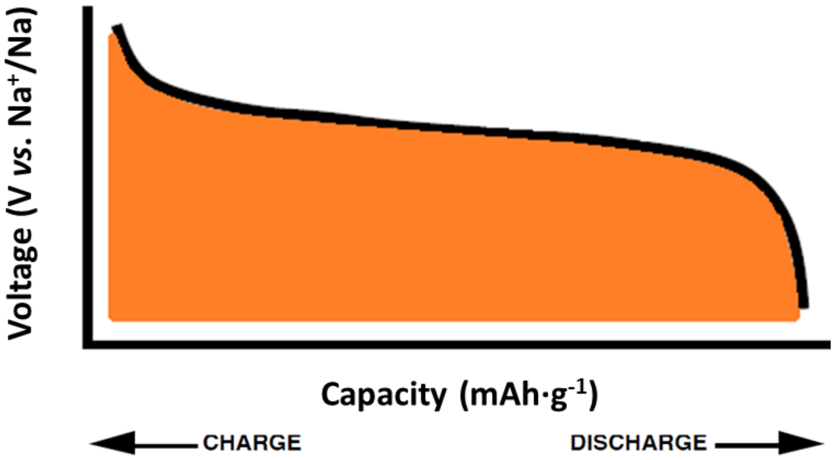

Figure 6.1. Battery charge/discharge curve (black line) and its specific energy (delimited area colored in orange), assuming absence of irreversibilities and inefficiencies.

---

[1] M. Armand, J-M. Tarascon. *Nature* 2008, **451**, 652-657. "Building better batteries".

[2] J. W. Choi, D. Aurbach. *Nat. Rev. Mat.* 2016. DOI: 10.1038/natrevmats.2016.13. "Promise and reality of post-lithium ion batteries with high energy densities".

6.1.2. Electrode´s election

6.1.2.1. *Cathode election*

The cathodes deployed in the full cell build-up included all cathodes already examined in this thesis work in organic media, that is, sodium Prussian Blue (Na-PB, $Na_{0.75}[Fe_{2.08}(CN)_6]\cdot 3.4H_2O$), sodium Prussian White (Na-PW, $Na_{1.70}[Fe_{2.15}(CN)_6]\cdot 0.19H_2O$) and potassium Prussian White (K-PW, $K_{1.59}Fe_{2.20}(CN)_6\cdot 0.26H_2O$).

Despite Na-PB provides less attractive electrochemical properties against sodium than the A-PW phases (A = Na, K), its even easier synthesis (at RT and air atmosphere) and thereby less expensive, encouraged its utilization as cathode material in a sodium-ion full cell.

The superior performance of the alkali-rich A-PW phases *vs*. Na^+/Na, which exhibited large capacities at even 1C (over 140 $mAh\cdot g^{-1}$) with reasonable high coulombic efficiency values (above 98%), is beyond discussion. Thus, promising results are expected from a sodium-ion full cell containing them as cathodes. Specially in the case of K-PW, that features a significant increment of 0.35 V in the upper voltage plateau with respect to Na-PW as well as an impressive capacity retention (80% of the initial capacity after 500 cycles at 1C).

6.1.2.2. *Anode election*

The materials studied as electrodes for NIB batteries are standardly tested *vs*. Na metal with the purpose of finding out their potential intrinsic electrochemical intrinsic properties for this new technology. However, as in lithium-ion batteries, the use of metallic anode so far entails several risks and safety concerns for practical applications. The sodium plating along the charging process leads to the formation of dendrites[3] and, elapsed certain cycles, the subsequent shortcut of the battery, inducing thermal run-away of the cathode, what could provoke flame generation. Additionally, the thermal stability of sodium is half than that of lithium (being 97.7 and 180.5 ˚C the melting point of Na and Li metals, respectively), presenting a higher risk of melting.[4] Besides, the SEI layer that forms on metallic sodium has not been stabilized and short cycle-life is expected. Thus, sodium needs to be replaced by another anode material.

In this thesis, the electrochemical activity of Na-PB as anode *vs*. Na^+/Na in organic media (chapter 4, section 4.2.2.1) has been proved for the first time. However, and despite the optimization with SBR/CMC binder, the material is only capable of achieving 180 $mAh\cdot g^{-1}$ along the first charge and becomes an impractical anode after 10 cycles at C/10, since it retains less than 80% of the initial capacity. Aside from the lower capacity and the higher operating voltage (0.5 V *vs*. Na^+/Na) compared to other candidates, some other limitations include its huge irreversibility in the first discharge and the possibility of undergoing through conversion reaction.

---

[3] D. Kundu, E. Talaie, V. Duffort, L. Nazar. *Angew. Chem. Int. Ed.* 2015, **54**, 3431-3451. "The Emerging Chemistry of Sodium Ion Batteries for Electrochemical Energy Storage".

[4] M. Dahbi, N. Yabuuchi, K. Kubota, K. Tokiwa, S. Komaba. *Phys. Chem. Chem. Phys.* 2014, **16**, 15007-15027. "Negative electrodes for Na-ion batteries".

The different anode materials investigated for NIB were exposed at the beginning of this thesis (in Chapter 1, section 1.3.5.2). Taking into account diverse parameters, such as low cost, environmental impact, capacity and operating voltage (see Figure 6.2), hard carbons (HC hereinafter) emerge as the firmest candidate for market applications[5] and will be the anode chosen for the sodium-ion full cells construction here developed.

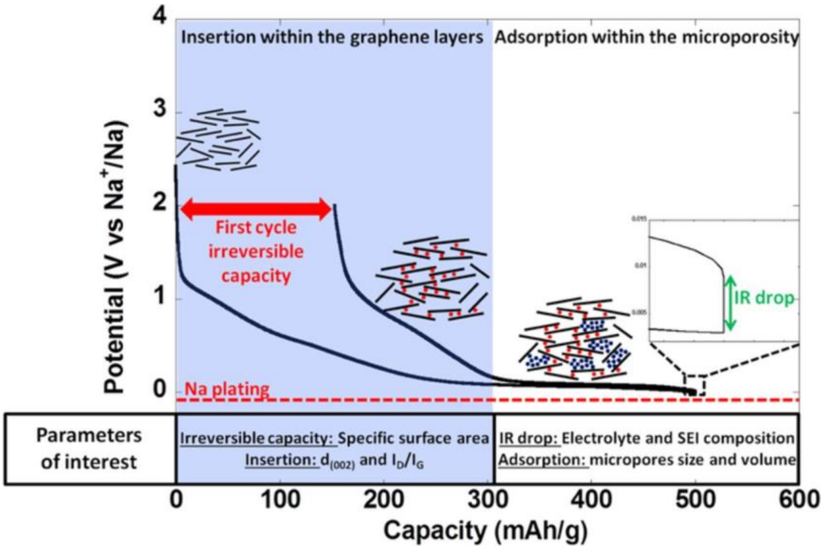

Figure 6.2. Typical potential *vs*. capacity profile for hard carbon (HC) when tested against sodium metal as counter and reference electrode, accompanied of a schematic representation of the Na$^+$ ion storage inside the HC structure.[6]

6.1.2.3. *Electrochemical characterization of HC*

Commercial hard carbon (HC) was used as anode in the assembly of Na-ion full cells.

Despite the optimized electrolyte for Na-PB (and transferred to A-PW by analogy) has proved to be 1M $NaPF_6$ in EC: PC: FEC 49:49:2 % vol., the effect that the utilization of FEC additive has upon HC for Na$^+$ insertion is still under debate. Komaba´s group demonstrated the improvement of the capacity retention of their hard carbon along the cycles by FEC addition,[7] whereas Palacín´s group evidenced a decline in the reversible capacity and the coulombic efficiency in their hard carbon if the FEC additive was included in the electrolyte formulation.[8] Such differences might be ascribed to the variability of carbons used for different studies, since the structure of HC changes depending on the synthesis conditions (carbon sources and carbonization temperature).[4] Under these circumstances, the commercial HC used in this study was tested both with 1M $NaPF_6$ in EC: PC 50:50 % vol. and 1M $NaPF_6$ in EC: PC: FEC 49:49:2 % vol. and the results obtained are displayed below, in Figure 6.3.

---

[5] D. A. Stevens, J. R. Dahn. *J. Electrochem. Soc.* 2000, **147**, 1271-1273. “High Capacity Anode Materials for Rechargeable Sodium-Ion Batteries”.

[6] E. Irisarri, A. Ponrouch, M. R. Palacín. *J. Echem. Soc.* 2015, **162** (14), A2476-A2482. “Review – Hard Carbon Negative Electrode Materials for Sodium-Ion Batteries”.

[7] S. Komaba, T. Ishikawa, N. Yabuuchi, W. Murata, A. Ito, Y. Ohsawa. *ACS Appl. Mater. Interfaces* 2011, **3** (11), 4165-4168. “Fluorinated Ethylene Carbonate as Electrolyte Additive for Rechargeable Na Batteries”.

[8] A. Ponrouch, A. R. Goñi, M. R. Palacín. *Electrochem. Commun.* 2013, **27**, 85-88. “High capacity hard carbon anodes for sodium ino batteries in additive free electrolyte”.

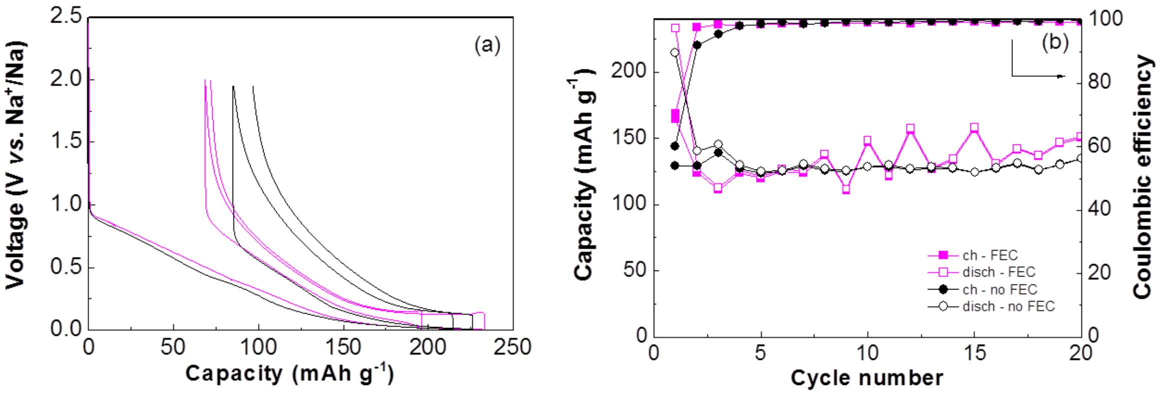

Figure 6.3. a) Voltage profile and b) cyclability and coulombic efficiency of hard carbon *vs.* Na^+/Na at i= $1\cdot10^{-4}$ A, in the voltage range of ΔV = 5 mV - 2.0 V, along the first 20 cycles when using 1M $NaPF_6$ in EC: PC 50:50 % vol. (black line/ dots) and in EC: PC: FEC 49:49:2 % vol. (pink line/ squares).

Laminated electrodes of hard carbon were prepared as described in chapter 2 (see section 2.2.4.2.1), getting a mass loading of active material on the order of 1.5 mg. The electrodes were cycled in the cut-off voltage from 5 mV to 2.0 V *vs*. Na^+/Na (Figure 6.3.a), showing the characteristic voltage profile observed in hard carbons (Figure 6.2). An initial slopping-voltage region from ca. 1.0 V to 0.1 V attributed to the Na^+ intercalation between graphene sheets, followed by a plateau region below 0.1 V associated to the adsorption of Na^+ in the nanopores are observed.[5] Over 120-130 $mAh\cdot g^{-1}$ of reversible gravimetric capacity was achieved at a current of 0.1 mA. Interestingly, the hard carbon tested with FEC, showed lower polarization. As illustrates Figure 6.3b, the coulombic efficiency values are almost coincident regardless of the use of FEC or not. However, it is obvious that the stability of the HC is far superior as long as no FEC is added to the electrolyte mixture. The oscillation of the capacity by the FEC presence might be ascribed to the formation of an unstable SEI layer. Consequently, the Na-ion full cells will be assembled with 1M $NaPF_6$ in EC: PC as electrolyte.

6.1.3. HC/Na-PB full cell development – Results and discussion

The development of the HC/Na-PB full cell was initiated at CIC energiGUNE and continued at Argonne National Laboratory. At Argonne, the work was performed under the supervision of the Group Leader of Materials Dr. Christopher Johnson. It was decided to use 1M $NaPF_6$ in PC as electrolyte, instead of the mixture containing EC, with the intention of making posterior measurements at low temperatures without solidifying the electrolyte and thus, check if the battery keeps on working/ functioning in extreme situations. Although finally, such measurement conditions, could not be applied.

The change of electrolyte, requires to test both the Na-PB cathode and the HC anode with the new 1M $NaPF_6$ in PC electrolyte at a fixed current density.

Laminated electrodes of Na-PB were prepared as usual, following the procedure detailed in chapter 2 (see section 2.2.4.2.1). The mass loading of Na-PB oscillates about 3 mg. The electrochemical performance of a Na-PB half-cell cycled in the voltage cut-off from 2.4 to 4.2 V is depicted in Figure 6.4a. Reversible specific discharge capacities of 86 mAh·g^{-1} were reached. From the cell, 0.3 mAh were obtained and this value was considered to make the charge balance calculation with the hard carbon. A positive to negative electrode capacity ratio of 1:1.3 was stablished as targeted point. As already reported in chapter 5 (section 5.1.), the first charge reflected the half-sodiated content of the Na-PB and corresponds to the oxidation of Na-PB ($NaFe^{III}[Fe^{II}(CN)_6]$) into BG ($Fe^{III}[Fe^{III}(CN)_6]$) at 3.55 V *vs.* Na$^+$/Na. Along the discharge, the lower voltage process becomes also available, and both the reduction of BG to Na-PB at *ca.* 3.44 V *vs.* Na$^+$/Na and subsequent reduction of Na-PB to Na-PW ($NaFe^{II}[Fe^{II}(CN)_6]$) at *ca.* 2.8 V were observed.

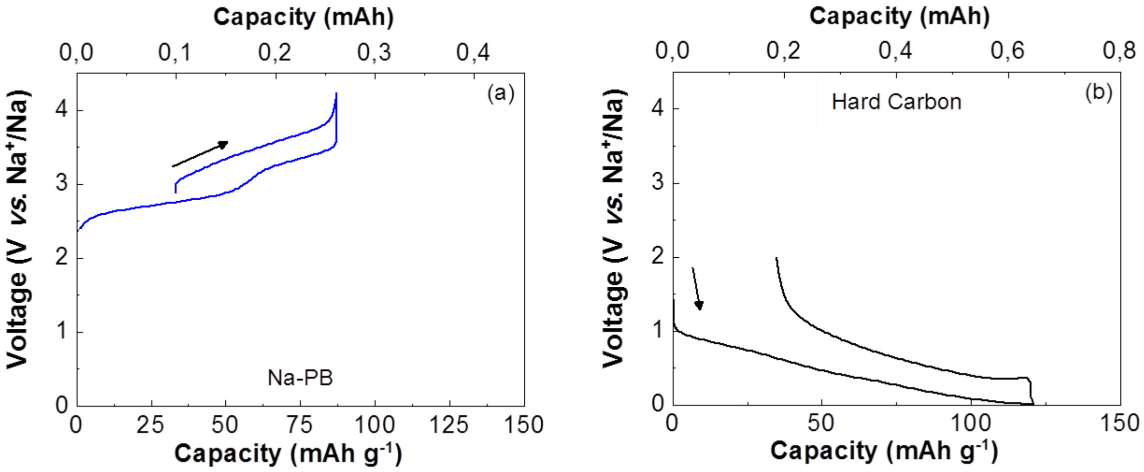

Figure 6.4. Capacity *vs.* voltage profile of the first cycle of a) Na-PB half-cell (in blue), tested in the range of 2.4 V - 4.2 V *vs.* Na$^{+/}$Na and b) HC half-cell (in black) cycled in the 5 mV - 2.0 V *vs.* Na$^{+/}$Na range, at a current of 2·10^{-4} A, using 1M $NaPF_6$ in PC.

Laminated electrodes of HC were prepared by mixing 90 % of active material with 7% of PVDF and 3% of carbon super P. The electrochemical behavior of a HC half-cell, cycled in the range of 5 mV - 2.0 V *vs.* Na$^+$/Na using 1M $NaPF_6$ in PC (shown in Figure 6.4.b), is pretty similar to that displayed with 1M $NaPF_6$ in EC: PC 50: 50 % vol. Again two regions are clearly distinguished, a sloppy-voltage region from 1.2 to 0.1 V *vs.* Na$^+$/Na and a plateau region below 0.1 V. In this case, HC exhibited reversible gravimetric capacities of 87 mAh·g^{-1} at a current of 2·10^{-4} A.

For the full cell construction, pre-cycling of the hard carbon was carried out against metallic sodium in a coin cell, using 1M $NaPF_6$ in PC. HC was discharged and subsequently charged between 5 mV and 2.0 V vs. Na$^+$/Na, holding it at the constant voltage of 2.0 V for few hours, in order to assure the complete formation and stability of the charged state. In the same way, Na-PB was oxidized and reduced between 2.4 and 4.2 V vs. Na$^+$/Na, to avoid the coulombic inefficiency of the first cycle derived from the partial sodium content present in the pristine material. Na-PB was maintained at the constant voltage of 2.4 V also for several hours. These pre-cycled electrodes were extracted from the sodium half-cells to assemble the sodium full cell HC/Na-PB in a coin cell CR2032, using 1M $NaPF_6$ in PC.

The open circuit voltage (OCV) of the full cell raised from 0.86 to 1.86 V during the 12 hours of resting, before cycling. To hinder the plating of sodium, the voltage window for the full cell operation was carefully selected. The HC/Na-PB full cell was cycled in the 0.5 - 4.05 V *vs.* Na$^+$/Na voltage range, starting by charging. For a better understanding, the charge of a full cell means that the cathode is being charged while the anode is being discharged. In other words, during the charge process of the full cell, Na^+ ions are deintercalated from the Na-PB cathode, causing the oxidation of Fe^{2+}-N to Fe^{3+}-N. These Na^+ ions diffuse through the electrolyte to finally be inserted into the hard carbon.

Even if Na-PB and HC were pre-cycled, the full cell exhibited some irreversibility (ca. 40 mAh·g^{-1}) along the first cycle (as shown in Figure 6.5.a), which was also present in subsequent cycles (see Figure 6.5.b) although to a smaller exent.

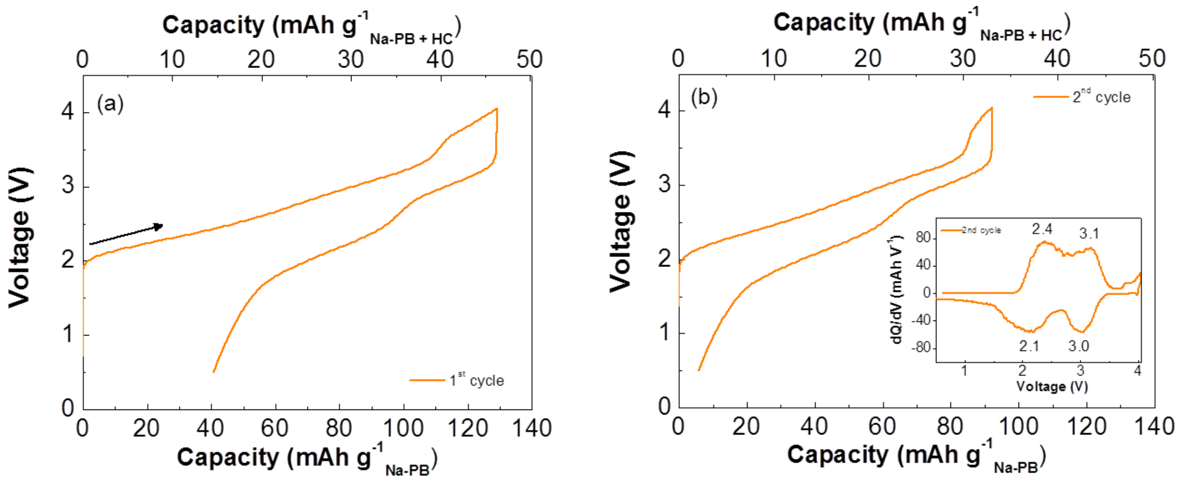

Figure 6.5. Capacity *vs*. voltage profile of the sodium-ion full cell HC/Na-PB a) along the first cycle and b) second cycle (inset) dQ/dV vs. V curve of the second cycle, when cycled in the voltage range from 0.5 to 4.05 V range at a current of $1·10^{-4}$ A, using 1M $NaPF_6$ in PC.

As the inset of Figure 6.5.b illustrates, the dQ/dV vs. V curve corresponding to the second cycle of the full cell, presents two maxima in charge, at 2.4 and 3.2 V, and two minima during the discharge at 3.0 and 2.1 V. As expected, these voltages at which the redox processes occur are shifted towards lower values regarding the cathode *vs*. Na^+/Na (whose plateau appeared at 2.95 and 3.65 V in charge and at 2.8 and 3.4 V *vs*. Na^+/Na during discharge) and towards higher voltage values with respect to the anode. Thus demonstrating that the HC/Na-PB full cell is a true combination of the materials that integrate it, HC and Na-PB.

The sodium-ion full cell HC/Na-PB is capable of delivering reversible capacities up to 89 mAh·g$^{-1}_{cathode}$ (considering the mass loading of active material of the cathode, Na-PB, that was of 2.98 mg) or 32 mAh·g$^{-1}_{cathode + anode}$ (based on the mass loading of both active materials, Na-PB and HC) and retain even 80% of the initial capacity lapsed 50 cycles, when cycled at $1·10^{-4}$ A (see Figure 6.6.a). The coulombic inefficiency encountered initially (68.5 % in the first cycle) is also overcome after 10 cycles, reaching values > 98% (and over 99% after 20 cycles). The integration of the voltage vs. capacity electrochemical curve of the second discharge provided a specific energy of **70** Wh·Kg$^{-1}_{cathode + anode}$, as Figure 6.6.b shows. Once determined the energy, and knowing the capacity of the discharge curve, the average operating voltage could be calculated applying equation (Eq. 6.1. The average voltage of the HC/Na-PB full cell turned out to be of 2.2 V.

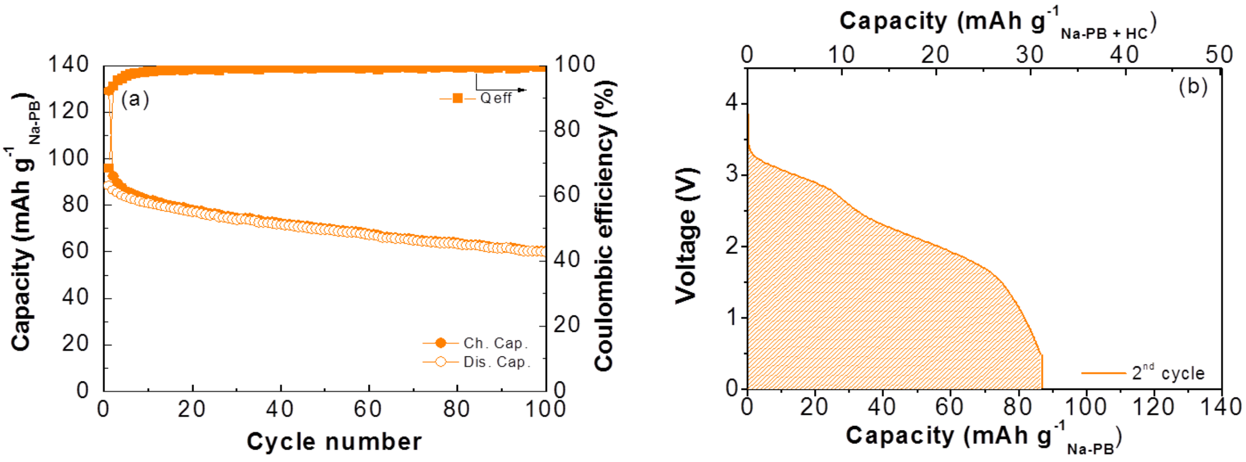

Figure 6.6. a) Cyclability, coulombic efficiency and b) second discharge curve (for calculating the energy density) of the full cell HC/Na-PB, tested in the cut-off voltage from 0.5 - 4.05 V,using 1M $NaPF_6$ in PC and a current of $1{\cdot}10^{-4}$ A.

Only a recent work has reported the performance of a Na-PB@C composite as cathode material in a full cell, using also commercial hard carbon as anode. The full cell was cycled over the voltage range of 2.0 - 4.0 V at a current density of 100 mA·g^{-1}, using 1M $NaPF_6$ in EC: DEC 1: 1 % vol. On the basis of the cathode mass, an initial discharge of 50 mAh·g^{-1} was achieved, followed by a reversible discharge capacity of 120 mAh·g^{-1} in the second cycle that fades down to ca. 100 mAh·g^{-1} (83.3% of capacity retention) after 25 cycles.[9]

The values obtained in this thesis work for the HC/Na-PB full cell are reasonable for a sodium-ion battery. However, better long-term stabilities would be required and higher energy would be desirable. Since the Na-PB deployed in the studied full cell was synthesized by co-precipitation method at room temperature, a large amount of $[Fe(CN)_6]^{4-}$ defects is presumed on its structure, what could be undoubtedly one of the causes for the capacity decay. A superior cyclability could be acquired, for instance, by replacing the Na-PB here deployed by a highly crystalline Na-PB almost free of such defects.[10] Additionally, the role of the electrolyte should not be forgotten. The presence of EC in the mixture, would promote the formation of a more stable SEI layer. Furthermore, it is also beyond discussion that a better mass balance could provide higher amount of energy upon time which is desirable for these type of batteries. In any case, this attempt of the HC/Na-PB full cell serves as starting point and proof of concept for the utilization of Na-PB in real battery application, although several implementations are still required.

6.1.4. HC/A-PW full cell development – Results and discussion

The development of the HC/A-PW (A = Na, K) full cell took place entirely at CIC energiGUNE. In these cases, it was decided to use 1M $NaPF_6$ in EC: PC 50: 50% vol. as electrolyte and the electrochemical operation of A-PW as well as the HC anode were re-examined at a fixed current of $1{\cdot}10^{-4}$ A.

---

[9] Y. Jiang, S. Yu, B. Wang, Y. Li, W. Sun, Y. Lu, M. Yan, B. Song, S. Dou. *Adv. Funct. Mater*. 2016, **26** (29), 5315-5321. “Prussian Blue@C Composite as an Ultrahigh-rate and Long-Life Sodium-Ion Battery Cathode”.

[10] Y. You, X-L. Wu, Y-X. Yin, Y. Guo-Guo. *Energy Environm Sci*. 2014, **7**, 1643. “High-quality Prussian blue crystals as superior cathode materials for room-temperature sodium-ion batteries”.

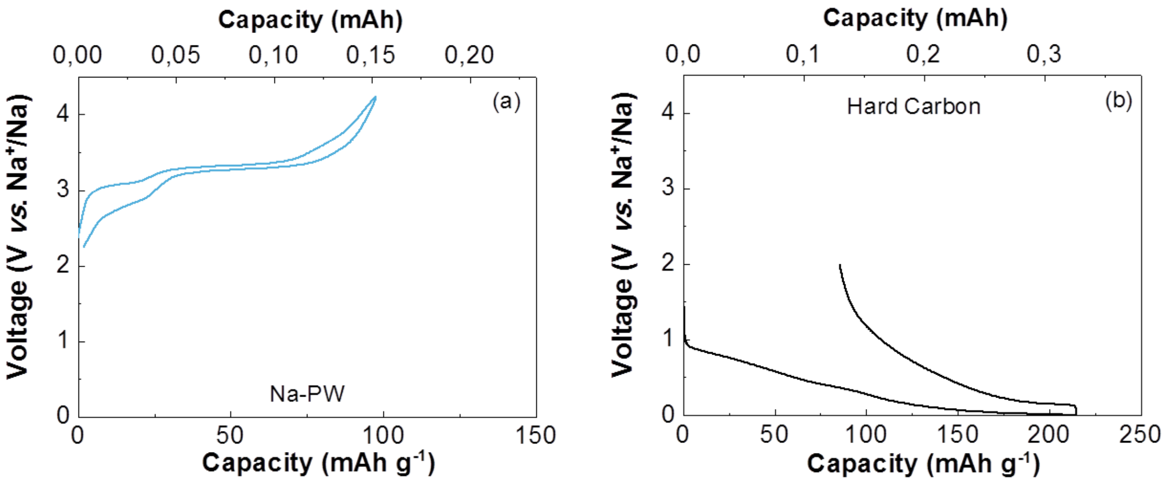

Figure 6.7. Capacity *vs*. voltage profile of the first cycle of a) Na-PW half-cell (in blue), tested in the 2.25 V - 4.25 V *vs*. $Na^{+/}Na$ range and b) HC half-cell (in black) cycled in the 5 mV - 2.0 V *vs*. $Na^{+/}Na$ range, at a current density of $1·10^{-4}$ A, using 1M $NaPF_6$ in EC: PC 50:50 % vol.

Some electrodes already prepared of A-PW, containing 70% of active material with 20% of ketjen black and 10% of PVDF (see section 2.2.4.2.1 for further details), were deployed for the electrochemical investigations of the full cell assembly. The active mass loading of the Na-PW and K-PW electrodes selected resulted in 1.5 and 3.3 mg, respectively. Reversible gravimetric capacities of 95 and 90 $mAh·g^{-1}$ were delivered by Na-PW and K-PW half-cells, when tested in the voltage cut-off from 2.25 to 4.25 V *vs*. Na^+/Na (as shown Figure 6.7.a and Figure 6.8.a). From the cell, 0.15 mAh was obtained from Na-PW electrodes and 0.28 mAh from K-PW. Emulating the procedure followed in the previous section, these values were considered to make the mass balance calculation with the hard carbon.

The voltage profile of both Prussian White materials resembles those reported in chapter 5 (section 5.3.2). A pair of sloppy plateaus centered at 3.0 and 3.3 V *vs*. Na^+/Na are observed along the charge for Na-PW, whose reversible processes occur at 2.8 and 3.3 V during the discharge. For K-PW, two plateaus are distinguished at 3.0 and 3.7 V along the oxidation curve and, this time, three redox reactions at 2.7, 3.0 and 3.6 V are appreciated while discharging. The difference in the upper voltage plateau value is still evident between both phases, favoring K-PW in terms of specific energy, although a beneficial lower polarization is also appreciated on Na-PW.

In this occasion, laminated electrodes of HC were prepared by mixing 80 % of active material with 10% of PVDF and 10% of carbon super C-65®. The electrochemical tests of HC half-cells, cycled using 1M $NaPF_6$ in EC: PC (shown in Figure 6.7.b and Figure 6.8.b) exhibited the characteristic performance of hard carbons. Reversible gravimetric capacities close to 130 $mAh·g^{-1}$ and 100 $mAh·g^{-1}$ were respectively reached at currents of $1·10^{-4}$ A and $2·10^{-4}$ A. Again, for the full cell construction, pre-cycling of the hard carbon was carried out in half-cell *vs*. metallic sodium.

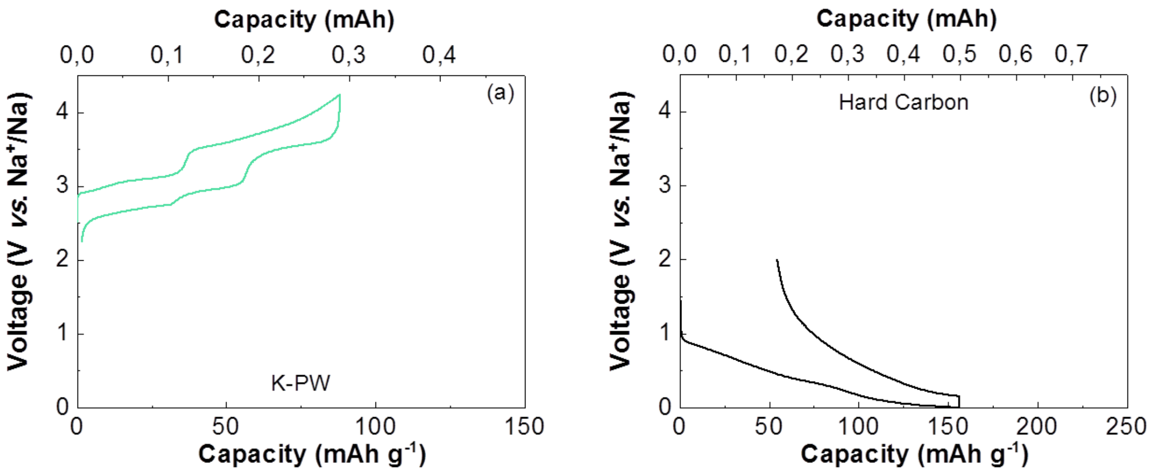

Figure 6.8. Capacity *vs*. voltage profile of the first cycle of a) K-PW half-cell (in green), tested in the 2.25 V - 4.25 V *vs*. $Na^{+/}Na$ range and b) HC half-cell (in black) cycled in the 5 mV - 2.0 V *vs*. $Na^{+/}Na$ range, at a current density of $2.5\cdot10^{-4}$ A, using 1M $NaPF_6$ in EC: PC 50:50 % vol.

Figure 6.9.a and b illustrates the second cycle of the CR2032 full cells HC/Na-PW and HC/K-PW. Again, a positive to negative charge ration of 1:1.3 was stablished as aim, resulting in an ideal 1:1 cathode: anode mass balance. At first sight, similar operation is observed for both materials, independently of the alkali present in the structure. Only the presence of an additional small pseudo-plateau is adverted in the full cell containing K-PW. However, when looking into detail the dQ/dV *vs*. V curves inset, a clear difference between both cells is evident. During the charge, the redox reactions occur at similar voltages (ca. 2.5-2.6 and 3.1 V) in both cells. Nevertheless, along the discharge, an intriguing shift towards lower voltages takes place in the K-PW based full cell (2.85 and 1.76 V) compared to Na-PW (3.0 and 2.2 V), resulting in higher polarization for K-PW. These lower voltages values encountered were surprising and contrast with the promising results expected for K-PW in the full cell, considering the 0.35 V higher plateau observed in half- cells NIB respect to Na-PW.

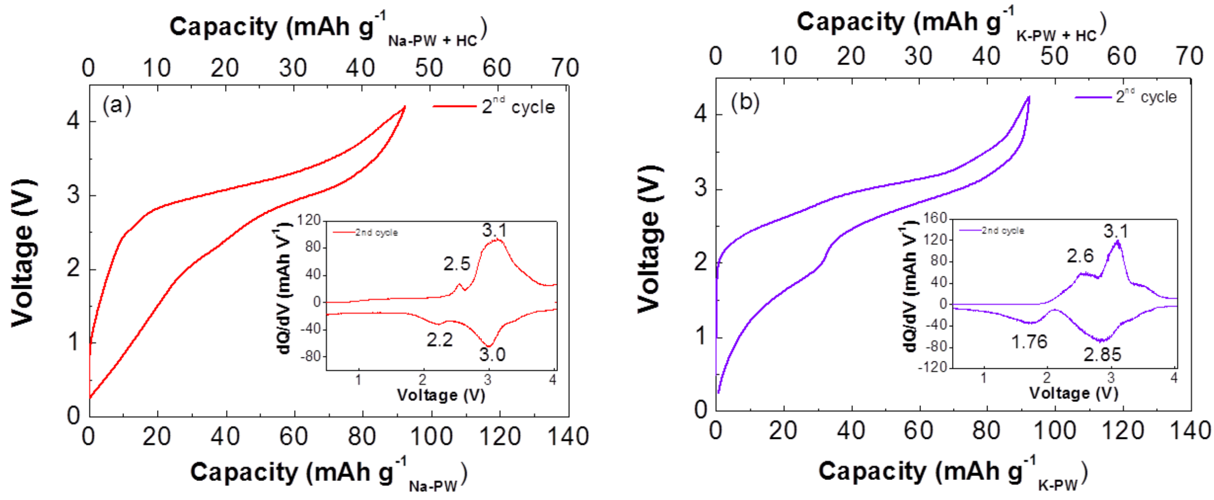

Figure 6.9. Capacity *vs*. voltage profile of the second cycle and its corresponding dQ/dV *vs*. V curve (inset) of the sodium-ion full cells a) HC/Na-PW and b) HC/K-PW, when cycled in the 0.25 to 4.05 V voltage range at a current of $1\cdot10^{-4}$ A or $2.5\cdot10^{-4}$ A, accordingly, using 1M $NaPF_6$ in EC: PC 50:50 % vol.

Reversible specific capacities of 92 mAh·$g^{-1}_{cathode}$ were released by the HC/Na-PW full cell (considering the active mass of Na-PW present in the cathode, that was of 1.5 mg), when it was cycled at $1\cdot10^{-4}$ A (see Figure 6.10.a). This value corresponds to a gravimetric capacity of 46 mAh·$g^{-1}_{cathode + anode}$ (based on the total mass of both active materials, Na-PW and HC). Coulombic efficiencies > 98% were delivered after 5 cycles and > 85 % of the initial capacity was retained after 50 cycles. The HC/Na-PW full cell is able to provide **110** Wh·$Kg^{-1}_{cathode + anode}$, as Figure 6.10.b shows, and an average operating voltage of 2.37 V.

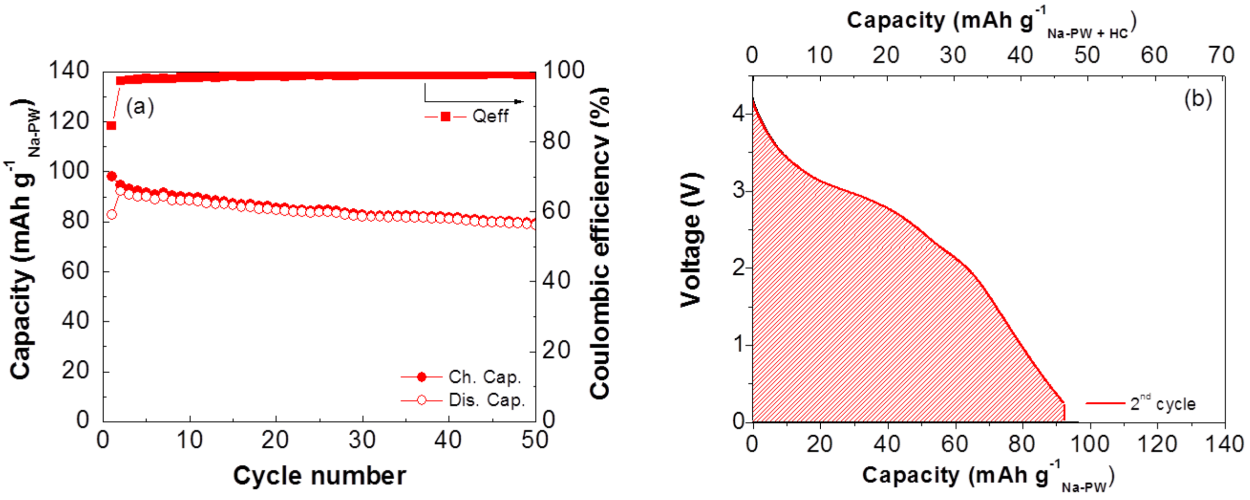

Figure 6.10. a) Cyclability, coulombic efficiency and b) second discharge curve (for calculating the energy density) of the full cell HC/Na-PW, tested in the cut-off voltage from 0.25 - 4.05 V,using 1M $NaPF_6$ in EC: PC 50:50 % vol. and a current of $1\cdot10^{-4}$ A.

To the best of our knowledge, only three works have reported the performance of Prussian White as cathode in sodium-ion full cells, using commercial hard carbon as anode.

In 2014, Yang *et al*. constructed a sodium-ion battery with the ternary $Na_{1.76}Ni_{0.12}Mn_{0.88}[Fe(CN)_6]_{0.98}\cdot\square_{0.02}$ Prussian White. The battery delivered a high capacity of 90.8 mAh·g^{-1} (based on the cathode mass) under 100 mA·g^{-1} and, after 200 cycles, the discharge capacity still remained 71.62 mAh·g^{-1} (78.9% of the initial capacity). The coulombic efficiency was reported to be of 88.2% in the first cycle and, then, increased to 95% in the subsequent cycles. The energy and power density the authors estimated were of 81.72 Wh·Kg^{-1} and 90 W·Kg^{-1}, respectively.[11]

The other two studies were performed by Goodenough´s group in 2015. Interestingly, rhombohedral purely iron-based Prussian White, R-$Na_{1.92}Fe[Fe(CN)_6]$, was one of the cathode materials investigated.[12] A full cell was assembled with this material, showing an initial discharge capacity of 119.4 mAh·g^{-1} (normalized by the mass of R-$Na_{1.92}Fe[Fe(CN)_6]$) at 10 mA·g^{-1} in the voltage window ΔV = 1.0 - 3.8 V, with a first-cycle coulombic efficiency of 78%. After 50 cycles, up to 94% of the capacity was maintained. At a current density of 100 mA·g^{-1}, comparable to that used in this thesis for Na-PW, only one cycle was shown, whose discharge capacity was ca. 102 mAh·g^{-1}. Regarding the second full-cell test, rhombohedral

---

[11] D. Yang, J Xu, Z-Z. Liao, Y-S. He, H. Liu, Z-F. Ma. *Chem. Commun.* 2014, **50**, 13377-13380. "Structure optimization of Prussian Blue analogue cathode materials for advanced sodium ion batteries".

[12] L. Wang, J. Song, R. Qiao, L.A. Wray, M.A. Hossain, Y.-D. Chuang, W. Yang, Y. Lu, D. Evans, J.-J. Lee, S. Vail, X. Zhao, M. Nishijima, S. Kakimoto, J.B. Goodenoug. *J. Am. Chem. Soc.* 2015, **137**, 2548-2554. "Rhombohedral prussian white as cathode for rechargeable sodium-ion batteries".

$Na_{2-\delta}Mn[Fe(CN)_6]$ was the cathode selected.[13] Based on the mass of $Na_{2-\delta}Mn[Fe(CN)_6]$, reversible capacities of 105 $mAh\cdot g^{-1}$ over the voltage range $1.5 \leq V \leq 3.8$ V were obtained at 100 $mA\cdot g^{-1}$, with coulombic efficiencies close to 100%. A moderate performance of 96 $mAh\cdot g^{-1}$ was also showed at 200 $mA\cdot g^{-1}$. No reference to the energy density was unfortunately mentioned in any of these works.

On view of the previous discussion, it can be conclude that the values obtained in this thesis work are comparable with those already reported in the literature, despite the mass balance is not optimal.

Likewise, the HC/K-PW full cell exhibited on the order of 94 $mAh\cdot g^{-1}_{catohde}$ discharge specific capacities (based on the active mass of K-PW present in the cathode, that was of 3.3 mg), when it was cycled at $2.5\cdot 10^{-4}$ A, as Figure 6.11.a displays. A gravimetric capacity of 47 $mAh\cdot g^{-1}_{cathode + anode}$ was obtained, considering besides the mass of the anode. Coulombic efficiencies of ca. 99% were achieved after the first cycle and roughly 80 % of the capacity was retained after 100 cycles. The HC/K-PW full cell is also able to provide **109** $Wh\cdot Kg^{-1}_{cathode + anode}$, as Figure 6.11.b depicts, and an average operating voltage of 2.32 V.

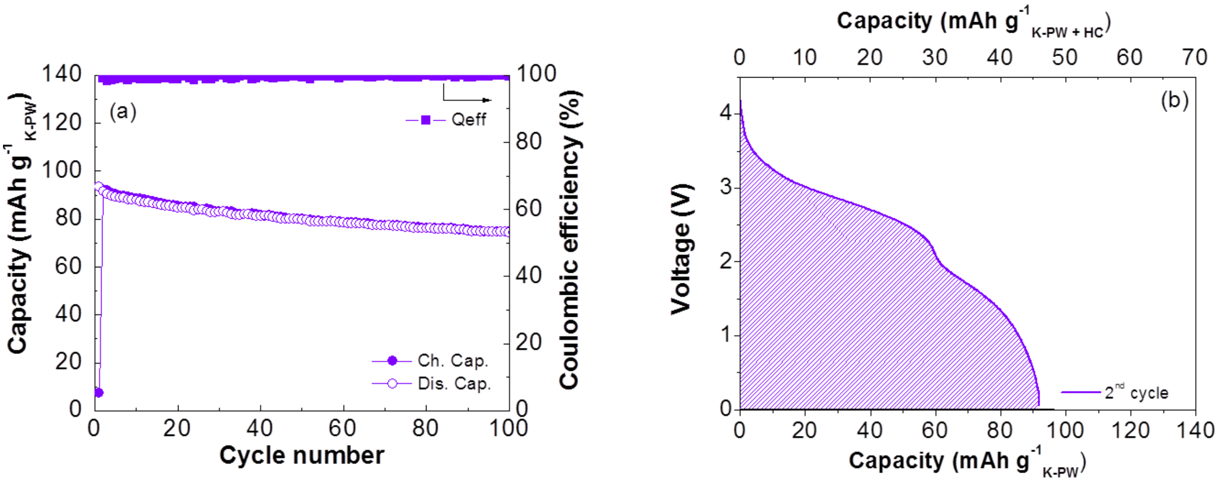

Figure 6.11. a) Cyclability, coulombic efficiency and b) second discharge curve (for calculating the energy density) of the full cell HC/K-PW, tested in the cut-off voltage from 0.25 - 4.05 V, using 1M $NaPF_6$ in EC:PC 50:50 % vol. and a current of $2.5\cdot 10^{-4}$ A.

6.1.5. HC/Na-PW and HC/A-PW results comparison

In order to compare the intrinsic electrochemical properties of the material, the values obtained in the full cells using the same anode (commercial hard carbon) with the different Prussian Blue cathodes, examined in previous sections, are here summarized in Table 6.1.

---

[13] J. Song, L. Wang, Y. Lu, J. Liu, B. Guo, P. Xiao, J-J. Lee, X-Q. Yang, G. Henkelman, J. B. Goodenough. *J. Am. Chem. Soc.* 2015, **137** (7), 2658-2664. “Removal of Interstitial H_2O in Hexacyanometallates for a Superior Cathode of a Sodium-Ion Battery”.

Table 6.1. Experimental values obtained in the second discharge curve of the sodium-ion full cells with hard carbon, using the anodes listed below. The capacity and specific energy calculations were made taking into account the mass of the active material of the corresponding cathode in each case.

Cathode	Capacity ($mAh·g^{-1}_{cath}$)	Capacity ($mAh·g^{1}_{cath + an}$)*	Average operating voltage (V)	Specific energy ($Wh·Kg^{-1}_{cath + an}$)	Current (A)
Na-PB	86	32	2.2	70	$1·10^{-4}$
Na-PW	92.14	46	2.37	110	$1·10^{-4}$
K-PW	91.57	47	2.32	109	$2.5·10^{-4}$

*cath = cathode, an = anode

Even though similar reversible gravimetric capacity values are observed in the three different full cells with hard carbon (roughly 90 $mAh·g^{-1}$), an improvement of 40 $Wh·Kg^{-1}$ is observed when using a Prussian White phase with respect to Na-PB, as a result of the higher average operating voltage of the formers. It is somewhat curious, however, the fact that the specific energy obtained for both HC/Na-PW and HC/K-PW full cells was coincident. Despite the higher polarization observed in HC/K-PW, what obviously affects the specific energy density, a pretty similar average voltage to that of HC/Na-PW is obtained, making possible the previous fact. It is also noteworthy the good capacity retention observed in all full cells. Over 80% and > 85% of the initial capacity was retained by Na-PB and Na-PW after 50 cycles, and even 80% was maintained after 100 cycles in the K-PW containing cell.

6.1.6. Concluding remarks

The development of three organic sodium-ion full cells, using the non-expensive and easily synthesizable Prussian Blue or Prussian White phases as cathode and the convenient commercial hard carbon as anode, have been investigated and contrasted.

Respectively, **70**, **110** and **109** $Wh·Kg^{-1}_{\textbf{cathode + anode}}$ were delivered by the HC/Na-PB, HC/Na-PW and HC/K-PW full cells. Almost coincident discharge specific capacities and average operating voltage values were observed for both Prussian White phases. Intriguingly, along the discharge, inferior voltage redox values than expected were observed in the HC/K-PW full cell and further work to understand the reasons behind it and to overcome it, if possible, is required. Nice cycle-stability and reasonable coulombic efficiencies have been displayed in all the full cells here attempted, especially in the HC/K-PW cell.

In any case, and despite a better mass balance could provide a desirable larger energy upon time, the HC/Na-PB, HC/Na-PW and K-PW full cells developed in this thesis work serve as proof of concept for the utilization of Prussian Blue and Prussian White materials in real battery applications.

Chapter 7

Conclusions and perspectives

7.-) CONCLUSION AND PERSPECTIVES

The discussion of the results described in this work allows us to extract the following conclusions:

- New synthetic routes have been developed to obtain the titanium Prussian Blue derivative (Ti-PBA), $Ti[Fe(CN)_6]$.
- No electrochemical activity was found for Ti-PBA when explored in the anodic range for organic Na-ion batteries.
- The study of the electrochemical performance of purely iron based Prussian Blue (A-PB), $A_{1-x}Fe_{1+x/3}[Fe(CN)_6]\cdot yH_2O$ (A = Na, K), as anode in organic Na-ion and Li-ion batteries, revealed a promising performance.
- Prussian Blue and its analogues have been investigated for the first time as anode for Na-ion batteries.
- CMC binder and a composite CMC/SBR binder allowed optimizing the electrochemical operation of Na-PB as anode in Na-ion batteries.
- A conversion (or displacement) reaction mechanism has been proposed and confirmed for the first time for this type of materials, given the high capacities (up to 450 $mAh\cdot g^{-1}$) provided when K-PB was tested as anode for LIB.
- A new *in-situ* Mössbauer cell has been developed in this thesis work, with the aim of enabling follow the Fe oxidation evolution of Fe-based electrode materials.
- 1M $NaPF_6$ in EC: PC: FEC 49: 49: 2 % vol. and PVDF have proved to be the optima electrolyte and binder combination for exploiting the electrochemical properties of Na-PB in the cathodic range for organic Na-ion batteries.
- Faster Na^+ charge transfer and lower polarization were experimented in the electrochemical performance of Na-PB as cathode in aqueous media compared to organic Na-ion batteries.
- A novel synthesis procedure using mild conditions has been developed for the preparation of cubic alkali-rich Prussian White (A-PW), $A_{2-x}Fe_{1+x/2}[Fe(CN)_6]\cdot yH_2O$ (A = Na, K), unlike the rhombohedral or monoclinic reported in the literature.
- The investigation of Na-PW and K-PW as cathode materials in Na-ion batteries revealed promising electrochemical properties, such as high capacities (> 140 $mAh\cdot g^{-1}$), reasonable coulombic efficiencies (> 98%) and long-term cycling stability (80% elapsed 500 cycles in the case of K-PW) at moderate current densities (1C).
- The insertion of K^+ in K-PW at the upper redox process lead to a beneficial increase of 0.35 V in its voltage plateau value.
- Three sodium-ion full cells of Na-PB, Na-PW and K-PW were successfully assembled using commercial hard carbon as anode. The reasonably high energy density of both PW phases (218 $Wh\cdot Kg^{-1}_{cathode}$) makes these materials suitable cathodes for real Na-ion batteries.

From the knowledge acquired during the development of this work, some perspectives are given in the field of sodium-ion batteries:

- Since Na-ion batteries are far from reaching the high energy densities achieved in Li-ion batteries, the research on cathode and anode materials should be focused on the low cost, abundance, non-toxicity and easiness of synthesis thereof, with the aim of being competent with the already stablished Li-ion technology.
- Although less investigated in Na-ion batteries, the role of electrolyte, binder and additives is essential for a superior functioning of the battery. The most suitable combination of them however could be dependent of the electrode materials that compose it.
- A thorough study of the SEI layer formed in Na-ion batteries, strongly affected by the electrolyte, binder and additives, would also be highly recommendable to determine its stability, thickness and solubility and thus be able of overcoming the problems arising from it.
- Additional test of the electrode materials in full cells would be advisable to estimate their electrochemical properties in a real application Na-ion battery. These properties could differ from those already obtained in Na-ion half cells mostly due to issues coming from the electrode cross influence.

APPENDIX

In this section, the supplemental information is provided in order to complete the information explained in the text.

Chapter 2: Experimental techniques

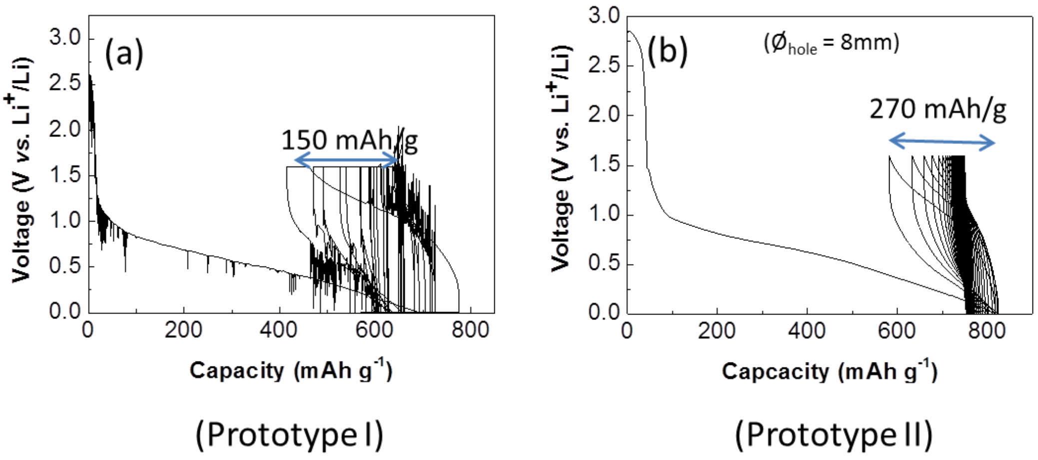

Figure A 0.1. Electrochemical performance of the in-situ Mössbauer prototypes I and II.

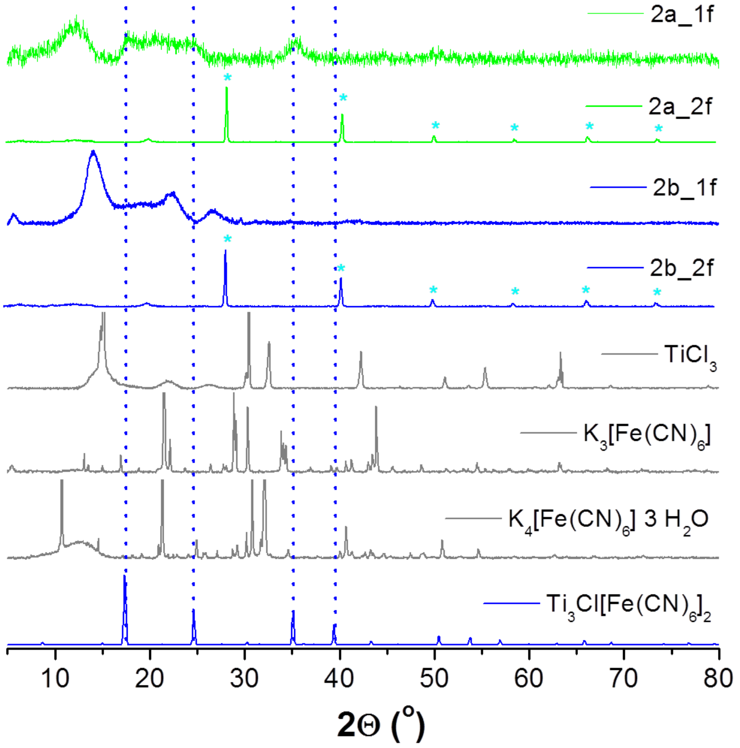

Figure A 0.1. Comparison of the X-ray patterns of the products **2a_1f**, **2a _2f** (in green) and **2b_1f**, **2b_2f** (in blue), the starting reagents ($TiCl_3$, $K_3[Fe(CN)_6]$ and $K_4[Fe(CN)_6]\cdot 3H_2O$ - in gray) and the desired product $Ti_3Cl[Fe(CN)_6]_2$ (in blue). KCl reflections have been highlighted in **2a_2f** and **2b_2f** with asterisks colored in cyan.

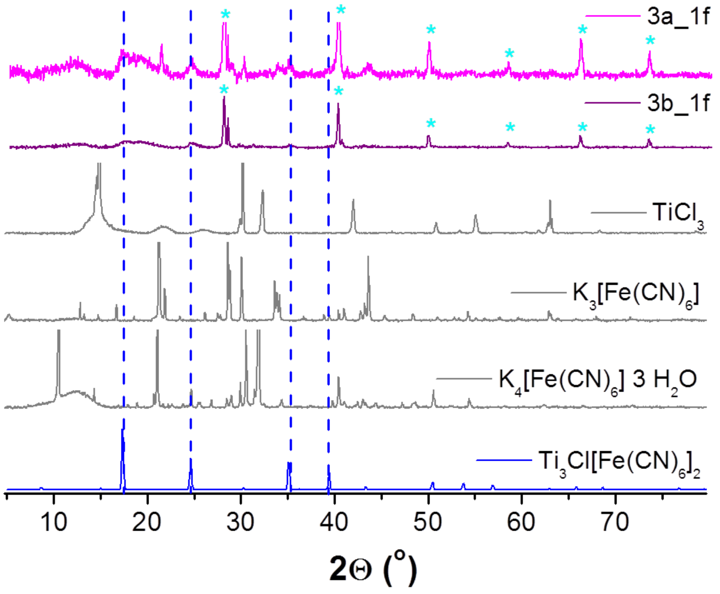

Figure A 0.2. Comparison of the X-ray diffractograms of the products **3a_1f** (in pink), **3b _1f** (in purple), the starting reagents ($TiCl_3$, $K_3[Fe(CN)_6]$ and $K_4[Fe(CN)_6]\cdot 3H_2O$ - in gray) and the desired product $Ti_3Cl[Fe(CN)_6]_2$* (in blue). KCl reflections have been highlighted in **3a_1f** and **3b_1f** with asterisks colored in cyan.

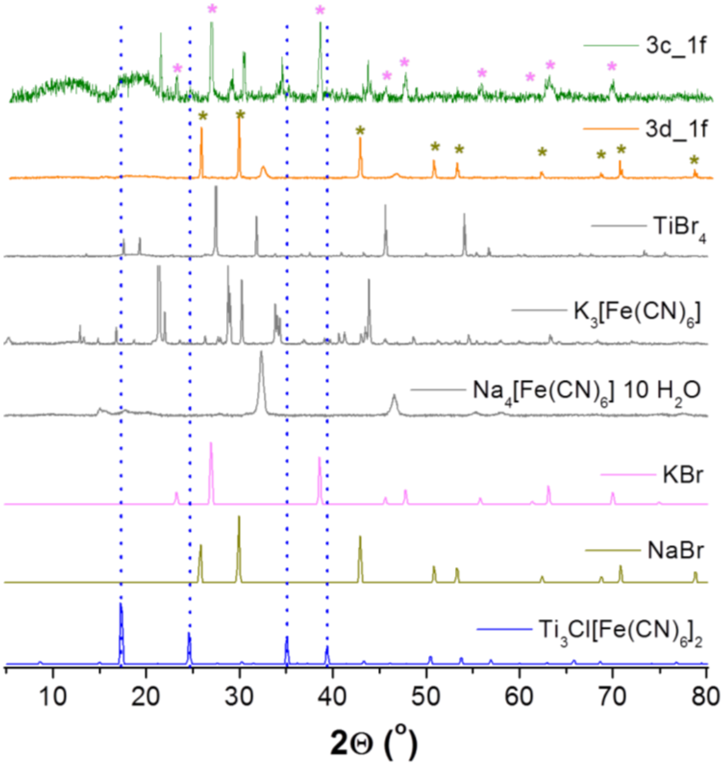

Figure A 0.3. Comparison of the X-ray diffractograms of the products **3c_1f** (in olive green), **3d _1f** (in orange), the starting reagents ($TiBr_4$, $K_3[Fe(CN)_6]$ and $Na_4[Fe(CN)_6]\cdot 10H_2O$ - in gray), the byproducts (KBr (whose reflections have been highlighted in 3c_1f with asterisks in coral) and NaBr (whose reflections have also been highlighted in 3d_1f with asterisks in dark yellow)) and the desired products $Ti_3Cl[Fe(CN)_6]_2$ (in blue).

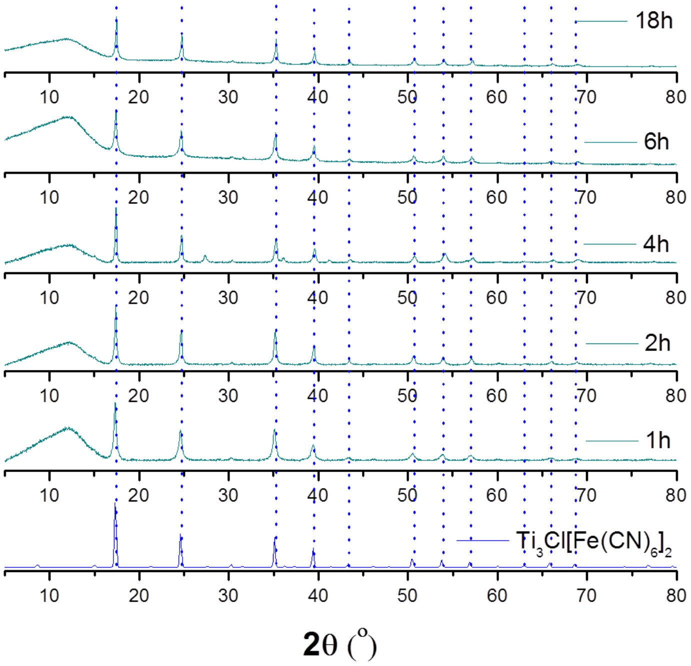

Figure A 0.4. XRD patterns of Ti-PBA prepared in aqueous media through route 4b, using different times of reaction.

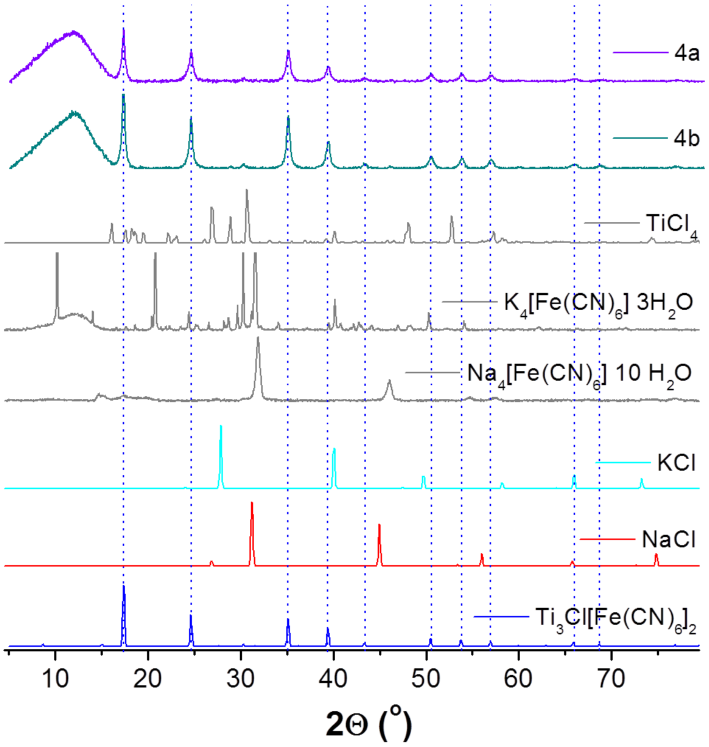

Figure A 0.5. X-ray diffractograms of the products **4a** (in violet) and **4b** (in turquoise) after 1h of reaction, the starting reagents ($TiCl_4$, $K_4[Fe(CN)_6]\cdot 3H_2O$ and $Na_4[Fe(CN)_6]\cdot 10H_2O$ - in gray), the byproducts (KCl (in cyan), NaCl (in red)) and the product $Ti_3Cl[Fe(CN)_6]_2$ (in blue).

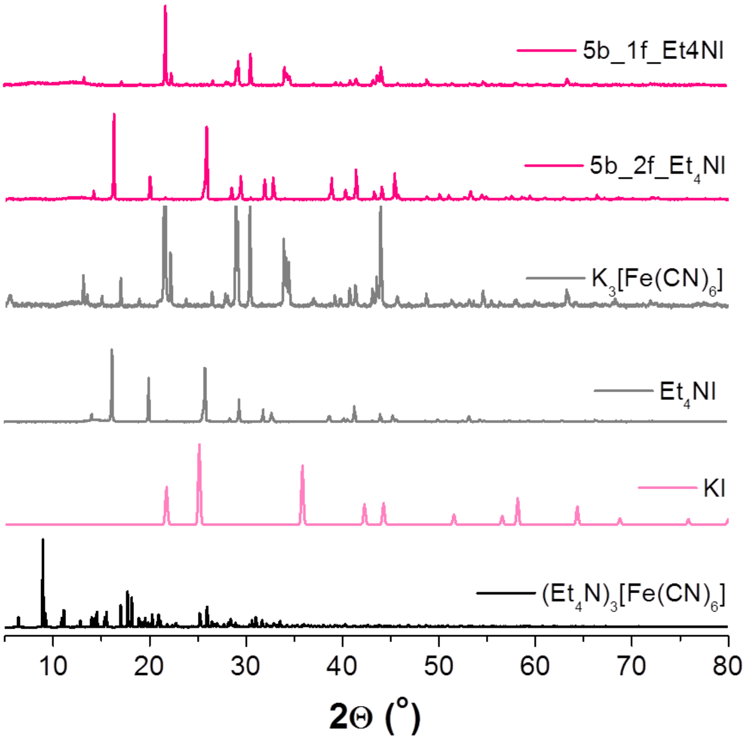

Figure A 0.6. PXRD comparison of the products **5b_1f_Et_4NI** and **5b_2f_Et_4NI** (in pink) obtained in the attempt of preparing the $(Et_4N)_3[Fe(CN)_6]$ precursor using Et_4NI as reactant, the starting reagents ($K_3[Fe(CN)_6]$ and Et_4NI - in gray), the byproduct (KI - in pale pink) and the desired precursor $(Et_4N)_3[Fe(CN)_6]$ (in black). The $(Et_4N)_3[Fe(CN)_6]$ X-ray diffractogram was simulated from the .cif file acquired from the CSD (Cambridge Structural Database).

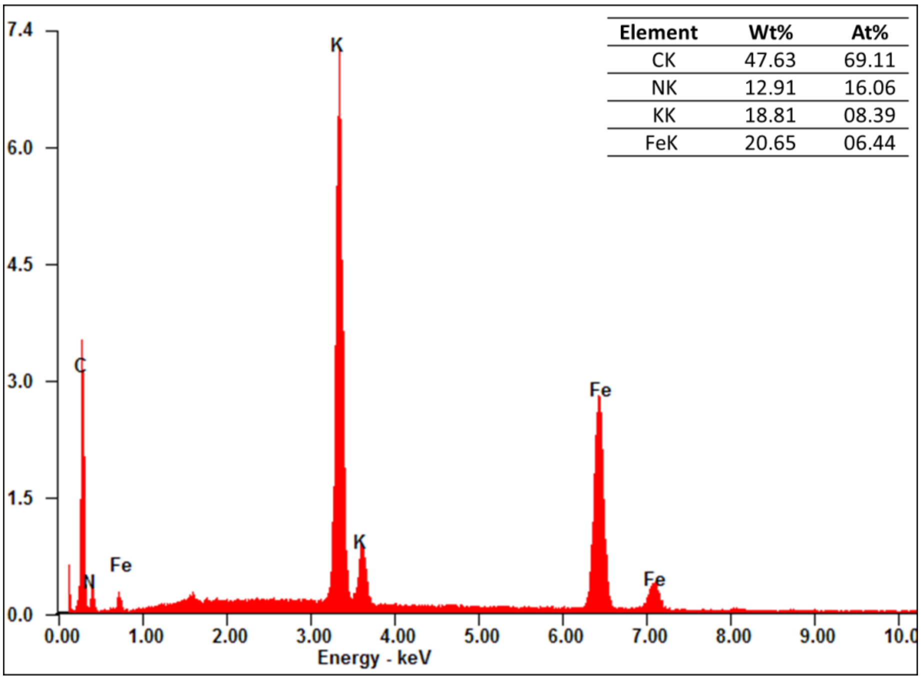

Element	Wt%	At%
CK	47.63	69.11
NK	12.91	16.06
KK	18.81	08.39
FeK	20.65	06.44

Figure A 0.7. EDX analysis of **5c** (the precursor synthesized to obtain $(Me_4N)_3[Fe(CN)_6]$).

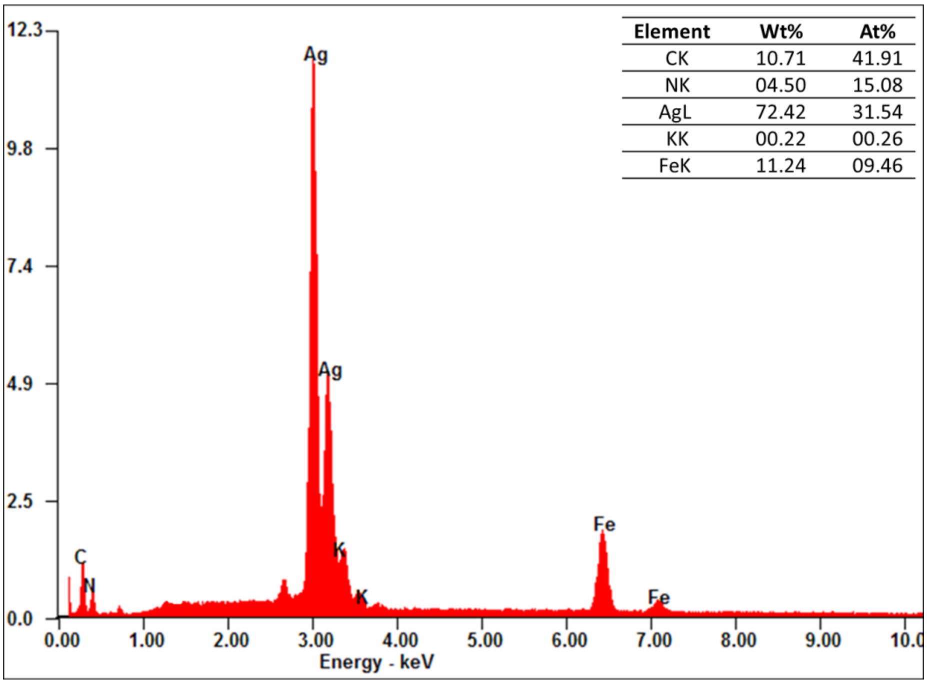

Element	Wt%	At%
CK	10.71	41.91
NK	04.50	15.08
AgL	72.42	31.54
KK	00.22	00.26
FeK	11.24	09.46

Figure A 0.8. EDX analysis of **5d** ($Ag_3[Fe(CN)_6]$ precursor).

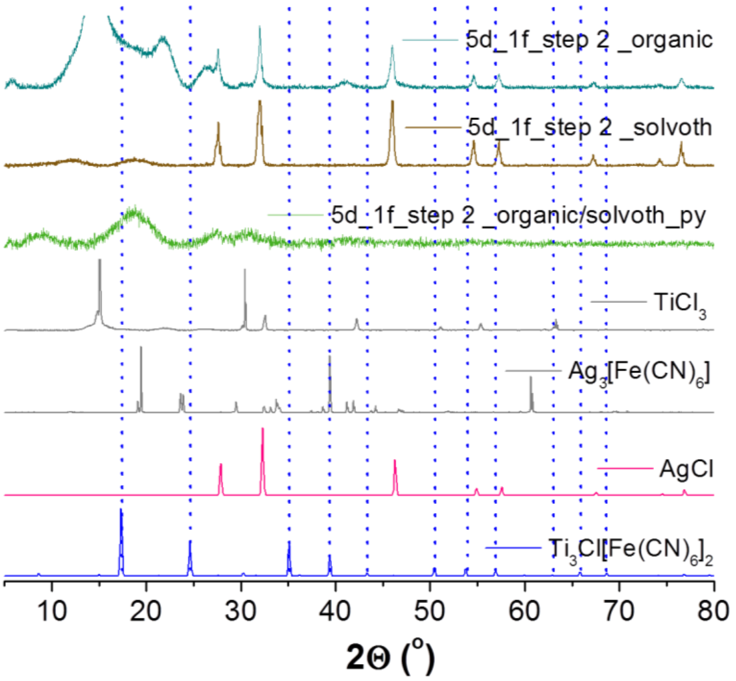

Figure A 0.9. XRD of the product **5d_1f_step 2_organic**, **5d_1f_step 2_organic_py**, **5d_1f_step 2_solvothermal**, the reactants $TiCl_3$, $Ag_3[Fe(CN)_6]$ (in grey), and the products AgCl and Ti-PBA.

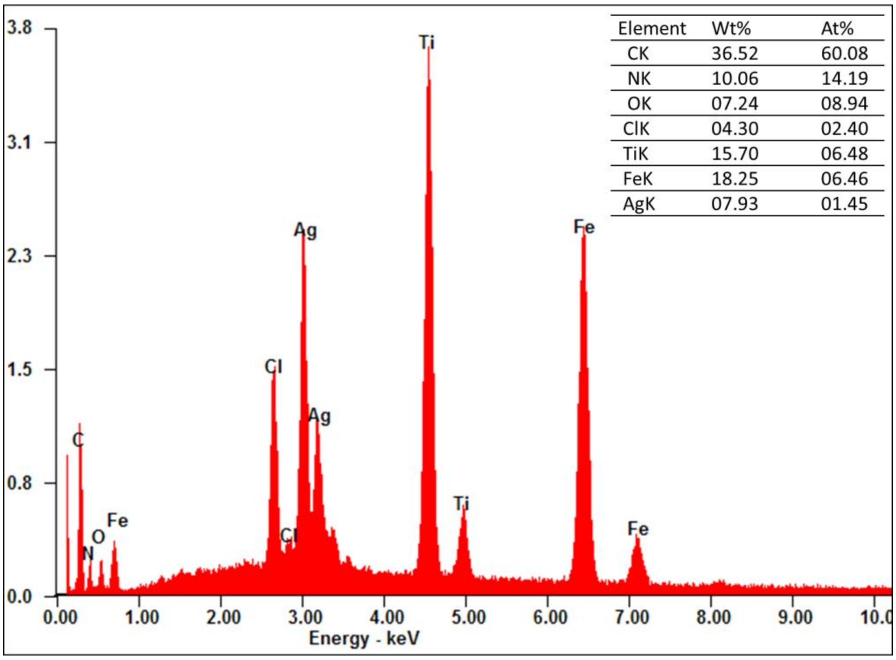

Element	Wt%	At%
CK	36.52	60.08
NK	10.06	14.19
OK	07.24	08.94
ClK	04.30	02.40
TiK	15.70	06.48
FeK	18.25	06.46
AgK	07.93	01.45

Figure A 0.10. EDX analysis of **5d_1f_step2_organic/solvoth_py** (the compound obtained from making react the $Ag_3[Fe(CN)_6]$ precursor with $TiCl_3$, that was posteriorly washed with pyridine).

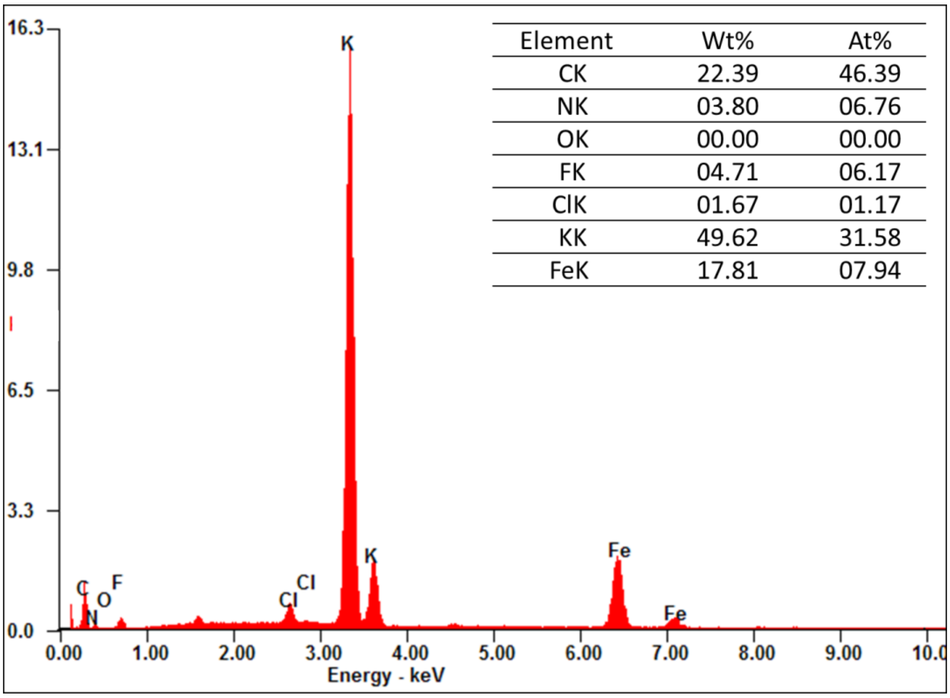

Element	Wt%	At%
CK	22.39	46.39
NK	03.80	06.76
OK	00.00	00.00
FK	04.71	06.17
ClK	01.67	01.17
KK	49.62	31.58
FeK	17.81	07.94

Figure A 0.11. EDX analysis of **6b_K**, prepared through the trifluoroacetate route.

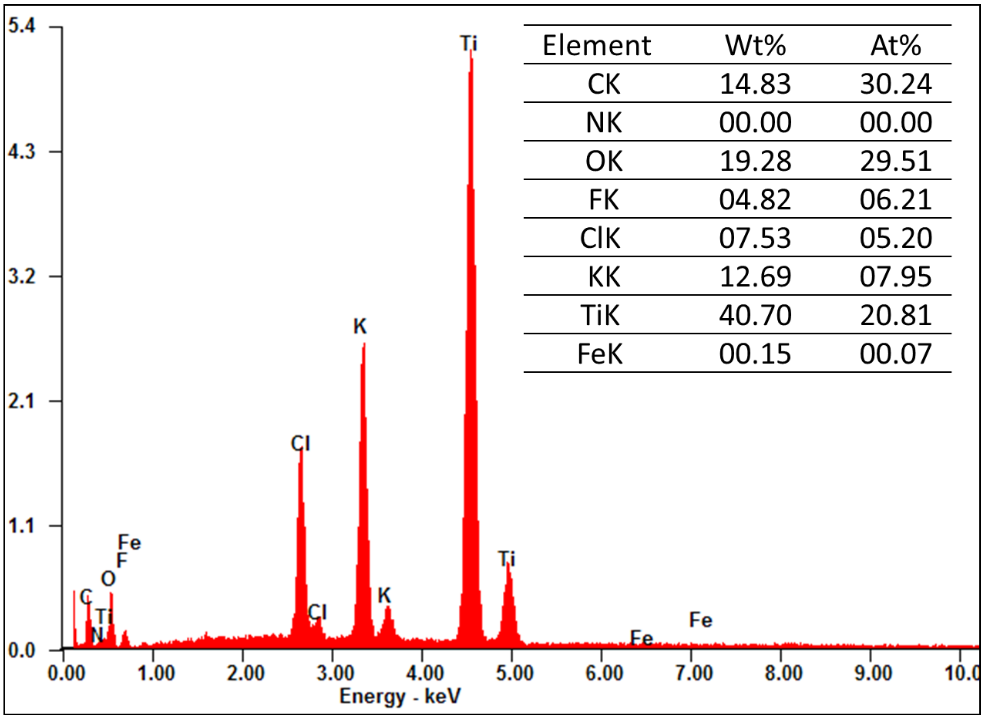

Element	Wt%	At%
CK	14.83	30.24
NK	00.00	00.00
OK	19.28	29.51
FK	04.82	06.21
ClK	07.53	05.20
KK	12.69	07.95
TiK	40.70	20.81
FeK	00.15	00.07

Figure A 0.12. EDX analysis of **6a_K**, prepared through the trifluoroacetate route.

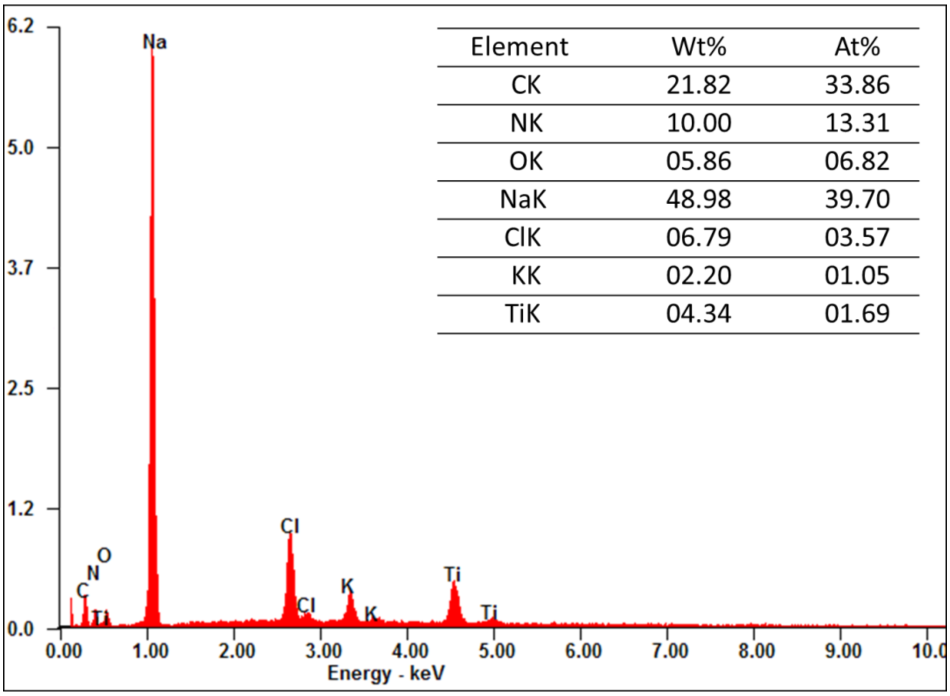

Element	Wt%	At%
CK	21.82	33.86
NK	10.00	13.31
OK	05.86	06.82
NaK	48.98	39.70
ClK	06.79	03.57
KK	02.20	01.05
TiK	04.34	01.69

Figure A 0.13. EDX analysis of **6a_Na**, prepared through the trifluoroacetate route.

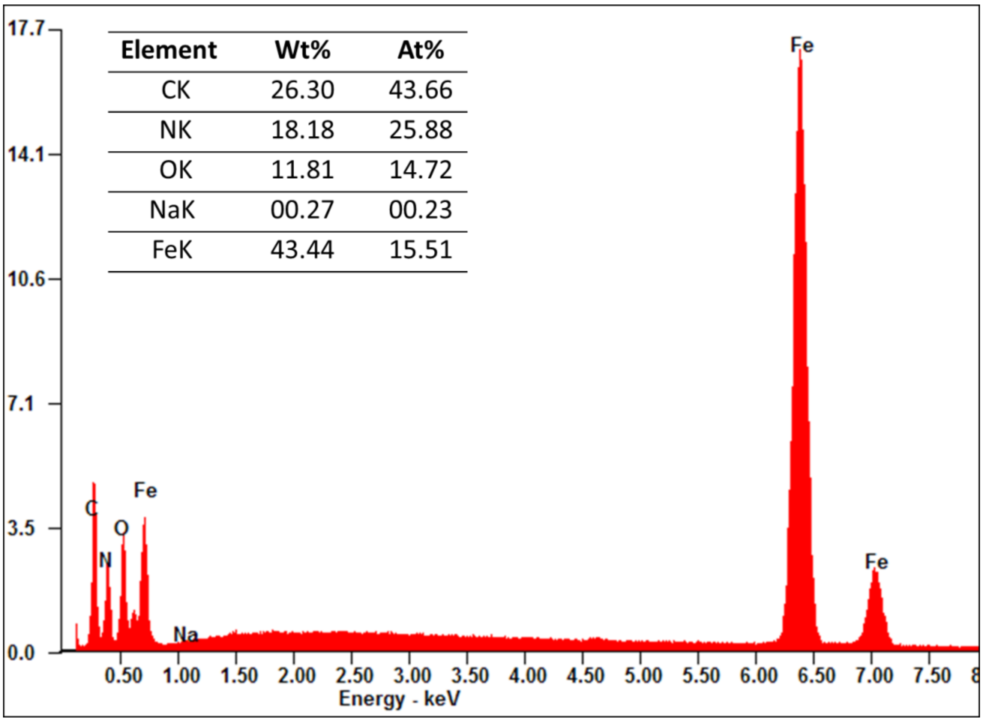

Element	**Wt%**	**At%**
CK	26.30	43.66
NK	18.18	25.88
OK	11.81	14.72
NaK	00.27	00.23
FeK	43.44	15.51

Figure A 0.14. EDX analysis of Na-PW prepared following Jiang´s methodology.

Table A 0.1. Atomic coordinates for cubic Na-PW (R_{exp} = 21.03, R_p= 51.8, R_{wp}= 39.3, χ^2= 3.49).

S.G. *F m* -3 *m*		a= 10.350 (5) Å			
Atom	Wyck.	x/a	y/b	z/c	occ
Fe1	4a	0	0	0	1
Fe2	4b	0.5	0.5	0.5	0.6721 (3)
C	24e	0.1832 (2)	0	0	0.656 (2)
N	24e	0.2988 (2)	0	0	0.656 (2)
O	32f	0.355 (4)	0.	0	0.088 (2)
Na	8c	0.25	0.25	0.25	0.6219 (7)

(B_{ov} = 1 was refined instead of each atomic B_{iso}, due to broad wide peaks).

Table A 0.2. Atomic coordinates for cubic K-PW (R_{exp} = 5.52, R_p= 5.83, R_{wp}= 7.67, χ^2= .1.93).

S.G. *F m* -3 *m*		a= 10.117 (6) Å			
Atom	Wyck.	x/a	y/b	z/c	occ
Fe1	4a	0	0	0	1
Fe2	4b	0.5	0.5	0.5	0.5367 (7)
C	24e	0.18810	0	0	0.538 (4)
N	24e	0.30370	0	0	0.538 (4)
O	32f	0.41488	0	0	0.496 (2)
Na	8c	0.25000	0.25000	0.25000	0.6475 (5)

(B_{ov} = 1 was refined instead of each atomic B_{iso}, due to broad wide peaks).

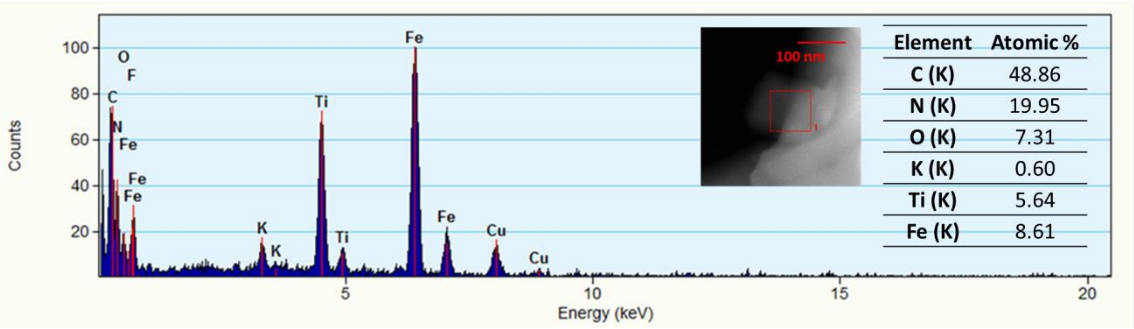

Element	Atomic %
C (K)	48.86
N (K)	19.95
O (K)	7.31
K (K)	0.60
Ti (K)	5.64
Fe (K)	8.61

Figure A 0.1. EDX analysis of the Ti-PBA obtained by aqueous route 4a.

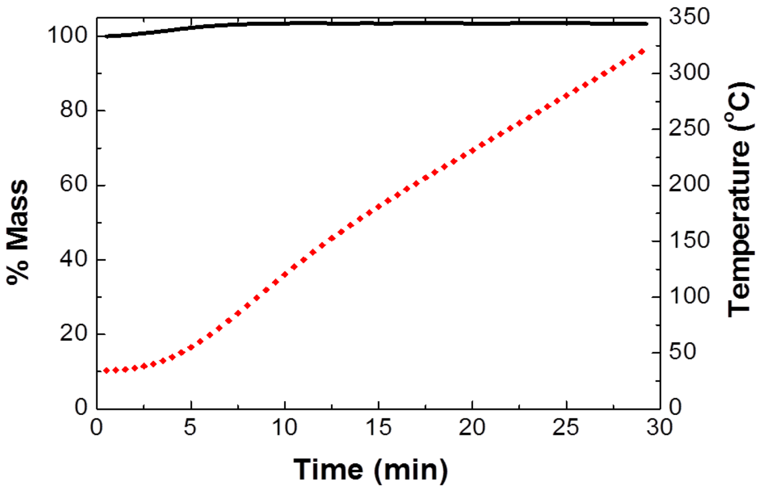

Figure A 0.2. Thermogravimetric analysis of pristine sodium Prussian White (K-PW), scanned from 30 to 325 °C using N_2 atmosphere and a temperature step of 10 K·min^{-1}. K-PW was synthesized following the modified methodology of Jiang, using ascorbic acid.

K-PW presented no zeolitic or physisorbed water present in the channels.

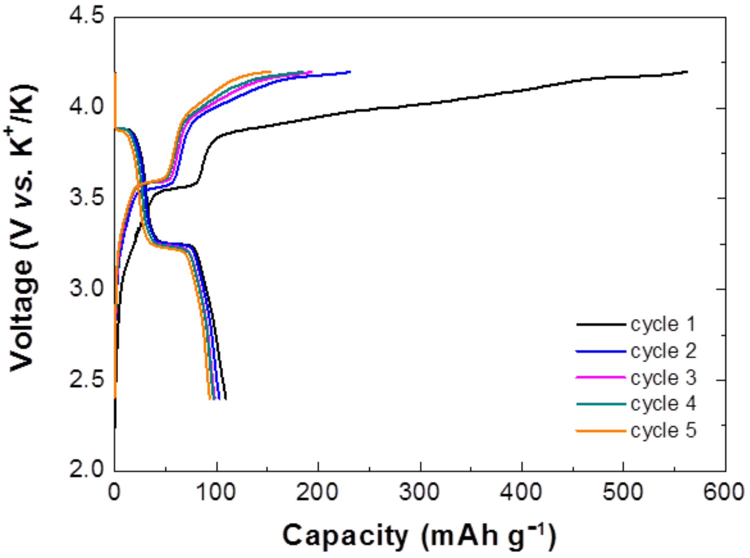

Figure A 0.1. Voltage *vs*. capacity curve of K-PW cycled *vs*. K^+/K in the voltage range from 2.4-4.2 V, using 1M KPF_6 in EC: DMC 50:50 % vol.

Contributions from this work:

List of publications:

1.- A.J. Fernández-Ropero[†], **M.J. Piernas-Muñoz**[†], E. Castillo-Martínez, T. Rojo, M. Casas-Cabanas. *Electrochimica Acta* 2016, **210**, 352-357. "Electrochemical characterization of $NaFe_2(CN)_6$ Prussian Blue as positive electrode for aqueous sodium-ion batteries". († These authors contributed equally to this work)

2.- **María José Piernas-Muñoz**, Elizabeth Castillo-Martínez, Oleksandr Bondarchuk, M. Armand, T. Rojo. *J. of Power Sources* 2016, **324**, 766-773. "Higher voltage plateau cubic Prussian White for Na-ion batteries".

3.- **Mª José Piernas-Muñoz**, Elizabeth Castillo-Martínez, J. L. Gómez-Cámer, T. Rojo. *Electrochimica Acta* 2016, **200**, 123-130. "Optimizing the electrolyte and binder composition for Sodium Prussian Blue, $Na_{1-x}Fe_{x+(1/3)}(CN)_6{\cdot}yH_2O$, as cathode in sodium ion batteries".

4.- **Mª José Piernas-Muñoz**, Elizabeth Castillo-Martínez, V. Roddatis, M. Armand, T. Rojo. *Journal of Power Sources* 2014, **271**, 489-496. "$K_{1-x}Fe_{2+x/3}(CN)_6{\cdot}yH_2O$, Prussian Blue as a displacement anode for lithium ion batteries".

List of presentations:

1.- Oral presentation. **Mª José Piernas-Muñoz**, Elizabeth Castillo-Martínez, Michel Armand and Teófilo Rojo. "Prussian Blue and Prussian White as low-cost materials for Sodium Ion Batteries". MRS Fall Meeting 2015. November 29th to December 4th, 2015. Boston (Massachusetts), (USA).

2.- Poster. **Mª José Piernas-Muñoz**, Elizabeth Castillo-Martínez, Vladimir Roddatis, Michel Armand and Teófilo Rojo. "Prussian Blue as anode for Li- and Na-ion batteries". ABAA8 2015. September 30th to October 2nd, 2015. Bilbao, (Spain).

3.- Oral presentation. **Mª José Piernas-Muñoz**, Elizabeth Castillo-Martínez, Michel Armand and Teófilo Rojo. "Prussian Blue as negative and positive electrodes in lithium and sodium-ion batteries". 227th ECS Meeting. Electrochemical Society (Chicago), April 2015 (USA). Oral presentation.

4.- Oral presentation. Antonio Jesús Fernández Ropero, **Mª José Piernas-Muñoz**, Marine Reynaud, Begoña Acebedo Morante, Elizabeth Castillo Martínez, Damien Saurel, Teófilo Rojo Aparicio and Montserrat Casas Cabanas. "Na-ion aqueous batteries for stationary energy storage systems". 227th ECS Meeting. Electrochemical Society (Chicago), April 2015 (USA).

5.- Invited lecture. Elizabeth Castillo-Martinez, Aitor Eguía-Barrio, Maider Zarrabeitia, **Mª José Piernas-Muñoz**, María Lopez-Herraiz, Javier Carretero-Gonzalez, Montse Casas-Cabanas, J.M. Lopez del Amo, Miguel Angel Muñoz, Vladimir Rodattis, Michel Armand and Teófilo Rojo. "In the search of anode materials for low cost sodium ion batteries." XIII Meeting of SBPMat. Federal University of Paraíba (João Pessoa), September-October 2014 (Brazil).

6.- Poster. **Mª José Piernas-Muñoz**, Elizabeth Castillo-Martínez, Vladimir Roddatis, M. Armand, Teófilo Rojo. "First time proposed conversion or displacement reaction in PB when acted as anode in Li-ion batteries". XIII Meeting of SBPMat. Federal University of Paraíba (João Pessoa), September-October 2014 (Brazil).

7.- Poster. **Mª José Piernas-Muñoz**, E. Castillo-Martínez, Juan Miguel López del Amo, Michel Armand, Teófilo Rojo. "The reaction mechanism of paramagnetic Prussian Blue as electrode material in rechargeable batteries studied by solid state NMR". New Developments in Experimental and Theoretical Techniques for the Study of Paramagnetic Inorganic Materials conference and workshop. University of Cambridge, September 2014 (United Kingdom).

8.- Oral presentation. **Mª José Piernas-Muñoz**, E. Castillo-Martínez, Vladimir Roddatis, Michel Armand, Teófilo Rojo. "Prussian Blue, a new anode material exhibiting displacement or conversion reaction in Li-ion batteries". XXXV Meeting of Electrochemistry of the Spanish Royal Society of Chemistry and 1st E3 Symposium Mediterranean Symposium: Electrochemistry for Environment and Energy. University of Burgos, July 2014 (Spain).

9.- Póster. **Mª José Piernas-Muñoz**, E. Castillo-Martínez, Vladimir Roddatis, Michel Armand, Teófilo Rojo. "Prussian Blue, $K_{0.86}Fe_2(CN)_6$, as new anode material in Li-ion batteries". – **1st poster prize**. 2nd Workshop in the Advances of Li-Battery Research. University of Liverpool. Liverpool, April 2014 (United Kingdom).

10.- Póster. **Mª José Piernas-Muñoz**, E. Castillo-Martínez, Vladimir Roddatis, Michel Armand, Teófilo Rojo."Prussian Blue as anode in Li-ion batteries and its reaction mechanism". 2nd International Forum on Progress and Trends in Battery and Capacitor Technologies – Power our Future 2014. Vitoria-Gasteiz, April 2014 (Spain).

11.- Poster. **Mª José Piernas-Muñoz**, E. Castillo-Martínez, Vladimir Roddatis, Michel Armand, Teófilo Rojo."Prussian Blue as anode in Li and Na-ion batteries". 1st Symposium on sodium batteries. Vitoria-Gasteiz, October 2013 (Spain).